ERASMUS MUNDUS JOINT DOCTORATE
INTERNATIONAL RELATIVISTIC ASTROPHYSICS PH.D.

PH.D. THESIS

Application and Analysis of the Induced Gravitational Collapse in some Gamma-ray Bursts - Supernovae

PH.D. CANDIDATE
Miloš Kovačević

THESIS ADVISOR
Prof. Remo Ruffini

Sapienza Università di Roma
Université de Nice – Sophia-Antipolis

Rome
Submitted: September 2017
Defended: April 2018

Abstract

The title of the thesis is related to a larger study by a scientific group which I have been part of during the PhD course. The study of the group is related to developing Fireshell model in order to explain gamma-ray bursts; Induced Gravitational Collapse model in order to explain their connection to supernovae; and interpreting individual gamma-ray bursts, and groups of them, within these models. The thesis is a compilation of various work done by me during the duration of the PhD course related to the topic stated in the title. Not everything done during the PhD is presented in the thesis mainly due to time limitations. One of the non-included work consists of analysis of high-energy data from numerous gamma-ray bursts obtained by Fermi-LAT and Fermi-GBM space-based detectors, automating such analysis, looking for peculiarities and trying to find patterns in it, and trying to determine weather such features are intrinsic or due instrumental effects.

The thesis is structured as follows: In Chapter 1 history of Gamma-ray burst discoveries and general conclusions which came from them will be presented. In Chapter 2 general information will be presented on the Fireball model, which is a mainstream model used to explain gamma-ray bursts. Then the general information on the Fireshell model will be presented. This will take a form of a short review of the work done by the group on the topic. In Chapter 3 the general information on the Induced Gravitational Collapse model will be presented. Again this will be a short review of the work done by the group. Since late 2013, I contributed in part to some of the analysis of high energy data and to lesser extent on statistics of gamma-ray burst observational properties.

In Chapter 4, I will present my work which started with systematic analysis of Swift-BAT and Swift-XRT data with the aims of detecting thermal black body emission in the late prompt phase of gamma-ray bursts. This involved close examination of data analysis techniques and writing Python scripts in order to automatize data analysis as much as possible. Then the results of several detected black bodies will be compared to each other in the rest-frame of gamma-ray burst host galaxy. Afterward the corrections due to relativistic expansion of the black body will be derived. Next a small simulation of spectrum from a black body with mildly relativistic expansion, and with varying velocity and temperature, will be done and the simulation applied to GRB 151027A. Finally the results will be compared to predictions of Induced Gravitational Collapse model. It was found that they are not in contradiction with the model.

In Chapter 5 the work which involved cross-correlation of gamma-ray burst and supernova catalogs in order to find potentially unnoticed connections up to mid 2014 will be presented. One probable such connection was found between Ic supernova and low-luminosity gamma-ray burst, and the rate of such events were calculated. It was found they overlap with previous estimates. I was one of the people leading the work. Next I will update the work with the same analysis up to year 2017 applying different statistical methods and involving more catalogs. The novel results indicate possible connection between short gamma-ray bursts and type IIn supernovae. The investigation of such possibility will

be carried out and its implications will be examined.

List of publications

- Kovacevic, M.; Izzo, L.; Wang, Y.; Muccino, M.; Della Valle, M.; Amati, L.; Barbarino, C.; Enderli, M.; Pisani, G. B.; Li, L.. (2014). A search for Fermi bursts associated to supernovae and their frequency of occurrence. A&A, 569, A108.

- Ruffini, R.; Wang, Y.; Enderli, M.; Kovacevic, M.; Bianco, C. L.; Muccino, M.; Penacchioni, A. V.; Pisani, G. B.; Rueda, J. A. (2015). GRB 130427A and SN 2013cq: A Multi-wavelength Analysis of an Induced Gravitational Collapse Event. ApJ, 798, 10.

- Ruffini, R.; Aimuratov, Y.; Becerra, L.; Bianco, C. L.; Chen, Y. C.; Karlica, M.; Kovacevic, M.; Melon Fuksman, J. D.; Moradi, R.; Muccino, M.; Pisani, G. B.; Primorac, D.; Rueda, J. A.; Wang, Y. (2017). On the nature of prompt emission, X and gamma ray flares and extended thermal emission in GRB 151027A. Submitted to ApJ.

- Ruffini, R.; Muccino, M.; Kovacevic, M.; Oliveira, F. G.; Rueda, J. A.; Bianco, C. L.; Enderli, M.; Penacchioni, A. V.; Pisani, G. B.; Wang, Y. (2015). GRB 140619B: a short GRB from a binary neutron star merger leading to black hole formation. ApJ, 808, 190.

- Ruffini, R.; Muccino, M.; Aimuratov, Y.; Bianco, C. L.; Cherubini, C.; Enderli, M.; Kovacevic, M.; Moradi, R.; Penacchioni, A. V.; Pisani, G. B.; Rueda, J. A.; Wang, Y. (2016). GRB 090510: A Genuine Short GRB from a Binary Neutron Star Coalescing into a Kerr-Newman Black Hole. ApJ, 831, 178.

- Ruffini, R.; Rueda, J. A.; Muccino, M.; Aimuratov, Y.; Becerra, L. M.; Bianco, C. L.; Kovacevic, M.; Moradi, R.; Oliveira, F. G.; Pisani, G. B.; Wang, Y. (2016). On the Classification of GRBs and Their Occurrence Rates. ApJ, 832, 136.

- Ruffini, R.; Muccino, M.; Bianco, C. L.; Enderli, M.; Izzo, L.; Kovacevic, M.; Penacchioni, A. V.; Pisani, G. B.; Rueda, J. A.; Wang, Y. (2014). On binary-driven hypernovae and their nested late X-ray emission. A&A , 565, L10.

- Ruffini, R.; Izzo, L.; Muccino, M.; Pisani, G. B.; Rueda, J. A.; Wang, Y.; Barbarino, C.; Bianco, C. L.; Enderli, M.; Kovacevic, M.. (2014). Induced gravitational collapse at extreme cosmological distances: the case of GRB 090423. A&A, 569, A39.

- Muccino, M; Bianco, C. L.; Izzo, L.; Wang, Y.; Enderli, M.; Kovacevic, M.; Pisani, G. B.; Penacchioni, A. V.; Ruffini, R. (2014). The genuine short GRB 090227B and the disguised by excess GRB 090510. GrCo, 20, 3.

- Ruffini, R.; Aimuratov, Y.; Bianco, C. L.; Enderli, M.; Kovacevic, M.; Moradi, R.; Muccino, M.; Penacchioni, A. V.; Pisani, G. B.; Rueda, J. A.; Wang, Y. (2015). Induced

gravitational collapse in FeCO Core-Neutron star binaries and Neutron star-Neutron star binary mergers. IJMPA, 30, 28n29.

- Ruffini, R.; Rodriguez, J.; Muccino, M.; Rueda, J. A.; Aimuratov, Y.; Barres de Almeida, U.; Becerra, L.; Bianco, C. L.; Cherubini, C.; Filippi, S.; Gizzi, D.; Kovacevic, M.; Moradi, R.; Oliveira, F. G.; Pisani, G. B.; Wang, Y. (2016). On the rate and on the gravitational wave emission of short and long GRBs. Arxiv, 1602.03545.

- Pisani, G. B.; Ruffini, R.; Aimuratov, Y.; Bianco, C. L.; Kovacevic, M.; Moradi, R.; Muccino, M.; Penacchioni, A. V.; Rueda, J. A.; Shakeri, S.; Wang, Y. (2016). On the Universal Late X-Ray Emission of Binary-driven Hypernovae and Its Possible Collimation. ApJ, 833, 159.

- Rueda, Jorge A.; Aimuratov, Y.; de Almeida, U. Barres; Becerra, L.; Bianco, C. L.; Cherubini, C.; Filippi, S.; Karlica, M.; Kovacevic, M.; Fuksman, J. D. Melon; Moradi, R.; Muccino, M.; Penacchioni, A. V.; Pisani, G. B.; Primorac, D.; Ruffini, R.; Sahakyan, N.; Shakeri, S.; Wang, Y. (2017). The binary systems associated with short and long gamma-ray bursts and their detectability. IJMPD, 26, 9.

- Ruffini, R.; Aimuratov, Y.; Becerra, L.; Bianco, C. L.; Karlica, M.; Kovacevic, M.; Melon Fuksman, J. D.; Moradi, R.; Muccino, M.; Penacchioni, A. V.; Pisani, G. B.; Primorac, D.; Rueda, J. A.; Shakeri, S.; Vereshchagin, G. V.; Wang, Y.; Xue, S.-S. (2017). The cosmic matrix in the 50th anniversary of relativistic astrophysics. IJMPD, 26, 10.

- Ruffini, R.; Wang, Y.; Aimuratov, Y.; Barres de Almeida, U.; Becerra, L.; Bianco, C. L.; Chen, Y. C.; Karlica, M.; Kovacevic, M.; Li, L.; Melon Fuksman, J. D.; Moradi, R.; Muccino, M.; Penacchioni, A. V.; Pisani, G. B.; Primorac, D.; Rueda, J. A.; Shakeri, S.; Vereshchagin, G. V.; Xue, S.-S. (2018). Early X-Ray Flares in GRBs. ApJ, 852, 53R.

Acknowledgments

I acknowledge the support provided by the Erasmus Mundus Joint Doctorate program through grant 2013-1471, awarded by the EACEA of the European Commission; support and help provided by colleagues and friends at Erasmus program, Sapienza University of Rome and ICRANet.

Contents

Abstract **i**

Contents **v**

Introduction **1**

1 Gamma-Ray Bursts **3**
1.1 History of GRB discoveries . . . 3
1.1.1 Vela . . . 3
1.1.2 CGRO-BATSE . . . 3
1.1.3 BeppoSAX . . . 5
1.1.4 Swift . . . 7
1.1.5 Fermi . . . 9
1.1.6 Other satellites and detectors . . . 10
1.2 Astrophysical conclusions and assumptions from observations . . . 10
1.2.1 Isotropic energy, luminosity and energy source . . . 10
1.2.2 Duration of a pulse and compactness problem . . . 11
1.2.3 Locations of GRBs and their progenitors . . . 12

2 Fireball and Fireshell Models **13**
2.1 Fireball Model . . . 13
2.1.1 Central engine . . . 13
2.1.2 Fireball evolution . . . 14
2.1.3 Shocks . . . 14
2.1.4 Jets . . . 16
2.1.5 Afterglow . . . 16
2.2 Fireshell Model . . . 17
2.2.1 Black holes . . . 17
2.2.2 Central engine . . . 18
2.2.3 Expansion of fireshell plasma . . . 20
2.2.4 P-GRB . . . 21
2.2.5 Extended afterglow . . . 21
2.2.6 Fitting the GRB . . . 23
2.2.7 Long and short GRBs in the fireshell model . . . 25

3 Induced Gravitational Collapse **27**
3.1 GRB-SN in the Fireball model . . . 27
3.2 Different episodes in GRB light curve . . . 28
3.3 The IGC . . . 29
3.4 X-ray afterglows of IGC GRBs . . . 33

3.4.1 Overlapping . . . 33
3.4.2 Very energetic GRB 130427A . . . 34
3.5 Binary systems and two families of GRBs . . . 35

4 Thermal X-ray emission in the late prompt - early afterglow phases 37
4.1 Data Analysis . . . 39
4.1.1 Swift BAT and XRT data . . . 39
4.1.2 Software . . . 40
4.1.3 Pile-up . . . 42
4.1.4 Other difficulties . . . 42
4.1.5 MCMC . . . 44
4.2 Preliminary results . . . 45
4.2.1 Two black bodies . . . 49
4.3 GRB 151027A . . . 51
4.3.1 Temperature from the first time interval . . . 53
4.3.2 151027A in the IGC scenario . . . 55
4.4 Thermal spectrum from relativistically expanding sphere . . . 55
4.4.1 Basic equation . . . 56
4.4.2 Non-expanding sphere . . . 57
4.4.3 Relativistic movement of a surface element . . . 58
4.4.4 Pulse from an expanding sphere . . . 60
4.4.5 Continuous emission from an expanding sphere . . . 63
4.4.6 Wave fronts from different velocities and temperatures . . . 69
4.5 Simulation of spectrum . . . 72
4.5.1 The code . . . 72
4.5.2 151027A . . . 76
4.5.3 Double black body . . . 79
4.6 Concluding remarks . . . 81

5 New GRB-SNe connections 83
5.1 Technical details . . . 86
5.1.1 SN catalog . . . 86
5.1.2 GRB catalogs . . . 89
5.1.3 Program scripts . . . 91
5.2 Analysis of long GRB - SN Ib/c connections, 2014 . . . 92
5.2.1 Statistics of potential connections . . . 93
5.2.2 The sample of Ib/c connections . . . 94
5.2.3 Discussion . . . 96
5.3 New statistical approach . . . 98
5.3.1 On randomness . . . 98
5.3.2 Confidence level . . . 99
5.3.3 Generating random positions and dates . . . 103
5.3.4 Removing same GRBs . . . 103
5.3.5 Time windows . . . 104
5.3.6 Example of changes to distributions for long Fermi GRBs and Ia SNe 104
5.4 Analysis of long GRB - SN Ib/c connections, 2017 . . . 105
5.4.1 The sample of Ib/c connections . . . 107
5.5 Analysis of short GRB - SN IIn connections . . . 110

5.5.1 The sample of BATSE short GRBs – SN IIn connections 112
5.5.2 Fermi short GRB – SN IIn connections 114
5.5.3 Short GRBs – IIn SNe, no direct evidence 116
5.5.4 Rates 121
5.5.5 Properties of IIn-GRBs 123
5.5.6 Mechanisms behind IIn-GRBs 125
5.5.7 Future work 127

Bibliography

Introduction

Gamma-ray bursts were discovered in the 1970s. They are transient astronomical phenomena lasting from fraction of a second to several tens or hundreds of seconds. They emit most of the radiation as γ-rays, mainly in the keV range, but also in the MeV and even GeV. The discovery of their redshifts in the '90s, which can range from 0.01 up to 8, helped to classify them as cosmological astrophysical phenomena. With the known distance (calculated from the redshift) it was possible to calculate isotropic energy emitted which can range from 10^{48} to 10^{55} erg. This is an enormous amount of energy, especially when considering it is released in the interval of tens of seconds - luminosity can reach $10^{53} - 10^{54}$ $\mathrm{erg/s}$. For comparison the total rest mass/energy of the Sun is about 2×10^{54} erg. Gamma-ray bursts are by far the most luminous objects on the stellar scale and consequently they are among the most distant observed objects. In the '90s a supernova was associated to a burst and since then many more associations were discovered. This means that gamma-ray bursts are a stellar phenomena, related to the "death" of a star, as opposed to, for example, active galactic nuclei which are galactic phenomena. Based on some basic astrophysical principals and observational evidence, gamma-ray burst emitting ejecta has to move at ultra-relativistic speed. In fact it is by far the fastest moving (known) object with velocities that can reach values of several hundred Lorentz factors. For comparison the jets of active galactic nuclei, the second most fastest objects, move with velocities on the order of 10 Lorentz factor.

The Collapsar model explains the central engine of gamma-ray bursts. Gamma-ray bursts happen when a massive star burns trough its nuclear fuel and the iron core of a star collapses into a black hole. The infalling material from the rest of the core and inner envelopes onto the black hole creates an ultrarelativistic jet along the rotation axes. The released gravitational potential energy is also responsible for supernova which accompanies gamma-ray burst. The rest of the scenario is explained within the Fireball model. The jet is composed of series of fireballs moving with ultrarelativistic but different velocities. The fireballs are thin shells within the jet cone consisting of photon-lepton plasma with small amount if baryons. The collision between these fireballs produces gamma-ray emission which is detected as gamma-ray burst. Collimated and boosted emission from an ultrarelativistic jet would explain enormous observed fluence.

Another way to explain gamma-ray burst dynamics is the Fireshell model and gamma-ray burst - supernova connection is explained by Induced Gravitational Collapse model. The basis for the latter is a close binary system composed of a Ic pre-supernova star and a neutron star. When the star explodes as supernova its ejecta accretes onto the companion neutron star. The neutron star then collapses into a black hole. The Fireshell model then states that gravitational energy of collapsing material into a black hole is completely converted, via process of vacuum polarization, into a relativistically expanding sphere of electrons, positrons and photons - the fireshell. When the fireshell sphere interacts with circum-burst medium, the emission occurs. The enormous isotropic energies of gamma-

ray bursts are explained by total conversion of gravitational potential energy to fireshell plasma, and by very high efficiency of fireshell emission.

CHAPTER 1

Gamma-Ray Bursts

This chapter contains some basic information on Gamma-ray bursts (GRB). Firstly the history of main GRB discoveries and instruments which made them will be presented. Then some observational features will be presented and general astrophysical conclusions and assumptions which come out of them.

1.1 History of GRB discoveries

This section will present in chronological order mayor observational discoveries on GRBs and spacecrafts-instruments which made them.

1.1.1 Vela

Vela satellites were launched by the US in the 1960s in order to monitor nuclear bomb detonations, namely to assure compliance with the 1963 Partial Test Ban Treaty. Satellites were equipped with gamma-ray and X-ray detectors.

On July 2, 1967 a burst (~ 10 s) of gamma-rays was detected. This was the first ever observed GRB - GRB 670702[1]. At the time it wasn't known where this GRB came from. After several more burst discoveries it was possible to crudely localize them based on different arrival time of bursts at different satellites. It was discovered that they didn't come from the Earth or the Sun. Therefore, they are of cosmic origin. Results from the Vela satellites were declassified in 1973 and astronomical community was introduced to a new phenomena. At that point nothing else was known about GRBs except their cosmic origin.

1.1.2 CGRO-BATSE

Next important discovery came from Burst And Transient Source Experiment, or BATSE for short. It was a gamma-ray detector on board of NASA's Compton Gamma-Ray Observatory (CGRO) satellite which operated from 1991 to 2000.

Thanks to the instrument capabilities BATSE detected about one GRB per day during its 9 year operation. BATSE also managed to localize most of them to within few degrees.

[1]The GRB naming convention follows the format GRB YYMMDD. In the case of multiple detections on a single day, additional letters B, C, D... are added to successive bursts while the first burst has a letter A as suffix.

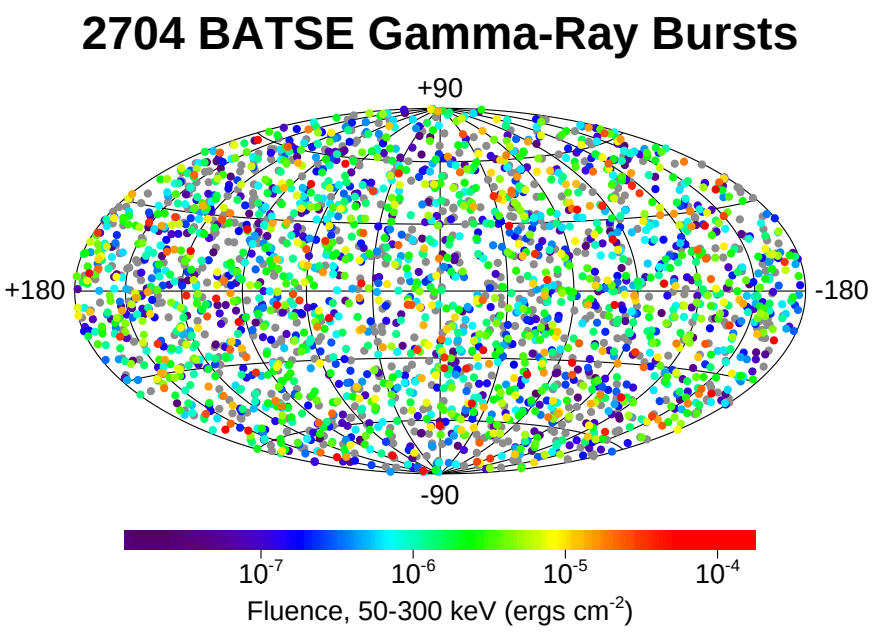

Figure 1.1: Galactic coordinates map of the 2704 GRBs detected by BATSE. The color code refers to the fluence of the bursts; gray dots indicate incomplete data. Credits: CGRO BATSE Team.

The map of GRB locations is given in Figure 1.1. The isotropic distribution was proof that they were not from the Milky Way galaxy. If they were, their distribution would not be isotropic but much more concentrated towards Milky Way plane. This strongly pointed towards cosmological origin although galactic halo and solar scenarios were not totally disregarded.

Another important discovery by the BATSE was GRB detailed temporal structure, i.e. the light curve.. The duration of a burst[2] can be from few milliseconds to several minutes. Light curves are composed of many pulses, usually with a fest rise and slow (exponential of power-law) decay, but can also be symmetrical. A single GRB can have pulses of different intensities and durations, which often overlap. Sometimes a GRB is composed of a single pulse. An example of several BATSE GRB light curves is given in Figure 1.2. Each GRB has a unique light curve.

Thanks to the BATSE and other gamma-ray detectors on board CGRO it was possible to observe the spectral shape of GRBs. It was discovered that the spectra of GRBs are non-thermal (no black body emission). The spectra can be described by the *Band* function (Eq. 1.1). This function represents two smoothly joined power-law functions.

$$N(E) = K \begin{cases} \left(\dfrac{E}{100}\right)^{\alpha} \exp\left[\dfrac{-E(2+\alpha)}{E_p}\right] & , \; E \leq \left(\dfrac{\alpha-\beta}{2+\alpha}\right) E_p \\ \left(\dfrac{E}{100}\right)^{\beta} \exp\left(\beta-\alpha\right) \left[\dfrac{(\alpha-\beta)E_p}{(2+\alpha)}\right]^{\alpha-\beta} & , \; E > \left(\dfrac{\alpha-\beta}{2+\alpha}\right) E_p \end{cases} \tag{1.1}$$

Here, N is the flux in units of: photons, per unit area, per unit time, per unit energy; α is the first power-law photon index (lower energy index); β is the second photon power-law index (high energy index); E_p is the peak energy. In most cases α parameter varies

[2]The duration of a burst is given by the T_{90} parameter. This parameter is the time interval in which 90% of energy is detected, starting from the point when 5% of energy is detected and ending at 95%.

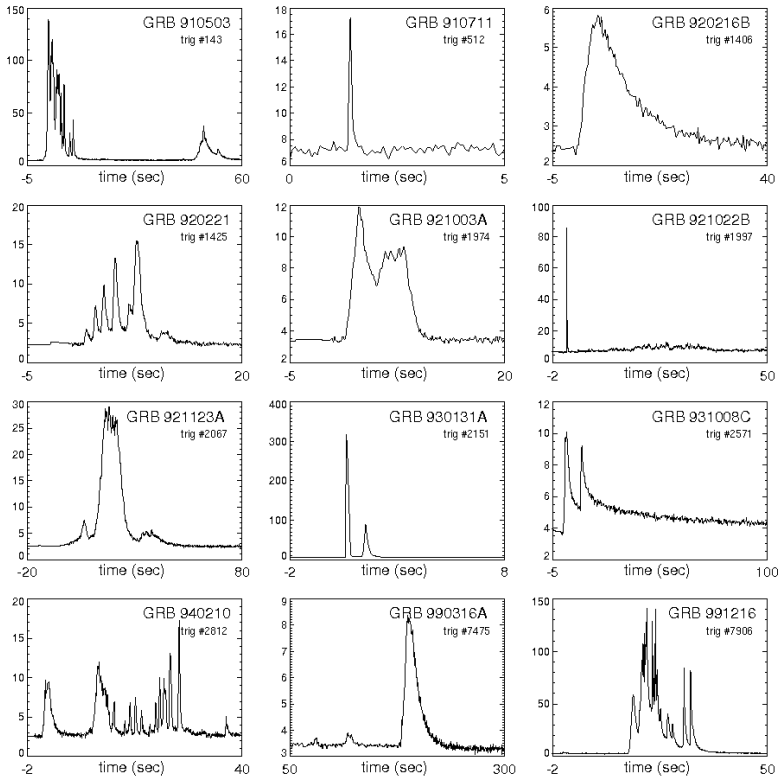

Figure 1.2: Twelve GRB ligth curves as seen by BATSE (in units of 10^3 counts/s) demonstrating their diversity in duration (milliseconds to tens of minutes), in temporal structure, and in pulse shape. Credits: BATSE Archive.

between $-1.5 \leq \alpha \leq 0.5$, β between $-2.5 \leq \beta \leq -2$, while the peak energy is in the range of $100\ \mathrm{keV} \leq \mathrm{E_p} \lesssim\ \mathrm{MeV}$. An example of typical GRB spectrum (the Band function) is given in Figure 1.3.

It should be noted that this is referred to time integrated spectra (T_{90} time interval). In most cases there is a spectral evolution within each pulse, such that E_p evolves from higher energy to lower.

Plotting the number of bursts vs. their duration, a bimodal structure can be seen (Figure 1.4) with separation around $2\ \mathrm{s}$. The first group is called *short* GRBs, and the second *long* GRBs. This division of GRBs was confirmed by subsequent detectors and it is the main division of GRBs to this day. The bimodal distribution fallows the spectrum hardness[3] , which is related to E_p. Therefore, the two groups of GRBs can be divided into *short-hard* and *long-soft*.

1.1.3 BeppoSAX

BeppoSAX was a satellite equipped with gamma-ray and X-ray detectors and it operated from 1996 to 2002. It was a product of scientific collaboration based in Italy and contribution by Netherlands. The name *Beppo* comes from physicist Giuseppe Occhialini and SAX stands for *Satellite per Astronomia a raggi X*, Italian for *satellite for X-ray astronomy*.

[3]Harder spectra have a bigger ratio of high energy photons to low energy ones.

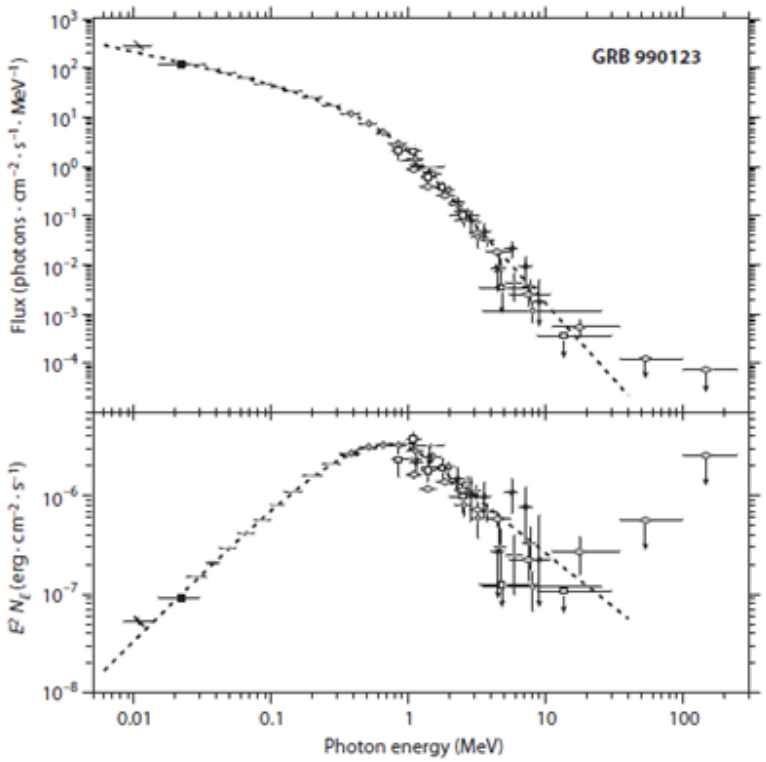

Figure 1.3: Flux spectrum (top) and spectral energy distribution (bottom) of GRB 990123, fitted with a Band function. Data points are from detectors on-board CGRO. Figure reproduced from (Briggs et al., 1999). Power-law functions on a log-log plot look like straight lines with power-law index being the slope. The plot $E^2 \times Flux$ vs. $\log E$ shows at which energy decade $d(\log E)$ most energy is released. Flux is multiplied by energy once since we are interested in energy, not number of photons, and the second time since we are interested in released energy per unit logarithm of energy $d(\log E)$, not per unit energy dE. On thr lower plot the average slope of first power-law will be $\alpha+2 \approx 1$, and the slope of second power-law will be $\beta+2 \approx -0.5$. This means that there is a peak and it is at E_p energy. This is the reason why they are GRB, i.e. why most of the energy is released in gamma-ray domain, because the peak is in the gamma-ray domain.

At this point it was predicted that GRBs should emit an *afterglow* - softer (in the X-ray domain), longer, weaker and slowly fading emission which starts after the standard emission ends. Thanks to its capabilities BeppoSAX managed to observe first ever afterglow in the GRB 970228 (Frontera et al., 1998). The intensity of the afterglow had been reducing slowly and could be detected for couple of days in the X-ray domain. The localization of the afterglow was precise and fast enough to allow follow up by the optical telescopes which detected the optical counterpart of the afterglow. The localization by the optical telescopes allowed the detection of the host galaxy of the GRB. This in turn allowed the redshift of the galaxy, and by extension the redshift of the GRB, to be measured and it turned out to be cosmological $z = 0.695$ (Bloom et al., 2001). Soon after more GRB redshifts were measured and they were all cosmological. This definitely proved that GRBs are cosmological objects. Knowing distance[4] it was possible to calculate the overall emitted energy[5] and luminosity of GRBs. This was the moment when it was discovered that GRBs could release very large amounts of energy at very short time intervals.

Thanks to the good and fast localization of GRBs by BeppoSAX, many optical follow

[4]Distance is calculated from the redshift assuming standard cosmological model (ΛCDM model).
[5]Total electromagnetic/photon energy of GRB.

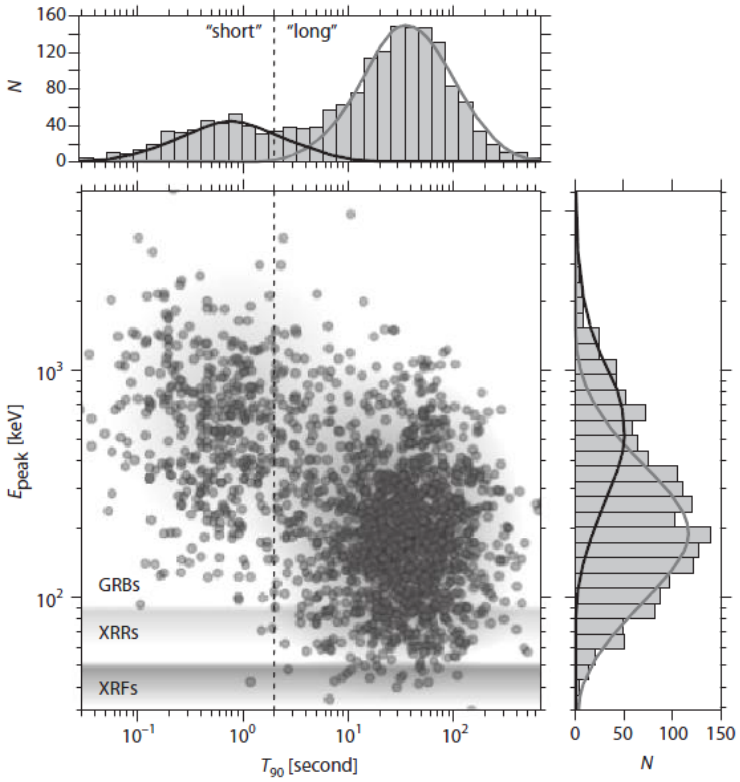

Figure 1.4: This diagram evidences the bimodal GRB distribution of BATSE events in terms of duration (horizontal axis) and spectral hardness (vertical axis), evaluated through the peak energy E_p of the spectral energy distribution. Two regions can clearly be distinguished, even if there is a significant overlap between them. Outset histograms show the number of events in appropriate time and energy bins.

ups were possible. This resulted in another important discovery. BeppoSAX detected long burst GRB 980425 and optical follow up showed a presence of a supernova about one day after GRB and at the same location. The supernova was a type Ic supernova, it was more luminous and had higher speed of expanding ejecta than typical core-collapse supernovae (Iwamoto et al., 1998). Although there were some hints of earlier GRB-supernova connection (Galama et al., 2000), this one is considered to be the first "good enough" evidence. GRB 980425 was a very low energy GRB $E_{iso} \sim 10^{48}$ erg and it wasn't certain at the time if all GRBs could be connected to supernovae or only low energy ones. In the coming years many more connections were discovered. Energy of GRBs varied from low to high and all the supernova were type Ic or Ib, very luminous, had high speed of expanding ejecta and were connected to long GRBs. At this point it was known that most of long GRBs are a stellar phenomena and connected to the "death" of a massive star, more precisely to the core collapse of a massive star without hydrogen envelope.

1.1.4 Swift

Swift is a satellite equipped with gamma-ray, X-ray and ultraviolet-optical detectors. It was launched in 2004 and is still operational. It is primarily NASA's project with strong participation from institutions in US, UK, Italy. The name *Swift* comes from the spacecraft's ability to rapidly slew.

One of the important discoveries by Swift is a detailed X-ray afterglow light curve

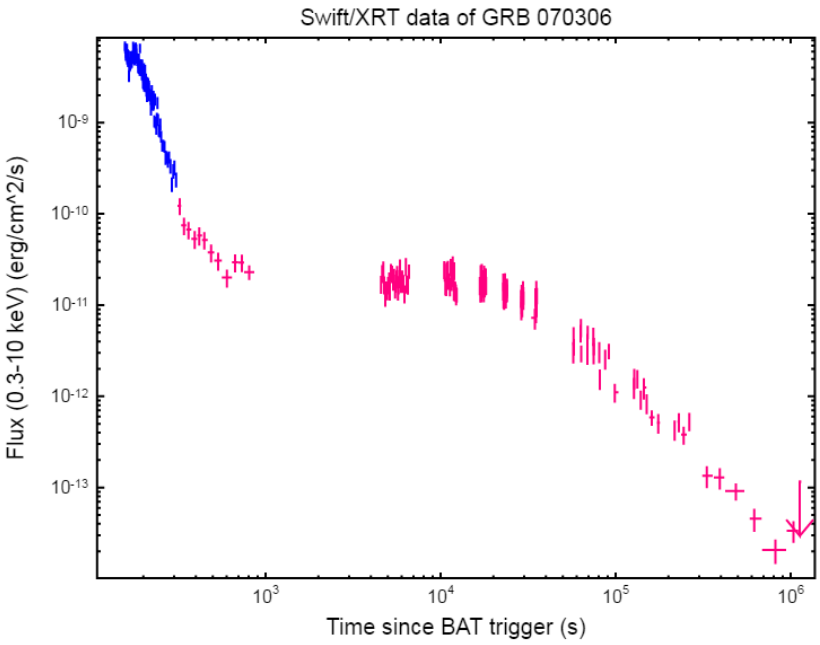

Figure 1.5: The afterglow of GRB 070306. The typical three phases can be seen - the steep decay, the plateau and the shallow decay. The light curve comes from XRT instrument ($0.3 - 10$ keV energy band) on board Swift. The flux is corrected for absorption which is present bellow 2 keV, i.e. the flux intensity is as if there is no absorption. The time is counted since the start of the GRB. Different colors correspond to different operation mode of XRT. The gaps are due to occultation of GRB by Earth since Swift satellite orbits Earth every 90 minutes. Credits: Swift Archive and University of Leicester.

(Figure 1.5). The typical structure of the afterglow is: it starts with a steep decay just after the main part (the *prompt* phase) of the GRB. After that there is a kind of *plateau* where intensity is almost constant. After that the emission continues to fade as a power-law with shallow decay. In some cases *flares* are present in the afterglow. They have a shape of the pulse similar to pulses in the prompt emission but last much longer and are softer and weaker. They are, however, spectrally harder and brighter than the underlying continuum afterglow emission. In other cases light curves don't follow standard shape, but have, for example, single power-law decay from the start.

Thanks to Swift's capabilities, especially to rapid and precise localization of GRB, many optical follow-ups were possible. This helped in discovering many GRB host galaxies and redshifts[6]. Up to the year 2016 Swift detected about 1000 GRBs and about 300 of them have a measured redshift (distance). Swift is by far the satellite most responsible for large number of GRB redshift measurements. Numerous optical follow-ups also allowed discoveries of many other connections between GRBs and supernovae.

Examination of the host galaxies helped to further define the long and short division of GRBs. Long GRBs tend to appear in spiral (young) galaxies, especially in the parts of significant star formation. Short GRBs tend not to have preference for galaxy type or a specific position within the galaxy.

Swift raw (and semi-processed) data are publicly available few hours after observation and there are publicly available software for the analysis of this data as well as detailed

[6]Redshift can be determined from the spectral lines in the optical afterglow of a GRB or the host galaxy.

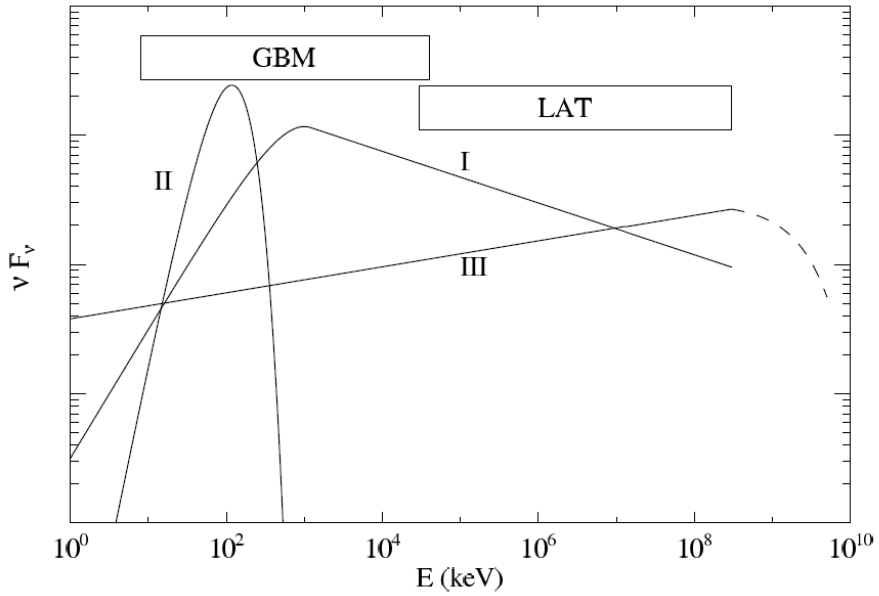

Figure 1.6: Three components in the prompt emission spectra found by Fermi: Band, underlying power-law and thermal.

explanation on their usage[7].

1.1.5 Fermi

Fermi Gamma-ray Space Telescope, or just Fermi, is a satellite launched in 2008 and is still operational. It is NASA's project with participation from institutions in US, France, Germany, Italy, Japan, and Sweden. It carries gamma-ray instruments with a very wide range of energy coverage - from few keV up to several hundred GeV. Formally known as GLAST (Gamma-ray Large Area Space Telescope) it was renamed in honor of physicist Enrico Fermi.

Fermi capabilities helped to further discover properties of the prompt emission. Aside from the Band function, additional components were discovered (Figure 1.6). In some GRBs a black-body thermal component was found, usually at lower energies than the Band's E_p. Thermal component shows evolution such that temperature of the black body monotonically decreases. Another component was an underlying power-law which can start from few keV all the way up to GeV range.

Thanks to its wide field of view Fermi observed many bursts. Up to 2016 Fermi observed about 1600 GRBs, managed to capture their spectra and spectra evolution.

Fermi also managed to discover that afterglows can have a high energy component (GeV domain). In fact, the most energetic photons discovered were detected after the prompt emission, during the afterglow. The record braking high energy photon came from GRB 130427A. It had an energy of $95\ \mathrm{GeV}$ ($128\ \mathrm{GeV}$ in the rest frame of the burst). It was detected about $250\ \mathrm{s}$ after the beginning of the burst, significantly after the prompt emission (Ackermann et al., 2014).

Fermi raw (and semi-processed) data are publicly available few hours after observation and there are publicly available software for the analysis of this data as well as detailed

[7] `http://www.swift.ac.uk/`

explanation on their usage[8].

1.1.6 Other satellites and detectors

The five mentioned missions were among the most crucial ones in GRB observations. The satellites and detectors on them were at the time most advanced in the field of GRB observations in the gamma-ray and X-ray domain. There were/are other satellites equipped with gamma-ray and X-ray detectors which complement the five mayor missions and help to improve statistics on GRB parameters such as host galaxy type, distance, duration, spectra, etc. These are: Wind-Konus, AGILE, INTEGRAL and XMM-Newton, Chandra, etc.

The most important energy interval for the study of Gamma-ray bursts is, of course, the gamma (and X-ray) domain. Optical detectors also played, and still do, important role. Sub arc-second localizations, position of GRB within the host galaxy, redshift measurement, etc. wouldn't be possible without optical observations. When it comes to GRBs, the more important optical (and near infra red) detectors today are: VLT, LBT, Keck Telescopes; GROND, PROMPT, ROTSE, and LT, Faulkes Telescopes, RATIR and others.

There are also radio telescopes observing the radio counterpart of the afterglow. These include VLBI, VLA, GMRT, ATCA, AMI, WSRT, etc. Radio afterglow can be detected for years after the GRB. Radio detectors can give the most precise localization ($\sim$ milliarcsecond). GRB 030329 was relatively close and had strong emission in the radio domain. Observations of the afterglow in the tens of days after it occurred made it possible, thanks to high precision of radio telescopes, to actually measure the angular size of a GRB emitting material. From there, knowing the redshift (distance), it was calculated that emitting ejecta in the afterglow phase was moving with relativistic speed[9] (Taylor et al., 2004).

Up to now GRBs were not detected in the TeV range. The main detectors observing in this range are MAGIC, HESS, VERITAS, HAWC.

1.2 Astrophysical conclusions and assumptions from observations

In this section astrophysical conclusions and assumptions which come from GRB observations will be presented. These are not really models but some facts and assumptions which come from basic physical principles. These are basis for different models.

1.2.1 Isotropic energy, luminosity and energy source

With the observed fluence and known distance, it is possible to calculate released isotropic energy E_{iso}[10]. This quantity can reach the values of $E_{iso} \sim 10^{54} - 10^{55}\ \mathrm{ergs}$. This is enormous amount of energy for a solar size source[11]. For comparison, maximum energy emitted by some supernovae in the form of photons is $E_{iso} \sim 10^{52}\ \mathrm{erg}$ (Dong et al., 2016). Moreover this amount of energy is released in a relatively short time period of tens of

[8] `http://fermi.gsfc.nasa.gov/ssc/`

[9] Lorenz factor γ 1, but not $\gamma \gg 1$

[10] The term *isotropic energy/luminosity* is the amount of energy/luminosity calculated assuming isotropic emission of an object.

[11] Weather one, two or more stars are involved, the system is stellar sized, unlike AGNs, for example, which is a system on the order of millions of stellar masses.

seconds, making GRBs the most luminous known objects in the universe with maximum $L_{iso} \sim 10^{53} - 10^{54}\ \mathrm{erg/s}$. This is the reason why it was possible to detect them all the way up to redshift 8. The most luminous ones could be detected even if they had been beyond redshift 10. The E_{iso} and L_{iso} refer to photons. The total released energy of GRB is even higher.

One of the objects that can produce this amount of energy is a black hole. The most energetic stellar phenomena, which are relatively understood, are core-collapse supernovae. Their energy comes directly from gravitational potential energy, i.e. from the kinetic energy of in-falling stellar material. This energy is later transformed into energy of the supernova (neutrinos, kinetic energy of ejecta, photons). It is reasonable to assume that a black hole is responsible for GRB energetics since the potential gravitational energy is even grater than the one neutron star has. All the supernova associated to GRBs were core-collapse SN and in vast majority of cases, when supernova could have been detected[12], it was detected. This further points to a scenario where a black hole is present and where GRBs are created when the inner core of the star collapses into a black hole.

Even with the black hole present it is hard to explain GRB enormous energies by conventional means and known astrophysical mechanisms. The amount of released energy can be few orders of magnitude smaller than E_{iso} if GRBs emit energy in the form of jets which are pointed towards the Earth. When there is a material falling onto a compact source - a super massive black hole in active galactic nuclei or stellar size black hole in X-ray binaries, the formation of jets occurs. It is reasonable to assume that jests also form in GRBs. Furthermore, it is reasonable to assume that a significant part of GRB total energy should be in the form of photons (gamma-ray photons), unlike standard core-collapse supernova where photons make up about 0.01 - 0.1 % of total supernova energy. This *efficiency* is important factor since if it is higher the total energy can be lower for a given E_{iso}.

There are also ideas in which energetics is explained by newly formed millisecond magnetars where rotational energy of the neutron star is transformed into GRB energy. The formation of the jet and high efficiency of conversion of total energy in to photons is also required.

1.2.2 Duration of a pulse and compactness problem

Thanks to the high temporal resolution of instruments the fine structure of the prompt light curve was observed. The shortest pulses have a duration on the order of $\delta t \approx 10\ \mathrm{ms}$. This can give information on the upper size of the emitting region. If an emitting region has a certain size and it emits an infinitesimally short pulse, the instrument far away would still detect a pulse with a duration of $\delta t \approx R/c$ where R is the radius of the source and c is speed of light. This means that an upper boundary on the GRB emitting region is $R \leq c\delta t \approx 3000\ \mathrm{km}$.

With typical values of E_{iso}, spectral shape, and R (volume), an average density of high energy photons can be calculated. From there the optical depth for electron-positron pair creation $2\gamma \rightarrow e^{\pm}$ can be estimated. This should be significant process since there are many photons with energies on the order of electron rest mass/energy ($0.511\ \mathrm{MeV}$) or higher. For typical GRB parameters it turns out that the value for this optical depth is very high, on the order of $\tau_{\gamma\gamma} \sim 10^{15}$. The process $2\gamma \leftrightarrow e^{\pm}$ would take place with very high rate and the higher energy photons would be trapped inside and with thermal

[12] With the current optical telescopes supernova can be detected up to redshift $z \approx 1$.

spectrum. Only small part from the surface would manage to escape and wouldn't produce the observed flux. Also, their spectrum should be thermal while observations show that higher energy photons have a power-law spectra (high energy part of the Band function). Another process that would take place with the presence of $e^{\pm}$ is Compton scattering of lower energy photons onto $e^{\pm}$. This process would significantly increase optical depth for lower energy photons and their number should be smaller and spectrum thermal - which is clearly against observations. This problem is called *compactness problem*.

The solution to this problem is if assuming that emitting region expands towards the Earth with ultra-relativistic speed[13]. First: The energy of the photons is boosted by expanding emitting region[14]. Photons have smaller energy in the rest frame of the emitting region then observations suggests and there would be less high energy photons able to undergo electron-positron pair creation. Second: the observed duration of a pulse wouldn't imply such a compact source. With emitting region expanding towards the Earth, a large size one would produce much shorter pulses than if it were not expanding.

For typical values of GRB parameters, in order for opacity to be low enough $\tau \sim 1$ so that material is transparent, relativistic speed of the emitting region should be on the order of $\gamma \sim 100$ and in some GRBs $\gamma \sim 1000$. This makes GRBs objects with the fastest moving material in the universe. For comparison, active galactic nuclei jets are moving with Lorentz factor in the range of $\gamma \sim 2 - 20$ while the ones observed in our galaxy have speed $\gamma \sim 2$.

1.2.3 Locations of GRBs and their progenitors

With the arc-second and sub-arcsecond localizations of GRBs it was possible to determine their location within the host galaxy. Long GRBs tend to occur in the most luminous parts (high star formation) of star-forming galaxies. Together with their connection to Ib/c SNe and requirement for a black hole, this points to the conclusion that progenitors of long GRBs are massive stars. Short GRBs don't seem to have a preference for the galaxy type or a location within the galaxy. They can even be found at large distances from the host galaxy center. Also they are not connected to supernovae. This, coupled with their short duration, points towards merger of compact objects - two neutron stars or a neutron star and a black hole.

[13] Speed with Lorentz factor on the order of $\gamma \sim 10 - 100$ or higher.

[14] The energy is first boosted by expanding plasma and later lowered by expansion of the universe. The second process is much lesser than the first and not relevant here.

CHAPTER2

Fireball and Fireshell Models

In this chapter main properties of the Fireball and the Fireshell model will be presented.

2.1 Fireball Model

In this section main properties of the Fireball model will be presented. This model was developed during the '90s, after CGRO-BATSE data came in, and is generally accepted model. There are open questions and uncertainties, and some details in the model were added and modified as new data from GRBs arrived during the 2000s and 2010s. However, the underling general picture still remains unchanged. The numerical values of certain important parameters in the model - such as Lorentz factor of the fireball, distance from central source, jet opening angle, peak energy of radiation, etc. - were derived taking typical values of parameters from GRB and other astronomical observations and applying them in the model. Since the model describes time evolution of GRB mechanism, the uncertainties in the model become more important as this time evolution progresses, and the model branches into several different scenarios later on. Which course is the most probable one can also depend on a specific GRB. This section presents the model as it describes time evolution of GRB mechanism and presents a typical course GRB takes (Figure 2.1). The main summary of the model can be found, for example, in (Piran, 1999), (Mészáros, 2006), (Kumar and Zhang, 2015).

2.1.1 Central engine

The fireball model doesn't go into details about the progenitors of GRB and the mechanism of creating large amounts of energy. It is probable that energy can be obtained from gravitational potential energy of collapse of a massive star core to a black hole (BH), merger of two compact objects into a BH, or, from rapid spin down of a magnetar. The scenario starts with large amount of energy $E_{tot} \sim 10^{54}$ erg being released in a relatively small volume (radius r_0). This energy will be in the form of gravitational waves, neutrinos and a *fireball* - a ball of electrons and positrons ($e^{\pm}$), gamma-rays (γ) and small amount of baryons. The amount of energy in the fireball is a fraction of total energy, on the order of $E_0 \sim 10^{50} - 10^{52}$ erg. The initial radius is $r_0 \sim 10^7$ cm which is several Schwarzschild radii of an ensuing BH. Gravitational waves and neutrinos will pass trough the fireball almost

without interaction.

2.1.2 Fireball evolution

The fireball consists of electrons and positrons, gamma-rays and small amount of baryons - mostly protons with total mass of $M_0 \sim 10^{-5}\ \mathrm{M}_\odot$. All these elements are coupled via electromagnetic interaction to each other and make up a single system. The amount of released energy is much greater than rest energy of baryons $E_0 \gg M_0c^2$. A parameter to describe the amount of baryons is defined as $\eta \equiv E_0/M_0c^2$. Pair annihilation between $e^\pm$ will create 2 γ photons and they will in turn create $e^\pm$ pairs, etc. This process $e^\pm \leftrightarrow 2\gamma$, along with Compton scattering, will make the fireball optically thick and in thermal equilibrium. The initial temperature is on the order of $kT_0 \sim 1\ \mathrm{MeV}$.

Due to enormous internal pressure the fireball will expand outwards. Because the fireball is optically thick, only photons from the surface will escape while the majority of them will stay inside the fireball system, so the fireball expansion can be considered adiabatic. Since $E_0 \gg M_0c^2$ the internal fireball pressure will be dominated by radiation which gives the adiabatic index of $\gamma_\alpha = 4/3$. Assuming radiation-dominated adiabatic expansion and considering relativistic dynamics gives the next picture:

The internal energy of the fireball will be transferred into bulk (outward) kinetic energy of baryons which are moving spherically outwards. The Lorentz factor Γ of baryons, and fireball as a whole, will increase linearly with radius r (distance from the BH) until it reaches value on the order of $\Gamma_{max} \sim \eta$ with numerical value on the order of $\Gamma \sim 10^2$. The (saturation) radius at which this happens is on the order of $r_s \sim r_0\eta$ with numerical value of $r_s \sim 10^9\ \mathrm{cm}$. After this the Lorentz factor will remain constant and the fireball will continue expanding with constant speed. At his point most of the fireball energy will be in the bulk kinetic energy of protons.

With expansion the fireball will actually have the form of a spherical shell. The width of a shell is $\delta r_0 \sim r_0$ and the initial spreading of the shell due to internal pressure is negligible. The spreading of the shell will reach significant values well beyond saturation radius r_s.

When the rest-frame temperature inside the fireball drops to value of $kT \approx 20\ \mathrm{keV}$, the reaction $2\gamma \rightarrow e^\pm$ stops and the last of $e^\pm$ annihilate. For typical values this happens before saturation radius r_s. However, there are still e^- which are associated to protons and, due to Compton scattering between photons and electrons, the fireball is still optically thick. The (photospheric) radius r_{ph} where the optical depth reaches value of $\tau \sim 1$, i.e. where the fireball becomes optically thin, is beyond the saturation radius r_s. Typical value is $r_{ph} \sim 10^{12}\ \mathrm{cm}$. At this point all the photons will escape and their spectrum will be thermal. This may explain thermal emission in some GRBs detected by Fermi. However, the spectra of most GRBs is highly non-thermal. Moreover, most of the fireball energy is in the form of bulk kinetic energy of the protons and only a small fraction is in the thermal-spectrum photons. This is highly inefficient way to produce radiation from the fireball energy. In order to have significant thermal emission, additional processes should take place that would boost the thermal spectrum photons to higher energies and intensity.

2.1.3 Shocks

In order to achieve higher efficiency the bulk kinetic energy of the protons needs to be transformed to radiation when the fireball is optically thin. The best assumption on how

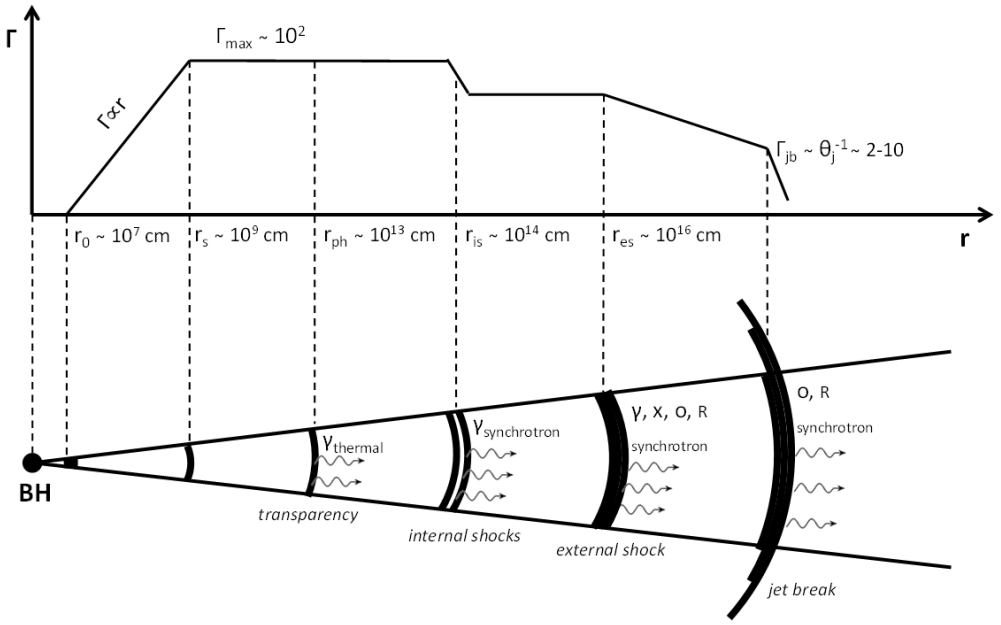

Figure 2.1: Evolution of fireball(s) and typical values for their Lorentz factor Γ and distance from the black hole r.

to do this is via shocks. When the fireball shell hits a standing or slower moving matter, a shock between two mediums will occur. The interaction between two mediums will happen via chaotic electric and magnetic fields (*collisionless shock*) and will increase internal energy (random kinetic energy) of particles (protons and electrons) in the mediums. Most of the energy in the fireball plasma is in the kinetic energy of protons but the shock will cause part of this energy to be transferred to electrons. The shock will also accelerate electrons via process *first order Fermi acceleration* to a power-law energy spectrum. Due to presence of magnetic fields a synchrotron emission from electrons is expected. The synchrotron emission from a power-law distributed electrons is a natural explanation for the GRB broken power-law spectrum. Photons produced by this emission are in the keV, MeV range. It is also possible that inverse Compton scattering of keV-photons onto accelerated electrons will occur as well as $2p \rightarrow 2p + \pi^{\circ} \rightarrow 2p + 2\gamma$ interaction, both of which could produce photons in the MeV and GeV range.

At one point the fireball shell has to hit the external medium which has surrounded the star before collapse. If only this *external shock* is present it would produce only one peak in the light curve. This could be the case for single peak GRBs. In order to explain general multi-peak GRB light curve a series of shocks needs to happen. This is possible if the central engine produces several fireballs over some period of time and with different properties so they accelerate to different Lorentz factors. When the faster shell caches up with the slower one, a shock occurs. Each of these *internal shocks* would then be responsible for each peak in the GRB light curve. After the collision two shells merge into a single shell. For typical parameters of GRBs, the internal shocks can transform about 5-20% fireball energy to radiation. The internal shocks take place around $r_{is} \sim 10^{13}$ cm.

The afterglow is created when the shell(s), which have all merged together, hit the external medium, either interstellar medium or an ejected material (wind) from a progenitor star.

The shock, either internal or external, in the text above is the *forward shock*. In both

cases there will also be a *reverse shock*. When the two mediums collide, both of them will have shocked and unshocked zones. The forward shock is at the boundary of unshocked outer medium and shocked outer medium. The reverse shock is at the boundary of shocked and unshocked internal medium. The properties of reverse shocks are such that radiation produced by them will be synchrotron as well but the peak of emission should be at lower energies and the emission should be lower in intensity. Reverse shocks are used to explain optical flashes during the prompt emission in some GRBs.

2.1.4 Jets

Isotropic energy of GRBs can reach values of $E_{iso} \sim 10^{54} - 10^{55}\ \mathrm{erg}$ and this is only the energy in the form of photons. The fireball energy is greater then this and the total energy even more so. In order to explain such high energies with a single star, a fireball, and the consequent radiation, is expected to be highly collimated, i.e. in the form of a narrow jet. Therefore, the fireball is actually a small part of a spherical shell moving with high Lorentz factor away from the BH.

In the non-jet/spherical case of a fireball which is moving with high Lorentz factor $\Gamma \gg 1$, an element of the shell only interacts with the surrounding elements if they are very close, within a light cone (interaction cone) of half angle of Γ^{-1} while it is decoupled from the rest of the fireball shell. Furthermore if the jet half angle is larger then the half angle of interaction $\theta_j > \Gamma^{-1}$, the element in the jet "doesn't know" whether it is in a jet or a sphere. This means that in the jet case of the fireball, the behavior will be similar as in the spherical case once $\Gamma \gg 1$. Also, while $\Gamma \gg 1$ the jet expands too rapidly in radial direction (away from the BH) and the sideways expansion of the jet is negligible. Therefore, main results derived from the spherical case then hold also for the jet case.

2.1.5 Afterglow

When the fireball(s) finally reach the external medium, either interstellar medium or a stellar wind, an afterglow is created. Just like in the internal shock case this *external shock* will accelerate electrons which will radiate via synchrotron process. The main difference is that this shock will happen on a longer time scale, Lorentz factor will decrease more slowly, electrons will radiate more in the soft X-ray domain ($\sim 10\ \mathrm{keV}$) as well as in optical and radio, and the intensity will be lower and longer lasting. Typical value for distance at which external shock happens is $r_{es} \sim 10^{16}\ \mathrm{cm}$.

At some point in the afterglow phase Lorentz factor Γ of the fireball/jet will lower to value of $\Gamma \sim \theta_j^{-1}$, numerical value around $\theta_j \sim 5^\circ$ and $\Gamma_{jb} \sim 2 - 10$. Before this point most of the radiation came only from part of the jet $\theta \sim \Gamma^{-1}$ due to relativistic speed of the jet. After this point the entire jet is visible and the emitting surface will not continue to increase but will remain constant. Another important factor is that when $\Gamma \sim \theta_j^{-1}$ the jet will start to spread sideways significantly and accumulate much more medium matter which will cause Γ to decrease more rapidly. These two factors will cause rapid decrease in luminosity which is referred to as the *jet break*. Since the radiation across all the bends comes from the same mechanism in the afterglow phase, the jet break, which is caused by the geometrical effects of the jet, will cause the luminosity to decrease in all the bands at the same time, i.e. jet break should be achromatic.

Spreading of the jet after $\Gamma \sim \theta_j^{-1}$ will also cause the jet to become visible in the direction it wasn't visible before. The observer along this direction would miss the prompt

emission and the early phases of the afterglow but would see afterglow in the late phase, after jet brake. These kinds of afterglows are referred to as *orphan afterglows*. They haven't been discovered so far, probably due to observational difficulties.

2.2 Fireshell Model

In this section main properties of the Fireshell model will be presented. The basis of the model revolves around extracting large amounts of energy from a charged black hole (BH). This is done via process of electron-positron pair creation from strong electric field - a type of *vacuum polarization*. The model was being developed during the '70s focusing on BHs independently of GRBs. At the time little was known about GRBs, namely weather they are cosmological objects (large E_{iso}) or not. In the late '90s with the first measurements of GRB redshifts - which meant $E_{iso} \sim 10^{53}$ erg - the model received new attention in the contexts of GRBs. The model could naturally explain large values of E_{iso} without the need to assume jetted emission. The subsequent detection of some bursts with $E_{iso} \sim 10^{54}$ or even 10^{55} erg in the years and decades to follow, further strengthen this position. Central engine in the Fireshell model is the main aspect of the model. The fireshell model also directly explains the origin and gives precise dimensions for the ball/shell of electrons, positrons and subsequent gamma-rays, a system which is termed *fireball* in the Fireball model and *fireshell* in the Fireshell model. From this point on system evolves similarly like in the Fireball model although there are some key differences.

Review of the Fireshell model and associated topics can be found in (Ruffini et al., 2007a) which is a summary based on published papers, conference proceedings, workshops and other media prior to the end of 2007. Work revolving around black holes and energy extraction can be found in (Ruffini and Wheeler, 1971; Christodoulou and Ruffini, 1971; Damour and Ruffini, 1975; Preparata et al., 1998; Ruffini and Vitagliano, 2002; Cherubini et al., 2002; Ruffini et al., 2003b; Ruffini and Vitagliano, 2003; Cherubini et al., 2009; Ruffini and Xue, 2011; Han et al., 2012; Belvedere et al., 2012) and others. Physics of electron-positron pairs created from critical electric field is covered in (Ruffini et al., 2003c, 2007b; Aksenov et al., 2007; Kleinert et al., 2008; Aksenov et al., 2010; Han et al., 2010; Benedetti et al., 2011) and others. Initial evolution of the fireshell plasma, up to the point of reaching interstellar medium, and its radiation are described in (Ruffini et al., 1999, 2000; Bianco et al., 2001) and others. Interaction of fireshell with interstellar medium and its radiation are studied in (Ruffini et al., 2001a,b, 2002; Bianco and Ruffini, 2004; Ruffini et al., 2004b, 2005b; Bianco and Ruffini, 2005c,a, 2006) and others. Application of fireshell model to specific bursts can be found in (Ruffini et al., 2004a, 2005a; Bernardini et al., 2005; Ruffini et al., 2006; Bernardini et al., 2007; Caito et al., 2009, 2010; de Barros et al., 2011; Patricelli et al., 2012; Muccino et al., 2013a,b) and others.

This section will describe the Fireshell model as it describes time evolution of a GRB system (Figure 2.3) starting at energy extraction from black holes.

2.2.1 Black holes

Black holes (BH) can be divided into four categories based on rotation and electric charge. The simplest case is the non-rotating and non-charged BH - the Schwarzschild BH. Non-rotating but charged BH is called the Reissner–Nordström BH. Rotating but not charged BH is called Kerr BH. Black hole that is both rotating and charged is called Kerr–Newman BH.

The total energy of the BH system can be described as:

$$E^2 = \left(M_{ir}c^2 + \frac{Q^2}{4M_{ir}} \frac{c^2}{G} \right)^2 + \frac{L^2}{4M_{ir}^2} \frac{c^6}{G^2} \tag{2.1}$$

where G is gravitational constant, c is the speed of light and M_{ir} is *irreducible mass*. In CGS[1] units Coulomb's constant is set to $k_e \equiv 1$. This equation was derived from Einstein-Maxwell equations - general relativity in combination with Maxwell electromagnetic laws.

First term $M_{ir}c^2$ is the rest mass/energy of the BH. Second term related to charge Q is equal to energy of electric field. If the BH is not charged then this term is zero. Last term related to angular momentum L corresponds to rotational energy. If the BH is not rotating this term is zero. If a mass M of the BH system is defined as $E = Mc^2$ than this energy/mass M incorporates also energy from electric field and rotation along with the "real" mass M_{ir}.

Einstein-Maxwell equations for the BH system also give limitation on the maximum angular momentum and maximum electric charge a BH can have for a given mass. This in turn gives maximum amount of rotational energy and electric (electromagnetic) energy for a given value of total energy of BH system. In the case of Kerr BH maximum amount of rotational energy BH can have is about 29% of the total energy E. In the case of Reissner–Nordström BH, maximum amount of electromagnetic energy is exactly 50% of the total energy E. For both rotating and/or charged BH it is theoretically possible to extract this energy.

Kerr BH "drags" the space around it in the direction of rotation. Because this effect is present outside the event horizon it is possible to interact with the BH system in such a way to extract its rotational energy. This can be done either by sending a particle in specific orbit around BH which then decays into two particles, or by use of magnetic fields. Theoretically all the rotational energy of a BH can be extracted in which case BH stops rotating and becomes a Schwarzschild BH.

Reissner–Nordström BH has an electric field which is present outside the event horizon. The field was created by charged progenitor star (or material surrounding it). When it fell inside the event horizon during a collapse to the BH, its electric field outside the horizon remained. Because of this it is possible to extract energy of the electric filed. This can be done by a process of vacuum polarization of the field itself, or by the decay of outside particles into two oppositely charged particles. Theoretically all the electromagnetic energy of a BH can be extracted in which case BH stops being charged and becomes a Schwarzschild BH.

Schwarzschild BH has only a stationary gravitational field outside the event horizon and any interaction with it cannot decrease the BH mass/energy which is given by $E = M_{ir}c^2$. The precise definition of irreducible mass/energy (in any BH type) is that it is a part of the BH system energy that cannot be lowered, only increased[2].

2.2.2 Central engine

Extracting energy from a charged black hole via vacuum polarization is the key aspect of the fireshell model.

[1] The centimetre–gram–second system of units.

[2] By means of processes within Einstein-Maxwell framework, not counting quantum processes such as Hawking radiation.

The model was fully developed for a non-rotating charged BH, i.e. Reissner–Nordström BH. It will be refereed to as *electromagnetic black hole* (EMBH). The energy equation 2.1 for this system reduces to:

$$E = M_{ir}c^2 + \frac{Q^2}{4M_{ir}}\frac{c^2}{G} \tag{2.2}$$

Electric field $\mathcal{E}$ of EMBH behaves almost as electric field of a charged particle $\mathcal{E} = Q/r^2$ (CGS units, $k_e \equiv 1$). This electric field extends from the event horizon r_+ out to infinity. As stated before maximum charged BH has an amount of electric energy of 50% of total BH system energy E.

Within the framework of quantum field theory (QFT), namely quantum electrodynamics (QED), vacuum is not simply "empty space" but has a certain energy associated to it. In the presence of electric filed this energy reacts with it. One of the consequences is *vacuum polarization*. Much like in the ordinary polarization of dielectrics vacuum polarization reduces the initial electric field. Also, as dielectric breaks down when electric field reaches a certain critical value, vacuum also has a "breaking" point in which case an electron-positron pairs are created out of vacuum. The stronger the electric field more likely this process becomes. The process becomes significant when electric field reaches critical value of $\mathcal{E}_c = \frac{m_e^2 c^3}{e\hbar} \sim 10^{16}\ \mathrm{V/cm}$, where m_e is electron/positron mass, $\hbar$ is reduced Planck constant. This is also the limit where other QED effects come into play. The value of $\mathcal{E}_c$ is so large that it is beyond any contemporary experimental technique. However, electric field around EMBH can easily reach this value or much higher.

The volume around EMBH where electric field strength is larger then critical is called the *dyadosphere*. It extends from the event horizon r_+ out to r_{ds} which is the radius where $\mathcal{E}$ drops to $\mathcal{E} = \mathcal{E}_c$ (Figure 2.2).

Electron-positron pair energy (rest mass/energy plus their kinetic energy) is created at the expanse of EMBH electric field energy. Pairs will be created until electric field everywhere within the dyadosphere drops to $\mathcal{E} = \mathcal{E}_c$. To calculate number of pairs and their energy, as well as their distribution within the dyadosphere, EMBH electric field is imagined as being created by a series of thin spherical capacitors of thickness similar to electron Compton wavelength $\sim \lambda_e = \hbar/m_e c \sim 10^{-10}\ \mathrm{cm}$. Pairs in a single capacitor (at a given distance r) will be created until the "walls" of the capacitor are de-charged to the point when $\mathcal{E} = \mathcal{E}_c$. Energy of pairs in a certain capacitor (at a given distance r) will be equal to the difference between energies of initial $\mathcal{E}$ and critical $\mathcal{E}_c$ (final) electric field (Figure 2.2).

Main formula which comes from above arguments determines the amount of energy released in the form of $e^{\pm}$-pairs $E_{e^{\pm}}$:

$$E_{e^{\pm}} = \frac{Q^2}{4M_{ir}}\frac{c^2}{G}(1 - \frac{r_+}{r_{ds}})(1 - (\frac{r_+}{r_{ds}})^2) \tag{2.3}$$

Radius of event horizon r_+ and dyadosphere r_{ds} are determined by mass M_{ir} and charge Q of the EMBH. Therefore, the $E_{e^{\pm}}$ is completely determined by these two parameters. For a maximally charged BH the relation is: $E_{e^{\pm}} \simeq \frac{M}{M_\odot} 0.9 \times 10^{54}$ erg where M is the total mass of the EMBH system. This is valid for a wide range of stellar BH masses $M \sim 1M_\odot - 100M_\odot$ and beyond. EMBHs with smaller charge will, of course, have less $E_{e^{\pm}}$. For EMBH to be maximally charged its progenitor star should have just one net elementary charge e per 10^{18} nucleons.

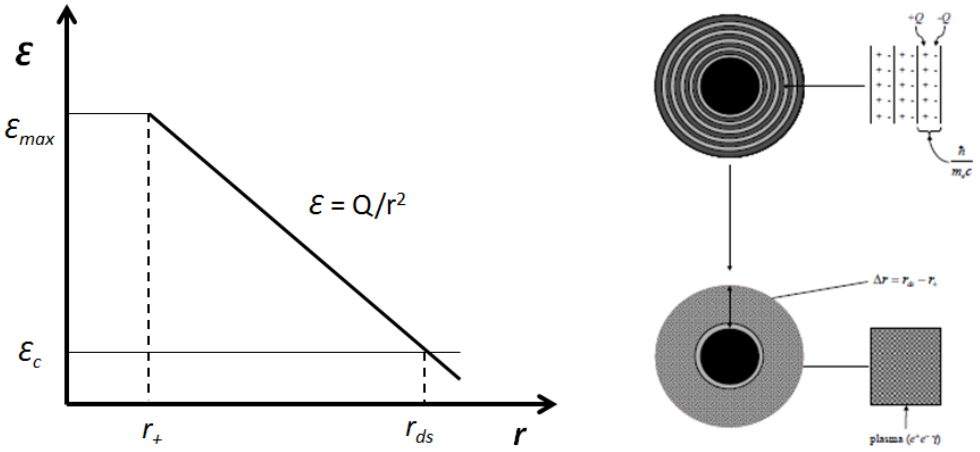

Figure 2.2: **Left:** Electric field $\mathcal{E}$ as a function of radius r from the center of EMBH. Electric field will have maximum value at the horizon r_+ and will drop to critical value $\mathcal{E}_c$ at r_{ds}. The volume between r_+ and r_{ds}, the dyadosphere, is place where electron-positron pairs are created. Coordinate r is from the reference system at infinity where space-time is flat, i.e. it is not affected by gravity of EMBH. **Right:** Modeling electric field in the dyadosphere as being made by a series of thin capacitors. The figure on the right was reproduced from (Ruffini and Vitagliano, 2002).

The processes of pair creation is completed on the order of $\sim \lambda_e/c = \hbar/m_e c^2 \sim 10^{-19}$ s. This means that there are no EMBH with electric fields larger then critical because they discharge instantly. The process of pair creation should happen when the EMBH is forming, during the collapse of the progenitor star. Charged progenitor core can exist in a neutron star. Neutron star will still have some protons and electrons. Heavier protons will concentrate towards the core while lighter electrons will be closer to the crust.

When formed electrons and positrons will begin to move in the electric filed and their own local field will cause resulting electric field to change which will effect the pairs, etc. The final result is an oscillation of electric field as well as concentration of pairs. Consequences of these processes are important when electric field is close to critical. However, for pair creation process around EMBH these effects are not relevant.

The final result is a shell of electron-positron pairs in the range $r_+ \lesssim r \lesssim r_{ds}$ with high amount of internal energy. Due to large optical depth for pair annihilation and consequent pair creation $e^{\pm} \leftrightarrow 2\gamma$, as well as other interactions, $e^{\pm}$-γ plasma is in thermal equilibrium. The plasma is termed *fireshell*. Dimensions and energy of the fireshell are uniquely determined by mass and charge of the EMBH. For a stellar size EMBH typical values are $r_+ \sim 10^6$ cm, $r_{ds} \sim 10^8$ cm, $kT \sim$ MeV.

2.2.3 Expansion of fireshell plasma

The fireshell plasma will start to expand due to enormous internal pressure. Fireshell is assumed not to have any baryon matter and expands as a pure $e^{\pm}$-γ plasma with radiation dominated internal pressure. Since the plasma is optically thick, most of the photons will remain trapped inside and expansion can be considered adiabatic. All the specifics of the plasma are known for a given EMBH mass and charge, and expansion can be precisely determined, i.e. exact dependence of plasma Lorentz factor on radius $\Gamma(r)$. This is done considering relativistic dynamics within general theory framework (curved space-time) as gravitational interaction of the BH is expected to affect the plasma expansion. The picture

that emerges is: The internal energy of the plasma is transferred into outward bulk kinetic energy of the electrons and positrons, i.e it cools as it expands with increasing intensity (Lorentz factor). The thickness of the fireshell remains the same[3] during the expansion. The affect of the BH gravitational field on the plasma expansion is found to be marginal.

Fireshell theory assumes that remnants of the progenitor star are located beyond initial dyadosphere, at $r \sim 100 r_{ds} \sim 10^{10}$ cm, with a width of about $\sim 10 r_{ds} \sim 10^{9}$ cm, and that they form a spherical shell. New parameter B termed *baryon load* is defined as $B = \frac{M_B c^2}{E_{e^\pm}}$ where M_B is mass of baryon remnant. As the $e^\pm$-γ plasma expands it will hit and engulf the baryon shell which will become part of the fireshell plasma. To model the collision next assumptions are used: collision is completely inelastic, geometry of the plasma shell doesn't change, baryon shell quickly comes in thermal equilibrium with plasma. This assumptions should hold if: $B < 10^{-2}$; number of fireshell electrons is much greater then that of baryons $> 10^6$; Lorentz factor of plasma is $\Gamma \gtrsim 100$ at the collision time. All of these factors are true for typical values of mass and charge of EMBH. After plasma hits and engulfs the baryon shell, system will heat up, Lorentz factor will suddenly drop, after that it will start to rise again as the internal energy is transferred to outward bulk kinetic energy of the baryons. When almost all of the internal energy is transferred to outward bulk kinetic energy of baryons, the final Lorentz factor will be $\Gamma = 1/B$.

2.2.4 P-GRB

However, before this asymptotic value is reached, plasma will cool enough for $2\gamma \to e^\pm$ reaction to stop and last of the $e^\pm$ will annihilate; concentration of baryon-associated electrons will drop enough for plasma to become transparent and photons escape from the plasma carrying energy with them. After this *proper GRB* (P-GRB) emission, plasma will continue to expand with constant Lorentz factor, the one it had just before the P-GRB. This happens around $r \sim 10^{14}$ cm. Since photons were in thermal equilibrium, their spectrum will be thermal with temperature around $kT \sim 10$ keV and the duration of the P-GRB should be a fraction of a second. The P-GRB is emitted at the same time from a spherical surface with different Doppler boost towards the detector, and emitting surface has a certain thickness. These geometrical effects will cause the final spectrum of P-GRB to be quasi-thermal.

Initial energy of the fireshell $E_{e^\pm}$ will be divided between energy of P-GRB and energy that remained in the fireshell. This ratio is determined mainly by baryon load B but also the initial energy $E_{e^\pm}$ itself. If the baryon load is smaller, there will be less baryon-associated electrons, and transparency will be reached earlier, when more energy is in the form of internal energy and not bulk kinetic energy of baryons. Smaller the parameter B, P-GRB will be stronger with respect to fireshell kinetic energy.

2.2.5 Extended afterglow

As the fireshell baryons expand outwards they will reach the *circum-burst medium* (CBM) which starts at around $r \sim 10^{17}$ cm. This medium can be interstellar medium or material from a wind created by progenitor star. This interaction produces emission which is termed *extended afterglow*.

In modeling the interaction of fireshell with CBM next assumptions are used: geometry of the fireshell doesn't change; CBM is cold (marginal internal energy) and at rest; collision

[3] In the reference frame of the host galaxy, not in the co-moving frame of the plasma.

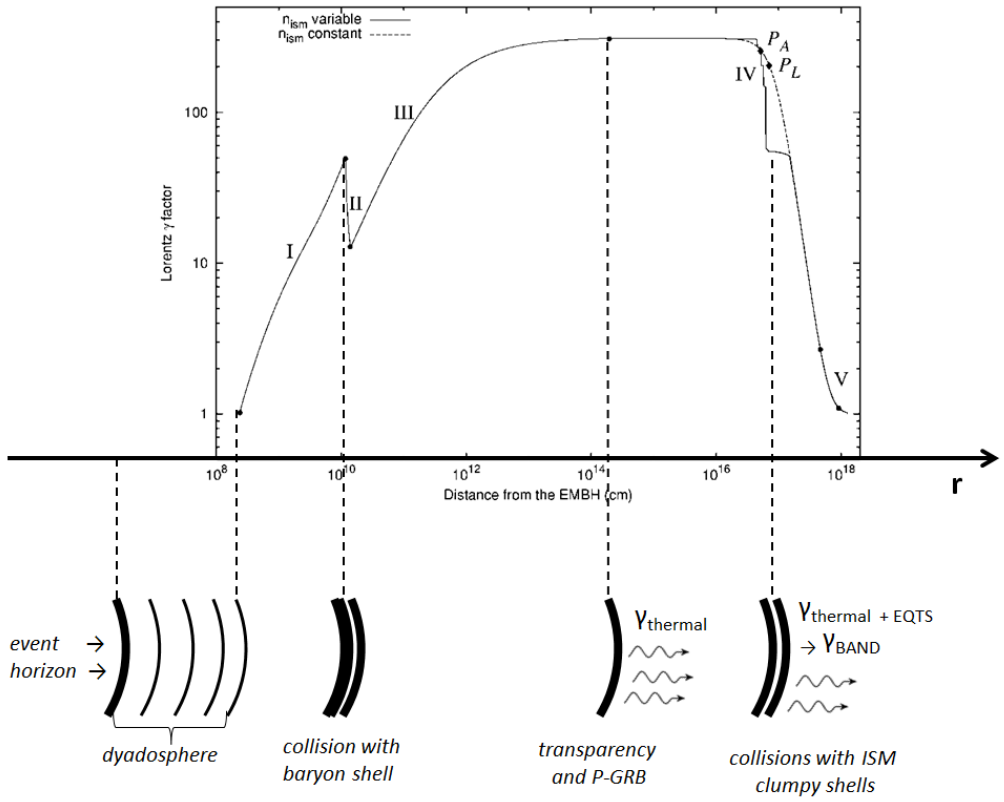

Figure 2.3: Evolution of the fireshell Lorentz factor with distance from BH as applied to GRB 991216. First faze corresponds to expansion of pure $e^{\pm}$-γ plasma. Second faze corresponds to interaction of fireshell plasma with baryon remnant. Third faze corresponds to expansion of $e^{\pm}$-γ-$baryon$ plasma up to P-GRB. Fourth faze starts after P-GRB and involves also the interaction with ISM which gives rise to extended afterglow. Fifth faze corresponds to slowing down of plasma to relativistic speeds and onset of regular afterglow. Dashed line in faze 4 correspond to constant CBM density while solid line corresponds to ISM distributed in thin shells. Image reproduced from (Ruffini et al., 2002)

is inelastic; energy gained from collision is radiated immediately (fully radiative scenario). The model gives precise dependence of fireshell velocity on engulfed CBM mass M_{CBM}, initial Lorentz factor Γ_0 and baryon mass M_B - $\Gamma(M_{CBM}, M_B, \Gamma_0)$.

In order to determine light curve and spectrum as seen by detector, a concept of *Equitemporal Surfaces* (EQTS) was introduced. Since the emitting region is expending spherically at ultra-relativistic speed, photons arriving at the same time at the detector have been emitted at different times and at different places on the expanding fireshell sphere. The equitemporal surface is an imaginary surface such that photons emitted at intersections of the EQTS and fireshell as it expands, arrive at the same time at the detector. Then, from the precise evolution of the fireshell, a light curve can be modeled. If the CBM is assumed to be constant, extended afterglow would be seen as a single peak, following the P-GRB. At this point it should be noted that what is considered prompt emission, which is defined by the T_{90} parameter, in the fireshell model it is composed of P-GRB and the extended afterglow.

In order to explain general multi-peak structure of light curve, CBM is assumed to be distributed in thin shells such that thickness of each shell $\sim 10^15$ cm is greater than the distance between them $\sim 10^16$ cm. Interaction with each shell is responsible for each peak in the prompt light curve.

The resulting spectrum at each point in observational time will be a convolution of many different spectra over the corresponding EQTS. It is assumed that gained energy - which comes from interaction of the fireshell with CBM shell - is completely radiated away as thermal radiation. Then, from the known evolution of the fireshell and CBM distribution, it is possible to model resulting spectrum at each point of observational time. Because of convolution over EQTS, resulting spectrum will be non-thermal and similar to Band function. Observed reduction of peak of the Band function in the peaks of GRBs can naturally be explained in Fireshell model. Since each peak corresponds to a CBM shell, then first radiation from the front of the fireshell (direct Doppler boost) will come and later radiation from the edges of the fireshell (lesser Doppler boost) will come. In order to make such a model completely compatible with observed spectrum in several precisely observed GRBs, two new parameters where introduced.

First is the *surface filling factor* $\mathcal{R}$ which is a function of distance $\mathcal{R}(r)$. It is a ratio between surface area of the fireshell that emits radiation to the total visible (from the detector point of view) surface area of the fireshell. The density and distribution of CBM determines the light curve and spectrum, and the parameter $\mathcal{R}$ is related to spectrum, more precisely to the peak of the Band function. Physical interpretation of $\mathcal{R}$ is that thin shells of CBM have a clumpy structure and as fireshell interacts with a certain CBM shell, only parts of the fireshell which hit these clumps will heat up and radiate. Since all the CBM shell is concentrated in the clumps, given parts of the fireshell will heat up more and the temperature, and the corresponding peak, will be higher. Increasing the $\mathcal{R}$ increases the peak of the spectrum. Typical values are $10^{-12} \lesssim \mathcal{R} \lesssim 10^{-8}$ which implies very clumpy structure of the CBM shells.

Second parameter is related to the assumption of pure thermal spectrum in the co-moving frame of the fireshell. In order to explain spectra in some high energy GRBs, a new assumption had to be made. It introduced new parameter α such that spectrum in the co-moving fireshell frame is defined as: $(E/k_BT)^\alpha \times F_{BB}$ where F_{BB} is the pure thermal flux of the black body, E is the energy of the photon, kT is temperature in units of energy. Parameter α changes the lower-energy slope of the black body spectrum. It is found that this parameter is in the range $\alpha \approx -1.8, -2.0$. This parameter remains constant throughout the burst. So far this parameter is only phenomenological, there is no physical explanation.

Mechanism for extended afterglow is also responsible for what is typically considered afterglow. When the fireshell expands to larger radii and Lorentz factor drops from ultra-relativistic to relativistic speeds, peaks in the light curve from interaction with CBM shells will be less intense, smoothed out and overlap with each other, peak of the spectrum will move to lower energies. This puts an end to prompt emission which is characterized with prominent gamma-ray peaks.

2.2.6 Fitting the GRB

The P-GRB is determined by two parameters: energy released in electron-positron pair creation $E_{e^\pm}$ and baryon load B. Distance of baryon shell from BH is found not to be important. Since all the energy $E_{e^\pm}$ is radiated away it is equated with isotropic energy of GRB E_{iso}. The next step is to determine the P-GRB emission in the prompt light curve by searching for a thermal (or quasi thermal) component. Usually the P-GRB also contains non-thermal component which might come from the early onset of the extended afterglow. When P-GRB is determined, the energy of the thermal component in P-GRB time interval

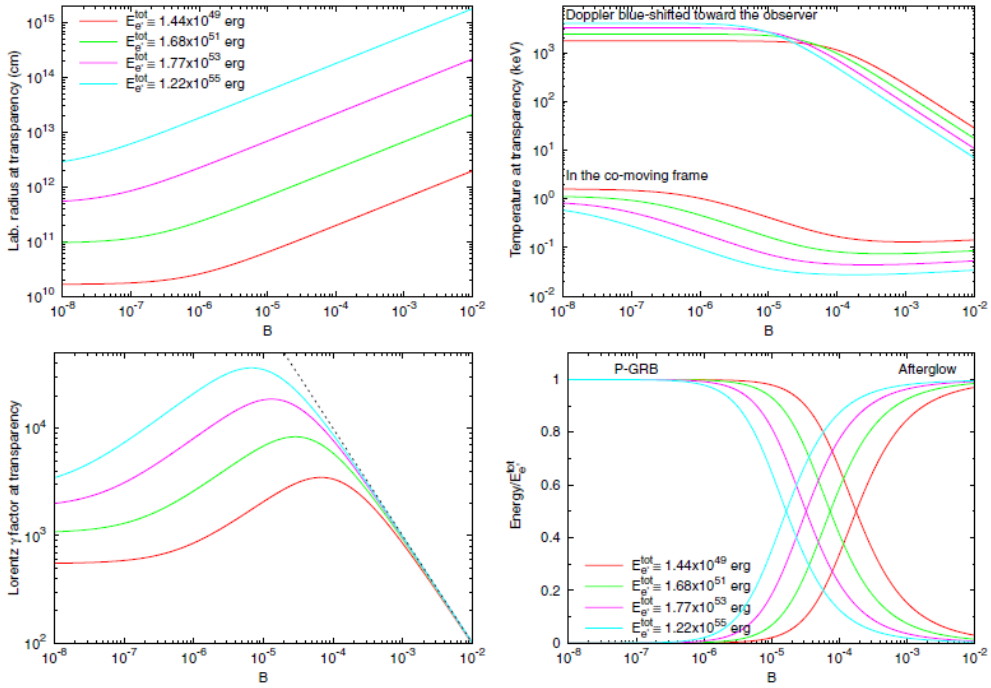

Figure 2.4: Properties of fireshell parameters at the point when transparency is reached and P-GRB is emitted. Dependence of fireshell radius (upper-left), temperature (upper-right), Lorentz factor (lower-left), ration between energy in P-GRB and total energy, all on baryon load parameter B for four different values of total energy. Figure taken from (Muccino et al., 2013a).

as well as its temperature can be determined. From P-GRB thermal energy and E_{iso} the baryon load can be determined, and from there, all other parameters related to fireshell (Figure 2.4). Since the temperature is uniquely determined from parameters B and E_{iso}, it is possible to do a crosscheck with the temperature determined from observations. The previous cases assumed that redshift is known. If it is unknown it is also possible to determine it thanks to this "extra known parameter" connection between P-GRB parameters.

The $E_{e^\pm}$ parameter is uniquely determined from EMBH mass and charge ratio. Knowing it offers a connection between these two EMBH parameters.

Extended afterglow (the rest of the T_{90} prompt emission), beside the $E_{e^\pm}$ and B parameters, is also defined by CBM density distribution $n_{CBM}(r)$, filling factor distribution $\mathcal{R}(r)$ and black body spectral parameter α. The fitting of these parameters is done via the fireshell evolution simulation. First the distribution of parameters are determined and then simulated light curve and spectrum are compered to the observed one. Each step in the fireshell evolution doesn't depend only on the current CBM shell and filling factor, but also on all the previous ones. When simulating light curve and spectra the EQTS surfaces have to be taken into account. Therefore, a single peak in the prompt emission and its spectrum are dependent on the entire fireshell evolution. Because of this it is very difficult to produce correct CBM and filling factor distributions. Also, this is the reason why Fireshell model isn't simply "inventing" parameters and their evolution until the model fits the observation. All the parameters of the fireshell model have to be self-consistent to produce the exact light curve of GRB and its spectral evolution. For example, if an arbitrary GRB light curve and spectral evolution are given, the unique solution within fireshell model should not exist.

2.2.7 Long and short GRBs in the fireshell model

From observational point of view there are long ($T_{90} > 2$ s) and short ($T_{90} < 2$ s) GRBs. The first ones are thought to come from collapsing core of a massive star, and the second from mergers of two compact stars. There is also a third group. These GRBs have an initial short peak (< 2 s) and extended emission which looks more like a stronger afterglow then the typical prompt.

Within the Fireshell model these groups are explained based on baryon load B and average CBM density n_{CBM}.

The typical long GRBs are the ones with $B \gtrsim 10^{-4}$ and $n_{CBM} \sim 1\ \mathrm{cm}^{-3}$ (typical for galaxy disk). For these values of B extended afterglow is much stronger then the P-GRB which sometimes is below detector threshold. For typical value of n_{CBM} most of the extended afterglow is contained within few tens of seconds. The entire T_{90} prompt emission is then basically just the extended afterglow.

If the baryon load is in the same range but CBM density is much lower $n_{CBM} \sim 10^{-3}\ \mathrm{cm}^{-3}$ (typical for galaxy halos), the extended afterglow still has more energy then P-GRB but is "deflated", i.e. its energy is spread over much longer time period and in the lower energy bands. In this case the P-GRB will have a more prominent peak then the peaks in the extended afterglow, which may even be below the detector threshold. This can explain the third observational group of GRBs where there is a short peak in the beginning and afterglow-like emission after it. The requirements for galactic halo CBM density points towards compact object mergers since orbiting compact objects are mostly thought to be in galactic halos. EMBH can be formed also from compact object mergers.

If the baryon load is very small $B \lesssim 10^{-5}$ most of the energy will be in the P-GRB and these would correspond to typical short ($T_{90} < 2$ s) GRBs. Density of CBM doesn't play a significant role here.

CHAPTER3

Induced Gravitational Collapse

Fireball and Fireshell model describe the Gamma-ray burst (GRB) event. The discovery of a first supernova (SN) associated to GRB in 1998, and many more other connection between long GRBs and SNe later on, related long GRBs to ”death” of massive stars. This helped define the GRB models but the models also need to be incorporated into a wider picture which would explain the simultaneous occurrence of both phenomena.

The Induced gravitational collapse (IGC) idea was introduced in order to explain GRB-SN connection with the Fireshell model for GRBs. The center of the idea revolves around a binary star system in which one star is responsible for GRB and other for SN. Initially, at the beginning of 2000s, the binary model assumed that GRB triggers the other star to become a SN. About five years later the opposite scenario was considered in which a SN triggers the other star to become a GRB. Namely, a SN ejecta accretes onto the companion neutron star (NS) close to the maximum mass. As the material accretes the NS collapses into a black hole (BH) releasing gravitational potential energy in the form of an expanding fireshell. This version of events was termed *induced gravitational collapse*. From 2012 and on the IGC scenario received new attention as basic equations and details were laid down for accretion of SN ejecta onto NS. Also, GRBs fitted within the Fireshell model up to 2012 and later on showed additional features - features outside of fireshell model - that point to additional mechanisms, namely ones which could come from binary interaction of two stars. Furthermore, new observational features were discovered in these ”IGC GRBs” that group them into a single class.

The IGC scenario was introduced as an expansion of the Fireshell model but it managed to get a life of its own. The binary scenario was expanded to include IGC-like events which would not lead to a BH formation and a GRB. The binary nature of the phenomena was further expanded to include also mergers of compact objects which produce short bursts. The new picture that emerged revolved around whether or not a BH was formed and consequently, whether the isotropic energy of burst is greater or lower than a limiting value of $\sim 10^{52}$ erg.

3.1 GRB-SN in the Fireball model

The Fireball scenario doesn’t go into details about central engine. In order to explain the GRB-SN connection, a description of central engine and its ability to produce both GRB and SN must exist. Reviews on this topic can be found in (Woosley and Bloom, 2006),

(Hjorth and Bloom, 2012).

In standard model for normal (non-GRB) core-collapse SN, at the end of a star's life, the center of iron core collapses and forms a neutron star (NS). The gravitational potential energy released by the collapse ($\sim 10^{53}$ erg) is transformed to neutrinos (about 99% of energy) which then escape freely trough the star, and partly transported to outer iron core and other outer layers which are then launched outwards as SN ejecta (about 1% of energy). In a sense the collapsing material of an inner iron core to a rigid NS "bounces of" the outer layers.

The standard central engine for a GRB Fireball model involves collapse of a center of iron core directly to a black hole (BH)[1]. The rest of the in-falling core and, later on, outer layers create an accretion disk around a BH and gravitational potential energy of disk material is extracted as it finally falls into BH. Since the inner core was rotating before the collapse, the resulting BH will probably rotate. The rotational energy of a BH can also be extracted via the processes involving magnetic fields in the accretion disk. The energy extracted launches a fireball jet normal to the plane of disk much like in the case of active galactic nuclei or X-ray binaries.

In order to have a SN with a GRB, part of the extracted energy needs to be transported to outer layers of the star and launch them outwards as SN ejecta. The extracted energy from accretion disk will launch a "wind" made out of protons and neutrons outward with speed of about 0.1 c. This wind will then push out the outer layers of star which will become SN ejecta. Another scenario is for the central iron core to collapse initially to NS which will "bounce of" outer iron core and layers like in normal SN. However, this push will not give enough outward momentum for all SN layers and some of them will fall back to NS creating a BH and an accretion disk which will launch a fireball jet.

Previous two scenarios are part of the *collapsar* model and it can be considered as standard one. There is also *supranova* model in which initially a differentially rapidly-rotating super-massive NS is formed. Because of differential and rapid rotation (large centrifugal force) NS can have a much larger mass then typical NS and not collapse to a BH. The SN is, then, created in a usual way. As NS rotation slows down, the gravitational collapse to BH happens with the rest of the scenario playing out as in collapsar model. The delay between SN and a GRB can be from few seconds to years depending when the NS collapses. Another scenario involves a magnetar. If the central engine is assumed to be a magnetar instead of a BH, then SN ejecta can be launched like in normal type SNe and magnetar high rotational energy is transformed in to a GRB jet.

3.2 Different episodes in GRB light curve

Fitting several GRBs within the Fireshell model showed that it is not possible to find a self-consistent set of parameters that would produce the light curve (LC). However, the "problem" seemed to be in the first parts of GRB LCs. If this part of the LC is excluded, the rest of the LC could be fitted within the Fireshell scenario. This first part also seems to be morphologically separate from the rest of the LC. Following these findings the GRB LC was divided into first part *episode 1* and second part *episode 2* with second part being interpreted as standard GRB. Spectral analysis of episode 1 also seems to show a common feature - a spectrum composed of thermal (black body) component and a power-law component. Time resolved spectral analysis of episode 1 seems to show peak of the black

[1] In the long GRBs. Central engine for short bursts is merger of two compact objects

body emission decreasing to lower energies (black body cools) and decreasing spectral hardness of power-law component.

Detailed analysis within the Fireshell model of episode 2 and time resolved spectral analysis of episode 1 have been done for these GRBs: GRB 090618 (Izzo et al., 2012a), GRB 101023 (Penacchioni et al., 2012), GRB 110709B (Penacchioni et al., 2013) and GRB 970828 (Ruffini et al., 2015a).

An example of GRB 090618 will be presented here as a prototype for the mentioned class of GRBs. This GRB was strong and relatively near, and the data collected provide good statistics. Figure 3.1 and Figure 3.2.

Attempting to model the entire T_{90} prompt emission within the Fireshell model fails to give consistent parameters. The first broad peak ($0 - 50$ s) in the GRB LC has been recognized as episode 1. The rest of the prompt emission is episode 2 - the classical GRB which can be modeled within the Fireshell model. Time resolved spectral analysis of episode 1 has shown that it can be well fitted with a black body (BB) of decreasing temperature and a power-law component of decreasing hardness. Assuming a BB is a perfect and uniform sphere, and with known redshift (distance) to the burst, the radius of the BB can be calculated for every time step during episode 1. The radius of the BB increases from $r_{BB} \sim 10^9$ cm to $r_{BB} \sim 10^{10}$ cm during the observed 50 s which is about 30 s in the GRB host galaxy (redshift time correction). Results of analysis of episode 1 are shown in Figure 3.1.

Emission of the BB contributes significantly to the emission of episode 1. The radius of the BB emitter during these first 50 s observational time is much smaller than the radius at which typical GRB emission is released - whether the Fireshell or Fireball model are in question. Given how BB radius changes with time, the calculated speed is about 0.1 c which is non-relativistic speed. Speed of the emitting ejecta in both Fireball and Fireshell models are ultra-relativistic. These findings further point to the idea that the episode 1 is not part of the classical GRB emission.

The rest of the prompt emission, the episode 2, can be fitted within the Fireshell model. The first four seconds of episode 2 ($50 - 54$ s) are recognized as P-GRB emission. Total energy of electron-positron pairs is equated to isotropic energy of episode 2: $E_{e^\pm} = 2.5 \times 10^{53}$ erg. Thermal emission in P-GRB is $E_{P-GRB,th} = 4.3 \times 10^{51}$ erg. From here the baryon load, Lorentz factor at transparency and temperature can be determined: $B = 1.98 \times 10^{-3}$, $\Gamma_0 = 495$, $kT = 29$ keV.

The rest of episode 2 is then extended afterglow. The density distribution of circum-burst medium (CBM) is modeled in order to produce given LC of episode 2 taking into account parameters from episode 1. The average density of CBM is $n_{CBM} = 0.6$ cm^{-3}. The filling factor varies in between $\mathcal{R} \approx 3 - 9 \times 10^{-9}$. The spectral parameter is $\alpha = -1.8$ for the entire duration of the extended afterglow. Results of analysis of episode 2 are shown in Figure 3.2.

Origin of the episode 1 within the IGC scenario is assumed to come from binary interaction between the SN ejecta and companion NS.

3.3 The IGC

The IGC scenario was created in order to explain connection between GRBs and SNe with the Fireshell model for GRBs. The scenario starts with a binary system composed of a massive star without its hydrogen and helium layers and a close orbiting NS. As

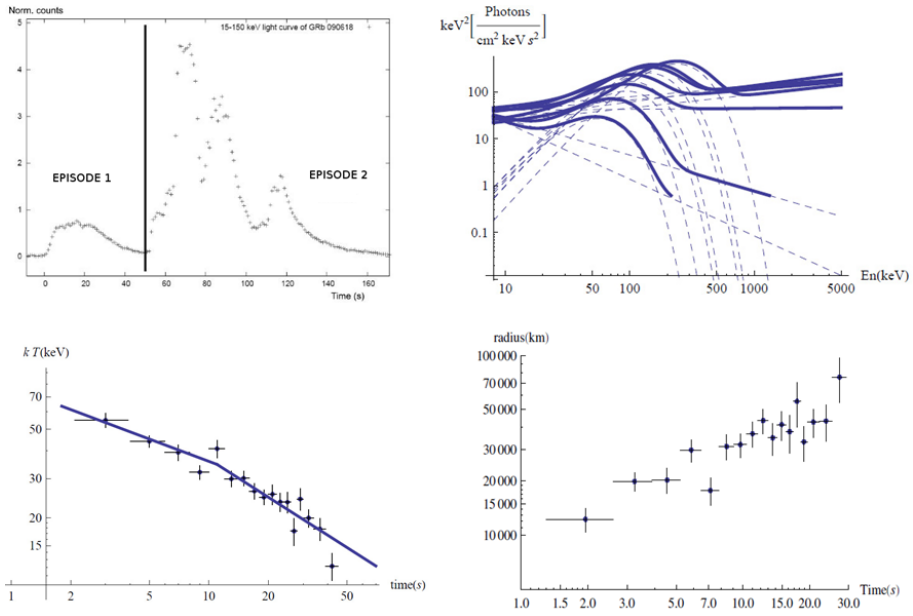

Figure 3.1: Episode 1 of GRB 090618. **Upper-left:** GRB 090618 light curve of its T_{90} prompt emission in the $15 - 150$ keV energy range seen by Swift-BAT instrument. Emission of Episode 1 is well separated from the rest of the prompt emission. **Upper-right:** Time resolved analysis of Episode 1 using data from the Fermi-GBM detectors and fitting with power-law component plus a black body (BB). Decrease of the peak of the BB can be seen as well as decrease of power-law spectral index. Spectrum is in the spectrum energy distribution form. Due to clarity, data points are not shown, only the model. **Lower-left:** Temperature of the BB with respect to observer time. The best fit of the decreasing temperature is a broken power-law. **Lower-right:** Radius of the BB emitter calculated assuming a perfect BB uniform spherical surface. Time is in the frame of the GRB host galaxy. Figures taken from (Izzo et al., 2012a).

the massive star goes SN, the expanding SN ejecta accretes on to NS which then, under additional mass, collapses to a BH creating a GRB. The details of the process have been studied in (Rueda and Ruffini, 2012), (Fryer et al., 2014), (Fryer et al., 2015), (Becerra et al., 2015).

The initial conditions are: The pre-SN star lacks hydrogen and helium layer. This is required from observational and theoretical point of view. All SNe associated to GRBs were type Ic[2]. Orbiting NS has to be close in order to accrete enough mass to collapse to BH. The radius of the pre-SN star is around $r \sim 10^9$ cm and with mass $M_{preSN} \sim 10\ \mathrm{M}_\odot$. The distance of NS with mass $M_{NS} \approx 2\ \mathrm{M}_\odot$ from the pre-SN should be around $a \sim 10^{10}$ cm with orbital period around $P \sim 10^2 - 10^3$ s. Hydrogen layer in a massive star is responsible for its enormous radius $R \gg a$. If a pre-SN star had a hydrogen envelope, the compact NS would orbit within it. The hydrogen envelope would be accreted onto NS or blown away by NS as it orbits the pre-SN star. Binary system with these kinds of stars and orbital parameters should be very rare, however, if each produces a GRB, then almost all of them will be detected.

The core of the pre-SN star collapses to a new NS and the ejecta is launched outwards. The initial speed of ejecta velocity is around $v_{ej} \sim 10^8$ cm/s. As the SN ejecta moves closer to the orbiting NS, a region around a NS where NS gravity is strong enough will capture parts of the moving SN ejecta and it will become gravitationally bound to NS. This

[2]Core-collapse SNe without hydrogen and helium in their spectra. Sometimes they were type Ib/c - without hydrogen but with traces of helium in their spectra.

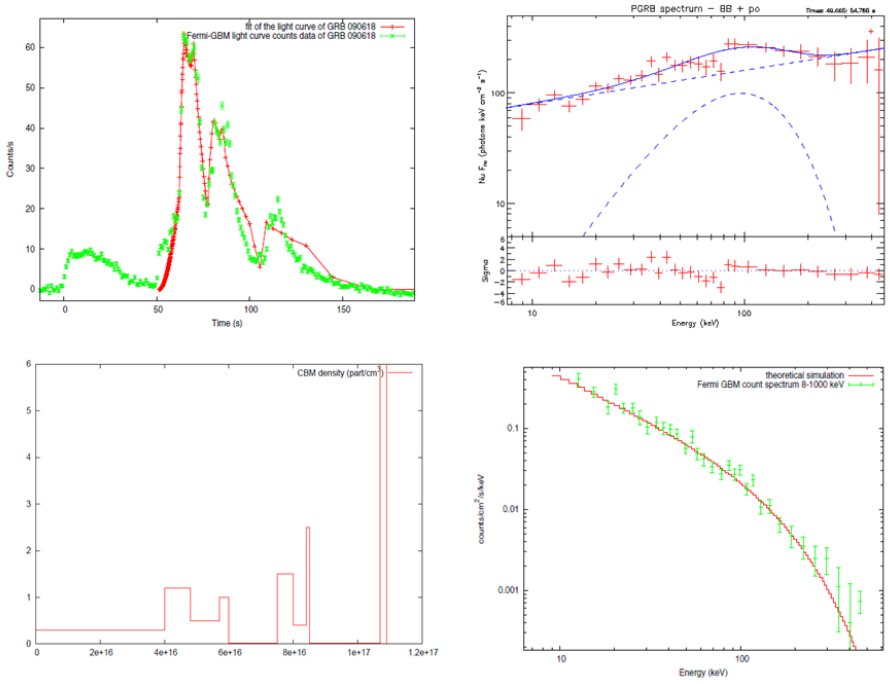

Figure 3.2: Episode 2 of GRB 090618. **Upper-left:** Entire T_{90} prompt emission in green, from the Fermi-GBM data. The red line represents simulated light curve of extended afterglow of episode 2 from the fireshell model. The P-GRB is small peak in the green data from time interval of $50 - 54$ s. **Lower-left:** Distribution of CBM density into thick shells that are responsible of producing peaks in the simulated light curve. **Upper-right:** Spectrum of the P-GRB emission fitted with BB plus a power-law component. The data are from Fermi-GBM detectors. **Lower-right:** Spectrum in the time interval $58 - 150$ s. Green points are data from the Fermi-GBM detector. The red line is simulated spectrum in this time interval from the Fireshell model. Figures taken from (Izzo et al., 2012a).

radius is *Bondi-Hoyle Radius* $r_{BH} \sim 10^8$ cm (Figure 3.3). The following accretion onto NS is very high (hypercritical) with $\dot{M} \gtrsim 10^{-3}$ $M_\odot$ s^{-1}. This is well above the Eddington rate - the rate at which radiation pressure caused by accretion becomes strong enough to stop accretion becoming more stronger. However, if the optical opacity is very high, the photons push outwards with speed lesser than infilling speed of accreting material - the photons are ”trapped in the flow” and accretion can be much higher. This is the case here and the radius at which photon trapping occurs is *photon trapping radius*. The inflowing material heats up as it piles up onto the NS, and produces an outgoing shock. Near the NS it is sufficiently hot to emit neutrinos that cool the in-falling material, allowing it to be incorporated into the NS. The shock moves outward as material piles up. At some point it will defragment and cause outflows which will accelerate to speed close to the speed of light. In this way about 25% of accreting material is ejected out. If the outflow moves out as a jet it would have a temperature of around 50 keV at radius of 10^9 cm, and as it cools and expands out, temperature of ~ 15 keV at 6×10^9 cm. This could be an explanation for the thermal emission in episode 1 as it coincides with observed temperature and radius evolution of the BB. The process of accretion onto NS before it collapses to BH lasts about $\sim 10^2$ s.

As the SN ejecta moves outwards and then is affected by orbiting NS gravity, it will have an angular momentum with respect to NS. Accreting matter will create a disk-like structure around NS. The angular momentum is much bigger then the maximum angular momentum NS can have before it starts to shed mass due to large centrifugal force. As the

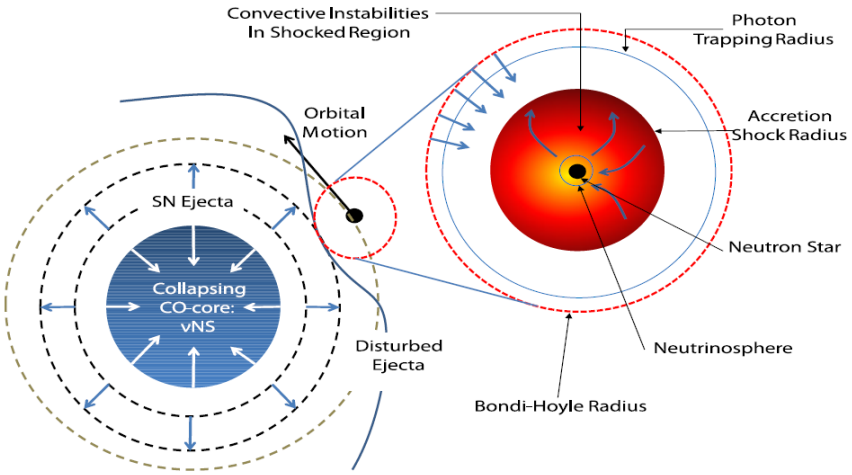

Figure 3.3: Interaction of SN ejecta with companion NS. Details are given in the text. Figure taken from (Fryer et al., 2015).

matter accretes it will spin up NS. In order for a mass to accrete on to NS, the accreting ejecta needs to lose angular momentum. The process in which angular momentum of an accreting disk gets decreased is by creation of a jet normal to the plane of accretion disk - similar process like in X-ray binaries. The jet could explain the power-law component seen in episode 1, or even high energy (GeV) emission if accretion continues after BH is formed.

For a wide range of pre-SN masses, orbiting periods, etc. the kick given to NS (later BH) by expanding SN ejecta isn't enough to unbound it from the new NS (previous pre-SN star). This is due to the fact that the system was very tightly bound (small distance between the stars) to begin with.

The rest of the SN ejecta (not accreted) will still be distorted by nearby orbiting NS and accreting matter. The SN ejecta will be significantly asymmetric. Radiation from accretion as well as highly expanding fireshell plasma (GRB ejecta) will interact with SN ejecta pumping energy into it and causing it to accelerate and radiate stronger. This is considered to be the explanation for the fact that SN associated to GRBs are faster and more luminous then non-GRB type Ic SNe. Specifically, the moment of interaction between GRB ejecta and SN ejecta is thought to be responsible for flares seen in the X-ray range after the prompt emission.

In principal, the IGC scenario can also be used with fireball model for GRBs. In both cases the NS can collapse to a BH. In the fireshell model the collapse creates a fireshell plasma while in the fireball model the collapse creates an accretion disk which then launches a fireball jet. The studding of binary systems and accretion of SN ejecta onto NS would be the same for both models since GRB doesn't yet happen in this time interval. The main difference arises when SN ejecta interacts with GRB ejecta - fireshell plasma in fireshell model or a fireball jet in fireball model. However, emission arising during the accretion is considered as possible explanation for features in episode 1 and episode 1 is a concept solely within the fireshell model.

3.4 X-ray afterglows of IGC GRBs

Although there are thousands of observed bursts, only few of them were strong and/or close enough to be well observed. Fewer still were observed by several space-based detectors in order to have good coverage of time and energy interval - which is important in order to do a detailed analysis. With recognition of distinct episodes in GRB T_{90} prompt LC, and their explanation within IGC theory, a group of *IGC GRBs* can be conceived. Apart from distinct episodes and SN associations[3], another observational features regarding these bursts are: isotropic energy which is always above $E_{iso} \gtrsim 10^{52}$ erg; common features within the X-ray afterglow.

3.4.1 Overlapping

Another feature shared between IGC GRBs is their X-ray afterglow. In (Pisani et al., 2013) and (Ruffini et al., 2014b) this has been studied. Swift-XRT instrument ($0.3 - 10$ keV) is most important in measuring X-ray afterglows of GRBs. If a GRB has a redshift it is possible to calculate X-ray afterglow luminosity (in a fixed energy band) in the rest-frame of GRB host galaxy which is an intrinsic property of GRBs. The LC of the afterglow can then be plotted against the rest-frame time. The common feature of IGC GRBs is that their X-ray afterglows (the luminosity) - after about $\sim 10^4$ s when the plateau faze ends - decay in a common power-law slope which overlap, regardless of E_{iso}. Another feature regarding the X-ray afterglows of these bursts is: the more energetic the burst is (the larger the E_{iso}), the plateau faze lasts shorter and the common power-law part starts earlier. Figure 3.4.

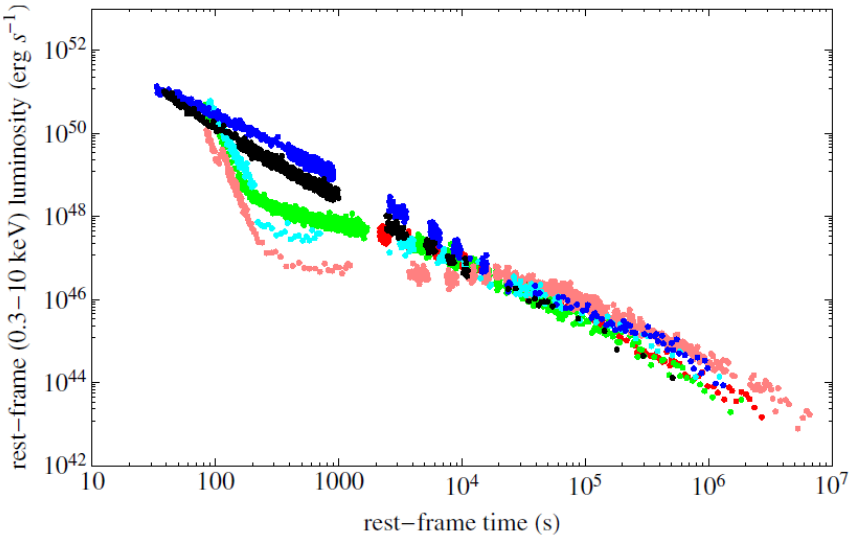

Figure 3.4: Rest frame luminosity of several GRB X-ray afterglows which were observed by Swift-XRT. The GRBs considered here were the ones with IGC characteristic: double episode in the prompt emission, SN association or a possibility of association if a GRB was closer then $z \lesssim 1$, $E_{iso} \gtrsim 10^{52}$; and well observed X-ray afterglow. The GRBs are: pink GRB 060729, $z = 0.54$; black GRB 061007, $z = 1.261$; blue GRB 080319B, $z = 0.937$; green GRB 090618, $z = 0.54$, red GRB 091127, $z = 0.49$, and in cyan GRB 111228, $z = 0.713$. Figure taken from (Pisani et al., 2013).

[3]Current optical detectors can observe SN if it is close enough, $z \lesssim 1$. If it is close enough, SN association can be certain or possible.

The overlapping feature gives a possibility to estimate the IGC GRB redshift if it is unknown.

Following the notion of episodes 1 and 2, the X-ray afterglow of IGC GRBs has been termed *episode 3*, and *episode 4* corresponds to optical SN emission 10-15 days after the start of GRB. It is not yet clear what is the physical reason behind the features of overlapping and nesting. It may have something to do with the emission of SN ejecta which has been affected by GRB ejecta, emission from a newly born NS, synchrotron emission of particles accelerated by Fermi mechanisms in the ejecta, or due to radiation from the heavy elements created in the r-process.

High redshift GRB 090423

This GRB is possibly the furthest one ever observed. Its redshift is at $z = 8.2$ which means it happened "just" $650\ \mathrm{Myr}$ after Big Bang[4]. In (Ruffini et al., 2014a) this burst has been analyzed within the IGC scenario. Its X-ray afterglow overlaps with other IGC GRBs and has an isotropic energy $E_{iso} \gtrsim 10^{52}\ \mathrm{erg}$. The SN couldn't be observed due to high redshift and for the same reason episode 1 was below the detector threshold. Having confirmed that this GRB belongs to IGC class means that IGC scenario has been playing out since very early time in the universe.

3.4.2 Very energetic GRB 130427A

This GRB was very energetic $E_{iso} \sim 10^{54}\ \mathrm{erg}$, relatively nearby $z = 0.34$, and was observed by many instruments. This provided ample amount of data for analysis. This was also the first very energetic GRB to have an associated SN. From this point on the GRB-SN association was confirmed for all the range of GRBs isotropic energies. The GRB was studied within the IGC scenario in (Ruffini et al., 2015c).

The late X-ray afterglow overlaps with other IGC GRBs. In fact, the overlapping was evident early on and a notice on upcoming SN detection was sent since it should be easily detected given the low redshift of the GRB. Indeed, several days later a SN was detected. Also, the common power-law decay starts very early on for this very energetic burst which also fulfills the second feature of IGC GRB X-ray afterglows. The afterglow of this GRB was well observed from optical (eV) to very high energy (GeV) and the afterglow LC seems to decay with a common slope in all these energy bands. This implies that the same mechanism is responsible for the afterglow at all the energies.

Given this energetic GRB close proximity, it was very fluent - to fluent. The burst had overloaded Fermi-GBM detectors and a detailed analysis was hard to do. The distinction of episode 1 and 2 was hasn't been done. There is also the possibility that the episodes overlap in time due to geometry of the IGC binary system and its position with respect to Earth.

The Swift-XRT instrument can deal with very high fluence and X-ray afterglow analysis can be done with ample amount of data. Analyzing first few hundred seconds of afterglow showed a spectrum consisting of a power-law (PL) component and a thermal (BB) component. The BB component temperature decreased from $0.5\ \mathrm{keV}$ to $0.1\ \mathrm{keV}$ in the time interval of about $250\ \mathrm{s}$. The time interval where BB was detected corresponds to a soft peak in the X-ray and Gamma-ray energy band which happened about $100\ \mathrm{s}$ after the start of the main prompt emission.

[4]Within the framework of Standard cosmological model.

With the known BB fluence and redshift (distance), a BB radius can be calculated. The radius changed from about 1×10^{13} cm to 3×10^{13} cm in about 200 s. This gives an apparent superluminal[5] velocity. After correcting for the relativistic expansion, a speed of 0.8 c is obtained. The radius of $\sim 10^{13}$ cm is much smaller then radius at which prompt GRB emission is emitted and even smaller then the one at which early afterglow is emitted - whether in fireshell or fireball model. This means that the BB emission cannot be from the GRB ejecta. It probably comes from the SN ejecta which expands slower the GRB one. Also, the expansion speed (Lorenz factor) of the GRB ejecta at the time of the early afterglow is much higher then in this case. The radius and expansion speed of the BB emitter are also different then the ones derived from thermal emission in episode 1 - which comes from accreting SN ejecta onto companion NS. The possible detection of a similar BB component in the early stages of afterglow has been reported for several GRBs, including GRB 090618.

Another interesting feature is the light curve of the GeV emission. It seems to be anti-correlated with the keV-MeV emission. When this emission peaks, whether in the main part of the prompt or in the soft peak at 100 s, the GeV emission is absent. As soon as the keV-MeV emission lowers, the GeV emission emerges. So far there is no clear physical explanation for this within the IGC model.

3.5 Binary systems and two families of GRBs

In the work of (Ruffini et al., 2015b), (Ruffini et al., 2016c), (Ruffini et al., 2016b), (Ruffini et al., 2016a) and similar, a new concept was being introduced.

The standard division of GRBs is into long and short burst. Apart from the T_{90} duration of prompt emission, there are others observational features that support this division. These features point to the scenario where progenitors of long bursts are massive stars while progenitors of short burst are mergers of two compact objects (BH, NS, white dwarf).

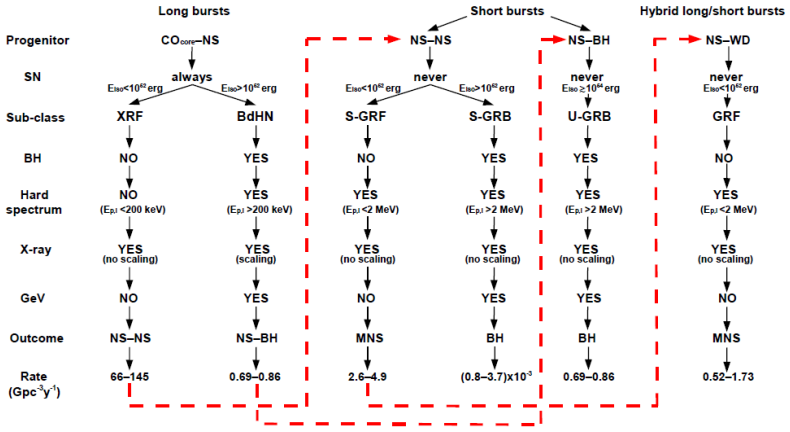

Figure 3.5: Characteristics, rates, progenitors and end results of binary systems producing GRBs. Details are given in the text. Figure taken from (Ruffini et al., 2016c).

The new picture that emerged from extending IGC scenario also differentiates between long and short bursts, and connects long to death of massive stars and short to mergers

[5]Due to (ultra)relativistic movement or expansion ($v \approx c$), the apparent speed may seem like larger then speed of light.

of compact objects. The difference is that progenitors of long are binary systems and not single stars. Apart from duration there is also a new parameter in extended-IGC scenario which further differentiates GRB classes - whether or not a BH is formed. This is a factor for both long and short types. Based on numerous observational features and basic energy evaluation, the minimum energy associated to BH formation is $\sim 10^{52}$ erg. This threshold energy is also the maximum energy that can be released without BH formation. Further differentiation of short GRBs comes from the type of compact objects that are merging.

Typical IGC GRBs are in the second column in Figure 3.5. They belong to the long class of GRBs when a BH is formed. If accretion onto the NS is not enough to collapse it into a BH, then only emission related to accretion on the NS is produced. The limiting value of $\sim 10^{52}$ erg was evaluated to correspond to energy threshold of creation of a BH. In the case a BH is not created then an X-ray flash (XRF) is emitted (first column in the figure). Short bursts are divided into three categories: Merger of two NSs with (fourth) or without BH creation (third), and a merger of a NS and a BH (fifth). The final class (sixth column) is made in a merger of NS and a white dwarf. The outcomes of some classes can be progenitors of others as can be seen in the Figure.

CHAPTER4

Thermal X-ray emission in the late prompt - early afterglow phases

Transition from the prompt emission to afterglow hasn't been well explored as prompt emission or the afterglow. The main reason for this lies in the instruments capabilities. From the start of the modern GRB astronomy in the 90s, many instruments were focused on observing prompt emission. The goal was to increase spectral and time resolution, as well as energy range. With the launch of Swift satellite at the end of 2004, the X-ray afterglow have been observed in detail and in great number for the first time. Still the late prompt and early afterglow emission remained elusive because Swift satellite needed about 100 seconds to point to GRB and start measuring with its narrow-view XRT (X-ray Telescope) in the soft X-rays. Meanwhile the wide-filed BAT (Burst Alert Telescope) triggered on the burst and measured the prompt emission in hard X-rays which usually fades away by the time XRT begins observing. Few bursts detected by Swift have such a temporal and spectral structure that they are detected by both BAT and XRT at the same time. Usually these bursts have longer and stronger prompt emission, or have a hard flare at the start of the afterglow.

The analysis done so far in the literature - focusing on joint Swift BAT-XRT analysis or just XRT at the beginning of the afterglow - has found evidence for thermal emission (Nappo et al., 2017; Ruffini et al., 2017b; Basak and Rao, 2015b,a; Ruffini et al., 2015d; Larsson et al., 2015; Peng et al., 2014; Piro et al., 2014; Bellm et al., 2014; Friis and Watson, 2013; Sparre and Starling, 2012; Starling et al., 2012; Page et al., 2011; Starling et al., 2011; Campana et al., 2006; Liang et al., 2006).

In general this late thermal emission can be divided into two types. One has a relatively constant intensity and temperature of about $\sim 0.1\ \mathrm{keV}$ (lower range of XRT band) over several hundreds of seconds. It was found mostly in close and weak Gamma-ray bursts (GRB) which have an accompanying supernova (SN). Often this thermal emission is assign to SN shock break out, either from stellar envelope or dense wind medium. The weak GRB is often considered not to be "real" cosmological GRB but coming from a stronger SN. The second type of thermal emission has a varying intensity and temperature of order a magnitude in the period of tens of seconds. Temperature can reach $\sim 1 - 10\ \mathrm{keV}$. In most cases temperature starts from the highest value and than monotonically decreases. The intensity usually follows this path but there are more exceptions. These can be found in typical cosmological GRBs.

The interpretation of the second type can be found within fireball model. In it the thermal radiation is boosted by a Lorentz factor of $\Gamma \sim 10 - 100$, ultrarelativistic but smaller than during the prompt; however the process is practically the same as the one of thermal emission in the prompt phase within the fireball model. The speed $\Gamma \sim 10 - 100$ is not related to the speed of the photosphere. There is a relativistic jetted outflow and photosphere is the place where the transparency drops to around one. The photosphere may not move at all. The values of photosphere radius, Lorentz factor, comoving temperature, etc. are obtained within the fireball scenario (taking into account initial conditions and the fireball equations) in combination with observed values. Continues transparency/opacity changes in space and time have to be considered, i.e. the photosphere is not a sharp surface (where opacity suddenly drops from 'infinity' to zero) but photons come from a certain volume with different probability of emission. This then has to be coupled to (ultra)relativistic expansion in order to calculate thermal spectrum. Further effects such as different levels of thermalisation in the emitting volume and anisotropy of local photon fields, inverse-Compton scattering of thermal photons by electrons, radiative diffusion in the fireball wind before it reaches transparency radius, etc. may additionally affect the thermal emission. This has been studied in literature; for example (Mészáros and Rees, 2000; Daigne and Mochkovitch, 2002; Pe'er et al., 2007; Ruffini et al., 2013; Vereshchagin, 2014).

Similarly, with all the above considerations, thermal emission in the prompt phase is examined within the fireshell model starting from the dynamics of (ultra)relativistic plasma which then produces thermal emission. Literature concerning thermal emission in the prompt phase of the fireshell model: for example (Bianco et al., 2001; Ruffini et al., 2004b, 2005b; Bernardini et al., 2005; Bianco et al., 2011; Patricelli et al., 2012; Ruffini et al., 2014d).

Thermal emission in the late prompt - early afterglow phase in the fireshell model is explained within the wider IGC scenario. In it the late evolving thermal emission comes from the supernova ejecta expanding with mildly relativistic speeds $\Gamma \sim 2$ after it was hit by the fireshell plasma. Explaining thermal emission starting from the dynamics of the IGC system was done in (Ruffini et al., 2017b) where also comparisons were made with observations. Detailed modeling of motion of the plasma and transparency conditions is being presented in (Ruffini et al., 2018), however with no computation of spectrum.

Another approach to exploring late decaying thermal emission is the other way around, starting from observations and without assuming any model. The simplest case then is a perfect spherical black body with sharp surface and with uniform temperature. In this case if the black body is expanding then the velocity related to the boost of the spectrum is the same as the expansion speed of the photosphere. This assumption is considered to be valid enough when it comes to explaining thermal emission within the IGC scenario, i.e. explaining thermal emission as coming from the surface of the optically thick supernova ejecta. This method has been applied in (Izzo et al., 2012b) (although for thermal emission in Episode 1 - beginning of the burst) and in (Ruffini et al., 2014c, 2015d, 2018). From the simplest assumption of perfect spherical black body radius may be calculated and from there the expansion speed from time resolved analysis. If this expansion turns out to be superluminal then relativistic corrections should be applied.

Analysis in this chapter

Within systematic studies of thermal emission in Swift data, not much focus was given to searching for second type thermal emission with time resolved analysis in the joint Swift BAT-XRT data. This will be focus of the chapter. The spectrum of thermal emission looks like a bump, but a broad one and, unless it is well localized in the lower-middle XRT band, it doesn't really show in just XRT or just BAT band. Wider energy range is needed. Another factor to recognizing it is to find a decreasing temperature in time resolved analysis. Only bursts with redshift will be considered since then rest frame properties may be determined and potential thermal emissions compared.

Then thermal emission from a *spherically symmetric, expanding with constant velocity, sharp black body surface, with uniform and constant temperature* will be calculated starting from the very basis. Many of the results from this part are well known and might seem redundant. However, most of the equations from the literature are concerned with some assumptions of plasma dynamics which might be specific for those particular cases and usually they correspond to ultrarelativistic approximation. Some expressions from derivations will later be used in a code which computes observed spectrum from the above-mentioned thermal surface but with (inputted) varying velocity and temperature. It will be showed that just by changing velocity and temperature broader peaks or double peaks may appear in instantaneous spectrum.

4.1 Data Analysis

This section will be dedicated to instruments, data analysis software, methods and challenges.

4.1.1 Swift BAT and XRT data

Swift was launched at the end of year 2004 and is still operational in the year 2017. Instrument Swift-BAT energy range covers $15 - 150$ keV while Swift-XRT covers $0.3 - 10$ keV. The initial data (Level 0 data) after the burst are sent from the spacecraft to the ground where they are analyzed and Level 1 and Level 2 data are produced. Level 2 data are files which contain photons, their detection times, energy, etc. along with various instrument information. These data (photons) can be then binned in energy and time, along with other tasks, to produce files and responses for spectral fitting in software such as XSpec[1]. Level 2 data start to be available few weeks after the burst. The Swift team provides means for users to analyze Level 1 data but this might be helpful if there is a specific burst of interest and not really for systematic analysis of many bursts. Swift team also produces automatic light curves and spectra. This is available on the website here[2] where other information in regards to instruments, data analysis, etc. may be found.

XRT modes

Instrument XRT has different modes of operation with two main being window timing mode (WT) and photon counting mode (PC). XRT is an imaging instrument which means it records direction of photons and can produce images. This option is available in PC

[1] `https://heasarc.gsfc.nasa.gov/xanadu/xspec/`
[2] `http://www.swift.ac.uk/`

mode. PC mode is used when the intensity is below about one photon per second. Then there is time to read out each pixel in a square 600 $\times$ 600 pixel grid (24 $\times$ 24 arcminutes). When intensity is higher, then WT mode is used in which ten pixel rows are read out at the same time in order to be faster. Also the edges are truncated and this produces a semi one dimensional image (200 $\times$ 20 pixel grid). Data analysis of WT and PC modes are different in some respects. In this work only WT data will be used since the beginning of the afterglow or flares are intense and are recorded in WT mode. Also this means that background may be ignored (the intensity is almost always above 10 photons per second).

No mode distinctions exist for BAT data.

4.1.2 Software

Firstly the HEASoft software package [3] must be installed and access to calibration database CALDB[4] available.

XRT

Level 2 data are analyzed by FTools[5] which are a set of software meant for working with fits files.

General analysis of XRT data firstly involves *XSelect*[6] which can filter photons based on energy, time, region, grade (quality/precision), etc. using other FTools. It creates typical spectral PHA file which is read in XSpec. It has many other applications but for this work the mentioned are enough. To run all the necessary commands in XSelect it has to happen within XSelect environment, or, all the commands may be typed in a text file (with *.xco* extension) and invoked when starting XSelect which will then execute them all one by one. By adding an exit command at the end the whole process may be completed with a single command line. Due to point spread function a point source will look like a line in WT data image, so, photons need to be filtered by position. During region selection a DS9[7] program will be prompted showing WT image, then region may be selected and information saved as a text file with *.reg* extension. This file will be used during region filtering. Knowing the region information (position of center of circle, radius of circle and inner circle in the case of annulus), the same file may be written independently of DS9 and then used by XSelect.

The next step is to generate exposure map with *xrtexpomap* which takes the previously generated spectral file and instrument response files. All input parameters may be entered in a single command line when invoking the program.

Next step is to create an arf-response file with *xrtmkarf* with spectral file and exposure map. All input parameters may be entered in a single command line.

The final step may involve *grppha* which is mainly used to rebin the energy bins in order to have a minimum counts per bin. Since XRT data will be fitted with BAT data which can only be done with χ^2 statistics, the XRT data need to be bin to minimum of 20 counts per energy bin so they can be fitted based on χ^2. All input parameters may be entered in a single command line. Also bad channels which fall outside range $0.3-10$ keV should be marked.

[3] https://heasarc.nasa.gov/lheasoft/

[4] https://heasarc.gsfc.nasa.gov/docs/heasarc/caldb/caldb_intro.html

[5] https://heasarc.gsfc.nasa.gov/ftools/ftools_menu.html

[6] https://heasarc.gsfc.nasa.gov/docs/software/lheasoft/ftools/xselect/xselect.html

[7] http://ds9.si.edu/site/Home.html

The spectral file, the arf-response file, and RMF-response file (which is the same for all the burst in a given yearly periods) can now be loaded into XSpec and fitted.

XSpec has its own environment but similar to XSelect all the commands (including final ”exit” command) may be written to a text file with *.xcm* and then invoked when starting XSPec which will run all the commands and exit.

Python:

All of these tasks are one-dimensional and can be run one by one within a programing language such as Python. There is no need for special Python packages from which these tools may be run and operated. It is possible to invoked them from Python the same way they would be started from operating system environment, and all the FTool tasks can be completed with a single command line.

User just needs to choose time period (with respect to GRB trigger), binning, region extension, model to fit, and run the Python script which has been written in the course of this work to simplify and speed up analysis. Since XSelect and XSpec have their own environments, text files with *.reg*, *.xco*, and *.xcm* extensions may be written by Python and invoked with the tools. With XSpec there is possibility to export results in a text file, or to log the XSpec output to a text file (*.log* extension). These text files may be read with Python and fitting information obtained. For XSPec there is also option to use Python package PyXspec which is specially design to operate XSpec from Python.

Information such as trigger time, burst position, trigger number, instrument information, etc. - which are needed in these FTool sequences - may be obtained from LEVEL 2 data files with Python package PyFITS which is used to manipulate FITS files. This is the basic chain. Additionally, some unnecessary files will be created during sequences and may be deleted at the end; plots from XSpec may be saved or imported into Python and from there make the plots, information from fitting saved or used for additional calculation; option to include background, option to run just XSpec with different model; folders created, deleted, files moved, etc.

All of this can be repeated for many time bins by running the process over and over again (in a single script), just with different time periods, or by using Python module for multiprocessing which then runs all different time bins at the same time on different processors and combines results in the end. This can be useful when using small computer cluster with relatively strong processors like the one at G9 at La Sapienza University. Good practice is to allow for few seconds before new process starts because some times running XSelect at the same time on many processors may result in crash. Similar Python script has be written to do this.

BAT

First FTool is *batbinevt* which has many purposes including to filter photons from Level 2 files based on energy and time, and to do energy binning thus producing a spectral PHA file. Next *batphasyserr* and *batupdatephakw* are used to account for systematic errors. Then *batdrmgen* is run to produce response file. Then *grppha* to mark bad channels and other tasks. Finally XSpec may be run.

As in the XRT case all the commands with input parameters may be run on a single line and the processes are one dimensional. The Python script for BAT is similar to the one of XRT: inputs are time bin(s), binning, and other optional information such as light curve binning, mask weighing, checking the ”fkey” parameter, etc. Again, for different time bins, jobs may be distributed to different processors and results combined in the end.

Joint XRT-BAT

Finally script which implements two previous procedures is made to do joint analysis of XRT and BAT. The input parameters for both XRT and BAT are as in individual cases and final results contain fit information (parameters and statistics) and plots. Again the jobs for different instruments or time bins may be distributed to different processors.

4.1.3 Pile-up

If the intensity of the burst (prompt, afterglow or flare) is stronger than about 100 photons per second, then pile up may occur in WT mode. The photons come in to rapidly and there is no time to read out pixels, even in fast WT mode. What happens is that two photons may be read as one photon with energy which is sum of the two. The end result is that spectrum looks harder than it is.

Central pixels (ones which are centered on the position of the burst) have the most counts. The central pixels should be excluded (by choosing annulus region selection instead of circle) until the pile-up effect is gone. To determine how much pixels should be excluded XRT spectrum may be fitted for each excluded pixel until it stops to change. Since this requires doing the same process just with different inner circle radius, Python scripts have been written that distribute the work to different processors and the results are combined in the end. When doing this only one exposure map may be generated since it doesn't depend on the selection region. This then can be done for different time bins.

In practice this can only give an estimate, and also depends if the spectrum is fitted with models other than power-law, which might be important if the intrinsic spectrum is not power-law (if the thermal emission is also there for example). With the estimation, when doing joint XRT-BAT analysis few pixels may be added or excluded to check if this changes the final spectrum and to what level. With excluding pixels the XRT statistics gets weaker, and the outer region radius may be expended to include more photons, but if it gets to big the question of background might become important.

Other methods for estimating pile-up includes checking the ratio of photons with different grades and how it changes with exclusion of pixels (excluding pixels until it more-or-less stops to change). This is also uncertain since even if there is no pile-up the ratio changes.

The pile-up effect, and how much pixels should be excluded, can really become an issue when intensity is above 1000 photons per second.

4.1.4 Other difficulties

Low energy spectral residuals in Windowed Timing Mode

If the source is very absorbed in the $0.3-2\ \mathrm{keV}$ range, spectrum may show an artificial bump in the $0.4-1\ \mathrm{keV}$ range and a turn-up at very low energy range. The bump may disappear if only grade 0 photons are used instead of typical grades 0-2. This option is implemented in scripts. The turn-up doesn't disappear and the energy where it starts changed over years. It is important to keep these effects in mind because the artifacts resemble thermal spectral component.

Position-dependent WT RMFs

The reason why WT image is compressed in one dimension is because 10 rows are red at a time. The merged "big" row where the source lies means that the source could be at any of the 10 rows which were merged. Depending where it is can produce different WT images (due to multiple pixel events being split between merged rows) and then spectra. So, position dependent RMFs may be used. There are 3 of them for each ordinary RMF. It cannot be precisely determined where the source actually lies and which one to use. So, one strategy is to use all of them and select the one where the fit statistics is best (lowest χ^2). Second strategy is to do fitting with all three and find an average value for 3 different sets of parameters, and combine all the confidence intervals of 3 sets of parameters (errors). In other words, treat it as an additional systematic error.

Burst position on the XRT detector

The position of the burst read in the header of the Level 2 data file doesn't always correspond to the brightest pixel in the WT image. Additionally, the brightest pixel may change during course of several seconds or tens of seconds. This is due to uncertainty of XRT pointing, so the same sky position (RA and Dec) may "drift" on the XRT detector plane as the satellite sways. The sky position should be chosen where the brightest pixel is.

Binning BAT data

By default BAT data are binned into 80 bins in the *batbinevt*, and later, bins corresponding to range below and above $15 - 150$ keV are marked as bad in *grppha*. If the binning is custom and corresponds to $15 - 150$ keV, then during fitting values corresponding to first 2 or 3 BAT bins will have unusual lower value. It is not clear what causes this and unlike previous problems it is not officially recognized. A way to overcome this is to have additional 3 bins from $10 - 15, 16$ keV and then set them as bad in the *grppha*.

Additionally, default 80 bins are linearly equally spaced. It is more useful to have them logarithmically equally spaced and the number of such bins can be entered in the script (not counting first 3 bad bins).

Intrinsic column density

Intrinsic column density is an unknown factor. The value may be taken from Swift automatic analysis. Two values are from WT data and later PC data. Value from WT data is more precise but it may be wrong due to spectrum in XRT range being different than power-law (which was used to obtain column density) and varying. The PC data value is less precise but the spectrum in this later time is much more constant and powerlaw-like. Intrinsic column density may be left as a free parameter during fitting. Since it has to have the same value for different time bins, all the spectra may be fit simultaneously in XSpec with column density being the same parameter for all time bins. Value of intrinsic density is important if the thermal emission is in the lower band of the XRT range. Otherwise value(s) from automatic analysis may be taken and kept constant.

XRT-BAT normalization constant

These two instruments may have some unaccounted instrumental error so additional parameter during fitting may be a normalization constant. Since it has to be the same for all time bins (and at least very similar for other bursts), all the spectra may be fitted in XSpec with normalization parameter being the same for all time bins. Both instruments are on the same satellite, pointing in the same direction. In literature it was often found that normalization constant was close to one, and was kept as such during fitting. Ignoring it should not produce relevant effects.

Number of energy bins for XRT and BAT

XRT data should be binned minimum to 20 counts per bin. Depending on the intensity of the burst and excluded central pixels this may give different number of bins. BAT data should be binned in such a way to have at least half number of bins with errors smaller than the value. If XRT or BAT has many more bins than the other, then that one will affect χ^2 statistics much more and other instrument wont play much role. So, number of bins should be similar. This goes for the underlying component which can be power-law or cutoff-powerlaw, or Band function. If the thermal component is significantly in the range of one instrument, XRT for example, than XRT should have good resolution in order to follow the bump of the thermal component.

Another thing is as binning change within some excepted intervals, the values obtained from the fit will change. In some cases this may produce significant differences in parameter values, errors, and comparisons between models.

Final remark

All the above mentioned should be kept in mind when reading results of from the fit. Small errors of the parameter may not mean it is likely close to that value. There may be underlying uncertainties which are beyond fitting in XSpec. Even if all the above uncertainties didn't exist, it is hard to claim detection of the thermal emission. Black body spectrum is distinguished by a steep index of $+1$ before the peak which then falls of exponentially. Even if thermal peak isn't deformed by mildly relativistic motion, or lack of complete thermalization, to detect it would require a black body peak to be significantly above underlying component. In vast majority of cases this is not true and at best adding a black body component is done to detect curvature of underlying component or a bump. Then, assuming it is a black body, the evolution of its temperature, luminosity and calculated radius may be followed. From there it may be discuses weather the results have physical sense. For example, radius should start from smaller value and only increase with time (also relativistic correction should be taken into account).

4.1.5 MCMC

When XSPec finds the best fit (minimum χ^2), the values correspond to that minimum. With the "error" command it is possible to find interval based on change of χ^2. For example, changing the parameter where χ^2 changes by 2.706 corresponds to 90% confidence for that parameter. This than may give asymmetric errors. Similar may be done in whole parameter space to determine correlation between parameters and calculate error on flux for example. This statistical method would correspond to frequentest approach.

However, the parameter value corresponding to minimum χ^2, although it may be the most probable value, it may not be the mean value. Difference is bigger if the probability distribution for the parameter is more asymmetric. Within XSpec there is a way to implement Marcov Chain Monte Carlo (MCMC). The basic idea is that for a given data (and their errors) and model, the chain will "walk" trough parameter space and eventually after some number of initial steps, it will start to trace the probability distribution in the parameter space. Then the more steps taken (10^4, 10^5, etc.), the better resolution of this probability function. The final output can be a fits or a text file with all the sets of parameters. The idea is that these sets of parameters are as if they were taken from the probability distribution. This statistical method corresponds to Bayesian approach. XSpec implements parallel processing when doing tasks such as MCMC.

Lets say there are 10^5 steps and parameter sets. The mean value of a parameter is then simply the average of all 10^5 generated parameters. The 90% confidence interval (for example) is found by sorting all 10^5 by value and then excluding the first and last 5%. This may be done within Python or within XSpec with "error" command which will than calculate errors based on MCMC results. XSpec offers a way to calculate flux with errors and will use MCMC results to do this. However, when trying to calculate unabsorbed flux (lower energy interval of $0.3\ \mathrm{keV}$), or flux of just one component, with the command "cflux", there are some problems. Specific flux may be calculated within Python by taking all 10^5 parameter sets. Then, all the 10^5 unabsorbed fluxes for, say, black body and power-law are calculated, their values sorted, average value found, and 90% confidence interval found by excluding first and last 5%. These fluxes then take into account not just probability distribution of each parameter, but also the correlation between parameters since MCMC chain traced probability distribution in whole parameter space. This is also the way for calculating any other value and its errors based on parameters found in fit, such as radius of the black body, its apparent speed of expansion, etc. Python script has been written to do this.

The particular use of this method here is when the peak of the black body lies between XRT and BAT ranges ($10 - 15\ \mathrm{keV}$) and the temperature is not well constrained. In this case the value corresponding to minimum χ^2 and the main value may be different by a significant factor. This then translates to different values of radius since it depends much more on temperature ($R^2 \propto T^{-4}$) then on flux ($R^2 \propto F$). In this analysis the Goodman-Weare type of MCMC will be used.

4.2 Preliminary results

Taking into consideration details from previous section, the analysis of Swift GRBs with simultaneous data in XRT-BAT was done. Selected GRBs have strong intensity in XRT-BAT to allow time resolved analysis, and redshift to determine rest frame properties. When the work was being done, the selection was up to end of year 2015 / beginning of 2016. The MCMC method wasn't used. Values and errors from the best fit were taken, and errors of calculated values were determined by error propagation.

In many cases fit will improve if additional component is added such as black body. To select GRBs with probable black body, models were compared based on χ^2, strength of the black body compared to the underling component, systematic residuals in *model minus data* when using only underlying component. For the underlying component, power-law and cutoff-powerlaw were used. Also Band function was used sometimes. Band function

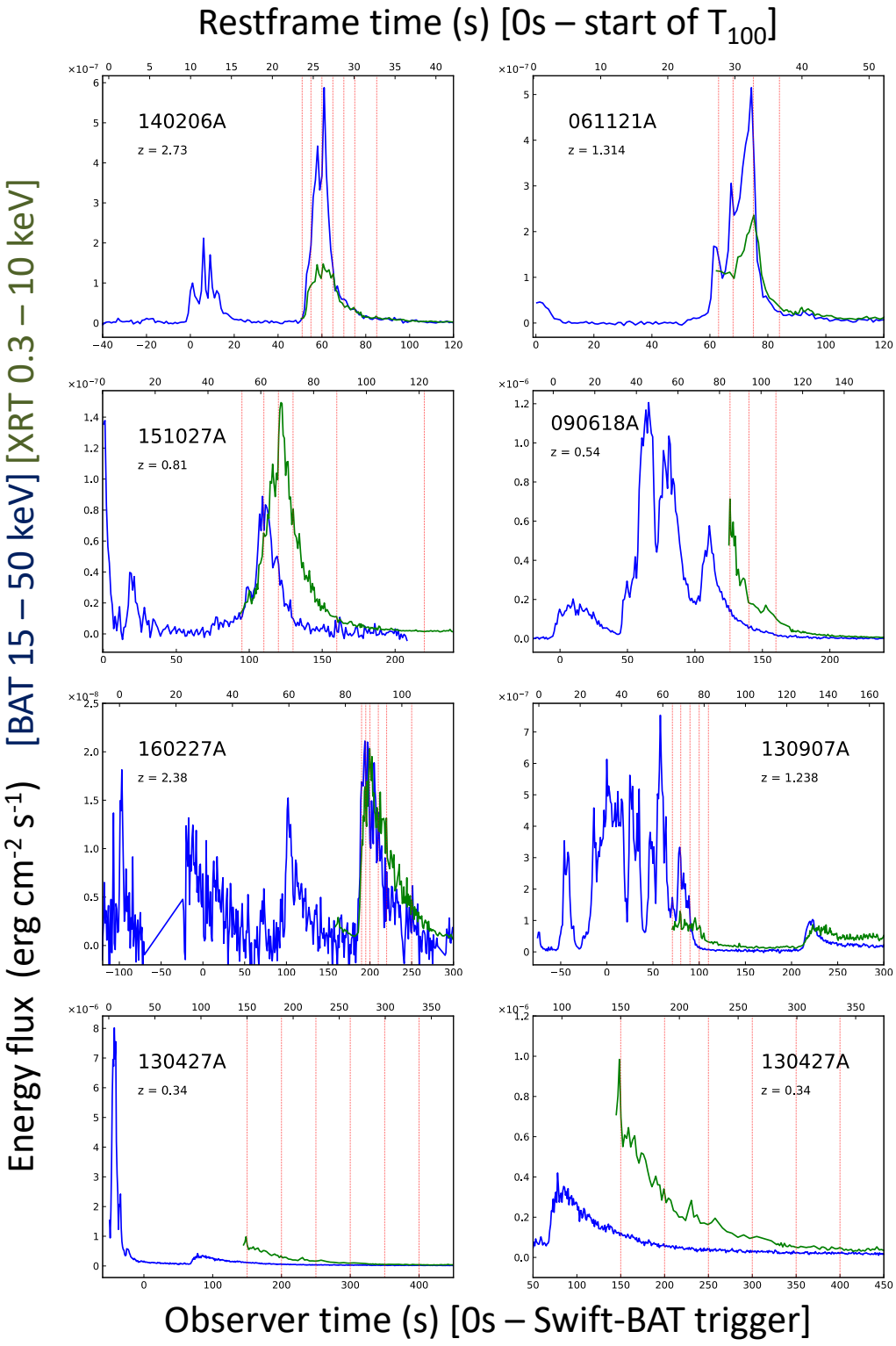

Figure 4.1: GRBs with time intervals where evidence for thermal component is relatively good. On each plot name of the burst and redshift z are shown. On the bottom axis is the observer time with respect to Swift-BAT trigger while on the upper axis is restframe time with respect to the very beginning of the burst which was determined as the start of the T_{100} interval which was obtained from automatic analysis on the Swift website. In some cases the start of this interval is much before the trigger. Blue lines are light curves of BAT detector while green correspond to XRT. Further details are in the text.

was also used to mimic power-law plus black body, and Band with exponential cutoff to mimic cutoff-powerlaw plus black body (with turnover at Band corresponding to peak of the black body). When the intensity was strong enough, fits with two black bodies were tried.

In the end these GRBs have relatively good evidence for a strongly evolving black body component: 140206A, 061121A, 151027A, 090618A, 160227A, 130907A, 130427A. On Figure 4.1 light curves of the XRT and BAT are presented along with time intervals where thermal emission was found. For GRB 140206A and 061121A, the time interval corresponds to the main part of the prompt emission. The XRT prompt detection is possible due to the fact that there was a precursors which triggered BAT so Swift had time to point XRT and catch the prompt. For 151027A thermal emission was in the second peak which was well separated from the first and has similar energy. For the rest the thermal emission was found in the slope of the last peak of the prompt emission, flare or in the extended emission.

In Figure 4.3 parameters of 7 bursts are shown. In the **upper-left** evolution of the temperature with time is shown. Time is in the rest frame of the burst as well as temperature, i.e. both are as if they were observed from the GRB host galaxy. Temperature is not the comoving temperature, i.e. no correction for relativistic motion is shown. It can be seen that temperature spans the range from $10 - 0.1\ \mathrm{keV}$ and for each burst starts from highest value and monotonically decreases up to an order of magnitude. In the **upper-right** is evolution of the luminosity of the black body with rest frame time. Unlike temperature, it seams there is detectable fast rise in luminosity and than slower decay about order of magnitude. Luminosity corresponds to whole black body luminosity calculated from black body formula, not just from specific energy range of detectors.

In the **lower-left** is shown radius for each burst with rest-frame time as calculated simply by $L = 4\pi R^2 \sigma T^4$ where L is luminosity (the one from previous case), T temperature as seen from the host galaxy and R the radius. No correction for relativistic motion has been applied. For all cases radius increases monotonically from lowest to highest value. This apparent radius may be used to see if the motion is relativistic or no. From evolution of radius with time, approximate velocities are: 130427A ($2.5\ \mathrm{c}$), 061121A ($1.1\ \mathrm{c}$), 090618A ($0.9\ \mathrm{c}$), 151027A ($0.8\ \mathrm{c}$), 130907A ($0.7\ \mathrm{c}$), 140206A ($0.6\ \mathrm{c}$), 160227A ($0.5\ \mathrm{c}$). Some bursts show superluminal velocities and clearly need correction. Other have non-negligible fraction of speed of light.

In the **lower-right** is crude comparison between black body isotropic energy calculated as integrated luminosity over time period where thermal emission was found, and, total energy of GRB. It can be seen that black body isotropic energy spans less than order of magnitude in range while isotropic energies of GRBs span about two orders of magnitude.

In Figures 4.4 and 4.2 spectral energy distribution of time resolved analysis is shown for bursts 140206A, 061121A, 151027A, 160227A and 130907A. Bursts 090618A and 130427A have an evidence for a second black body and will be shown later. The time intervals correspond to observation time since the GRB burst.

Bursts 160227A, 130907A, 130427A have started main part of emission before BAT trigger time. The $t = 0\ \mathrm{s}$ in the Figure 4.3 for these bursts corresponds to actual start of the burst and not trigger time of BAT. For bursts 090618A and 130427A the XRT started observing after the peak of the extended emission. If it started observing earlier, it may be reasonably assumed that black body would exist and that evolution would be in similar matter as others. If data for these two bursts are extended to earlier times (espe-

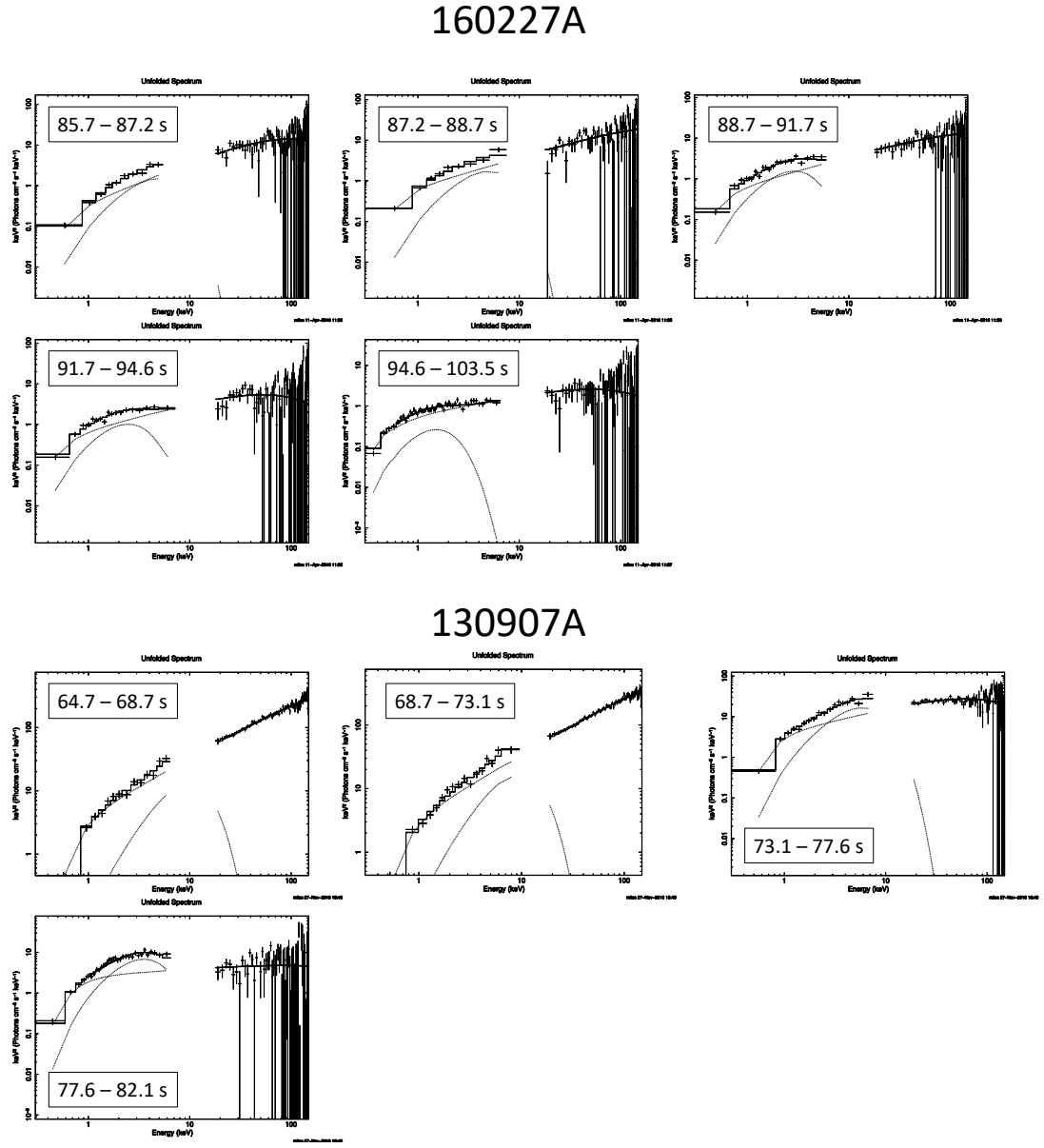

Figure 4.2: Spectral energy distribution of time resolved analysis of bursts 160227A and 130907A. First burst is fitted with cutoff-powerlaw and black body while the second is a combination of cutoff-powerlaw and just power-law. Time intervals correspond to restframe time centered on the start of T_{100}.

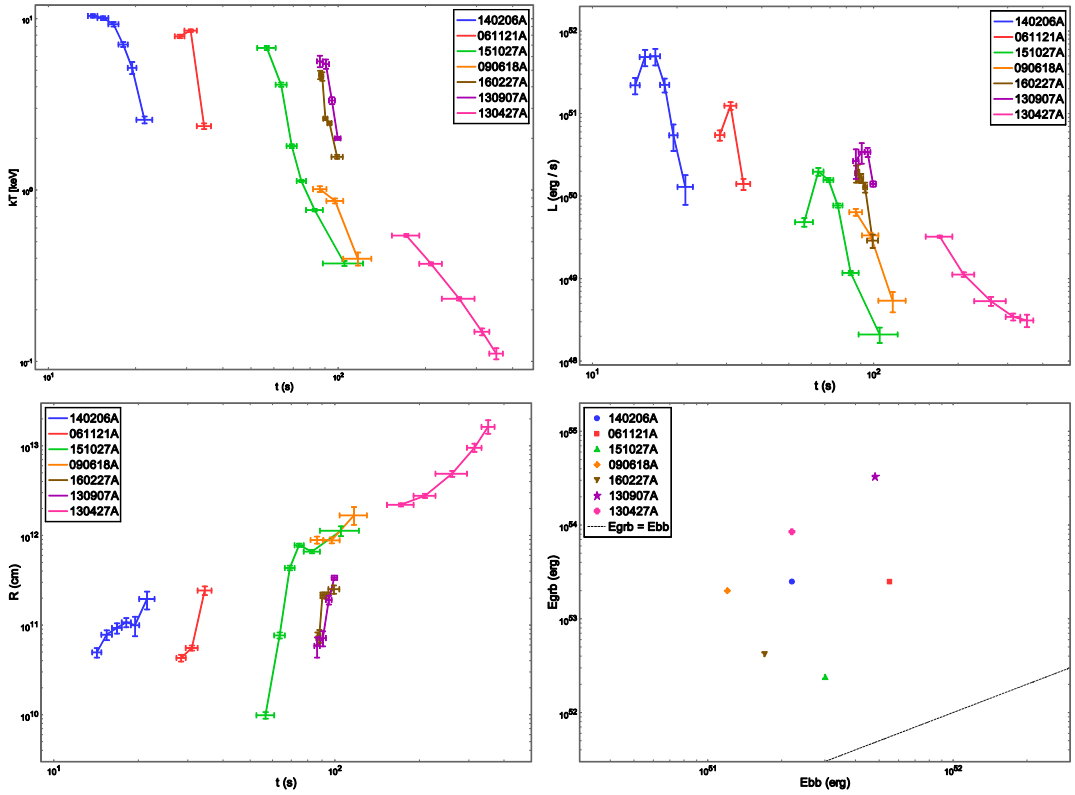

Figure 4.3: Parameters from the spectral fit versus rest frame time. Rest frame temperature, luminosity, calculated radius and approximate ration of isotropic energy in thermal emission versus the entire burst. More details in the text.

cially 130427A), the parameters would be closer to the ones of bursts 151027A, 130907A and 160227A which show some clustering in parameter evolution. As mentioned before, thermal emission in bursts 140206A, 061121A happens during main part of the prompt emission. This may be reason why the parameters of their thermal emission seam to be outliers. Finally, the question might be asked do the detector sensitivity and limitations produce seemingly similar evolution of thermal emission. For example, it is known that within each pulse in the prompt emission, the peak evolves monotonically towards lower energies. Something similar might happen at the end of prompt emission where the spectra has a bump or curvature which is not due to thermal emission, and it evolves monotonically towards lower energies (which might be interpreted as black body cooling). Then the detectability of this bump/curvature may dictate intensity and change in luminosity (if it is assumed it comes from thermal emission). In the end these two may produce the calculated radius to only increase. This is something that should be kept in mind.

4.2.1 Two black bodies

In the bursts 090618A and 130427A relatively good evidence for two black bodies was found. In both cases the lower temperature black body is the one from the previous analysis, the one shown on the Figure 4.3 for these bursts, and it follows the pattern previously described. When fitting with just one black body the lower temperature one is recovered with similar parameters and evolution.

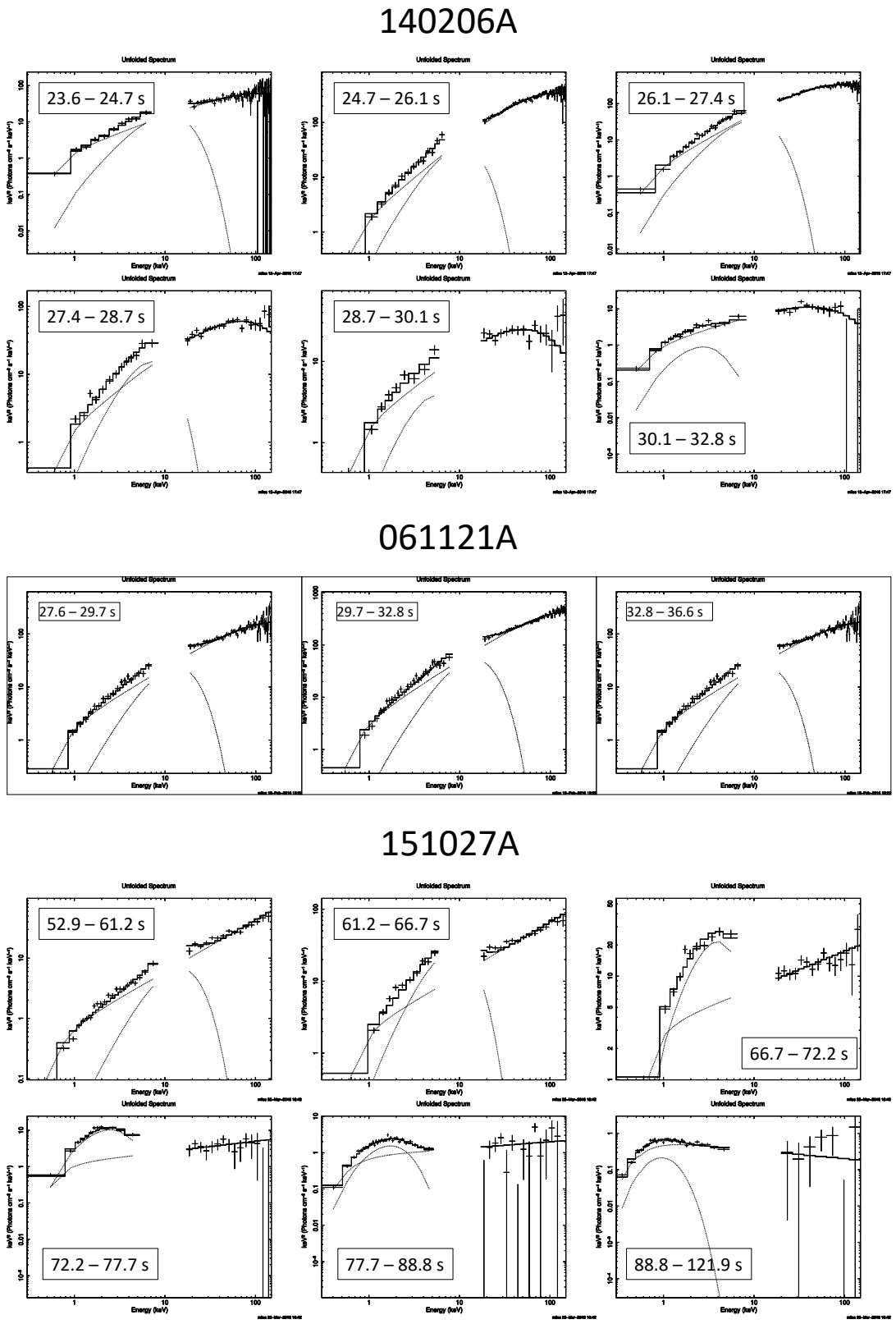

Figure 4.4: Spectral energy distribution of time resolved analysis of bursts 140206A, 061121A and 151027A. The first two bursts are fitted with cutoff-powerlaw and a black body while the last one is fitted with power-law with a black body. Time intervals correspond to restframe time centered on the start of T_{100}.

The second black body retains relatively constant temperature. In the case of 090618A, the temperature is around $kT_2 \approx 2.1\ \mathrm{keV}$. The luminosity in the first time bin is about 3 times higher than lower black body, and then drops more intensely about 3 times, while the lower black body drops about 2 times. For 130427A, the temperature of the higher black body relatively constant in the range of $kT_2 \approx 1.5 - 2\ \mathrm{keV}$. The luminosity in the first time bin is almost the same as the lower black body, but than it drops rapidly by about factor of 5, then 2, and than it remains the same, while the lower one drops more gradually and continuously without stooping. The parameters of the lower-temperature black body is in line with the one reported in (Ruffini et al., 2015d) which was found in the XRT data. In the Figure 4.5 time resolved analysis is shown.

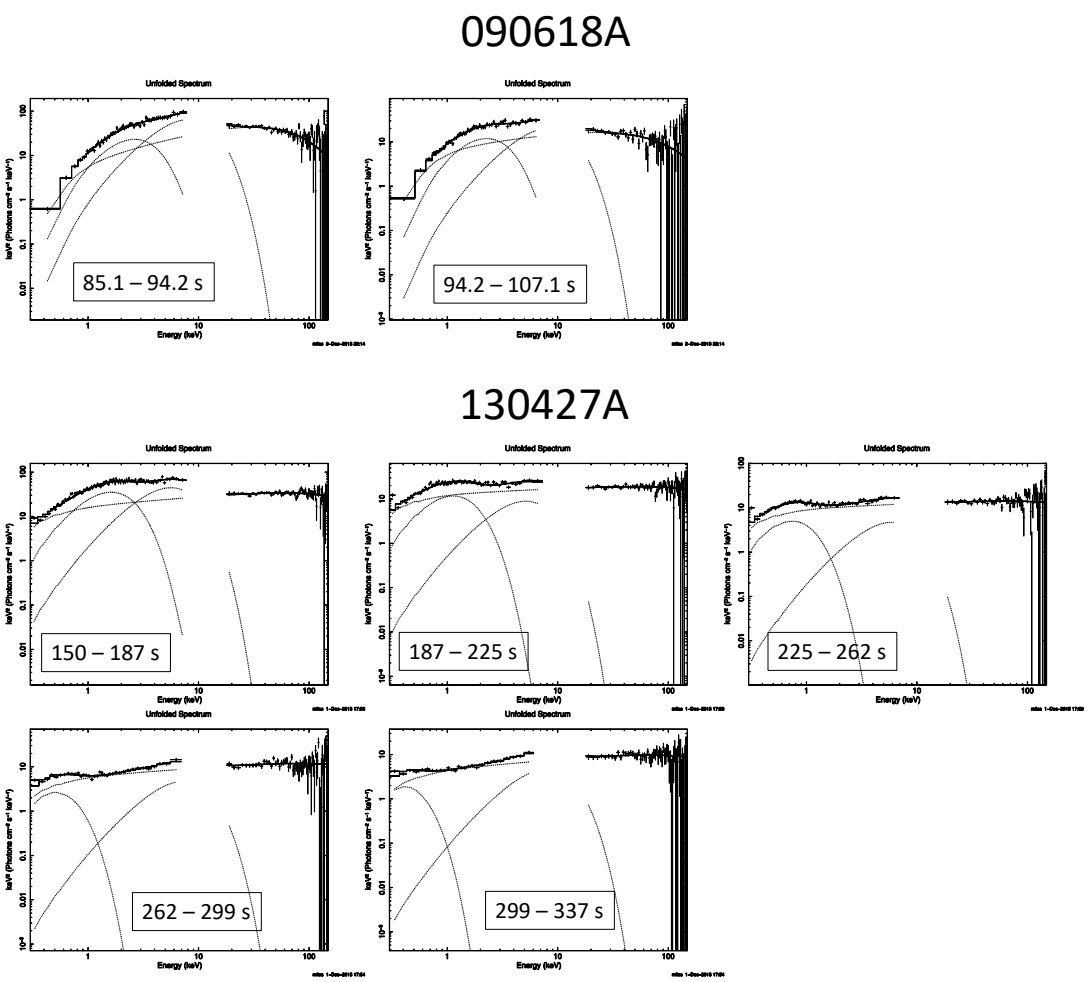

Figure 4.5: Spectral energy distribution of time resolved analysis of bursts 090618A and 130427A. Time intervals correspond to restframe time centered on the start of T_{100}. Both bursts are fitted with cutoff-powerlaw and a two black bodies. More details in the text.

4.3 GRB 151027A

This GRB has the strongest evidence for a black body and was analyzed in more detailed taking into account MCMC. The exclusion of central pixels was done in conservative way, i.e. for an interval, more were taken out rather than less. If, for example, less pixels

Time bin s	Model	α	L_u $\times 10^{49}$ erg/s	kT keV	L_{BB} $\times 10^{49}$ erg/s	R $\times 10^{10}$ cm	χ^2/DoF	Ftest
95 - 100	PL+BB	$1.349^{+0.024}_{-0.036}$	$20.4^{+1.5}_{-1.5}$	$2.2^{+1.1}_{-1.1}$	$1.34^{+1.1}_{-0.88}$	$6.4^{+14}_{-3.8}$	109/107	2×10^{-7}
100 - 110	PL+BB	$1.293^{+0.029}_{-0.031}$	$45.2^{+1.5}_{-1.6}$	$2.57^{+0.43}_{-0.50}$	$5.3^{+2.1}_{-2.2}$	$9.3^{+3.6}_{-2.9}$	66.9/77	1×10^{-5}
110 - 120	PL+BB	$1.392^{+0.028}_{-0.033}$	$63.0^{+1.9}_{-1.8}$	$2.17^{+0.22}_{-0.26}$	$15.8^{+3.6}_{-3.8}$	$22.6^{+4.5}_{-3.6}$	81.7/85	9×10^{-13}
120 - 130	PL+BB	$1.732^{+0.049}_{-0.057}$	$27.1^{+1.8}_{-1.9}$	$1.10^{+0.14}_{-0.12}$	$15.2^{+2.0}_{-1.9}$	87^{+19}_{-17}	101/103	9×10^{-27}
130 - 140	PL+BB	$1.82^{+0.11}_{-0.14}$	$9.0^{+1.6}_{-1.6}$	$0.617^{+0.046}_{-0.043}$	$6.3^{+1.0}_{-1.0}$	177^{+30}_{-28}	50.1/53	9×10^{-15}
140 - 150	CPL+BB	$1.65^{+0.15}_{-0.16}$	$5.3^{+1.4}_{-1.4}$	$0.469^{+0.065}_{-0.064}$	$2.61^{+0.70}_{-0.70}$	197^{+67}_{-52}	18.2/27	9×10^{-6}
150 - 160	PL+BB	$2.40^{+0.45}_{-0.34}$	$2.07^{+6.1}_{-6.1}$	$0.386^{+0.061}_{-0.061}$	$1.17^{+0.41}_{-0.38}$	195^{+81}_{-55}	23.4/27	2×10^{-5}
160 - 180	PL+BB	$2.15^{+0.29}_{-0.34}$	$1.43^{+0.38}_{-0.33}$	$0.193^{+0.032}_{-0.030}$	$0.52^{+0.29}_{-0.32}$	520^{+240}_{-250}	48.7/38	3×10^{-2}

Table 4.1: Time resolved analysis of GRB 151027A. Details are in the text.

are excluded, the temperature of thermal component gets higher in the first half of time bins.

In the Table 4.1 are results of the fit. First 6 intervals are fits from both BAT and XRT data while last 2 are just from XRT since emission in BAT range almost disappears. Models used are power-law and black body (PL+BB) or cutoff-powerlaw and black body (CPL+BB). Only in the sixth interval significant deviation from powerlaw is present and cutoff energy may be constrained within 90% significance. Parameter α corresponds to power-law or cutoff-powerlaw index. Parameter L_u is luminosity of the underlying component. If it is power-law, then the energy range used is $0.3 - 150$ keV in the observer frame. For the last two intervals it is in $0.3 - 10$ keV range. If it is cutoff-powerlaw, then it the range is from 0.3 keV to "infinity" since it converges because of the exponential cutoff. Parameter kT is temperature of the thermal component. Parameter L_{BB} is luminosity of the black body component corresponding to whole energy range. Parameter R is the apparent radius of thermal emission. The last two columns contain statistical information, with χ^2/DoF corresponding to best fit with thermal component, and Ftest corresponding to comparison between this statistic and the one with just underlying component (power-law or cutoff-powerlaw).

Values for fit parameter kT and calculated parameters L_u, L_{BB}, and R in the Table 4.1 are main values and their errors correspond to central 90% interval. This was obtained based on MCMC with 10^5 steps with exclusion of first 10^4. Main values of kT and 90% interval are very similar to the ones corresponding to minimum χ^2 and 90% interval based on $\Delta\chi^2 = 2.706$. The only exception is for the first time bin.

In Figure 4.6 same time resolved analysis is shown. The time sequence is from left to right, up to down. First 8 plots correspond to XSpec command "ldata" which shows data as it is regardless of fitted model. The effective area correction has been applied so the data and model look like they are not convolved by instrument response. Additionally difference between data and model is shown in units of 1σ. The last 8 plot correspond to XSpec command "eeufspec" and present spectral energy distribution. Here the model is in the focus while the data may change if the model changes. In both cases the models correspond to best fit values, i.e. the values from minimum χ^2 and not the main values. However, both are very similar (except for the first interval).

In Figure 4.7 parameter evolution from Table 4.1 is shown. The time is rest frame time for all 4 plots. The temperature is rest frame temperature but not comoving temperature, i.e. as it would be seen from the host galaxy. The overall trend can be seen that temperature monotonically decreases, radius increases, luminosity increases and then more slowly decreases. The last plot corresponds to apparent velocity (in units of speed of light) based on evolution of apparent radius. This has also been calculated based on

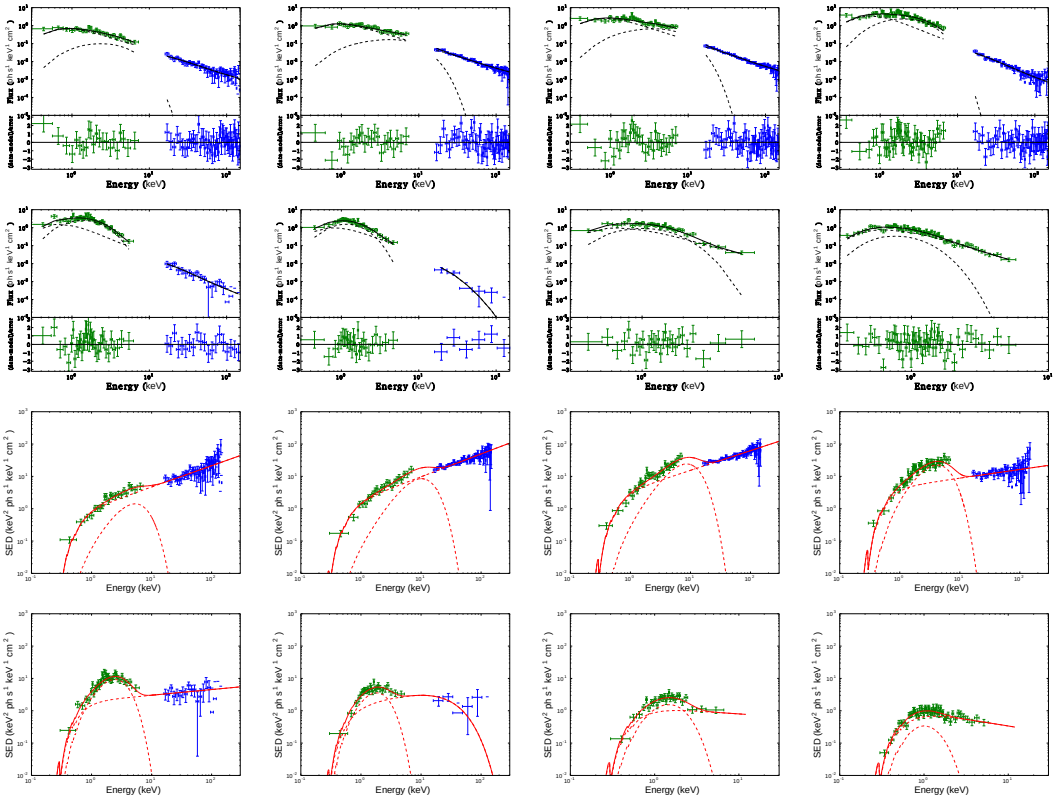

Figure 4.6: Plotted spectra from time resolved analysis of GRB 151027A. Details are in the text.

MCMC results from radii (two sets of radii for one set of speed). In principal this may give velocities which lower limit is negative. It seems that at first the speed increases and than decreases, and increases abruptly. However, when dealing with radii on the order of magnitude 10^12 cm, small variation in fit results may give large absolute differences in radii, and hence velocity, than when dealing with radii of magnitude $10^{11}, 10^{12}$ cm for the same travel time. Also important to note that last two intervals have only XRT data and are less reliable.

4.3.1 Temperature from the first time interval

The parameters from first time interval diverge the most from a common trend, including the decreasing temperature trend. The temperature value and errors from minimum χ^2 is $kT = 1.33^{+0.61}_{-0.26}$ keV while from MCMC it is $kT = 2.2^{+1.1}_{-1.1}$ keV. This is a difference of almost factor of 2. In the first plot on Figure 4.8 are the results from MCMC for temperature. The 10^5 values are plotted against the χ^2. Each empty circle is one value. With so many, they will outline the χ^2 "well" for the parameter. The minimum of χ^2 can be seen to indeed lie close to value of $kT = 1.3$ keV. However the whole distribution is skewed significantly to the higher values and the main value is very different. Even the large unsymmetry of errors from the χ^2_{min} results shows that distribution is skewed towards higher energies.

Additionally, there seams to be change in "slope of the well" near value of $kT = 2.5, 2.6$ keV. This might mean that temperature distribution is more complicated than just skewed, or it could mean that there is another thermal component at higher tempera-

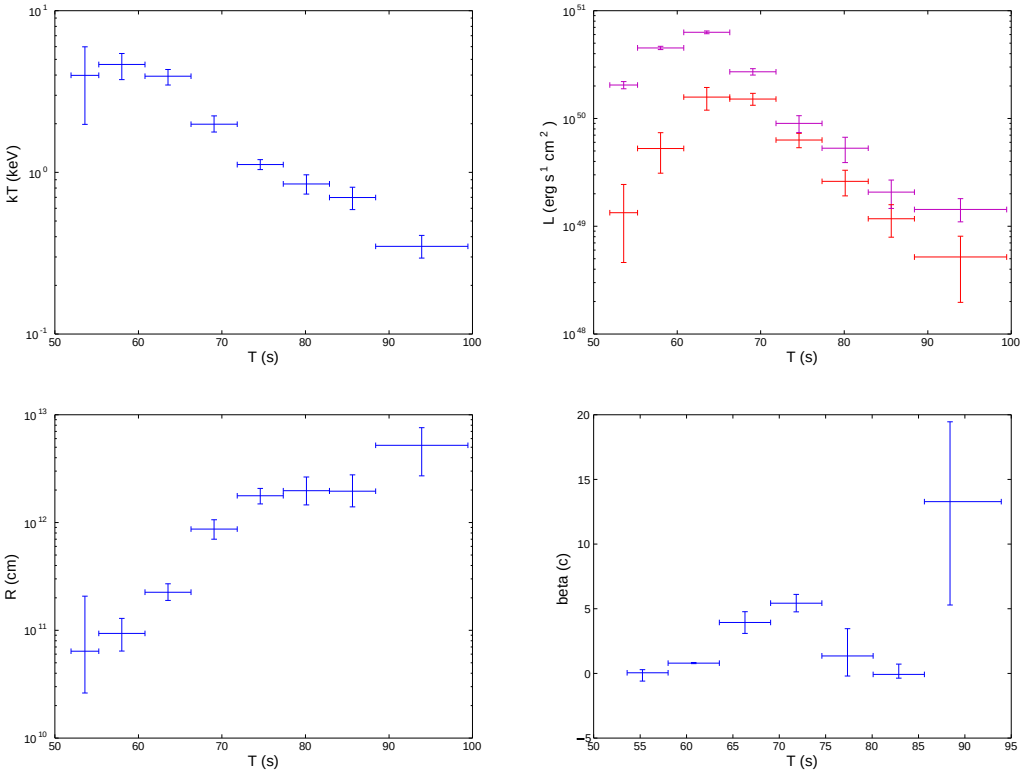

Figure 4.7: Evolution of parameters for 151027A. In the luminosity plot, red points correspond to black body while purple are from underlying component. Further setails are in the text.

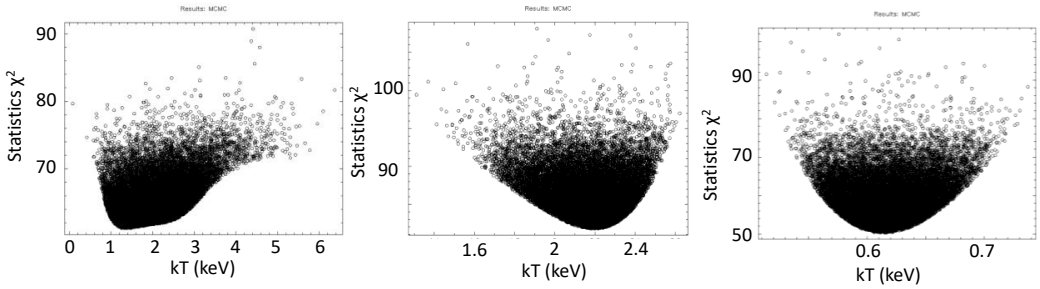

Figure 4.8: Results from MCMC related to temperature. From left to right, the first plot corresponds to first time interval $95 - 100$ s, the second to $110 - 120$ s time interval, and the last one to $130 - 140$ s time interval.

ture, but cannot be detected due to non-existence of local χ^2 well (local minimum) due to influence of first black body. Then this higher black body may be the one which correspond to the one from all the other time intervals, and the one of $kT = 1.3$ keV (which would now have the main value closer to χ^2_{min} 1.3 keV value) is not related to it. The second plot on Figure 4.8 corresponds to temperature from third time interval. The distribution is skewed towards lower temperatures, but less and without "deformities". The third plot corresponds to fifth interval and χ^2 "well" is almost symmetric.

In any case, the main value and errors of the first-interval temperature are found considering MCMC results as coming from just one black body. The large errors reflect the wide distribution. With these error the temperature cannot be said to contradict the decreasing trend, however the main value is lower than the main value in the next time interval. The normalization constant may be raid directly from luminosity since that is how it is defined in XSpec. From the plot the first point in luminosity fits well in the initially increasing trend. Finally the radius has large errors due to large errors of temperature. The main value of first radius is actually lower then the one of next and may be considered to fit well with monotonically increasing trend of radius, but the large asymmetric upper error has to be kept in mind.

4.3.2 151027A in the IGC scenario

Following the work (Ruffini et al., 2018), GRB 151027A was analyzed from the Induced Gravitational Collapse point of view in (Ruffini et al., 2017a) (Figure 4.9). The burst was interpreted as binary driven hypernova. The T_{90} prompt emission is made out of two peaks. The first one is identified as original GRB with the P-GRB component and extended afterglow. The second one is identified as *gamma-ray flare* which corresponds to interaction of fireshell plasma with supernova ejecta. Finally the flare in the afterglow (after T_{90} interval) is identified as *X-ray flare* which corresponds to late interaction of fireshell plasma with supernova ejecta.

4.4 Thermal spectrum from relativistically expanding sphere

Here the emission from *spherically symmetric, expanding with constant velocity, sharp black body surface, with uniform and constant temperature* will be derived. Although the focus is on mildly relativistic velocities, the derivations are valid for all values of Lorenz factor γ and for completeness the presented results will range from non-relativistic to ultra.

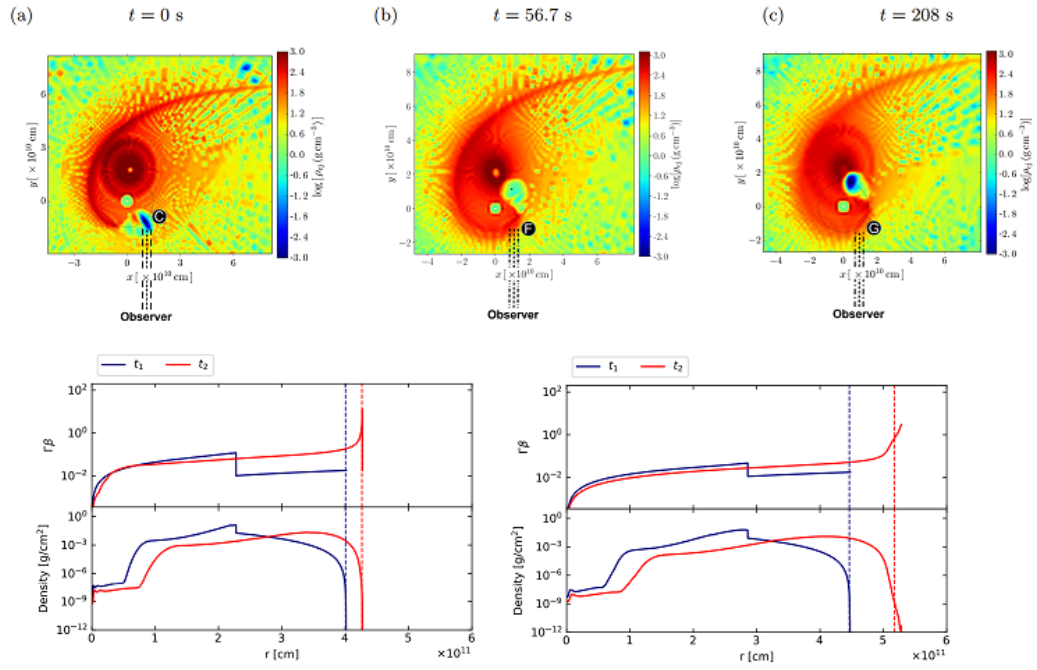

Figure 4.9: **The upper image** contains three snapshots of the density distribution of the SN ejecta in the equatorial plane of the progenitor binary system. The time t = 0 indicates the instant when the NS companion reaches, by accretion, the critical mass and leads to the formation of a BH (black dot). **The lower-left image:** Numerical simulation of the Gamma-ray flare. Above is the distribution of the velocity inside the SN ejecta at the two fixed values of the laboratory time t (before the plasma reaches the external surface of the ejecta) and t2 (the moment at which the plasma, after having crossed the entire SN ejecta, reaches the external surface). Bellow is the corresponding distribution of the mass density of the SN ejecta in the laboratory frame. **The lower-right image:** The same as in the left, except for the X-ray flare. Images are taken from (Ruffini et al., 2017a).

4.4.1 Basic equation

Spectrum of a black body is described as:

$$N_{ES^2\Omega} = \frac{2}{h^3c^2}\frac{E^2}{\mathrm{e}^{\frac{E}{kT}} - 1}\cos\theta \tag{4.1}$$

where $N_{ES^2\Omega}$ are emitted photons in a unit of time, per unit of energy, from a unit of surface, in a unit of space angle. Subscript indexing will reflect these differential quantities. Only *per time* subscript is omitted since it will always be present and is implied. For the purposes of this section the units will be: $\mathrm{photons}\ /\ \mathrm{s}\ \mathrm{keV}\ \mathrm{cm}^2\ \mathrm{sr}$. Temperature (internal kinetic energy) kT is in units of keV, energy of photons (spectrum) E in keV. Constants such as speed of light in $c \approx 3\times10^{10}\ \mathrm{cm/s}$, Planck constant $h \approx 4.14\times10^{-18}\ \mathrm{keV\ s}$. Angle θ is an angle between the *normal* to surface element, and direction of space angle (photons direction).

Peak of the $N_{ES^2\Omega}$ spectrum is found by $\frac{d}{dE}\left[N_{ES^2\Omega}\right] = 0$. If $\frac{E}{kT} \equiv x$ then it gets to $\frac{xe^x}{e^x-1} = 2$. The numerical (3-digit) solution is $x = 1.594 \approx 1.5$. So, the peak of $N_{ES^2\Omega}$ spectrum is at energy which is at $E_p \approx 1.5 \times kT$. Peak of the spectral energy distribution $E^2 \times N_{ES^2\Omega}$ is found in the same way and it comes down to $\frac{xe^x}{e^x-1} = 4$. The numerical (3-digit) solution is $x = 3.921 \approx 4$. The peak of spectral energy distribution is at $E_p \approx 4\times kT$. This is useful when looking at plots.

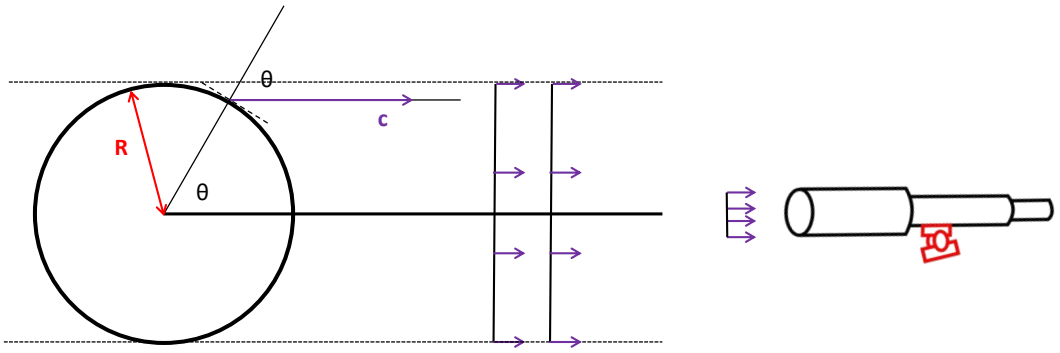

Figure 4.10:

The same quantity as $N_{ES^2\Omega}$ or any other $N_{...}$ but expressed as amount of energy, not number of photons, will be marked as F. In the basic case, $F_{ES^2\Omega} = E \times N_{ES^2\Omega}$ as well as any other case $F = E \times N$. The emitted energy is then in units of keV. The emitted energy over whole spectrum is obtained from integrating $F_{ES^2\Omega}$ over whole energy range. The final solution is $F_{S^2\Omega} = \frac{1}{\pi}\sigma T^4 \cos\theta$ where θ is the same angle as before and σ is the Stefan–Boltzmann constant. Integrating $F_{S^2\Omega}$ over half space angle: $F_{S^2} = \sigma T^4$. For unit consistency the σT^4 may be expressed as $\frac{2\pi^5}{15h^3c^2}(kT)^4$, with $\frac{2\pi^5}{15h^3c^2} \approx 6.416 \times 10^{33}\ \mathrm{s}^{-1}\ \mathrm{keV}^{-3}\ \mathrm{cm}^{-2}$.

4.4.2 Non-expanding sphere

First the method will be applied to still sphere (Figure 4.10) which will later be extended to expanding one.

Angle θ is between normal to the $\mathrm{d}S^2$ surface and the direction of emission. It is also the angle between lines which connect center of the sphere to the surface element and the detector. Detector is far enough to have all the directions from each element reaching the area of detector - be practically parallel. This introduces wave fronts which are perpendicular to the main line connecting sphere with detector. Sphere has a temperature T, radius R and distance to detector d.

In order to get luminosity it can be done like:

$$L \equiv F = 4\pi R^2 F_{S^2} = 4\pi R^2 \sigma T^4$$

In order to get energy flux at detector:

$$F_{A^2} = \frac{L}{4\pi d^2} = \frac{R^2 \sigma T^4}{d^2}$$

It can also be done integrating each element of the sphere. It is needed to integrate these elements taking care of sphere shape and different direction of radiation for each element (with respect to surface of element) in order to have them all radiate in the same direction (towards detector). So, element of the sphere $\mathrm{d}S^2$ is:

$$\mathrm{d}S^2 = R\sin\theta \mathrm{d}\varphi \times R\mathrm{d}\theta = R^2 \mathrm{d}\varphi \sin\theta \mathrm{d}\theta$$

Each element will emit towards detector and it is described by the quantity $F_{S^2\Omega}$:

$$F_{S^2\Omega} = \frac{1}{\pi}\sigma T^4 \cos\theta \tag{4.2}$$

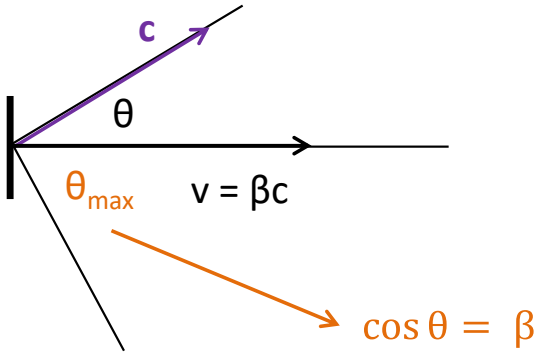

Figure 4.11:

Since it is axially symmetric with respect to φ it can be integrated over φ and this will give radiation from the line circle towards the detector:

$$F_{S\Omega} = \int_0^{2\pi} F_{S^2\Omega} R \sin\theta \, d\varphi = 2\pi R \sin\theta F_{S^2\Omega}$$

$$F_{S\Omega} = 2R\sigma T^4 \sin\theta\cos\theta$$

Now, to get F_Ω:

$$F_\Omega = \int_0^{\frac{\pi}{2}} F_{S\Omega} R \, d\theta = 2R^2\sigma T^4 \int_0^{\frac{\pi}{2}} \sin\theta\cos\theta \, d\theta$$

$$F_\Omega = R^2\sigma T^4$$

In order to get luminosity of the sphere it is needed to multiply by total solid angle:

$$L \equiv F = F_\Omega 4\pi = 4\pi R^2 \sigma T^4$$

In order to get energy flux at detector:

$$F_{A^2} = \frac{F_\Omega}{d^2} = \frac{R^2\sigma T^4}{d^2}$$

4.4.3 Relativistic movement of a surface element

In this case the movement is in direction normal to its surface which is the case of the expanding sphere. In Figure 4.11 angle θ is between normal to the $\mathrm{d}S^2$ surface and the direction of emission. It is also an angle from direction of movement and direction of emission. Speed is $\beta = \frac{v}{c}$, Lorentz factor is $\gamma = \frac{1}{\sqrt{1-\beta^2}}$, and relativistic Doppler factor is $D = \frac{1}{\gamma(1-\beta\cos\theta)}$, and when $\theta = 0$ ($\cos\theta = 1$), $D_{max} = \frac{1}{\gamma(1-\beta)}$. When $\beta \to 1$, $D_{max} \approx 2\gamma$.

The element won't radiate in half space angle but from $\theta = 0$ to θ such that $\cos\theta = \beta$. When considering comoving frame of the surface, the $\cos\theta = \beta$ angle corresponds to $\theta' = 90°$. Even just considering simple motion, photons sent at angles beyond $\cos\theta = \beta$ will immediately get "swallowed up" by the moving surface. This is a well known effect, see for example (Bianco et al., 2001). The minimum relativistic Doppler factor is then $D_{min} = \gamma$.

β	0.1	0.3	0.9	0.99	0.999	0.9999	0.99999	0.999999
γ	1.005	1.048	2.294	7.089	22.37	70.70	223.5	702.5
D_{max}	1.106	1.363	4.359	14.11	44.71	141.4	446.9	1405

Table 4.2:

Some basic values of β, γ and D_{max} in Table 4.2 ranging from non-relativistic motion to ultra-relativistic seen in the prompt emission of few GRBs.

Change (boost) of thermal spectrum

How will the value $N_{ES^2\Omega}$ in the rest frame of BB surface change when it is boosted, i.e. what will detector which is in rest with respect to host galaxy see.

First, each photon's energy will be boosted by D. Spectrum will shift to higher energies. So, every E in $N_{ES^2\Omega}$ needs to be $\times\frac{1}{D}$ to account for the shift to higher energies. This will cause spectrum to "stretch", so each keV interval in the boosted spectrum will have $\frac{1}{D}$ less photons than the spectrum in the rest frame (just due to stretching). So, entire spectrum will go down by D, i.e, $N_{ES^2\Omega}$ should be also $\times\frac{1}{D}$.

Second, movement of the BB towards the detector will cause increase in intensity by a factor of $\frac{1}{1-\beta\cos\theta}$ (ordinary Doppler factor). And, since the BB was accelerated and is moving, the time will go slower in the rest frame of BB by a factor of γ and this will decrease the intensity of boosted spectrum. So, the $N_{ES^2\Omega}$ should be $\times\frac{1}{\gamma}\frac{1}{1-\beta\cos\theta}$, i.e, $N_{ES^2\Omega}$ should be $\times D$.

Third, beaming in the direction of movement will cause an increase in intensity. The solid angle $\mathrm{d}\Omega'$ in the rest frame of BB will be "squeezed" to $\mathrm{d}\Omega$ and this will cause an increase in intensity. Some basic equations are: $\mathrm{d}\Omega' = \sin\theta'\mathrm{d}\varphi'\mathrm{d}\theta'$, $\mathrm{d}\Omega = \sin\theta\mathrm{d}\varphi\mathrm{d}\theta$. Connection between θ' and θ can be presented as, for example, $\sin\theta' = \sin\theta D$. With basic trigonometric formula in both frames $\sin^2\theta' + \cos^2\theta' = 1$ and $\sin^2\theta + \cos^2\theta = 1$, any relation between $\sin\theta'$, $\sin\theta$, $\cos\theta'$, $\cos\theta$ can be found. It can also be found that $\mathrm{d}\theta' = \mathrm{d}\theta D$. Movement of BB is such that the beaming will happen only in line with θ and not in line with φ, so, $\mathrm{d}\varphi' = \mathrm{d}\varphi$. Finally, $\mathrm{d}\Omega' = D^2\mathrm{d}\Omega$. So, $N_{ES^2\Omega}$ should be $\times D^2$.

Fourth the $\cos\theta$ factor in $N_{ES^2\Omega}$ is in the rest frame of BB. It should be transformed to $\cos\theta' = \frac{\cos\theta-\beta}{1-\beta\cos\theta}$.

Finally,

$$N^r_{ES^2\Omega} = \frac{2}{h^3c^2}\frac{(\frac{E}{D})^2}{\mathrm{e}^{\frac{E/D}{kT}}-1}\frac{1}{D}DD^2\frac{\cos\theta-\beta}{1-\beta\cos\theta}$$

$$N^r_{ES^2\Omega} = \frac{2}{h^3c^2}\frac{E^2}{\mathrm{e}^{\frac{E}{DkT}}-1}\frac{\cos\theta-\beta}{1-\beta\cos\theta} \tag{4.3}$$

The $N^r_{ES^2\Omega}$ is boosted/relativistic spectrum, the one detector in the GRB host galaxy would see. Values E and θ are in the frame of host-galaxy/detector (laboratory frame). Temperature T is the "real" temperature, i.e. the comoving BB temperature. So, the boosted BB spectrum will be similar to normal BB spectrum but with different angle dependence and temperature boosted by factor D (which also depends on the angle).

In order to obtain $F^r_{ES^2\Omega}$, $N^r_{ES^2\Omega}$ should just be multiplied by $\times E$.

$$F^r_{ES^2\Omega} = \frac{2}{h^3c^2}\frac{E^3}{\mathrm{e}^{\frac{E}{DkT}}-1}\frac{\cos\theta-\beta}{1-\beta\cos\theta}$$

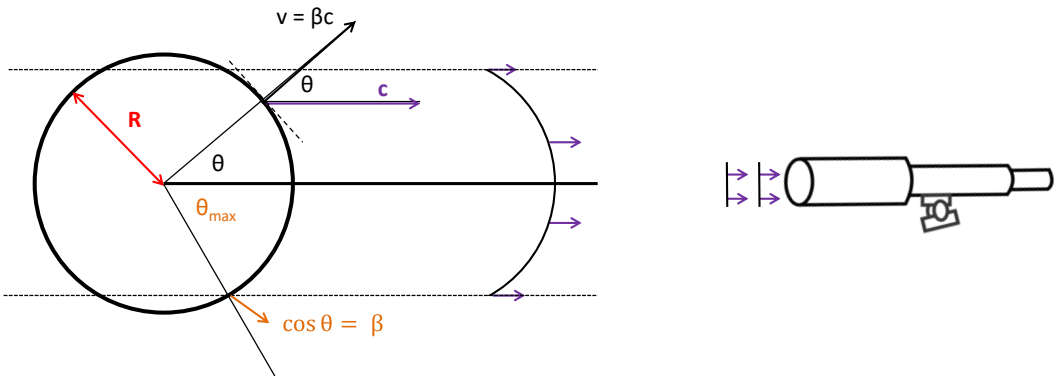

Figure 4.12:

In order to obtain $F^r_{S^2\Omega}$, $F^r_{ES^2\Omega}$ needs to be integrated over E, which is mathematically similar process as with normal (non-relativistic) BB.

$$F^r_{S^2\Omega} = \frac{1}{\pi}\sigma(DT)^4 \frac{\cos\theta - \beta}{1 - \beta\cos\theta} \tag{4.4}$$

Change of spectrum such that new temperature will increase by a factor of $\times D$ and flux from an element of surface be proportional to $(DT)^4$ is obtained in (Bianco et al., 2001).

4.4.4 Pulse from an expanding sphere

There is an infinitesimal short pulse from an expanding sphere. Sphere has a temperature T (BB rest frame) and radius R at the time of emission. Sphere expands uniformly in all directions with speed β. This pulse will be detected over time interval of $R(1-\beta)/c$ but doesn't matter. Let's say we wait until detector measures everything and then examine the spectrum. In case of flux, since they are s^{-1} quantities, the obtained values would change in $R(1-\beta)/c$ time interval. But let's say that we wait for all the photons/energy to collect, and then divide the photons/energy by the (infinitesimal) time the pulse was emitted in the rest frame of the galaxy. Similar goes for luminosity. The PEM pulse examined in the (Bianco et al., 2001), although lasts very short in the detector time range, is actually made for a certain time interval in the laboratory frame and is more similar to the case in the next subchapter.

Each part of the expanding sphere will behave just like the speeding element from the previous chapter. It necessary only to integrate these elements taking care of sphere shape and different direction of radiation for each element (with respect to surface of element) in order to have them all radiate in the same direction (towards detector). Angle θ for each element will be the same as in the previous chapter. Specifically, θ for each element will be the angle between normal to the element surface, and the direction of emission. Also, θ is angle between line center-element and line center-detector.

As before, element won't radiate in the half sphere solid angle but in the angle from $\theta = 0$ to angle where $\cos\theta = \beta$. This also means that detector will "see" only part of the sphere in the same angle range. So, there would be no difference for detector whether it's a sphere or a jet (sphere cut by the cone) with the same or bigger opening angle θ. Again, this is a well known effect (Bianco et al., 2001).

β	0.1	0.3	0.9	0.99	0.999	0.9999	0.99999	0.999999
γ	1.005	1.048	2.294	7.089	22.37	70.70	223.5	702.5
D_{max}	1.106	1.363	4.359	14.11	44.71	141.4	446.9	1405
B	1.07	1.25	3.60	11.3	36.0	115	360	1150

Table 4.3:

Spectrum

The spectrum of element surface is defined by equation 4.3.

$$N^r_{ES^2\Omega} = \frac{2}{h^3c^2}\frac{E^2}{\mathrm{e}^{\frac{E}{DkT}}-1}\frac{\cos\theta-\beta}{1-\beta\cos\theta}$$

Integrating over φ:

$$N^r_{ES\Omega} = 4\pi R\sin\theta N_{ES^2\Omega} = \frac{4\pi R}{h^3c^2}\frac{E^2}{\mathrm{e}^{\frac{E}{DkT}}-1}\frac{\cos\theta-\beta}{1-\beta\cos\theta}\sin\theta$$

and over θ:

$$N^r_{E\Omega} = \frac{4\pi R^2}{h^3c^2}E^2\int_0^{\arccos\beta}\frac{1}{\mathrm{e}^{\frac{E\gamma}{kT}(1-\beta\cos\theta)}-1}\frac{\cos\theta-\beta}{1-\beta\cos\theta}\sin\theta\,d\theta$$

Integral will be marked I_e. To make the integral more simple $x \equiv \cos\theta$ and $\mathrm{d}x = -\sin\theta\mathrm{d}\theta$.

$$I_e = \int_\beta^1 \frac{1}{\mathrm{e}^{\frac{E\gamma}{kT}(1-\beta x)}-1}\frac{x-\beta}{1-\beta x}\,dx$$

and:

$$N^r_{E\Omega} = \frac{4\pi R^2}{h^3c^2}E^2 I_e$$

There is no analytical solution to I_e. Solving numerically for each E, the spectrum is very similar to black body spectrum with boosted temperature by a new value B, coming from sphere of radius R, and with additional constant A:

$$N^r_{E\Omega} \approx A \times \frac{2\pi R^2}{h^3c^2}\frac{E^2}{\mathrm{e}^{\frac{E}{B\times kT}}-1}$$

The value B is defined by taking the peak energy E_p of the new spectrum and identifying new temperature as $B\ kT \approx E_p/1.59$. In the Table 4.3 are values for B for different β.

As expected value B is in between $D_{min} = \gamma$ which comes from the very edge and D_{max} which comes from the tip. The broadening of spectrum is little for any β. If β is low than there won't be much difference from normal BB. As β goes to 1, there will be more boosting but the part of the sphere which the detector "sees" gets less and less until it is only small part at the very tip which is going directly towards detector. So, as $\beta \to 1$, there will be more boosting but not much broadening of the spectrum.

Parameter A is found in the limit when $E \ll kT$ which makes $\mathrm{e}^{\frac{E\gamma}{kT}(1-\beta x)} - 1 \to E\gamma(1-\beta x)/kT$ and I_e can be solved analytically. In this case:

$$A = \frac{2}{\gamma}\frac{1}{\beta^2}\big(\beta - \ln(1+\beta)\big)$$

β	0.1	0.3	0.9	0.99	0.999	0.9999	0.99999	0.999999
γ	1.005	1.048	2.294	7.089	22.37	70.70	223.5	702.5
D_{max}	1.106	1.363	4.359	14.11	44.71	141.4	446.9	1405
$f_{\beta 5}$	1.15	1.59	13.7	141	1.42×10^3	1.42×10^4	1.41×10^5	1.40×10^6
$f_{\beta_1 5}$	1.57	2.02	14.2	142	1.42×10^3	1.42×10^4	1.41×10^5	1.40×10^6

Table 4.4:

Flux & Luminosity

Energy flux $F_{S^2\Omega}$ from surface element is defined in equation 4.4:

$$F^r_{S^2\Omega} = \frac{1}{\pi}\sigma(DT)^4 \frac{\cos\theta - \beta}{1 - \beta\cos\theta}$$

$$F^r_{S^2\Omega} = \frac{1}{\pi}\sigma T^4 \frac{1}{\gamma^4} \frac{\cos\theta - \beta}{(1 - \beta\cos\theta)^5}$$

Similar to previous part integration goes over φ and then θ:

$$F^r_\Omega = 2R^2\sigma T^4 \frac{1}{\gamma^4} \int_0^{\arccos\beta} \frac{\cos\theta - \beta}{(1 - \beta\cos\theta)^5} \sin\theta \mathrm{d}\theta = 2R^2\sigma T^4 \frac{1}{\gamma^4} I_5$$

Integral is I_5. To make it more simple $x \equiv \cos\theta$ and $\mathrm{d}x = -\sin\theta\mathrm{d}\theta$.

$$I_5 = \int_\beta^1 \frac{x - \beta}{(1 - \beta x)^5} \mathrm{d}x$$

The solution to the integral is:

$$I_5 = \frac{\beta(4 - 3\beta) - 1}{12\beta^2(1 - \beta)^4} + \frac{1 - \beta^2}{12\beta^2(1 - \beta^2)^4}$$

Now, to define the $f_{\beta 5}$ as $f_{\beta 5} \equiv 2\frac{1}{\gamma^4} I_5$.

$$f_{\beta 5} = 2(1 - \beta^2)^2 \Big(\frac{\beta(4 - 3\beta) - 1}{12\beta^2(1 - \beta)^4} + \frac{1 - \beta^2}{12\beta^2(1 - \beta^2)^4} \Big)$$

When $\beta \to 1$:

$$f_{\beta 5} \approx \frac{17}{12} \frac{1}{1 - \beta} = f_{\beta_1 5}$$

$$F^r_\Omega = R^2\sigma T^4 f_{\beta 5}$$

Values of $f_{\beta 5}$ for various β are given in Table 4.4:

Luminosity is:

$$L = L^r = 4\pi F^r_\Omega = 4\pi R^2\sigma T^4 f_{\beta 5}$$

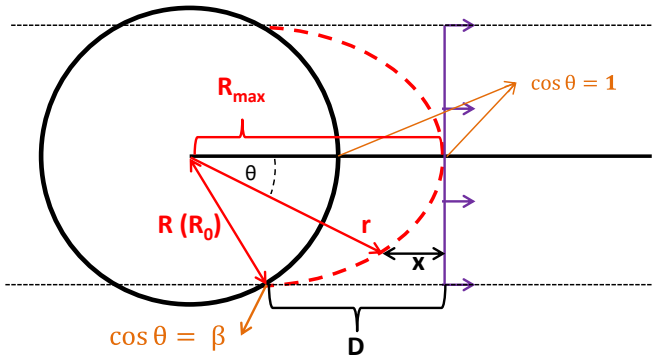

Figure 4.13:

4.4.5 Continuous emission from an expanding sphere

For the same reasons as in previous part, sphere will radiate from cone where θ goes from 0 to where $\cos\theta = \beta$. However, in this case wave fronts will be made from different parts of sphere emitting at different times and different radius. First, the edge of the cone will radiate at radius $R(R_0)$ and those photons will be "chasing" front part of the sphere. The last part to contribute to the wave front will be the front part at R_{max} (Figure 4.13).

From Figure 4.13 several independent equations come. First one involves time to create a wave front and is made up of time sphere expanded from R to r and time photons traveled to complete the wave front. So, 1) $\Delta t = \frac{r-R}{\beta c} + \frac{x}{c} = const.$ and for extreme cases it turns to: 2) $\Delta t = \frac{D}{c}$ and: 3) $\Delta t = \frac{R_{max}-R}{\beta c}$. From geometry of the picture: 4) $r\cos\theta + x = R_{max}$ which for extreme case(s) turns to: 5) $R\beta + D = R_{max}$. The equations 1, 2, 4 and 5 can be used to eliminate 4 parameters: D, Δt, x and R_{max} (this is generally not possible but here is because the special relation of the parameters and equations). The remaining parameters are connected:

$$r = \frac{R(1-\beta^2)}{1-\beta\cos\theta}$$

The equation describes an ellipse in polar coordinates. Value r is the "radius of this ellipse" as seen from the more distant focus (center of the sphere), β turns out to be eccentricity of the ellipse, R is radius when the edge of the cone has emitted photons and started creation of the wave front. R is also the a of the ellipse, i.e. the half of the longer width. When $\cos\theta = \beta$ the line of the tangent of the ellipse is normal to the line of the wave front. Of course, since everything is symmetric to angle φ the surface will be obtained by rotating ellipse across the φ angle.

This surface is the equitemporal surface (EQTS) explained in Chapter 2 when disusing Fireshell model, just for the constant velocity case which is a well known result (Rees, 1966). Literature concerning EQTS within the fireshell model - which were found starting from dynamics of the fireshell plasma, which gave dependence of velocity on time (or radius) - can be found in (Bianco et al., 2001; Bianco and Ruffini, 2004, 2005d,b, 2006). In it the EQTS are extremely elongated due to ultrarelativistic motion and are used to explain the prompt emission.

Additional useful equations:

$$R_{max} = R(1+\beta)$$

with R_{max} being the radius when the tip of the sphere has emitted photons and completed creation of the wave front. This can be obtained from above ellipse equation for $\cos\theta = 1$ or from adding equation number 3 to other 4 equations. Also:

$$\Delta t = \frac{R}{c}$$

where Δt is time interval when the edge of the cone emitted photons and started to create the wave front, to when the tip of the sphere emitted photons and finished the creation of the wave front. This can be obtained from adding equation number 3 to other 4 equations. Even though this time interval is longer and longer for successive wave fronts (bigger and bigger R), the wave fronts will still be separated from each other by the same amount of distance/time. It just means that each successive wave front took longer time to be created.

Spectrum

The spectrum of element surface is defined by equation 4.3.

$$N^r_{ES^2\Omega} = \frac{2}{h^3c^2}\frac{E^2}{\mathrm{e}^{\frac{E}{D\,kT}}-1}\frac{\cos\theta-\beta}{1-\beta\cos\theta}$$

Integrating over φ and then θ:

$$N^r_{E\Omega} = \frac{4\pi}{h^3c^2}E^2\int_0^{\arccos\beta} r^2\frac{1}{\mathrm{e}^{\frac{E\gamma}{kT}(1-\beta\cos\theta)}-1}\frac{\cos\theta-\beta}{1-\beta\cos\theta}\sin\theta\,d\theta$$

The value of R will be different for each θ, so it was replaced with r and has to be inside the integral. Putting the ellipse equation in place:

$$N^r_{E\Omega} = \frac{4\pi R^2}{h^3c^2}(1-\beta^2)^2E^2\int_0^{\arccos\beta}\frac{1}{\mathrm{e}^{\frac{E\gamma}{kT}(1-\beta\cos\theta)}-1}\frac{\cos\theta-\beta}{(1-\beta\cos\theta)^3}\sin\theta\,d\theta$$

Defining integral as I_{e3} and making integral more simpler $x \equiv \cos\theta$:

$$N^r_{E\Omega} = \frac{4\pi R^2}{h^3c^2}(1-\beta^2)^2E^2I_{e3}$$

with integral being:

$$I_{e3} = \int_\beta^1 \frac{1}{\mathrm{e}^{\frac{E\gamma}{kT}(1-\beta x)}-1}\frac{x-\beta}{(1-\beta x)^3}\,dx$$

As in the previous case, there is no analytical solution to I_{e3}. Solving numerically for each E, the spectrum is very similar to black body spectrum with boosted temperature by a new value B, coming from sphere of radius R, and with additional constant A:

$$N^r_{E\Omega} \approx A \times \frac{2\pi R^2}{h^3c^2}\frac{E^2}{\mathrm{e}^{\frac{E}{B\times kT}}-1} = N^{ab}_{E\Omega}$$

The value B is defined by taking the peak energy E_p of the new spectrum and identifying new temperature as $B\;kT \approx E_p/1.59$. In the Table 4.5 are values for B for different β.

Again, parameter A is found in the limit when $E \ll kT$ which makes also I_{e3} possible to be solved analytically. In this case:

β	0.1	0.3	0.9	0.99	0.999	0.9999	0.99999	0.999999
γ	1.005	1.048	2.294	7.089	22.37	70.70	223.5	702.5
D_{max}	1.106	1.363	4.359	14.11	44.71	141.4	446.9	1405
B	1.07	1.26	3.73	12.0	38.0	120	380	1200
$N^r_{E\Omega}/N^{ab}_{E\Omega}$ @$10E_p$	1.02	1.30	2.39	2.54	2.53	2.54	2.53	2.55

Table 4.5:

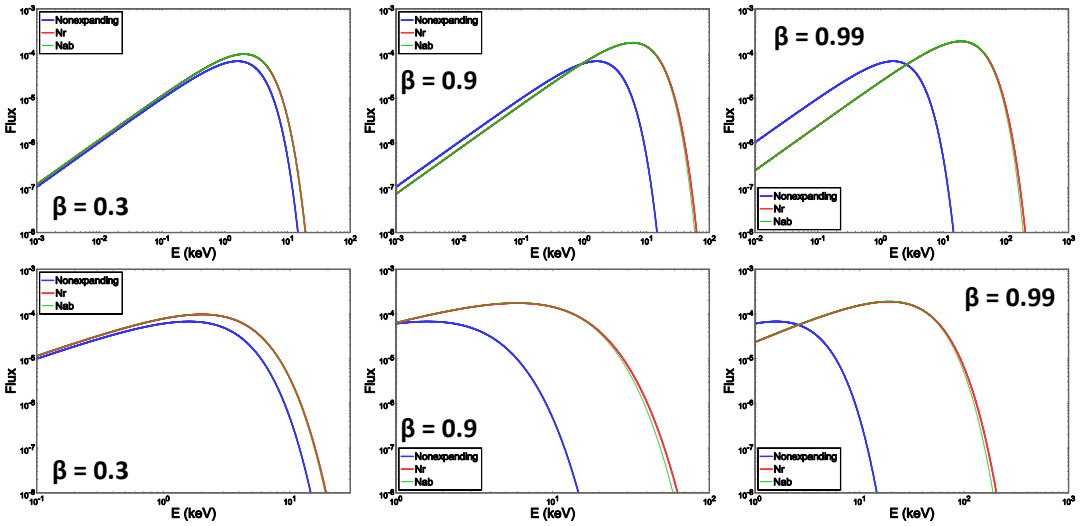

Figure 4.14: Thermal spectra for non-relativistic spectrum $N_{E\Omega}$ (blue), $N^r_{E\Omega}$ relativistic (red), and approximate $N^{ab}_{E\Omega}$ (green) are shown for three different expansion speeds. The (rest-frame) temperature of the BB is $kT = 1$ keV. The flux is in arbitrary units. Lower image is a zoomed in of upper one. Further details are in the text.

$$A = \frac{2}{\gamma}(1-\beta^2)^2\Big(\frac{1}{6\beta^2(1-\beta^2)^2} + \frac{2\beta-1}{6\beta^2(1-\beta)^2}\Big)$$

In Figure 4.14 spectra are compered in order to estimate broadening. In the low-energy phase $N^r_{E\Omega}$ and $N^{ab}_{E\Omega}$ are exatcly the same. The peak faze they are almost the same. The only difference (broadening) is seen after the peak. To quantify broadening of the spectrum, ratio of $N^r_{E\Omega}/N^{ab}_{E\Omega}$ is taken at 10 times the peak energy. Values are given in Table 4.5. As can be seen the broadening is small especially when considering that in BAT-XRT only the peak of BB is seen.

Noting again that R in $N^{ab}_{E\Omega}$ spectrum is the radius when the creation of the wave front started. Wave front was completed at radius of $R(1+\beta)$. It is not possible to assign a single radius to the spectrum like in the case of non-expanding sphere or a pulse from an expanding sphere.

The spectrum in this case is very close to pure black body while in (Bianco et al., 2001) the spectrum is broaden due to the fact that expansion velocity changes drastically and that emission is coming from a certain volume and is defined by a "screening factor". Additionally case of inverse-Compton scattering of photons by electrons is examined.

Flux & Luminosity

Energy flux $F_{S^2\Omega}$ from surface element is defined in equation 4.4:

β	0.1	0.3	0.9	0.99	0.999	0.9999	0.99999	0.999999
γ	1.005	1.048	2.294	7.089	22.37	70.70	223.5	702.5
D_{max}	1.106	1.363	4.359	14.11	44.71	141.4	446.9	1405
$f_{\beta 7}$	1.31	2.33	38.0	425	4.30×10^3	4.30×10^4	4.30×10^5	4.24×10^6
$f_{\beta_1 7}$	4.78	6.14	43.0	430	4.30×10^3	4.30×10^4	4.29×10^5	4.24×10^6

Table 4.6:

$$F^r_{S^2\Omega} = \frac{1}{\pi}\sigma(DT)^4 \frac{\cos\theta - \beta}{1 - \beta\cos\theta}$$

$$F^r_{S^2\Omega} = \frac{1}{\pi}\sigma T^4 \frac{1}{\gamma^4} \frac{\cos\theta - \beta}{(1 - \beta\cos\theta)^5}$$

Integration goes over φ and then θ:

$$F^r_{\Omega} = 2\sigma T^4 \frac{1}{\gamma^4} \int_0^{\arccos\beta} r^2 \frac{\cos\theta - \beta}{(1 - \beta\cos\theta)^5} \sin\theta \mathrm{d}\theta$$

As for the case of spectrum, the value of R will be different for each θ, so it was replaced with r and has to be inside the integral. Putting the ellipse equation in place:

$$F^r_{\Omega} = 2R^2\sigma T^4 (1 - \beta^2)^4 \int_0^{\arccos\beta} \frac{\cos\theta - \beta}{(1 - \beta\cos\theta)^7} \sin\theta \, d\theta$$

$$F^r_{\Omega} = 2R^2\sigma T^4 (1 - \beta^2)^4 I_7$$

Integral is I_7. To make it more simple $x \equiv \cos\theta$.

$$I_7 = \int_\beta^1 \frac{x - \beta}{(1 - \beta x)^7} \, dx$$

Solution to the integral is:

$$I_7 = \frac{\beta(6 - 5\beta) - 1}{30\beta^2(1 - \beta)^6} + \frac{1 - \beta^2}{30\beta^2(1 - \beta^2)^6}$$

Now to define $f_{\beta 7}$ as:

$$f_{\beta 7} = 2(1 - \beta^2)^4 I_7$$

$$f_{\beta 7} = 2(1 - \beta^2)^4 \Big(\frac{\beta(6 - 5\beta) - 1}{30\beta^2(1 - \beta)^6} + \frac{1 - \beta^2}{30\beta^2(1 - \beta^2)^6} \Big)$$

When $\beta \to 1$ it can be simplified as:

$$f_{\beta 7} \approx f_{\beta_1 7} = \frac{43}{10} \frac{1}{1 - \beta}$$

Finally:

$$F^r_{\Omega} = R^2\sigma T^4 f_{\beta 7}$$

with values for $f_{\beta 7}$ given in Table 4.6.

Luminosity is:

$$L = L^r = 4\pi F_\Omega^r = 4\pi R^2 \sigma T^4 f_{\beta 7}$$

Luminosity corresponds to wave fronts which were created from R to $R(1+\beta)$ and sent in all directions. If detectors were put all around the BB at a big distance in host galaxy, they would detect this luminosity. The emitted energy per unit time corresponds to time in the host galaxy rest frame. This is not luminosity which corresponds to genuine luminosity (emitted energy per unit of host-galaxy time) at the point when radius was just R. This luminosity corresponds to the one from the pulse example:

$$L = 4\pi R^2 \sigma T^4 f_{\beta 5}$$

It is the luminosity which would be obtained if detectors would be around the black body almost touching it.

Apparent radius from observations

Radius from previous part R is real radius (for example, freezing the time and then measuring the radius in the host galaxy). Although it is the radius at which wave front has started. The temperature T is real temperature of BB, i.e. its rest-frame temperature. Question is the value of apparent radius calculated from observations. Since relativistic motion is the topic here, change of values due to expansion of the universe will be neglected. Quantities such as observed temperature T_o and observational time t_o are taken as if detector were in the host galaxy of BB. The observed luminosity is the luminosity from previous part $L_o = L$. All of these host-galaxy observational parameters may may be calculated from real observation knowing the redshift.

The observed temperature will be connected to real one:

$$T_o = BT$$

Luminosity is

$$L = 4\pi R^2 \sigma T^4 f_{\beta 7}$$

and may also be expressed from observational parameters:

$$L = 4\pi R_o^2 \sigma T_o^4$$

where R_o is the apparent radius. Combining three equations:

$$R = R_o \times \frac{B^2}{\sqrt{f_7}}$$

Since $B \propto \frac{1}{\sqrt{1-\beta}}$, and $f_{\beta 7} \propto \frac{1}{1-\beta}$:

$$R \propto R_o \frac{1}{\sqrt{1-\beta}}$$

Precise values are given in Table 4.7. As can be seen they are very similar to γ so:

$$R \approx \gamma R_0$$

β	0.1	0.3	0.9	0.99	0.999	0.9999	0.99999	0.999999
γ	1.005	1.048	2.294	7.089	22.37	70.70	223.5	702.5
D_{max}	1.106	1.363	4.359	14.11	44.71	141.4	446.9	1405
$\frac{B^2}{\sqrt{F_{\beta 7}}}$	1.01	1.04	2.26	6.98	22.1	69.5	220	699

Table 4.7:

for any β.

Apparent radius R_o is calculated from observed temperature T_o and luminosity L (which is calculated from observed flux and known redshift). To obtain radius R, expansion speed β (γ) is needed.

Speed from observations

It's not possible to obtain speed from one wave front. Let's consider two wave fronts - front 1 and front 2.

$$R_1 = R_{1o}B^2\frac{1}{\sqrt{F_{\beta 7}}}$$

$$R_2 = R_{2o}B^2\frac{1}{\sqrt{F_{\beta 7}}}$$

These wave fronts will be detected over time period of Δt_o. This is the time between two wave fronts as they travel ($\Delta t_o c$ is the distance between them). The Δt_o won't be the same as Δt - time between when sphere went from R_1 and R_2 and started creation of the two wave fronts. The correct relation is:

$$\Delta t_o = \Delta t(1-\beta^2)$$

Speed β is the real speed:

$$\beta = (R_2 - R_1)/\Delta t$$

and the apparent speed is:

$$\beta_o = (R_{2o} - R_{1o})/\Delta t_o$$

Combining all equations:

$$\beta = (1-\beta^2)\frac{B^2}{\sqrt{f_{\beta 7}}}\beta_o$$

and since $B^2/\sqrt{f_{\beta 7}}$ is almost γ:

$$\beta \approx \frac{1}{\gamma}\beta_o$$

where γ is the real speed. Precise values of apparent velocity β_o are given for every real velocity β in Table 4.8.

Results obtained here assume that sphere has uniform and constant temperature and that expansion is constant. If there are several time bins from time resolved analysis,

β	0.1	0.2	0.3	0.4	0.5	0.6	0.7	0.8	0.9
β_0	0.100	0.204	0.316	0.438	0.581	0.758	0.990	1.35	2.10
β	0.93	0.96	0.99	0.993	0.996	0.999	0.9999	0.99999	0.999999
β_0	2.57	3.48	7.13	8.52	11.3	22.7	71.7	226	713

Table 4.8:

apparent velocity may be found for each two bins, and from there the real velocity and then radius. Approximation here is that for given time interval (between centers of two time bins) temperature and velocity may be considered as constant. Additional approximation, of course, is that values from time resolved analysis are averaged over time bin, but this is the case for every other analysis which involves time, energy, etc. bins, and has no special particularities here. The applicability of this approach is for the observed temperature-decaying thermal emission at the start of the afterglow phase.

4.4.6 Wave fronts from different velocities and temperatures

Temperature

The equation for spectrum of the wavefront:

$$N^r_{E\Omega} = \frac{4\pi R^2}{h^3 c^2}(1-\beta^2)^2 E^2 I_{e3}$$

with integral being:

$$I_{e3} = \int_\beta^1 \frac{1}{\mathrm{e}^{\frac{E\gamma}{kT}(1-\beta x)} - 1} \frac{x-\beta}{(1-\beta x)^3}\, dx$$

and $x \equiv \cos\theta$. The temperature kT and speed β are constant in this case. If the temperature depends on time, and speed is the same, then again a single wavefront will be made from parts of a sphere which form an ellipse as it expends. The temperature for a wavefront may be expressed with respect to angle $kT = kT(\theta)$, i.e. $kT = kT(x)$:

$$I_{e3} = \int_\beta^1 \frac{1}{\mathrm{e}^{\frac{E\gamma}{kT_{(x)}}(1-\beta x)} - 1} \frac{x-\beta}{(1-\beta x)^3}\, dx$$

and integral solution will depend on the function $kT(x)$. In most cases numerical integration will be needed and shape of the spectrum will depend on β as in previous section, and additionally on function $kT(x)$ parameters as well as initial value of kT for a given (initial) R. Depending on $kT(x)$ the spectrum may not be approximated as ordinary black body with different temperature and normalization.

The flux may be calculated with numerical integration of spectrum (since it was already calculated numerically) or following the equations from previous section:

$$F^r_\Omega = 2R^2\sigma(1-\beta^2)^4 I_{7,T}$$

In this case the temperature won't be constant but will have to go inside the integral with angle dependence for a given wavefront:

$$I_{7,T} = \int_\beta^1 T^4_{(x)} \frac{x-\beta}{(1-\beta x)^7}\, dx$$

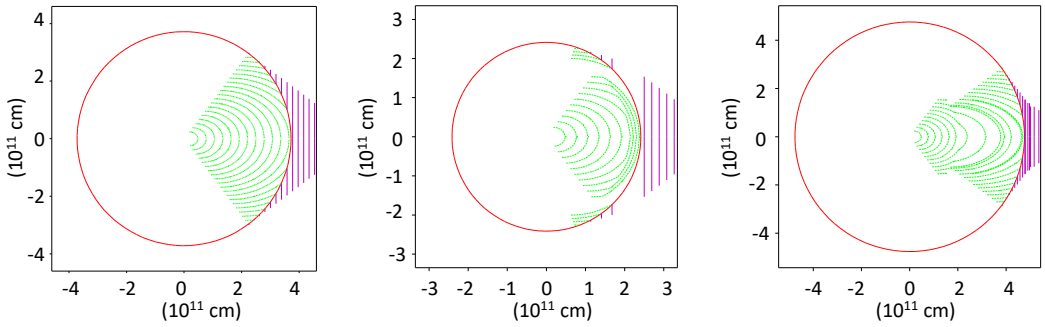

Figure 4.15: Wavefront surfaces from an expanding sphere. Green color corresponds to surfaces, red to the black body surface, and purple to wave fronts. Further details are in the text.

Speed

If velocity is also varying a single wavefront won't be made from an ellipse-shaped surface. In Figure 4.15 are presented three cases. The 2D plane corresponds to section of constant φ and is axially symmetric. All three start from initial radius of 3×10^{10} cm and to the time frame "captured" somewhere between $15 - 20$ s. The first one (left) corresponds to constant expanding velocity of 0.6 c. The surfaces are ellipses with eccentricity $\beta = 0.6$. The second (middle) corresponds to expanding velocity of $\beta_1 = 0.6$ which then drops to $\beta_2 = 0.3$ at 10 s. The wave fronts which were in the process of making during this shift have a "break". They are made out of two ellipses with eccentricities $\beta_1 = 0.6$ and $\beta_2 = 0.3$. If the first part is described by equation $r = R(1 - \beta_1^2)/(1 - \beta_1 \cos\theta)$ then the second part cannot be expressed with the same R and β_2, it should have a different R. Starting of just-β_2 surfaces is also present in the plot. The third plot (right) corresponds to expanding velocity of $\beta_1 = 0.6$ which then jumps to $\beta_2 = 0.8$ at 10 s. Again, wave fronts which were in the process of making during this shift have a "break", but in the opposite direction. As in previous case, the second ellipse equation has a different R. Starting of just-β_2 surfaces is also present in the plot and some completed ones as well. For the last two cases the "different R" depends where/when the break in the speed occurs for a given wave front.

Velocity may change continuously. In Figure 4.16 are presented three cases. The first (left) corresponds to expanding velocity which changes linearly with time from $\beta_1 = 0.3$ to $\beta_2 = 0.8$. The second (middle) corresponds to expanding velocity which changes linearly from $\beta_1 = 0.8$ to $\beta_2 = 0.3$. The third (right) corresponds to expanding velocity which changes linearly from $\beta_1 = 0.3$ to $\beta_2 = 0.8$ and then back to $\beta_1 = 0.3$.

The surface equation may be considered as a continuously changing ellipse equation with $\beta(\theta)$ and $R_{(0)}(\theta)$. However to obtain the form it should be started from basics and (Figure 4.13) may be used. Time to create a wave front is $\Delta t = t + \frac{x}{c} = const.$ where t is time needed from black body to go from R_0 to r. Now, this time cannot be expressed as $t = (r - R_0)/(\beta c)$ since β isn't constant. For extreme cases equation turns to $\Delta t = \frac{D}{c}$. From geometry of the picture $r\cos\theta + x = R_{max}$ which for extreme case(s) turns to $R_0\beta_0 + D = R_{max}$ where β_0 is initial value of β for the wave front. Combining them:

$$r\cos\theta = R_0\beta_0 + tc$$

If β is expressed as function of t (which goes from $t = 0$ to $t = \Delta t$) for a given wave front,

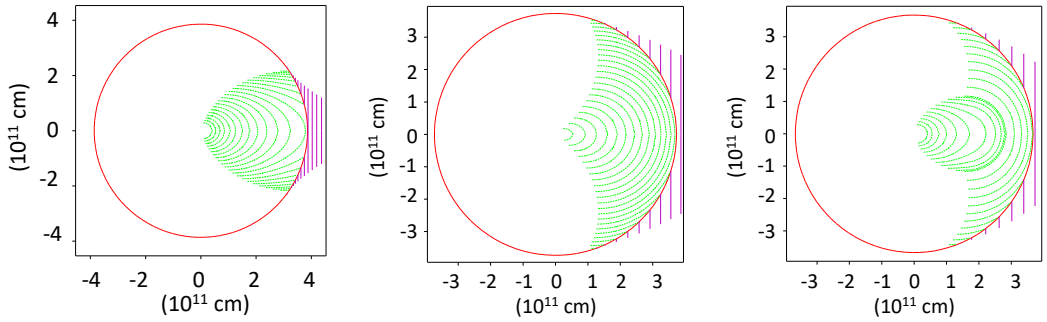

Figure 4.16: Wavefront surfaces from an expanding sphere. Green color corresponds to surfaces, red to the black body surface, and purple to wave fronts. Further details are in the text.

then r may be expressed as $r(t)$:

$$r = R_0 + \int_0^t \beta_{(t')} c \, dt'$$

This equation is the one obtained in (Bianco et al., 2001) for a general EQTS.

Then $\cos\theta$ may be expressed as $\cos\theta(t)$ and vice versa $t = t(\cos\theta)$. Then r may be expressed as function of $\cos\theta$ (and R_0 and β_0).

The spectrum of the wave front would be:

$$N^r_{E\Omega} = \frac{4\pi}{h^3 c^2} E^2 I_{e,r}$$

with integral being:

$$I_{e,r} = \int_{\beta_0}^{1} r^2_{(x)} \frac{1}{e^{\frac{E\gamma_{(x)}}{kT_{(x)}}(1-\beta_{(x)}x)} - 1} \frac{x - \beta_{(x)}}{(1 - \beta_{(x)}x)} \, dx$$

The flux would be:

$$F^r_\Omega = 2\sigma I_{5,T,r}$$

with integral:

$$I_{5,T,r} = \int_{\beta_0}^{1} T^4_{(x)} (1 - \beta^2_{(x)})^2 r^2_{(x)} \frac{x - \beta_{(x)}}{(1 - \beta_{(x)}x)^5} \, dx$$

Calculation of flux from a general EQTS was presented in chapters XXI - XXII in (Ruffini et al., 2003a) in which also integration over the EQTS with $\times D^4$ is the basis.

Absorbing back emitted photons

There is an additional complication when velocity increases, especially if it increases quickly and to a large value. In Figure 4.17 is shown example of an expanding sphere which starts from 3×10^{11} cm has initial velocity of $\beta_1 = 0.3$ and then jumps to $\beta_2 = 0.95$ at 10 s. Only the wave fronts which started when velocity was β_1 are shown in order to make it more clear.

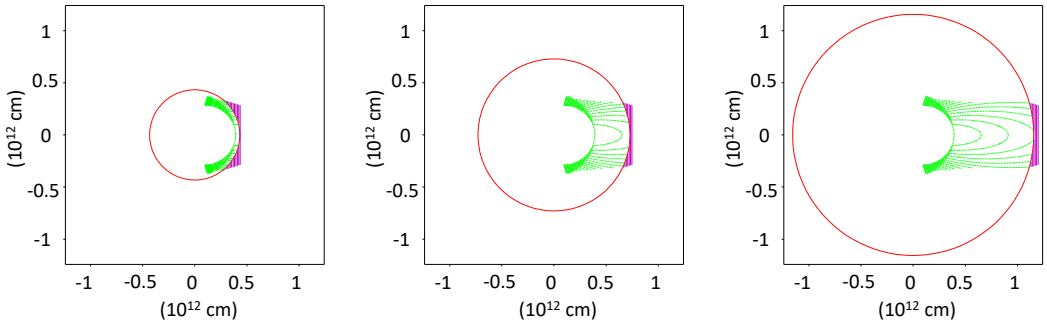

Figure 4.17: Wavefront surfaces from an expanding sphere. Green color corresponds to surfaces, red to the black body surface, and purple to wave fronts. Further details are in the text.

When the tangent to the surface is horizontal, it is the limiting case for the photons to exist. This is the case of the initial start of the wave front. It is also the limiting case when photons will be absorbed back to black body surface. If the tangent angle (with respect to horizontal axes) gets positive, then the photons will be absorbed back to black body and the wave front surface will decrease. In the first plot (left) the moment is shown just after the velocity jump. The drastic change of tangent angle (which gets positive) is seen. On the second plot (middle) open lines correspond to wave fronts which have been completely absorbed back and disappeared. The final plot (right) further shows this process as well as wave fronts that weren't completely absorbed, just have their surface decreased and then recompleted by black body during β_2 phase.

The previous analytical treatment, complicated as it is with varying velocity and temperature, is valid for wave fronts for which tangent to the surface has a negative angle (with respect to horizontal axis) all the way to completion of the front. The absorption of photons back further complicates matter. In order to obtain some useful resulting spectrum and flux with changing observer time, each wave front would have to be integrated numerically, and for each front parameters for integration would have to be different. Then possible decreasing of front because of absorption has to be taken into account. At this point it is easier to abandon the concept of wave fronts and simulate expansion and resulting spectrum directly. This will also make it easier to input changing speed and temperatures in tabular form if needed, not just analytical functions.

4.5 Simulation of spectrum

4.5.1 The code

Animation

Plots in Figures 4.15, 4.16 and 4.17 of surfaces which were traced by expanding black body as it created wave fronts, were frames from animation used to give simple visual inspection. It was made with Python animation module[8]. The main parameter is time t which goes from $t = 0$ to some value with certain resolution δt. Then velocity is given as a function of time $\beta(t)$. Then the radius R of the black body is calculated for each step. After

[8] `https://matplotlib.org/api/_as_gen/matplotlib.animation.FuncAnimation`

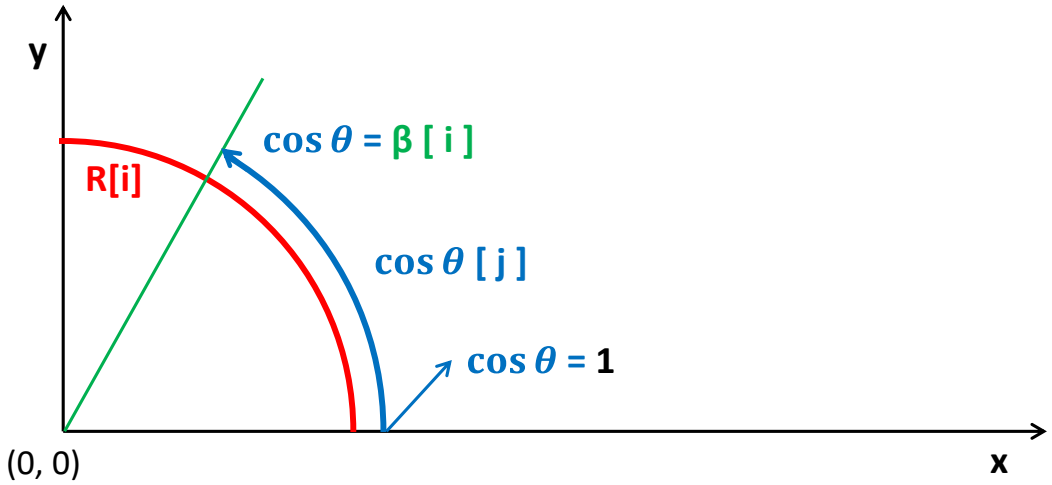

Figure 4.18: Plane in which simulation takes place.

that angle which traces full circle is defined with some resolution. Then the sets of $x(t)$ and $y(t)$ points for a black body may be expressed and black body expansion animated.

The wave fronts are defined to start at certain points in time. The initial value of coordinates x and y is defined from R and β at that time. Then the y coordinate remains the same while the x moves at the speed of light (this is the outer edge of the front). The intersection of wave front and black body is found by taking the same x and defining y from trigonometry of x and R. The two points are then connected with a line and wave front is defined. This intersection between wavefront and black body is also what defines the shape which black body traces as it expands.

In a nutshell this is how it was done, with additional details in regards to stopping animating shapes when they merge (wave front completion), or when they are completely absorbed by black body, and other details.

The concept

The idea is to abandon concept of wave fronts. Instead from taking observed quantities and calculating intrinsic ones based on some assumptions, the goal is to simulate black body expansion for a given velocity $\beta(t)$, simulate thermal emission based on $kT(t)$ and then simulate observed spectrum/flux and compare it to observations. So, the process goes from inputting $\beta(t)$ and $kT(t)$ in order to match observations.

The code is made in Python. The main parameter is time t which goes from $t = 0$ to some input value with certain input resolution δt (dt for simplicity). This is the first thing which determines resolution and will be indexed with i in arrays. So, $t[i]$. The velocity and temperatures are input parameters $\beta(t)$ and $kT(t)$ and have the same array length as t. So, $\beta[i]$ and $kT[i]$. From $t[i]$ and $\beta[i]$, $R[i]$ is calculated. The initial value of R is needed as input parameter.

The simulation takes place in an x-y plane which corresponds to cross section of constant φ (Figure 4.18). The center of the sphere is placed at coordinates x=0, and y=0. Only the upper-right quadrant is taken into account since lower part is symmetric to upper, and left part is of no interest as it is assumed that detector is far away on the right.

The second parameter which determines resolution is the angle θ. The plane corre-

sponds to $\theta = [0, \pi/2]$. However, since only the part of the sphere which goes to $\cos\theta = \beta$ will emit photons which will reach detector, the angle is defined $\cos\theta = [1, \beta[i]]$ for every step. The indexing with respect to angle will be marked by j in arrays. The number of angle steps is the same for each i-step, only the upper limit is different and is equal to $\beta[i]$. The number of elements is now $i_{max} \times j_{max}$.

The process of simulating expanding sphere emission by time steps and angle steps without considering wave fronts is similar to the one used to obtain the light curve in (Bianco et al., 2001) and chapter XXII in (Ruffini et al., 2003a).

Points

Instead of wave fronts each part of the sphere is considered as it emits. Since everything is symmetric with respect to φ one single part may be taken to be a φ-ring and is represented by single x and y coordinate on the plane. The parts will be different for different θ (index j) and t (index i). Additionally, the idea is to represent emission from these parts as it moves with speed of light. To define a *point*; it is a point on the plane which starts on the line of the black body and then moves along x-axis with the speed of light. So, additional indexing k is used for this movement. The point has 3 index - i, j and k. The i presents time when it was emitted. The j angle. Together i and j (with $R[i]$) presents starting point on the black body. They are the same for a single point. The k presents movement of the point with speed of light. The k has the same meaning as i, i.e. it represents elapsed time. So, k starts from the value of i and then increases with global time i. The y coordinate doesn't change with k for a point as the movement is along x-axis. Finally the x and y are 3D arrays (i, j, k) which represent x and y coordinates of all points on every step they take. The number of elements is $i_{max} \times j_{max} \times k_{max}$. The k may be considered as a third type of the resolution, but it is defined same as i, i.e. by dt. So, the resolution for crossed length of points/photons as they travel is $c\ dt$.

Excluding points which are absorbed back

Before calculating spectrum of each point, the absorbed points should be excluded. This is why it's important to mark position of a point for each step (with index k). Otherwise this wouldn't be necessary and is not necessary if speed is constant or monotonically decreases. In general case, for each point on each step the distance from center is compared to the current value of radius. If this value is lesser then one of radius, the point is excluded.

The question remains if the radius continues to expand beyond final time $t[i_{max}]$ with constant final speed $\beta[i_{max}]$ will it further absorb points. So, final time $t[i_{max}]$ needs to be extended enough and same process repeated. Since this will take more time then previous step, some points may be excluded from the start.

In Figure 4.19 plane is presented at $t[i_{max}]$. The points with x coordinate larger than $R[i_{max}]$ will never be absorbed. All of them may be excluded from checking. For the points with x coordinate lesser than $R[i_{max}]$, the ones below the $\cos\theta = \beta[i_{max}]$ line will never be absorbed. This is because the line $\cos\theta = \beta[i_{max}]$ (which is constant now) defines part of the sphere which emits photons and points already have a "head start". Points above this line and x coordinate lesser than $R[i_{max}]$ need to be checked for each step.

In principal for each point final coordinates, final values of R and β, equations may be put in place assuming sphere catches up to point. Then finding out if there is a solution

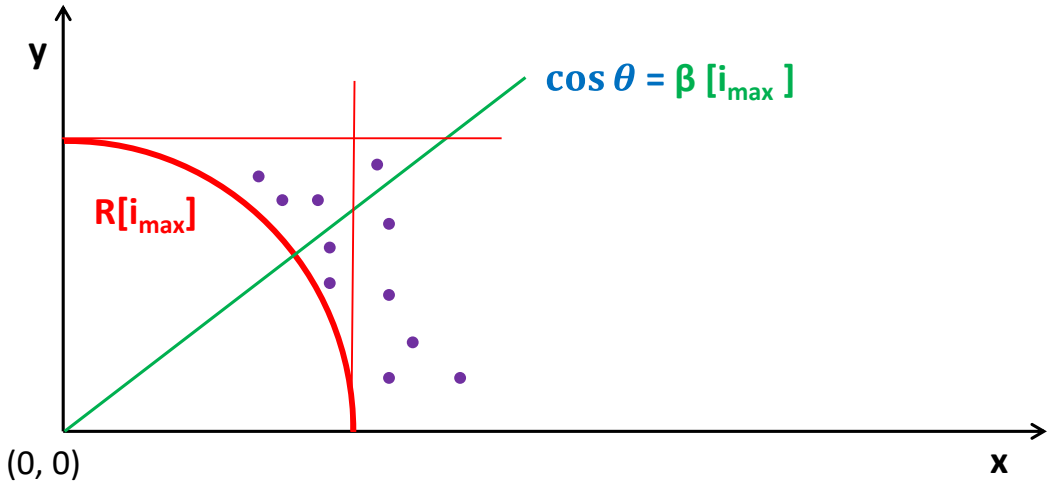

Figure 4.19: Plane in which simulation takes place at the last step. Purple dots represent *points*.

to this equation (in real numbers) it can be determined if point gets absorbed. However due to nature of the equations they would have to be solved numerically and possible nonexistence of solution (or a double solution if point enters and exits sphere during extended time) further complicates matter. In any way, for each point multiple calculations would have to take place.

Spectrum

Each point represents radiation from a φ-ring:

$$N^r_{ES\Omega} = \frac{4\pi R}{h^3c^2}\frac{E^2}{\mathrm{e}^{\frac{E\gamma}{kT}(1-\beta\cos\theta)}-1}\frac{\cos\theta-\beta}{1-\beta\cos\theta}\sin\theta$$

With dS being line element $R\,d\theta$:

$$N^r_{ES\Omega}R\,d\theta = dN^r_{E\Omega} = \frac{4\pi R^2}{h^3c^2}\frac{E^2}{\mathrm{e}^{\frac{E\gamma}{kT}(1-\beta\cos\theta)}-1}\frac{\cos\theta-\beta}{1-\beta\cos\theta}\sin\theta\,d\theta$$

Putting $x \equiv \cos\theta$:

$$dN^r_{E\Omega} = \frac{4\pi R^2}{h^3c^2}\frac{E^2}{\mathrm{e}^{\frac{E\gamma}{kT}(1-\beta x)}-1}\frac{x-\beta}{1-\beta x}\,dx$$

Since the ring has a certain thickness defined by j-resolution, the dx will be δx and equal to difference between $x[j]$ and $x[j+1]$. Putting other array values:

$$dN^r_{E\Omega}[i,j] = \frac{4\pi R^2_{[i]}}{h^3c^2}\frac{E^2}{\mathrm{e}^{\frac{E\gamma_{[i]}}{kT_{[i]}}(1-\beta_{[i]}x_{[j]})}-1}\frac{x_{[j]}-\beta_{[i]}}{1-\beta_{[i]}x_{[j]}}\,dx_{[j,j+1]}$$

Now, another index m has to be introduced to define energy resolution. Due to nature of black body spectra, steps should be placed equally logarithmic. So, $E = E[m]$ in the upper equation, and $dN^r_{E\Omega} = dN^r_{E\Omega}[i,j,m]$. The number of elements is $i_{max}\times j_{max}\times m_{max}$ minus the excluded pairs i,j from absorbed points. In order to reduce calculation time,

energy elements far away from the $kT_{[i]}$ peak (especially on the higher energy side) may be excluded from calculation and then equalized to zero.

In order to obtain observed quantities, $dN^r_{E\Omega}$ should be divided by comoving (in cosmological terms) distance squared d^2 calculated from the known redshift z. When the photon φ-ring reaches detector the value will drop by $z+1$ because of stretching along x-axis but will also increase by $z+1$ due to photons lowering of energy and more of them occupying keV interval. The values in array along m index should be shifted to lower energies. Since the energy intervals are in logarithmic equal spacing, all the elements should be shifted by same amount $z+1$.

Arrival time

The points (which haven't been absorbed) all travel with the same velocity c and the distance/time between them along x-axis will be the same. The first point (the one most to the right and with $i=0$) will be the first one to reach detector and it can be set as detector time zero. Then for each point starting position the distance/time can be determined as the distance from the first point. This time should be just multiplied by $\times(z+1)$ in order to get detector time.

Then all of the point times need to be order along with points corresponding spectra. Then for a given (detector) time bin, the corresponding points are selected and their spectra summed. In this way, more points correspond to stronger emission, and the quantity $dN^r_{E\Omega}$ should also be multiplied by $\times\, dt$ to correct for this.

Finally, the summed spectrum is the observed one corresponding to detector time bin. In order to obtain energy flux the final spectrum should be multiplied by $\times E$, then by dE which is the difference between $E[m]$ and $E[m+1]$, and then summed over all energy elements.

Turning on and off

Since there is a fixed time (from $t[i=0]$ to $t[i_{max}]$) the black body in this simulation suddenly turns on and later off, and has a turn on and off period (with respect to x-axis and detector). The turn on period is time which start corresponds to the first point, and end to the point when the back of the sphere (at $t[i=0]$) catches up to the tip of the sphere along x-axis. The turn off period is time which start corresponds to tip of the sphere (at $t[i_{max}]$), and end to the last point along x-axis.

To avoid this the time and other input parameters in the simulation can be set in such a way that: starting time of first (detector) time bin and ending time of detector last time bin do not correspond to turn on and off periods, but are in between. On the other hand the turn on or off period may have physical interpretation such as reaching suddenly transparency or previously transparent material suddenly becoming optically thick.

4.5.2 151027A

The simulation has been applied to this burst. From results of analysis of the burst in the previous section, it is clear that at some point it has relativistic expansion. If the expansion was not relativistic then apparent speed would be low for majority of time bins. The apparent speed seams to start as low. So, the initial values of radius and temperature can be taken as close to true, and initial speed as indeed relatively low. Then at maximum it reaches $\beta_a = 5$ which corresponds to $\beta \approx 0.97$ assuming uniform temperature

τ^s	t^s	kT^s	β^s	kT_o^s	L_o^s	Time bin	kT	L_{BB}
s	s	keV		keV	$\times 10^{49}$ erg/s	s	keV	$\times 10^{49}$ erg/s
	0 - 3	3.4	0.27	2.33	0.65	90 - 95		
3	4 - 7	3.4	0.27	2.33	1.78	95 - 100	$2.2^{+1.1}_{-1.1}$	$1.34^{+1.1}_{-0.88}$
6	8 - 14	3.4	0.30	2.39	5.31	100 - 110	$2.57^{+0.43}_{-0.50}$	$5.3^{+2.1}_{-2.2}$
12	15 - 23	3.2	0.35	2.33	13.0	110 - 120	$2.17^{+0.22}_{-0.26}$	$15.8^{+3.6}_{-3.8}$
18	24 - 75	0.55	0.895	1.14	14.2	120 - 130	$1.10^{+0.14}_{-0.12}$	$15.2^{+2.0}_{-1.9}$
48	76 - 128	0.24	0.895	0.600	6.77	130 - 140	$0.617^{+0.046}_{-0.043}$	$6.3^{+1.0}_{-1.0}$
76	129 - 181	0.2	0.895	0.434	3.20	140 - 150	$0.469^{+0.065}_{-0.064}$	$2.61^{+0.70}_{-0.70}$
103	182 - 233	0.13	0.895	0.329	2.25	150 - 160	$0.386^{+0.061}_{-0.061}$	$1.17^{+0.41}_{-0.38}$
131	234 - 338	0.07	0.895	0.194	0.58	160 - 180	$0.193^{+0.032}_{-0.030}$	$0.52^{+0.29}_{-0.32}$
187	339 - 444	0.02	0.895	0.120	0.10	180 - 200		
	445 - 499	0.02	0.895					

Table 4.9: Comparing results of simulation with observed values. Further details are in the text.

and velocity. This can be taken as a hint of maximum speed. Then the apparent speed decreases and again increases. Since radius is very big at this point, slight changes in its value correspond to large changes in apparent velocity. So, these values may be ignored. It was assumed that velocity monotonically increases to some value which then remains constant. Regarding the temperature it was assumed it monotonically decreases as is given by example of 151027A and other bursts in preliminary analysis. Although these temperatures are not comoving ones, in every case the temperature (as seen in host galaxy) goes down, so probably this reflects behavior of real (comoving) temperature.

Starting from these hints true values of temperature $kT(t)$ and velocity $\beta(t)$ were searched for by trying to match observed temperature and luminosity within 90% error for given observational time bins. It was also tried to place turn on and off periods around observational time bins. For a given true velocity distribution, times (true time) were calculated which approximately correspond to observational time bins. This was done by matching the points which come from tip of the sphere. Then velocities and temperatures were taken as constant within these periods and their values changed until they matched observations. The results are presented in Table 4.9.

The time t^s is the true time, i.e. the one which passes in the host galaxy as black body sphere expands. This is the global time of simulation. The kT^s are input values of comoving black body temperature, i.e. true temperature. The β^s is true input velocity of expansion. The kT_o^s and L_o^s are observed temperature and luminosity calculated from simulation for given observational time bins. These two quantities correspond to time periods which match exactly the given observational time bins. The time bins corresponding to t^s might not correspond exactly to observational time bins. Values kT and L_{BB} are observed quantities (luminosity is directly related to normalization constant as defined in XSpec) from previous section. First quantity τ is same as t^s and it shows time when back parts of the sphere emitted points/photons which ended up in the next observational time bin. This means that parameters in each t^s time bin affect also next observational time bin, or even the ones after.

First t^s time bin includes turn on time which is 1.3 s. It also follows the trend of non-increasing temperature and non-increasing speed, as well as initially increasing luminosity. The second-last t^s time bin is made to follow temperature and speed trends as well as having lower luminosity than the one from the previous bin. The last time bin just finishes with t^s time. Turn off time is 82 s. The observational time bins correspond to time elapsed

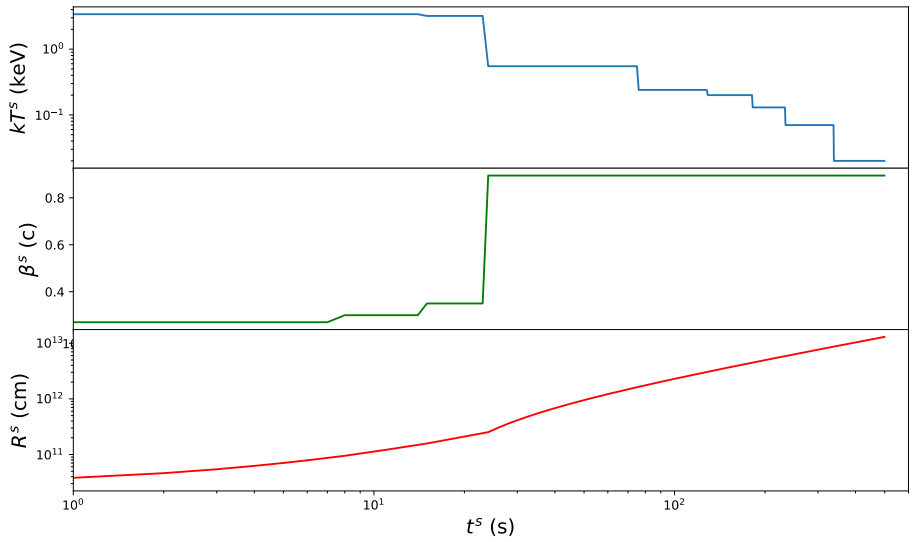

Figure 4.20: Input parameters in the simulation. Details are in the text.

since Swift trigger but this is just in order to be consistent with previous section. They may be considered to start from zero at 90 s.

Evolution of kT^s, β^s and radius R^s with time t^s is shown in Figure 4.20. The initial radius is chosen to be 3×10^{10} cm. The radius at $t = 338$ s which corresponds to ending of last observational time bin is $R = 8.7 \times 10^{12}$ cm.

Final temperature kT_o^s for a time bin was calculated based on the peak of the spectrum. This makes sense if the spectrum is close to that of a black body one. Given the varying velocity and temperature the final spectrum may be significantly distorted from black body one. So, visual inspection of spectra is needed and they are presented in Figure 4.21. The time bins correspond to observational ones with time zero corresponding to 90 s since Swift trigger. The first and last time bins don't have observational counterpart. As can be seen the spectra are blackbody-like and have a clear narrow peak.

In the Figure 4.22 are shown surfaces which were made by expanding black body as it created wave front for the velocity profile and initial radius of 151027A. The first plot (left) is focused on initial small velocity increase. The second (middle) on the final major velocity increase. Absorption of wave fronts happens during this phase. The final plot (right) focuses on part with final maximum constant velocity.

Discussion

The simulation matches nicely with observed values except for the luminosity of the second-last observational time bin where it is above 90 % interval. The input parameters were in a tabular form with sections matching closely the observational time bins. Sections may be selected differently or analytical function may be selected for input temperature and velocity. The time resolution was $dt = 1$ s starting from 0 s to 499 s. The resolution may be changed and it may have different values for different parts. It might be increased in the beginning when velocity profile is more complex and radius is smaller.

All in all, the observations were matched assuming expanding sphere with uniform

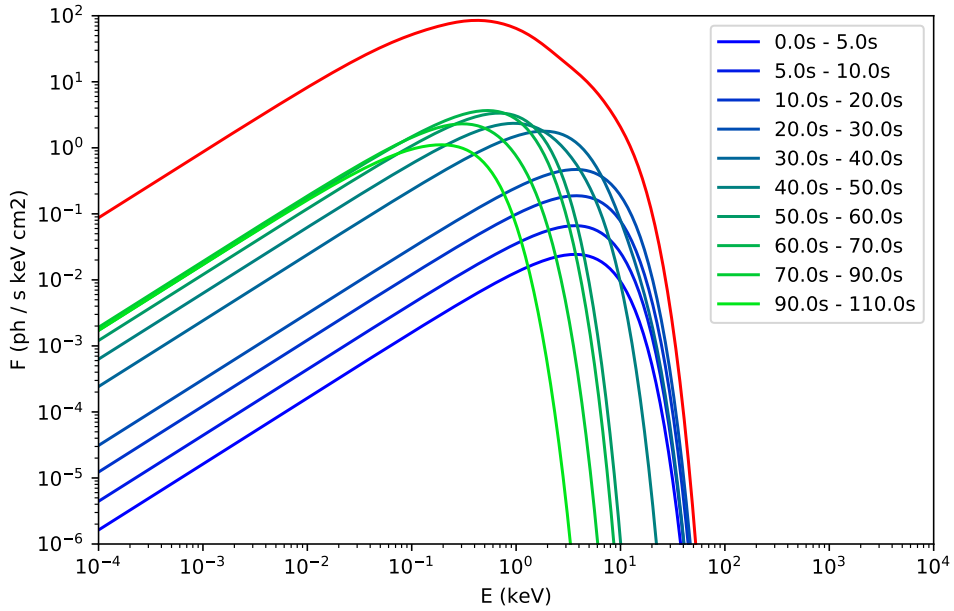

Figure 4.21: Final spectra from simulation. The red one is the cumulative one. Details are in the text.

temperature across its surface. The maximum velocity of $\beta^s = 0.895$ corresponds to Lorentz factor of $\gamma = 2.2$. Characteristic for this burst example is large velocity increase which coincides with sudden (absolute) temperature drop.

4.5.3 Double black body

With varying temperature, velocity, finite size of the emitter, it is possible to have a distorted black body spectrum. Instead of narrow peak of black body it is possible to have a broader peak or even a double peak. There is reasonable evidence for a double black body in some GRB (soft X-ray afterglow) spectra, so it might be produced by a single black body sphere with uniform but varying temperature and velocity.

The effect of having thermal spectrum in the co-moving frame of the emitting surface

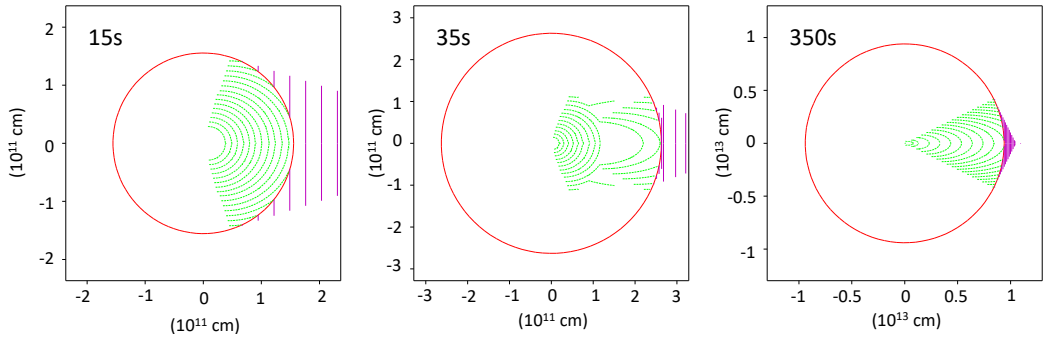

Figure 4.22: Wave front surfaces for velocity profile of 151027A. The time in the upper-right corner is simulation global time t^s.

which leads to an observed spectrum which is a convolution of thermal spectra over the EQTSs is a known effect and was presented in (Ruffini et al., 2004b; Bernardini et al., 2005). In it the EQTSs are obtained from fireshell dynamics and correspond to ultrarelativistic velocities $\Gamma \gtrsim 100$. It was shown that prompt non-thermal Band spectrum can be explained as convolution of different thermal spectra and it was applied to several GRBs. The changing of EQTSs to match the observation cannot be completely random but has to be done within the fireshell model by changing certain model parameters. In the case here the EQTSs, or the temperature change, are not determined by any model and can be in principal random. Focus is on mildly relativistic velocities $\Gamma \sim 2$ in order to explain spectra of temperature-decaying thermal emission in the beginning of the afterglow.

It is possible to produce a double peak even if the sphere doesn't expand. If the sphere is large enough, it will take time for wave front to be completed and if there is a sudden temperature change during creation of the front, the wave front will contain black body spectra with different temperatures. If the change of temperature is slower with respect to light crossing time of emitter, then the spectrum will have a single broader peak. If the change is shorter, then the spectrum might contain two bumps corresponding closely to initial and final temperature. On the left plot in Figure 4.23 are results of simulation of non-expanding sphere of radius 3×10^{12} cm which temperature drops instantly from 10 keV to 1 keV at about $t^s \approx 130$ s. As can be seen the change of temperature is recorded over several time bins with one of them showing clear double peak with same intensity.

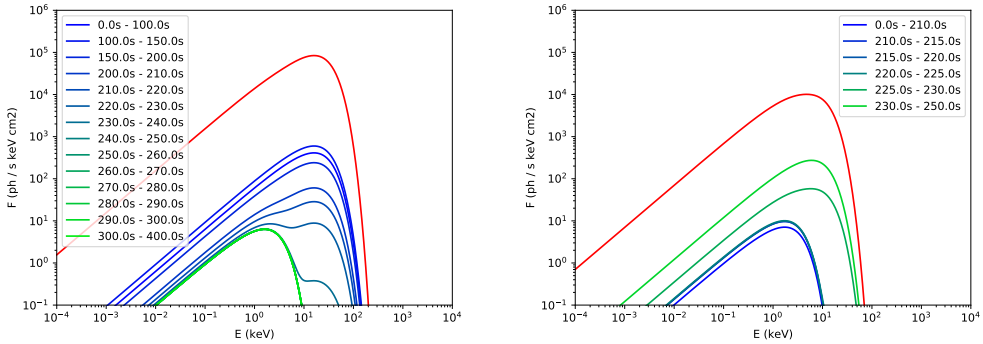

Figure 4.23: Examples of double or broaden black body peak. Details are in the text.

It is also possible to produce broaden or double peak just by change in velocity while comoving temperature remains the same. A single wave front would be composed of different β-ellipse surfaces and would contain blackbody spectra of all differently boosted temperatures. On the second plot of Figure 4.23 are results of simulation of expanding sphere which velocity changes suddenly from 0.1 c to 0.9 c at $t^s \approx 250$ s, with initial radius of 3×10^{12} cm and constant comoving temperature of 1 keV. At the point of change the resulting spectrum is broaden as it contains two black bodies with different boosted temperatures. If the temperature difference was greater the broaden peak would become double peak. In both plots redshift is zero and flux is in arbitrary units.

With both varying temperature and velocity, and different initial radius, many combinations can be made. In principal, double or broaden peak is more likely to happen if the radius is bigger, velocity and temperature changes more drastic.

In bursts 090618A and 130427A there is reasonable evidence for double peak. Based on preliminary analysis, the apparent radii of these bursts are relatively large even in the

first time bins $R_a \sim 10^{12}$ cm and for 130427A the radius goes beyond $R_a \sim 10^{13}$ cm. The apparent speed of ~ 1 c also points to relativistic expansion which implies real radius is actually bigger. Unlike 150127A where XRT data exists from the start of the peak in the light curve, in 130427A and 090618A the XRT data starts in the decaying part of the softer peak which came after the harder prompt emission. This means that probably the start of thermal emission, when temperatures should be higher, were missed. Given large radius (with respect to light crossing time) the higher temperature black body may show itself together with the lower one in the observed time bins. In a future work it would be interesting to examine data of both bursts in detail and do the simulation by trying to match both peaks in spectra by focusing also on period earlier then the first observed time bin.

4.6 Concluding remarks

In the Fireball model temperature-decaying emission in the late prompt - early afterglow phases is explained as coming from a late time central engine activity. The Lorentz factor is on the order of $\gamma \sim 10 - 100$, photosphere radius is at $R \sim 10^{13}$ cm. Double black body in Fireball model is often explained as coming from a cocoon surrounding the jet.

In the case of perfect spherical black body, Lorentz factor is about $\gamma \sim 2$ or nonrelativistic. Photosphere radius expands in the range $R \sim 10^{10} - 10^{13}$ cm. Double black body in the spectrum may come from the same black body with varying temperature and velocity.

Explaining this emission as coming from an expanding spherical perfect black body fits well into the IGC scenario. It is considered to come from interaction of fireshell plasma with supernova ejecta. The resulting Lorentz factor should be on the order of $\gamma \sim 2$ as is the case. From preliminary analysis all GRBs with reasonable evidence for a temperature-decaying thermal emission, have isotropic energies $E_{iso} > 10^{52}$ erg. The maximum luminosities and isotropic energies of black bodies are in a narrower range than GRB isotropic energies. GRB 151027A has a strong thermal emission which reaches luminosity of $L_{bb} \sim 10^{50}$ erg/s which is in line with maximum thermal luminosity of other bursts. This burst has total isotropic energy of 4×10^{52} erg (just above the 52-limit) while other burst can have above 10^{54} erg. This fits well within the IGC scenario in which strong thermal X-ray emission in the early afterglow comes from interaction of fireshell plasma with supernova ejecta, and only GRBs above the 52-limit produce fireshell plasma.

Often the spectrum is fitted with a perfect black body even if the parameters of the fit (temperature and flux) are later used in models which predict broaden black body. The progress should also occur in the observational part. The Swift has done a great job, but the black body, broaden or multi-peak black body, needs to be clearly identified and its evolution.

CHAPTER5

New GRB-SNe connections

Connections between Gamma-ray bursts (GRBs) and Supernovae (SNe) were discovered in the late '90s with the first GRB-SN connection of GRB 980425 and SN 1998bw[1]. In the next couple of decades many more connections were discovered, mainly thanks to the fast and precise localization of GRBs by the Swift satellite. The GRB-SN connection is made by detection of SN signatures in the GRB afterglow by the optical telescopes.

The optical light curve (LC) of a SN consists of a rising part which lasts from few days to several tens of days, the maximum, and the decaying part. When the SN and a GRB occur from the same phenomena, then the optical LCs and spectra of - GRB afterglow, the SN and host galaxy - are superimposed. In the beginning the GRB afterglow is too strong compared to SN rising LC. Later on, as the GRB afterglow fades, and SN LC rises to maximum, SN features can be detected. The most reliable feature of a SN is its spectrum (determined mostly by the lines) which is superimposed on two spectral components: the continuous spectrum of GRB fading afterglow, and, continues spectrum of GRB host galaxy which is constant in shape and intensity. Another feature is a bump in the light curve (LC) of the GRB optical afterglow and its reddening[2] , both of which are produced by the SN. The contribution by the host galaxy is usually smaller and easily subtracted since it is constant in time. Based on all these factors a SN detection can be made with different levels of certainty or it can be undetected even though it might be present. The basic differentiation of SN detection is whether it is based on a bump in optical LC or on a spectroscopic identification. The latter is considered in most cases a certain proof.

All GRBs connected to SNe were long GRBs ($T_{90} > 2$ s). Their isotropic energy spans entire range from $E_{iso} \sim 10^{48} - 10^{54}$ erg. SNe connected to GRBs were all type Ic or Ib (Ib/c) - core-collapse SNe with stripped hydrogen and, in most cases, stripped helium envelope. The speed of SN ejecta $v_{ej} \sim 0.03 - 0.1$ c was higher than non-GRB Ib/c SNe. They are more energetic and more luminous then non-GRB Ib/c SNe. Because of the last two factors these SNe are sometimes termed *hypernovae*. These GRB-SNe are, however, less luminous than special group of SNe called *superluminous supernovae* which are sometimes also termed hypernovae. The characteristics of most potentially detected

[1] SN is named by the four digit number corresponding to the year of discovery. First 26 SNe of the year have a capital-letter suffix starting from *A* for the first SN, *B* for the second, etc. up to *Z*. Following SNe have a two letter suffix in small letters, again in alphabetical order, *aa*, *ab*... *az*, *ba*, *bb*, etc. Since 2016 a three letter suffix is used after all two letter combinations are "spent".

[2] Crude spectral analysis based on several filters in optical band. The intensity in lower-energy filters (red color) becomes stronger than in the higher-energy filters (blue color).

SNe also point to the type Ib/c with features of other GRB-SNe Ib/c (more luminous, etc.).

For a recent review on GRB-SN connections from observational point of view see (Cano et al., 2016).

In Table 5.1 confirmed and potential GRB-SN connections are listed. The table is an extension of one from (Kovacevic et al., 2014). Similar table in (Cano et al., 2016) has been of help in making the new one.

All the SNe which have a confirmed detection in a GRB afterglow were type Ib/c SNe and vast majority of possible SNe detections are also of this type. These SNe are typically discovered within 20 days of a GRB when their LCs reach maximum. Aside from these, there are a couple of interesting possible connections among which SN 1997cy and GRB 970514 (Germany et al., 2000) stand out. SN 1997cy was a type II SN – a core-collapse SN with hydrogen lines in the spectrum. Among other spectral lines, this SN also exhibits narrow Balmer[3] emission lines in its spectrum which is typical of a subtype IIn SNe (*n* stands for narrow). Further investigation showed that this peculiar SN is actually a type Ia supernova which ejecta strongly interacts with a hydrogen-rich circum-stellar medium Ia-CSM (Silverman et al., 2013). This interaction gives rise to narrow hydrogen lines in the spectrum. Burst GRB 970514 was a short GRB with $T_{90} \approx 0.6\mathrm{s}$. SN 1997cy was discovered serendipitously two months after the GRB. Analysis showed that this SN was already in the decaying phase and it reached its maximum before. Given the small positional uncertainty of GRB position, its proximity to SN location, it seems this connection is real and not a coincidence (Germany et al., 2000). With the redshift of SN 1997cy $z = 0.063$, this would imply that GRB 970514 had an isotropic energy of $E_{iso} \approx 4 \times 10^{48}$ erg.

Except the previous special case all SNe connected to GRBs were discovered by observing the GRB afterglow with optical detectors. This in turn was made possible by relatively precise localization of GRB prompt emission. There are many cases when a GRB prompt emission wasn't precisely localized and no optical or soft X-ray follow-ups were possible. If a SN was physically connected to such a GRB then it might be possible that the SN was discovered serendipitously by optical telescopes. This is the main topic of this chapter. Are there any missed GRB-SN connections within the sample of detected GRBs and detected SNe?

Regarding SN types review on basic classification can be found, for example, in (Turatto, 2003; Pastorello, 2012). The classification is based on spectroscopic features which translate, with other observational evidence, into astrophysical features. In a nut-shell: basic division is on type I (SN progenitor doesn't have hydrogen envelope) and type II (has hydrogen envelope). Type Ia are thermonuclear SN without hydrogen envelope. Type Ib are core-collapse SN without hydrogen but with helium envelope. Type Ic are core-collapse SN without hydrogen and without helium envelope. Some broad-lined SNe Ib and Ic are known to be connected to GRBs and therefore put in one group Ib/c. Since they are similar from observational point of view, they are sometimes reported as Ib/c even without considering GRBs. Type II SNe are all core-collapse SNe. Type II can be divided based on the light curve shape into IIP and IIL. Type IIP exhibit a plateau in the LC after maximum while IIL have linear decay of LC after maximum. Type IIb are SNe in between type II and type Ib. They exhibit spectral features of type II (namely hydrogen lines) in the beginning and later on spectral features of type Ib. Type IIn are a special case and exhibit narrow hydrogen lines superimposed on medium and broader ones in the spectrum. This indicates interaction of SN energy (stored as kinetic energy of expanding

[3]Hydrogen lines corresponding to transition between orbit n = 2 and higher orbits.

GRB	E_{iso} (erg)	Discovered by	z	SN identification	SN name	Refs.
970228	1.86×10^{52}	SAX	0.695	bump		(Reichart, 1997)
980326	5.60×10^{51}	BATSE	1(?)	bump		(Bloom et al., 1999)
980425	6.38×10^{47}	BATSE	0.0085	spec.	SN 1998bw	(Galama et al., 1998)
990712	7.80×10^{51}	SAX	0.434	bump		(Zeh et al., 2004)
991208	2.59×10^{53}	Ulysses/Wind	0.706	bump		(Zeh et al., 2004)
000911	7.80×10^{53}	Ulysses/Wind	1.058	bump		(Lazzati et al., 2001)
010921	1.10×10^{52}	HETE	0.45	bump		(Zeh et al., 2004)
011121	9.90×10^{52}	SAX/Ulysses	0.36	bump	SN 2001ke	(Bloom et al., 2002)
020305	$0.7\text{-}4.6 \times 10^{51}$	HETE/Ulysses	0.2-0.5	bump		(Gorosabel et al., 2005)
020405	1.28×10^{53}	SAX/Ulysses	0.695	bump		(Masetti et al., 2003)
020410	2.20×10^{52}	SAX	~ 0.5	bump		(Levan et al., 2005)
020903	1.10×10^{49}	HETE	0.251	bump		(Bersier et al., 2006)
021211	1.30×10^{52}	HETE	1.006	spec.	SN 2002lt	(Della Valle et al., 2003)
030329	1.70×10^{52}	HETE/Wind	0.168	spec.	SN 2003dh	(Stanek et al., 2003)
030723	$< 1.6 \times 10^{53}$	HETE	< 1	bump		(Fynbo et al., 2004)
031203	9.99×10^{49}	INTEGRAL	0.105	spec.	SN 2003lw	(Malesani et al., 2004)
040924	1.10×10^{52}	HETE	0.86	bump		(Soderberg et al., 2006a)
041006	3.50×10^{52}	HETE	0.716	bump		(Soderberg et al., 2006a)
050416A	1.20×10^{51}	Swift	0.6528	bump		(Soderberg et al., 2007)
050525A	3.39×10^{52}	Wind/INTEGRAL	0.606	spec.	SN 2005nc	(Della Valle et al., 2006)
050824	$0.4\text{-}3 \times 10^{50}$	Swift	0.828	bump		(Soderberg et al., 2007)
060218	1.66×10^{49}	Swift	0.033	spec.	SN 2006aj	(Campana et al., 2006)
060729	1.60×10^{52}	Swift	0.54	bump		(Cano et al., 2011)
060904B	2.40×10^{52}	Swift	0.703	bump		(Cano, 2013)
070419	7.90×10^{51}	Swift	0.97	bump		(Hill et al., 2007)
080319B	1.30×10^{54}	Swift	0.937	bump		(Tanvir et al., 2010)
081007	2.50×10^{51}	Swift/Fermi	0.5295	bump	SN 2008hw	(Jin et al., 2013)
090618	2.90×10^{53}	Swift/Fermi	0.54	bump		(Cano et al., 2011)
091127	1.60×10^{52}	Swift/Fermi	0.49	bump	SN 2009nz	(Cobb et al., 2010)
100316D	9.81×10^{48}	Swift	0.059	spec.	SN 2010bh	(Chornock et al., 2010)
100418A	9.90×10^{50}	Swift	0.624	bump		(Holland et al., 2010)
101219B	4.39×10^{51}	Swift/Fermi	0.55	spec.	SN 2010ma	(Sparre et al., 2011)
101225A	1.20×10^{52}	Swift	0.847	bump		(Cano et al., 2016)
111209A	5.80×10^{53}	Swift	0.677	bump	SN 2011kl	(Kann et al., 2016)
111211A	5.70×10^{51}	Swift	0.478	bump		(de Ugarte Postigo et al., 2012)
111228A	7.52×10^{52}	Swift/Fermi	0.714	bump		(D'Avanzo et al., 2012)
120422A	1.28×10^{51}	Swift	0.283	spec.	SN 2012bz	(Melandri et al., 2012)
120714B	4.51×10^{51}	Swift	0.3984	spec.	SN 2012eb	(Klose et al., 2012)
120729A	2.30×10^{52}	Swift/Fermi	0.80	bump		(Cano et al., 2014)
130215A	3.10×10^{52}	Swift/Fermi	0.597	spec.	SN 2013ez	(Cano et al., 2014)
130427A	9.57×10^{53}	Fermi/Swift	0.3399	spec.	SN 2013cq	(Melandri et al., 2014)
130702A	7.80×10^{50}	Fermi	0.145	spec.	SN 2013dx	(Toy et al., 2016)
130831A	4.56×10^{51}	Swift	0.4791	spec.	SN 2013fu	(Cano et al., 2014)
140606B	3.50×10^{51}	Fermi	0.384	spec.	iPTF14bfu	(Cano et al., 2015)
150518	$> 5 \times 10^{49}$	Wind/MAXI	0.256	bump		(Pozanenko et al., 2015)
150818	1.00×10^{51}	Swift	0.282	spec.		(de Ugarte Postigo et al., 2015)
161219B	1.60×10^{50}	Swift	0.1475	spec.	SN 2016jca	(Ashall et al., 2017)

Table 5.1: The sample of 47 confirmed and possible GRB and SN Ib/c connections updated to 01 January, 2017. There are two potential GRB-SNe connections, based on the bump in the LC, prior to the first confirmed connection of GRB 980425 - SN 1998bw. The *PTF14bfu* is a SN, however it was not named by the standard SN convention. Isotropic energy is the one from the GRB prompt emission. References point to the SN discoveries (or potential discovery) and their connection to a GRB. It can be noted that all the redshifts are $z \leq 1$ which is a limit imposed by sensitivity of optical telescopes regarding detection of SNe. The satellites detecting GRBs: *SAX* stands for BeppoSAX satellite; *BATSE* is a detector on-board CGRO satellite; others are names of satellites. Often two or more satellites observed a GRB. Here focus is on the BATSE, Fermi and Swift. Their name is always shown if they detected a GRB. Names of other satellites are present if none of the three detected a GRB.

ejecta or radiation) with slow-moving pre-explosion ejected material from the progenitor. Such SNe can be type Ia-CSM (like SN 1997cy); they can be *supernova impostors* - stars which periodically eject large amounts of matter, and when the fresh ejected shell interacts with the older and slower moving one, energy is released and it gives rise to optical emission. This optical emission resembles a SN but is generally weaker; finally, they can be real type II SNe with SN energy interacting with slow-moving CSM which was ejected from the progenitor star prior to SN explosion. Short review of SNe IIn can be found (Habergham et al., 2014).

In the next section technical details regarding different SN and GRB catalogs, collecting information from them, and the computer script used to find all possible missed connections will be presented. Since new SNe and GRBs are discovered almost every day, the GRB and SN time limit for this work was chosen to be January 1, 2017. Then the search for missed connection between GRBs detected by Fermi and BATSE, and SNe Ib/c will be presented. This largely follows the work in (Kovacevic et al., 2014). Then the search for missed connection between short GRBs and SNe IIn will be presented.

5.1 Technical details

5.1.1 SN catalog

Sample of detected SNe was taken from two supernova catalogs.

Harvard catalog

One catalog is managed under *International Astronomical Union: Central Bureau for Astronomical Telegrams* (IAU: CBAT) with Harvard University[4]. The catalog itself can be found in the form of a text file on the website[5]. It lists all the SNe since 1885[6] up to the end of 2015. Here the catalog stops probably due to large increase of SN detections and difficulty of categorizing them. There are about 6500 SNe in this catalog. For each SN there are information regarding position in the sky, date of detection and a type of SN - all which is needed for cross-correlation with GRBs.

The information from the website can be directly loaded from the web into a programing language (for example Python[7]) or copied into a text file and then loaded to a programing language.

The date of the detected SN, which is in YYYY-MM-DD format, are transformed into Modified Julian Day (MJD)[8] format which is a 5 digit number for all the dates in the last hundred years or so, (and will be for the next century) and suitable for comparisons. In very few cases SN date is not listed. This happens for SNe which were initially named as SNe but for which there is a doubt whether the optical transient detected is SN at all or some other optical transient such as *luminous blue variable* star, *Eta Carinae* type star or even HII region. These "SNe" are, at this point, excluded. The date refers to date of discovery which can be before the maximum or after (more common).

SN positions have been determined with sub-arcsecond precision which is much smaller then typical prompt GRB positional uncertainty of Fermi and BATSE (several degrees or

[4] `http://www.cbat.eps.harvard.edu/iau/cbat.html`

[5] `http://www.cbat.eps.harvard.edu/lists/Supernovae.html`

[6] SN 1885A, first modern observation of a SN.

[7] `https://www.python.org/`

[8] For explanation see `http://tycho.usno.navy.mil/mjd.html`

tens of degrees). Therefore the SN positional errors can be neglected. In some cases the SN position is not given. Then the position of the host galaxy is used which is also listed in the catalog. The difference is, again, marginal (tens of arc-seconds) when compared to prompt GRB positional uncertainty.

Supernova types in the catalog follow typical classification: Ia, Ib, Ic, IIP, IIL, IIn, IIb. This is how SNe types are marked in the catalog. There are some specifications. For example, if a SN shows some peculiar characteristics, then an additional letter *p* is assigned to it. Or, if a classification is not certain, then a question mark *?* is also added. Sometimes the type of a SN is determined just as a type I or II without sub-classification, and sometimes SN is not classified at all. In Table 5.2 is shown how SN types from the Harvard catalog are marked and to which general type they refer.

Asiago catalog

Second catalog which was used is *Asiago* catalog managed by Padova Observatory[9] (Barbon et al., 2010). The online catalog can be found here[10][11] as a text file, and on the NASA's HEASARC (High Energy Astrophysics Science Archive Research Center) server here[12] in numerous forms including a fits (Flexible Image Transport System) file. This catalog also contains all the necessary information for cross-correlation with GRBs along with many other. The information from the fits file catalog can be easily red into programing language. Like Harvard, this catalog contains all the SNe since 1885 up to the end of 2015 (with several more SNe in December 2015 than in Harvard). There are about 6500 SNe in this catalog.

The date which is in YYYY-MM-DD format is transformed into Modified Julian Day. The date can refer to the date of discovery, the date of determined maximum or date of an estimated maximum. Position is given as RA and Dec in decimal degrees.

The type of SN follows typical classification: Ia, Ib, Ic, IIP, IIL, IIn, IIb. If the classification is uncertain then *:* or *?* is added and if SN shows peculiar features then *PEC* is added. The Asiago (HEASARC) catalog also differentiates type marked IIN?, which are supernova imposters, super-luminous supernova and some other specific types. There are SNe classified just as type I or II, and SNe which are not classified. In Table 5.2 it is shown how SN types from this catalog are marked and to which type they refer.

The naming convention in the Asiago (HEASARC) catalog is a little bit different than in Harvard - the double letters are all in capital and a "SN" is added in front. This needs to be transformed within a script to exactly match the names in Harvard catalog if SNe from both catalogs are to be compared.

Asiago catalogs 2014/15/16

Aside from the standard Asiago catalog of SNe recognized and named by the IAU convention, there are numerous more SNe detected by new wide field automatic optical telescopes. These are relatively new instruments and many SNe do not have an official IAU name. These SNe are named by the conventions corresponding to wide field telescopes transients.

[9] `http://graspa.oapd.inaf.it/about.html`
[10] `http://graspa.oapd.inaf.it/cgi-bin/sncat.php`
[11] `http://graspa.oapd.inaf.it/asnc/cat.txt`
[12] `http://heasarc.gsfc.nasa.gov/w3browse/all/asiagosn.html`

SN group	SN type	Harvard		Asiago	
Ib/c	Ic	Ic, Ic?, Ic-p	N = 252	IC, IC?, IC:, IC PEC, IC PEC:	N = 305 (261)
	Ib	Ib, Ib?, Ib-p, Ibn	N = 128	IB, IB:, IB ?, IB PEC, IBN	N = 169 (140)
	Ib/c	Ib/c, Ib/c?, Ibc, Ibc?, Ic/b	N = 94	IB/C, IB/C:, IB/C PEC	N = 90 (75)
Ia	Ia	Ia, Ia?, Ia-p, Ia-p?, Iap	N = 3001	IA, IA:, IA?, IA ?, IA*, IA PEC	N = 4398 (3123)
none	I	I, I?, Ip, I-p	N = 62	I, I:, I*, I PEC	N = 90 (87)
IIn	IIn	IIn, IIn?	N = 201	IIN, IIN:, IIN?, II N, IIN ?, IIN PEC	N = 280 (228)
IIb	IIb	IIb, IIb?	N = 83	IIB, IIB:, IIB: PEC	N = 137 (102)
IIP	IIP	IIP, IIP?, II-P	N = 226	II P, II P:, II P PEC, II* P	N = 486 (372)
none	IIL	IIL, IIL?, II-L	N = 6	II L, II L:	N = 28 (24)
none	II	II, II?, II-p	N = 1010	II, II:, II?, II ?, II PEC	N = 1157 (955)

Table 5.2: Harvard catalog contains SNe up to the end of 2015. Asiago catalog contains SNe up to the end of 2016. This includes Asiago (HEASARC) catalog till the end of 2013, and Asiago catalogs 2014/15/16. Numbers in brackets correspond to Aaiago (HEASARC) catalog till the end of 2015. SNe with uncertain or peculiar types are included in that general type. Sometimes letters/symbols are interchanged or put differently. Many SNe are marked as in-between types Ib and Ic - type Ib/c. There are only few cases of double identification of types other then Ib/c and they are not included. SN group refers to how SNe types are grouped for the purpose of cross-correlation with GRBs. SNe that were determined just as type I or type II are not included in the analysis. Due to low number of IIL SNe they are also not included.

Asiago catalog contains special annual sections containing IAU and non-AIU SNe for years 2014[13], 2015[14], 2016[15], etc. SNe in the annual sections for the previous years contain just IAU SNe as in the standard catalog. The wide-field optical telescopes have vastly increased the rate of SN detections. The number of non-IAU SNe has grown which has prompted IAU to introduce additional three-letter naming convention since 2016. Even so, there are still SNe in with non-IAU designations. For example, number of IAU SNe in the year 2014 is around 150 while Asiago catalog for 2015 (which contains IAU and non-IAU SNe) has around 950 SNe. The Asiago 2014/15/16 contain contain most of the important SNe but not all.

These catalogs are not on the HEASARC server and had to be copied from a web page to a text file and then loaded to a program.

Merging catalogs

The Harvard and standard Asiago catalogs are summary of all the observations and analysis of IAU SNe done by many optical telescopes and astronomers. They are practically the same. The Harvard catalog has two SNe not present in Asiago catalog, while Asiago has one not present in Harvard and several more SNe which are marked as LBV, eta-Car type stars, etc. in Harvard catalog.

The main difference is in the type of a SN. Often there are several observations and analysis of a single SN, and different analysis can make different classifications. In modern times SN classification is usually done by a computer program which compares SN spectrum to many different spectra and finds the closest match. There are also several different programs in use and they can produce different results. In most cases the type of a given SN in both catalogs is the same. However, in some cases it is different or is more precisely determined in one catalog (for example it is marked as type II? in one catalog and IIn in other). For the purposes of this work, selection of all the SNe of a given type is done in such a way to take into account also those SNe that have that type only in one

[13] http://graspa.oapd.inaf.it/cgi-bin/sncat_new.cgi?yr=2014
[14] http://graspa.oapd.inaf.it/cgi-bin/sncat_new.cgi?yr=2015
[15] http://graspa.oapd.inaf.it/cgi-bin/sncat_new.cgi?yr=2016

catalog. Taking all into account, this improves the statistics rather then diminishing it. Of course, if there are some particular SNe of interest (with high probability of belonging to a GRB) then their properties from both catalogs as well as other sources are checked.

The position and discovery dates of a given SN should be the same in both catalogs. To do a quick check to see if there are some errors in the catalogs, SNe from both catalogs are cross-correlated with each other. For some SNe there is a large discrepancy in position and discovery dates and these are further checked to see which catalog is "wrong" and afterwords it is corrected.

The IAU SNe from Harvard and Asiago catalog are taken up to the end of 2014. IAU and non-IAU SNe since the beginning of 2014 are taken from Asiago 2014/15/16 catalog(s).

Merging Harvard and standard Asiago catalog is important for SNe detected in the '90s - the period of time when CGRO-BATSE was detecting GRBs. Adding SNe from Asiago 2014/15/16 catalog is important for cross-correlation with GRBs detected by Fermi satellite which is still operational.

5.1.2 GRB catalogs

There were/are many GRB missions. In this work the GRB catalogs from the most important ones will be used such as CGRO-BATSE and Fermi-GBM. These two detectors have the largest number of detected GRBs and most precisely determined GRB parameters. The GRB catalog from the Swift-BAT instrument will not be used because the very precise localization of GRBs (few arc-minutes) made it possible for majority of them to be observed with optical telescopes, and if there was a SN connected to these GRBs then it was already discovered.

The main GRB parameters needed for cross-correlation with SNe are date, position and error of position. Another important parameter is the duration so difference between long and short GRBs can be studied. The GRB catalogs are not merged and are cross-correlated with SNe separately. This can be done because they contain different GRBs (different time periods).

CGRO-BATSE catalog

Burst And Transient Source Experiment (BATSE) is a wide field gamma-ray detector on board of NASA's Compton Gamma-Ray Observatory (CGRO) satellite which operated from 1991 to 2000. During this time it detected around 2700 GRBs with several degree localization accuracy. Field of view of BATSE is full sky, however due to proximity of Earth, it was something more than half of sky (with Earth blocking the other, smaller, half).

The official BATSE catalog can be found online here[16]; references (Meegan, 1997). The catalog is in the form of a text file. Due to the observational constraints, many GRBs out of 2700 don't have measured duration or fluence. So, the catalog is actually made out of several catalogs. The main catalog has 2702 GRBs and contains basic information such as date, position, etc; second catalog contains GRB durations and has 2135 GRBs; there are two catalogs for peak flux and fluence. In order to merge information from them into a single catalog, they all have to be read and same GRBs have to be matched by their trigger number which is the only parameter present in all the catalogs. Easier way is to

[16] https://gammaray.nsstc.nasa.gov/batse/grb/catalog/current/index.html

take the catalog from the NASA's HEASARC server[17] which contains all the information in a single catalog. The catalog can be read as a fits file. The GRBs which don't have measured duration or fluence have a set value of zero for these parameters. The RA, Dec, position error are given in decimal degrees while date is in MJD. Numerous other information regarding each GRB is also present. If there are several GRBs during one day, the names of these GRBs all have a "-" suffix. In order to differentiate them they were selected within a script and named by the standard convention of adding B, C, D, etc. to successive burst detected on the same day. Out of 2702 GRBs, 1540 are long ($T_{90} \geq 2$ s), 497 are short ($T_{90} < 2$ s, and > 0 s), and 665 don't have a constrained duration.

The positional error represents spacial-averaged statistical 1σ (68%) error. There is an additional 1.6° systematic error. BATSE team adds these two values in quadrature to get 1σ confidence interval. The same is done with this work. Out of long GRBs with the highest error radius, the 4 with the highest error have a significantly higher radius than the rest, and are excluded by setting a limit of $er(max, long) \leq 16^\circ$, which makes a final of 1536 long GRBs. Out of short GRBs with the highest error radius, the 2 with the highest error have a significantly higher radius then the rest, and are excluded by setting a limit of $er(max, short) \leq 20^\circ$, which makes a final 495 short GRBs. The average value of positional error for long GRBs is $er(avg, long) = 3.7^\circ$ with standard deviation $\sigma(long) = 2.4^\circ$. The average value of positional error for short GRBs is $er(avg, short) = 7.0^\circ$ with standard deviation $\sigma(short) = 3.8^\circ$.

Fermi-GBM catalog

Gamma-ray Burst Monitor (GBM) is an instrument on board NASA's Fermi satellite which was launched in 2008 and is still operational. Fermi-GBM, up to 1 January 2017, detected about 2000 GRBs with several degrees to few tens of degrees localization accuracy. Field of view of GBM is full sky, however due to proximity of Earth, it was something more than half of sky.

The official Fermi-GBM can be found on NASA's HEASARC server[18] in many forms including fits file; references (Gruber et al., 2014; von Kienlin et al., 2014; Bhat et al., 2016). The RA, Dec and positional error are given in decimal degrees while date is in MJD. Numerous other information regarding each GRB is also present including automatic spectrum. Out of 1980 GRBs, 1654 are long and 326 are short.

The positional error represents spacial-averaged statistical 1σ (68%) error. If a GRB was localized with arc-minute accuracy or more precisely by other satellites/instruments, then that position is given in the catalog and positional error is set to zero. If the Large Area Telescope (LAT) on-board Fermi detected a GRB with higher accuracy (several tens of arc-minutes), and there is no arc-minute localization by other instruments, then the LAT position and error are given. The error radius set to 50° means the GRB is not well localized, however only one GRB has this value. There is an additional 2-3 degrees (2.5°) systematic error associated to Fermi-GBM which is added in quadrature to statistical. For simplicity this is done for all GRBs, even the ones who were localized more precisely by other instruments. To exclude the tail of positional error distribution, the maximum error is set to $er(max, long) \leq 20^\circ$, which makes a final of 1640 long GRBs. For the short bursts this limit is set to $er(max, short) \leq 24^\circ$ which makes a final of 320 short bursts.

[17] https://heasarc.gsfc.nasa.gov/W3Browse/all/batsegrb.html
[18] https://heasarc.gsfc.nasa.gov/W3Browse/fermi/fermigbrst.html

The average value of error for long bursts is $er(avg, long) = 5.3^\circ$ with standard deviation $\sigma(long) = 3.5^\circ$. For short, $er(avg, short) = 8.7^\circ$ and standard deviation $\sigma(short) = 5.0^\circ$.

The GRB catalog is a subset of a larger trigger catalog[19] which contains all the gamma-ray triggers, not just the ones that turned out to be GRBs. Most of the non-GRB triggers are identified as, for example, terrestrial flashes, solar flares, etc. and only small part of them are unidentified and may come from a SN. Majority of these unidentified triggers have very large error radius and are not suitable for cross-correlation.

5.1.3 Program scripts

SN scripts

For all three catalogs - Harvard, Asiago (HEASARC), Asiago 2014/15/16 - a *program script* was created which reads SNe parameters (Name, RA, Dec, type, etc.), either from fits or text files, into 1D-array *variables*. All three scripts are then read into a final SN script. SNe from Harvard and Asiago (Hea.) are taken till the end of 2014, and the rest are taken from Asiago 2014/15/16. SNe from Harvard and Asiago (H.) are by most part doubles (same ones), and of course only one is taken. However, a number of double SNe have a different type (or a type is more precisely determined), and if a certain type of SNe is needed then the SN is taken even if it is of that type only in one of the two catalogs.

SN double is found by matching its name, then the types are compared, and this is repeated for all SNe. Also in this way it is possible to double-check information regarding position in the sky, date, etc. For example, the distance of the doubles is calculated and it should be very close to zero or around 1 arc-second. If it is more than that it means that one of the catalogs has a wrong positional information. Then other sources of SN information can be checked to determine which of the two catalogs is in question. Often the problem is in a "typo", a single digit in RA or Dec is entered wrong. This "typo" can give a rise to a huge or small discrepancy depending which digit is in question. The doubles with distances more or close to 1 degree were checked (about 10), while the rest were not (about 100 or more). Similar procedure has been done for dates which are more accurate in both catalogs.

The idea of the final SN script is to take all SNe from three catalogs into account and to easily select them based on type and/or date range (or any other parameter). The final SN script produces selected SNe parameters (RA, Dec, date, etc.) which can be used for cross-correlation with GRBs.

GRB scripts

For BATSE and Fermi a script has been created which reads the information from the fits file and creates variables as 1D arrays for all the GRB parameters - RA, Dec, error, date, T_{90}, etc. Within the script selection based on T_{90}, error radius or any other parameters can be done. The script with selected GRBs and their parameters can then be cross-correlated with SNe.

GRB-SN scripts

Final script uses the final SN script and a BATSE or a Fermi script. It then has all the SNe of a certain type and date range, and all the GRBs with a given T_{90} parameter. First,

[19] `https://heasarc.gsfc.nasa.gov/W3Browse/fermi/fermigtrig.html`

a time window (e.g. 30 days) is selected for a SN to happen after the GRB. Then, for a given SN, the script selects all the GRB with dates within time window of 30 days before the SN. Then, the distance of these GRBs from a SN position is calculated and compared to respective GRB positional errors. If a GRB error is larger then the distance to SN, that GRB is potentially connected to that SN. So, by this definition, potential connection between a GRB and a SN exists if a SN "happened" within a certain date range from a GRB and if it lies within GRB error radius. This is then done for all the SNe. In the end, all the potential GRB-SN connections are listed including their parameters. **Note:** The error 1σ radii encompass about 2/3 of GRB true positions, therefore this method is an approximation. This is related to other issues with the method which are discussed at the end of the chapter when considering future work.

Additionally:

- The time window can be given a series of values, and the script then automatically gives the number of potential connections for all the given time windows;
- If a time window is big enough, the same GRB might end up being connected to more than one SN. In this case the script can give the number of unique connections, i.e. exclude additional connections which have that GRB;
- Similar to the previous case it can also exclude connections which have the same SN but different GRBs, or, it can give the (maximum) number of GRBs any SN has associated to it for any time window;
- For GRBs, and/or SNe, random values of position and date can be selected instead of the real ones;
- In the case of random values, the script can, for example, be read into another script which can repeat the process any number of times and record connections for any number of random generated values and for all the time windows, and it can then compare it to the connections based on real positions and dates.
- The connections in different time windows are cumulative, i.e. connections in a bigger time window contain all the connections from the previous plus additional ones. In order to save time (computer resources), the script searches for connections in the first time window and then in the temporal range between the first and the second one, and so on. Then all connections are combined in the cumulative function. This is useful when repeating the process many times with different random values.
- Also, to save time, the job can be distributed to several cores in the processor. Each core can do the process for different temporal ranges or it can do entire cumulative function but for different random values. At the end all the results can be combined.
- Within the first or the second script, any other option-calculation can be implemented relatively simply.

5.2 Analysis of long GRB - SN Ib/c connections, 2014

This section describes work done in (Kovacevic et al., 2014). The goal was to find possible new physical connections between Ib/c SNe and long GRBs detected by Fermi-GBM. Most of the GRB connected to SNe were discovered by Swift-BAT since it can localize

Δt (days)	10	20	30	40	50	60	70	80	100	120	150	200	300	400	500	r_x (%)
$N_{Ib/c}(\Delta t)$	8	9	9	13	13	15	17	18	20	26	30	42	68	81	96	12
$N_{Ia}(\Delta t)$	10	23	30	42	51	64	77	85	108	131	164	213	338	440	519	66
$N_{IIp}(\Delta t)$	2	4	8	14	16	19	19	21	26	30	39	54	82	103	124	16
$N_{IIn}(\Delta t)$	1	2	4	6	8	9	9	9	11	11	14	21	30	38	51	6
$N_{tot}(\Delta t)$	31	67	98	136	166	209	240	260	314	378	471	627	893	1139	1399	100

Table 5.3: The cumulative number of each SN type associated within the error radius of Fermi long GRBs at different time intervals after the GRB date. In the first row the considered time intervals (in days) are listed. In the following rows the number of possible associations for each type of SN, respectively Ib/c, Ia, IIp and IIn, and the total number of SNe, for each considered time interval, are listed. In the last column the percentage r_x of the total number of each SN type over the total sample is shown. For brevity columns corresponding to time windows of 90 and 110 days are not shown in the table.

GRB precise enough to allow optical follow-ups. However, Swift-BAT has a practical field of view of 1.4 sr[20], which is about 6 times smaller then that of Fermi-GBM (FoV more than 8 sr[21]). Since many Fermi bursts are not well localized, it is possible that there are real physical connections between long GRBs detected by Fermi (and not detected by Swift) and serendipitously detected SNe.

An estimation was made as to how many SN-GRBs Fermi should have detected based on number of detections made by Swift. For reasons of completeness analysis was made for events with redshift $z \leq 0.2$. Up to middle of 2014 Swift has detected two such events: GRB 060218 - SN 2006aj and GRB 100316D - SN 2010bh. So, Fermi should have detected $2^{+2.6}_{-1.3} \times N_{Fermi}/N_{Swift} \approx$ 1-7 SNe-GRBs within $z \leq 0.2$ up to middle of 2014. Here, $N_{Fermi}/N_{Swift} \approx 1.5$ is simply the ratio of detected long GRBs by Fermi (during its 6 years of observation) and Swift (during its 10 years of observation). This takes into account different sky coverage of both detectors, their different sensitivities and different time period of operation. The 1σ error upper and lower limit attached to number of Swift observations ($2^{+2.6}_{-1.3}$) was derived from (Gehrels, 1986) assuming Poisson distribution in counting Swift's SN-GRBs. This error translates to interval of 1-7 SN-GRBs for Fermi. Confirmed number of SN-GRBs detected by Fermi ($z \leq 0.2$, up to middle of 2014) is just one (130702A - 2013dx), which means there are probably more connections which were missed.

5.2.1 Statistics of potential connections

The sample of 1147 long GRBs from Fermi catalog up to 31 May 2014 was considered. SNe from the Harvard catalog in the time period were considered. Then with the GRB-SN script potential connections were searched in a way that SN position should be within GRB error circle and occur a given period of time after the GRB. It is assumed that GRB and SN occur $\approx$ simultaneously. Since discovery of SN might correspond to period before-during-after maximum (and maximum can happen at different times), in order to determine optimal period of time, the script was run for many time windows. This was done also to help differentiate real connections from coincidences. To further help resolve this, the same process was done for other types of SNe known not to be connected to GRBs, such as type Ia or II. In the Table 5.3 number of potential connections is listed for different SN types and different time windows.

In order to assign a probability to the numbers in Table 5.3, next steps are made:

[20] https://swift.gsfc.nasa.gov/about_swift/bat_desc.html

[21] https://fermi.gsfc.nasa.gov/ssc/data/analysis/documentation/Cicerone/Cicerone_Introduction/GBM_overview.html

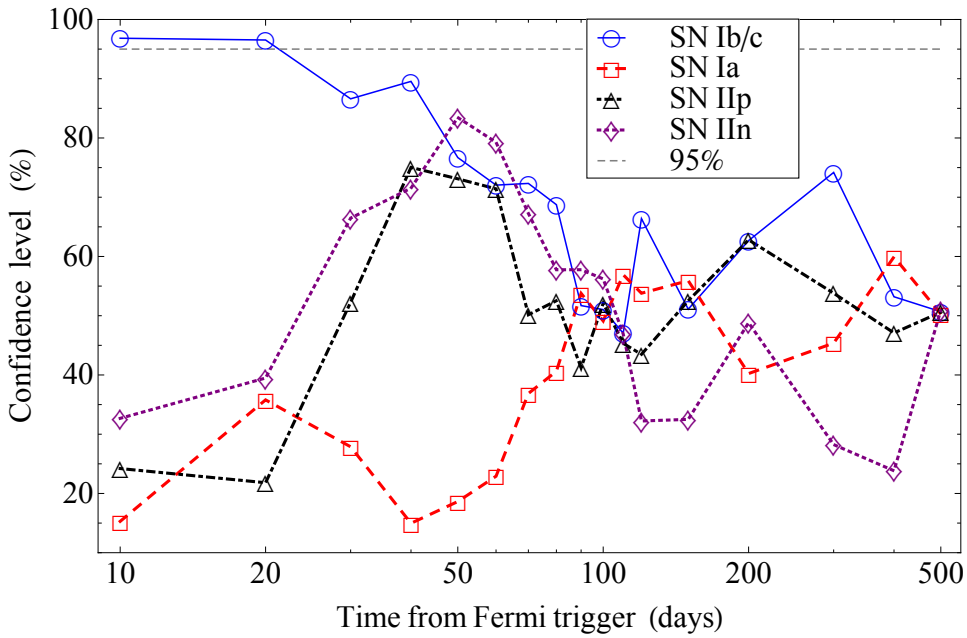

Figure 5.1: The statistical significance of the GRB-SN occurrence as a function of the temporal window. This plot shows the significance of the deviation of SNe Ib/c in the time interval $(T_0, T_0 + 20$ days) from the expected number of events assuming the relative proportion seen in the total SN sample.

Random distribution of SNe in the sky is assumed, and then spatial GRB-SN association follows the Poisson statistic, $e^{-\lambda}\lambda^n/n!$, where n is the number of observed associations and λ is the expected number of positive events, in a chosen temporal window Δt. The expected number of positive events can be evaluated from $N_{tot}(\Delta t)$ (last row in Table 5.3), times the percentage of each SN in the considered sample (see last column in Table 5.3). Therefore we have that $\lambda = N_{tot}(\Delta t) r_x$, where $x = \{$Ib/c,Ia,IIp,IIn$\}$. It is then compared with the observations $N_x(\Delta t)$, and evaluated the corresponding confidence levels. In this way probability is based on comparing number of potential connections between different types. Also, in this way probability is normalized to number of connections of all the SNe (all types).

The results of the computation are shown in Fig. 5.1. A simple comparison of significance tracks reported in Fig. 5.1 between SNe (Ib/c) and other SN types shows that, as expected, only SNe Ib/c within $\sim 30 - 40$ days after the GRB triggers are suggestive of the existence of physical associations with GRBs. From a simple application of Poissonian statistic in regime of small numbers (Gehrels, 1986), a threshold was derived of $\geq 95\%$ confidence level, which corresponds to $\Delta t = 20$ days. In the following only associations between GRBs and SNe within 20 days from the GRB trigger are considered.

5.2.2 The sample of Ib/c connections

The list of GRB-SN Ib/c associations that the script has pinpointed is reported in Table 5.4, together with observational properties of the bursts and possibly related SNe. There are 9 cases. Five of them are known: GRB 130702A - SN 2013dx, GRB 091127 - SN 2009nz, GRB 101219B - SN 2010ma and GRB 130427A - SN 2013cq. Only the first known one has $z \leq 0.2$. For all SNe the redshift is determined from spectral observations

GRB	RA GBM (deg)	Dec GBM (deg)	Error radius (deg)	T_{90} (s)	Fluence (0.01 - 1) MeV (erg cm$^-$2)	Peak flux (0.01 - 1) MeV (photon cm$^-$2)	SN	date discovery	RA SN (deg)	Dec SN (deg)	z
090320B	183.4	49.8	9.5	29.2	1.67×10^{-6}	4.35 ± 0.25	2009di	2009 03 21	174.2411	45.0141	0.13
090426B	17.6	-19.2	18.1	16.1	6.77×10^{-7}	2.03 ± 0.18	2009em	2009 05 05	8.6855	-8.3993	0.006
110911A	258.58	-66.98	50.0*	8.96	5.94×10^{-7}	2.38 ± 0.41	2011gw	2011 09 15	112.0709	-62.3552	0.01
120121B	235.67	-39.34	7.9	18.4	1.95×10^{-6}	2.66 ± 0.21	2012ba	2012 01 21	230.6047	-38.2012	0.017
130702A	228.15	16.58	13.02	59	6.3×10^{-6}	7.03 ± 0.86	2013dx	2013 07 08	217.3116	15.7740	0.145

Table 5.4: Main parameters of the Fermi GRB sample presented here and of the supernovae associated with these bursts. Also are reported already known GRB-SN connection ($z \leq 0.2$) that were found with script in the last row of the table. * Nominal maximum value for the error radius of bursts detected by a single GBM detector.

GRB	α	β	E_{peak} (keV)	E_{iso} (erg)
090320B	-0.65 $\pm$ 0.35	-2.42 $\pm$ 0.30	62.6 $\pm$ 12.0	9.13×10^{49}
090426B	-0.50 $\pm$ 3.12	-1.65 $\pm$ 0.15	39.9 $\pm$ 76.9	1.94×10^{47}
110911A	-0.47 $\pm$ 0.50	-1.36 $\pm$ 0.18	44.8 $\pm$ 20.1	6.22×10^{47}
120121B	-0.73 $\pm$ 0.21	-2.95 $\pm$ 0.89	92.2 $\pm$ 12.2	1.39×10^{48}

Table 5.5: Results of the spectral fits of Fermi-GBM observations for the 4 GRBs with evidence of association with a SN Ic.

of the host galaxy.

The values of E_{iso} reported in Table 5.5 are derived from the spectral analysis of Fermi-GBM data of GRBs, using a Band function as spectral model and assuming SN redshift. Analysis was done with Time-Tagged Events (TTE) Fermi-GBM spectra which combine a high time resolution (up to 2μs) with a good resolution in the spectral range. Spectra were fitted with RMfit package[22].

GRB 090320B - SN 2009di

GRB 090320B was detected by the 10 and 11 Fermi-GBM detectors and also by Wind-KONUS. The T_{90} duration reported by Fermi is 29.2 s, while unfortunately there are no further information from Wind-KONUS for this trigger. The possibly associated SN is SN 2009di (Drake et al., 2009a), which was discovered on 21 March 2009, just one day after the GRB detection. At the moment of the discovery, the unfiltered magnitude of the SN was 18.6. Spectroscopy made with the 5.1m Palomar Hale telescope identified SN 2009di as a type Ic SN. The redshift of the SN was reported to be $z = 0.13$. The distance of the SN position and the Fermi one is 7.8 degree, while the Fermi error radius is about 9.5 degree.

GRB 110911A - SN 2011gw

GRB 090426B was observed by the detectors 3 and 5 of Fermi-GBM, with a T_{90} duration of 16.1 s. SN 2009em (Folatelli and Morrell, 2009; Navasardyan and Benetti, 2009a; Monard, 2009a), associated with this GRB, was discovered on 5 May 2009. Follow-up observations made 6 days late confirm the presence of an unfiltered magnitude 16.6 supernova. Further spectroscopic observations made around May 19 confirm the Ic nature of this SN, which corresponds to several known SNe Ic observed about one month from the maximum light, which plays against an association with GRB 090426B. The distance from the Fermi position is 13.8 degree, to be compared with an error radius of 18 degree.

[22] `https://fermi.gsfc.nasa.gov/ssc/data/analysis/rmfit`

The redshift of this source was measured to be $z = 0.006$, which corresponds to a distance of 25.31 Mpc.

GRB 110911A - SN 2011gw

This GRB triggered Fermi detectors number 2 and 10. However, the signal from detector number 2 was dominated by noise, so only flux detected by number 10 is considered. This GRB was characterized by $T_{90} = 8.96$ s. SN 2011gw (Pignata et al., 2011) was discovered on 15 September by different observers, as an object of magnitude approximately 17.4. A spectrum obtained one month later, on 20 October, at NTT telescope revealed the Ib/c nature of this supernova, and a cross-check with the GELATO library found a match with other SNe at about two months post maximum. The redshift of this SN was reported to be 0.01 while the distance between the center of Fermi-GBM detectors and the SN was 48 degree, with an error radius of 50 degree. This large error box is due to the combination of two detectors that are located on the opposite sides of the Fermi spacecraft and increases the probability of a casual association for this GRB-SN event.

GRB 120121B - SN 2012ba

GRB 120121B was detected by Fermi detectors number 3 and 5 at 02h25m UTC. The T_{90} duration was 18.4 s. The best fit of the integrated spectrum of the GRB is a Band function with an intrinsic peak energy of $E_{p,i} = (92.2 \pm 12.2)$ keV. The SN associated to this GRB may be SN 2012ba (Pignata et al., 2012a). It was discovered on 21 January, the same day of the GRB trigger, as an object of unfiltered magnitude 16.6 still in rising phase. A spectrum obtained on 2 March (40 days after the discovery) with the 6.5-m Magellan II Clay telescope and then cross-correlated with the SNID libraries of SN spectra, showed a match with a type Ic SN more than 15 days after maximum. The redshift of the SN, $z = 0.017$ associated with the observed peak magnitude of 15.9, eleven days after the SN discovery, implied an absolute magnitude at maximum of -18.5, which is an upper limit to the intrinsic luminosity, considering the correction for dust extinction. This result suggests that SN 2012ba is a very luminous SN Ic, with an absolute magnitude similar to that of SN 2010bh, $R_{abs} \approx -18.5$ or even brighter, similarly to SN 1998bw $R_{abs} \approx -19$ (Bufano et al., 2012). The distance between the SN position and the Fermi center was of 4.1 degree, inside the Fermi error radius of 7.9 degree.

5.2.3 Discussion

Analysis discovered 5 GRB-SN connections within $z \leq 0.2$, and one of them was already known to be a physical association between GRB and SN: GRB 130702A - SN 2013dx. The optical afterglow of GRB 130702A (which was localized by Fermi and without Swift) was found by searching large 71 deg^2 area inside Fermi error circle (Singer et al., 2013). It could have easily been missed and with it, the emerging SN. The GRB was in between "cosmological" and underluminous, and had a relatively strong afterglow. The optical transient found showed signs of decreasing GRB optical afterglow (one of the reason it was identified with a GRB among numerous other optical sources in the area). Therefore, if a GRB-SN is serendipitously discovered before or close to maximum, it should show signs of decreasing GRB afterglow, unless the GRB is underluminous ($E_{iso} \sim 10^{48}$ erg) and its afterglow is week. So, the potential missed connections are most probably the ones that involve underluminous GRBs. That being said, it should be noted

that known GRB-SNe were observed with numerous and strongest optical instruments which were "staring" at a predefined position. Normal SNe are discovered by chance and observed by various instruments at various times, and even if a SN has a presence of an additional GRB-decaying-afterglow-like component, it might be missed.

After examination of the data, only SN 2012ba seems to be good candidate for being physical associated with a GRB (120121B). SN 2012ba was of type Ic and reached quickly a very bright maximum magnitude $R_{abs} \simeq -18.5$, about 11 days after the GRB trigger, which is very similar to the typical rising time and high luminosities of SNe associated with GRBs. To date there are only two other SNe associated with GRBs and classified as "Ic" (rather than "broad lines" Ic or Hypernovae): SN 2002lt, associated to GRB 021211, and SN 2013ez, associated to GRB 130215A. However, these observations do not imply that GRBs may be associated with "standard type Ic SNe". We note that in all three cases, 2012ba, 2002lt and 2013ez, SN spectra were secured 20-40 days past maximum, therefore even if the pre-maximum spectra showed significantly broader lines, than observed in the post-maximum spectra, this difference shortly vanished after maximum (if the SN ejecta carry little mass) such that it is not easy to distinguish between the two types of SNe. The isotropic energy of this Fermi GRB-SN candidate is $E_{iso} = 1.39 \times 10^{48}\mathrm{erg}$, which implies that this burst likely belongs to the low-luminosity subclass of GRBs.

Now, it is possible to independently estimate, admittedly on the very scanty statistic of one single object, the rate ρ_0 of local low-energetic long GRBs - type Ic SNe. For that a maximum distance of GRB 120121B for it to be detected by Fermi is needed. This can be estimated by examining count curve (in rmfit for example) of the burst in the most illuminated detector. The ratio of *unknown* peak of the curve (signal coming from maximum distance) to the square root of the *known* background (noise) is set to Fermi-GBM significance threshold of 4.5 (Band, 2003). From there the *calculated* peak (at maximum redshift/distance) is compared to the *known* actual peak (at z = 0.017), and the maximum redshift is calculated, and from there, the maximum (comoving) volume V_{max}. Background in Fermi-GBM oscillates at different points in orbit and orientation of the spacecraft, and the signal from GRB also depends on the orientation, etc. but the simplified approach is good enough for an estimation of z_{max} which will again be used for final estimation of rates. The maximum redshift for GRB 1202121B to be detected by Fermi-GBM is $z_{max} \approx 0.021$.

The estimated rate can then be written as:

$$\rho_0 = \frac{N_{LE}}{V_{max} f_F T} \,, \tag{5.1}$$

where $N_{LE} = 1$ is the number of found physical connections, $f_F \approx 0.7$ the average ratio of Fermi-GBM solid angle over the total one, and $T = 6$ y the Fermi observational period. From there a local rate for this GRB - SN Ic events of $\rho_0 = 77^{+289}_{-73}\ \mathrm{Gpc}^{-3}\ \mathrm{yr}^{-1}$, where the errors are upper and lower limit determined from the 95% confidence level of the Poisson statistic for a single count (Gehrels, 1986). It is important to note here that Fermi might have detected more SN-GRBs that were missed, not just by direct observations, but also here, simply because the SN wasn't detected (directly or serendipitously). In other words, other GRBs in the Fermi GRB catalog might be SN-GRBs but the accompanying SN is not in the SN catalogs for the script to match it to the GRB as a potential pair. So, the $N_{LE} = 1$ in the formula is in a sense a minimum.

There is growing body of evidence that low luminosity GRBs are less beamed that high luminosity GRBs, indeed f_b^{-1} is of the order of 10, or less (Guetta and Della Valle, 2007).

After taking into account this correction derived value is $\rho_{0,b} \leq 770^{+2890}_{-730}\ Gpc^{-3}\ yr^{-1}$, which is consistent with $\rho_0 = 380^{+620}_{-225}\ Gpc^{-3}\ yr^{-1}$ in (Guetta and Della Valle, 2007), $325^{+352}_{-177}\ Gpc^{-3}\ yr^{-1}$ in (Liang et al., 2007), and $230^{+490}_{-190}\ Gpc^{-3}\ yr^{-1}$ in (Soderberg et al., 2006b). This analysis confirms the existence of a class of more frequent low-energetic GRBs - SNe Ic, whose rate is larger than the one obtained extrapolating at low redshifts the rate for high-energetic bursts, i.e., $\rho = 1.3^{+0.7}_{-0.6}\ Gpc^{-3}\ yr^{-1}$ (Wanderman and Piran, 2010).

5.3 New statistical approach

5.3.1 On randomness

Regarding the cataloged supernovae:

- Distribution of SNe in the sky is not isotropic. The area around galactic equator has almost no SNe due to dust extinction of the galactic plane. There are clusters of SNe in the sky due to nature of observational programs and constraints.
- SNe are not detected with a constant rate. Number of detected SNe increases over the years as optical instruments become more numerous and sensitive. This is especially the case when considering the sample of SNe used in this work, namely the Asiago catalogs for 2015 and 2016 which together have around 1800 SNe, while the total number of SNe in the sample (starting from SN 1885A) is around 8300.
- There is a correlation between SN positions in the sky and detection dates with annual periodicity due to orbit of Earth around the Sun. Again, clustering can occur here.
- All above mentioned is present to a different degree for different types of SNe.

This can be seen on Figures 5.2, 5.3 and 5.4. In the figures type Ia SNe were chosen since their large number shows best different biases. Additionally, another type was used (Ib/c) to show that these biases are to a different degree for different type. Of course intrinsically SNe are distributed isotropically in the sky and they occur at a constant rate. It is the observations that make detected SNe appear biased.

GRB sky positions and detection dates are approximated as uniformly random. Both CGRO-BATSE and Fermi-GBM are space-based detectors. Their detectors are composed of several smaller detectors which are oriented to cover all the sky simultaneously. Gamma-rays do not suffer from passage in interstellar medium as optical photons do. The only obvious bias and periodicity is due to orbit of satellites around the Earth - as Earth occults part of the sky, satellites pass trough South Atlantic Anomaly (SAA)[23], and background rates (which affect sensitivity) vary. Orbits of both satellites are about 90 min which is much smaller than the smallest time period (10 days) used in the search for potential connections between GRBs and SNe and this periodicity bias is "smoothed out". The main biases which are not smoothed out are the lesser exposure of equatorial plane due to blockage of Earth, and different degree of exposure between two poles exists due to SAA (Hakkila et al., 1998, 2003). The approximation is extended to the error radii of

[23]Place above Earth, at the height of Fermi and CGRO orbits, where the Earth's magnetic field is different so the radiation from the Sun can reach "bellow" and disrupt instruments on satellites.

GRBs, and duration, which are assumed not to be correlated to position in the sky and/or detection date. The issue with exposure maps will be addressed in more detail at the end of the chapter when discussing future work.

The biases in GRB position and dates are significantly less then those of SNe. The contrast regarding isotropy and detection rates between GRBs and SNe can be seen on Figures 5.2, 5.3 and 5.4.

5.3.2 Confidence level

To calculate the probability that potential GRB-SN connections are physical, i.e. to calculate confidence level (CL), information on random (non-physical) connections should be known. This can be estimated (like in the work of 2014) as comparing number of connections of different SNe types to each other and normalizing them all to number of connections for all types. Or, calculating expected number of random connections based on SNe rates, GRB rates, and GRB error radius and assigning certain distribution to it (like Poisson for example). However large non-uniformity of SNe makes this difficult.

To overcome this, only GRBs or SNe have to be uniformly random, not both. In this case uniform randomness of GRBs is assumed. The given GRB positions and dates (the original ones) can be imagined to be one set of infinite number of GRB sets with uniformly random positions and dates. To find distribution of number of coincident connections, GRB positions in the sky and dates should be randomized many times while keeping the original SN positions and dates the same. The original values of GRB error radii are used. Then, all the different obtained number of connections for each set of random GRBs (the frequency of these numbers), will show the distribution of random connection number. The more random sets of GRBs there are, the obtained distribution is closer to true distribution. This distribution is discrete as number of connections is a whole number. It is the specific non-randomness of SNe (coupled with given GRB error radii) that dictates this distribution. Then, the original number of connections (based on original GRB positions and dates) should be compared to this distribution.

With randomizing GRBs any physical connection that exist in the original GRB set, will be erased. So, if there are physical connections, the original number of connections (physical + random) should be higher then the number of connections obtained from random GRB sets. The percentage of different GRB sets that gives number of connections lower than the original one will then be the CL. So, for example, if a $CL = 95\%$ then it means that in 95% cases the random GRBs will give less connections than the original one. Then, the value of $1 - CL$ (5%) gives the probability that the given number of connections is due to randomness, i.e. that there is not a single physical connection. In a sense, physical connections are *signal* while random connections are *noise*. If number of original connections is zero, then, CL is set to zero.

This may be considered as a type of Monte Carlo simulations. In this way it really doesn't matter what is assumed for underlying distribution of random connection number - Poisson (λ), Log-normal (μ, σ), or if it can be approximated by analytical function - the distribution, and with it the CL, are obtained directly. Once more to note that the original GRB positions and dates have to be random for this to work, otherwise the obtained distribution wouldn't correspond to the real one.

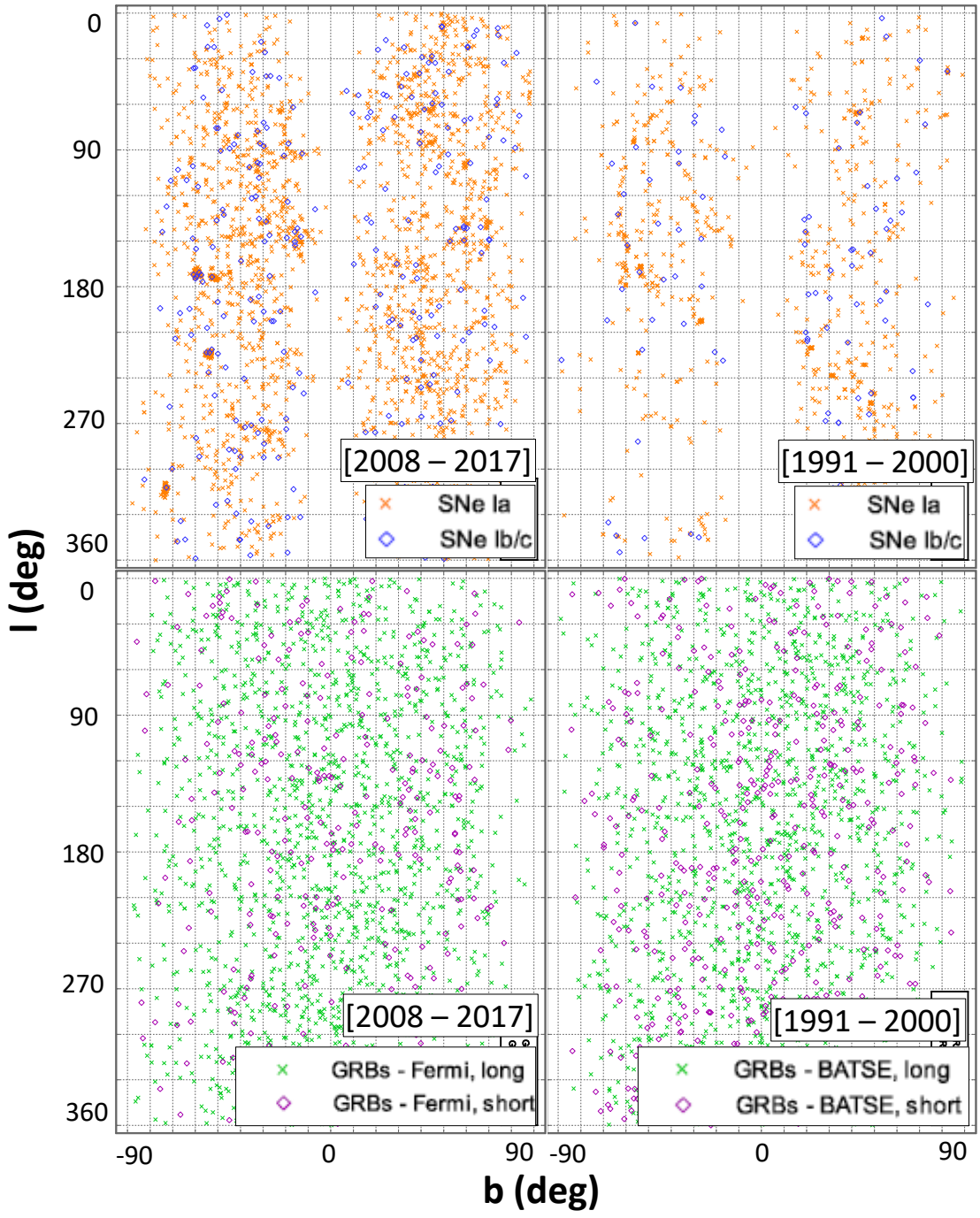

Figure 5.2: Positions of SNe and GRBs in the galactic coordinates - galactic longitude l and latitude b in degrees. **Upper-right:** SNe during the time interval of BATSE operation (1991 - 2000), plus couple of years more - around 750 Ia and 100 Ib/c. There are almost no SNe in the direction of galactic disk and there is a clustering in the shape of a large arc in the lower-left part. **Lower-right:** BATSE GRBs - about 1550 long and 500 short. Both long and short bursts are approximated as uniformly random. **Upper-left:** About 2200 Ia and 270 Ib/c SNe during the Fermi period (2008 - 2017). Again, absence of SNe in the galactic disk area, and clustering of SNe in certain patches of the sky. **Lower-left:** Fermi-GBM GRBs - about 1650 long and 320 short. Both long and short bursts are approximated as uniformly random. **Note:** Projection of the sky is on the flat rectangle surface. The area of the sky decreases and finally goes to zero as galactic latitude approaches $|b| \rightarrow 90°$. Lesser number of bursts (and SNe) at higher/lower latitude is due to this.

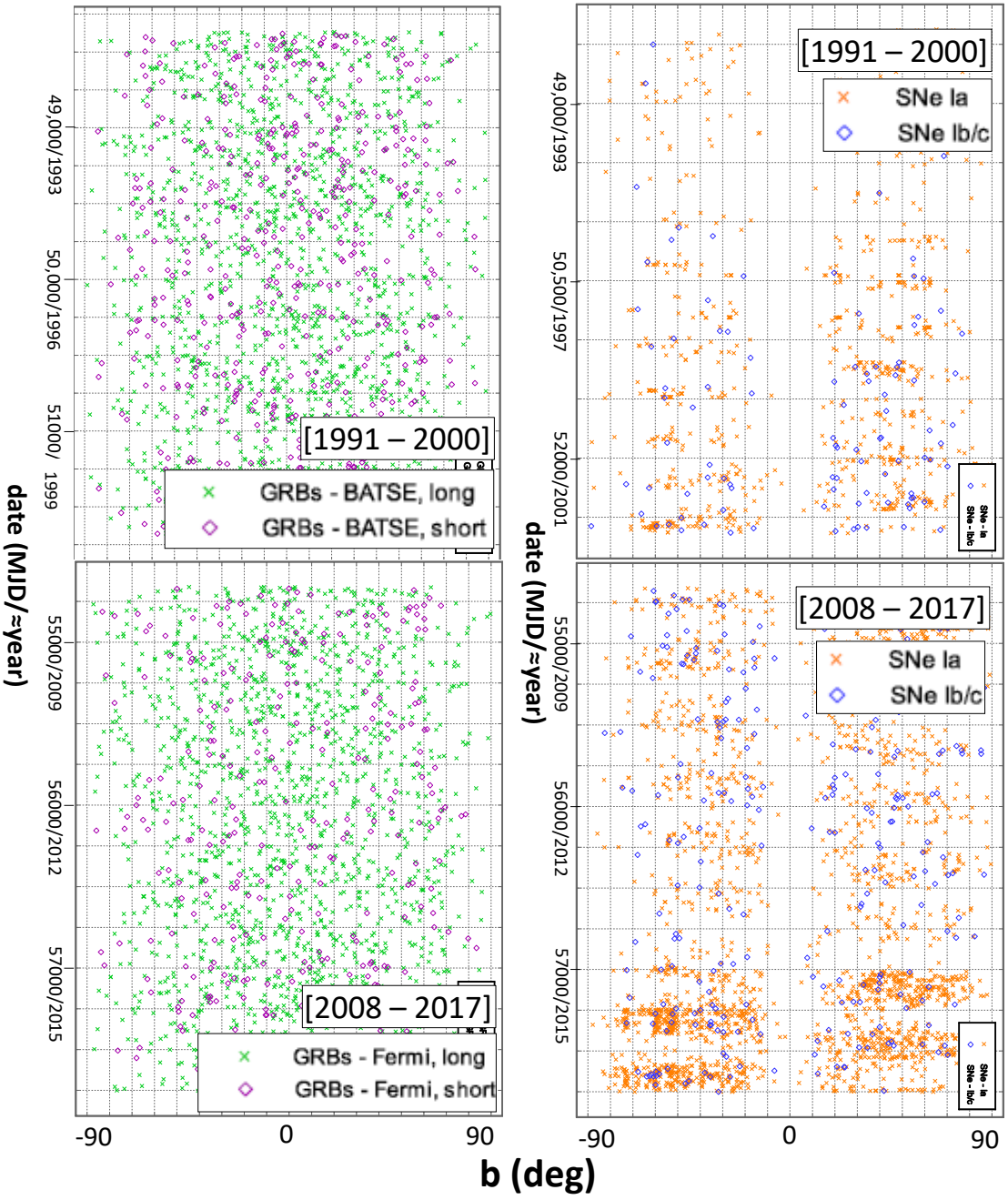

Figure 5.3: Correlation between SNe&GRBs dates with position (galactic latitude). Date is measured in Modified Julian Date, and galactic latitude b in degrees. The number and date intervals of GRBs and SNe is the same as in the previous figure. **Upper-right:** SNe during the time interval of BATSE operation (1991 - 2000), plus couple of years more. Number of detected SNe grows over passing years. Additionally, there is an annual periodicity in detection of SNe with respect to galactic latitude. SNe detections oscillate between upper and lower half of the (galactic) sky every year (switch happens every half a year). **Upper-left:** BATSE GRBs. Both long and short bursts are approximated as uniformly random on this plane, i. e. there is no correlation between position (latitude) and date. **Lower-right:** SNe during the Fermi period (2008 - 2017). Again, SNe detections increase over passing years and the same annual periodicity is present. Additionally, very large increase of SNe in the year 2015 (MJD $\approx$ 57.000) and 2016 is present. Also, this large increase is mostly affecting SNe Ia while not so much SNe Ib/c. **Lower-left:** Fermi-GBM GRBs. Both long and short bursts are approximated as uniformly random on this plane. **Note:** Note on the projection of the sky is the same as in the previous figure.

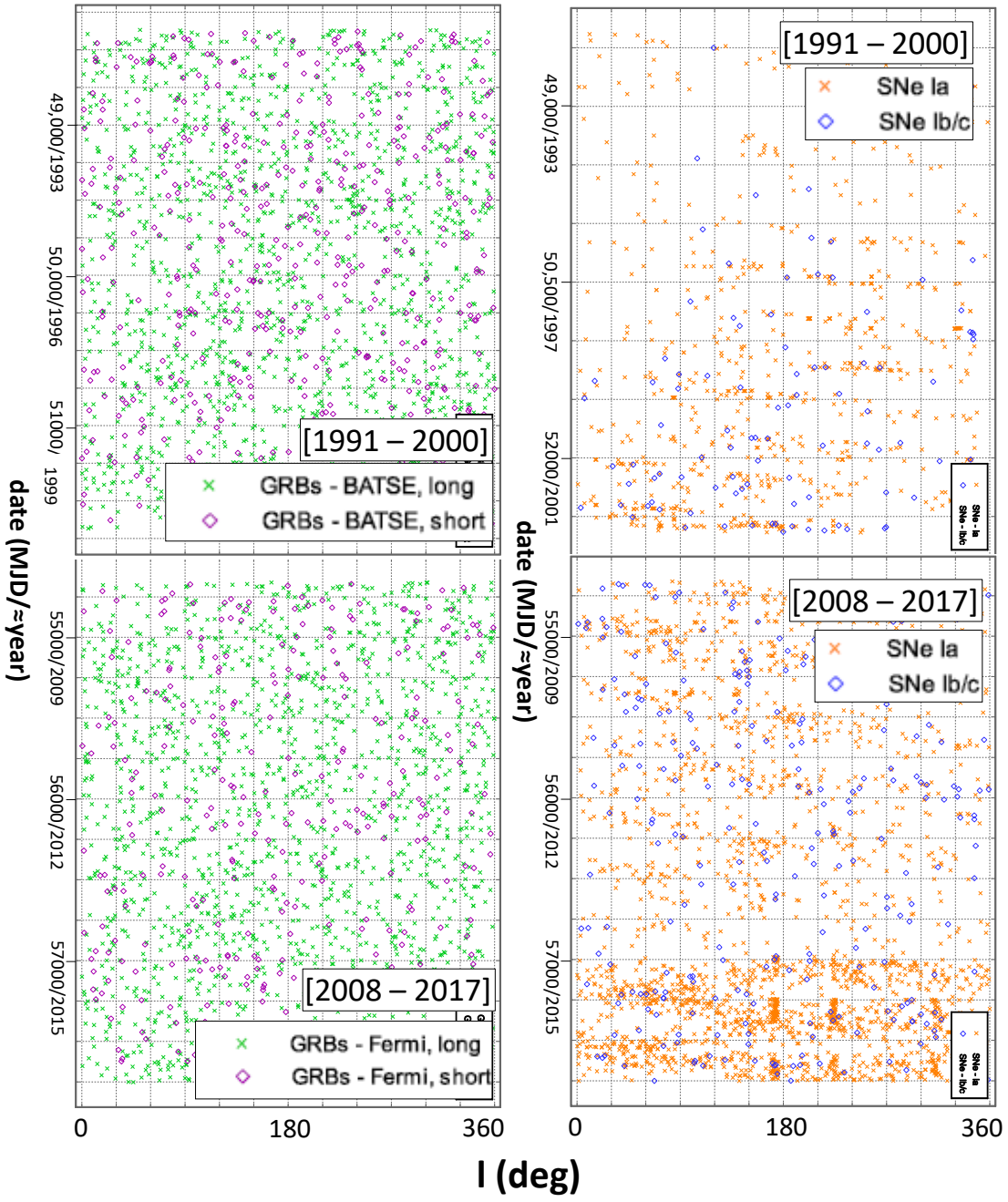

Figure 5.4: Correlation between SNe&GRBs dates with position (galactic longitude). Date is measured in Modified Julian Date, and galactic latitude l in degrees. The number and date intervals of GRBs and SNe is the same as in the previous figure. **Upper-rigth:** SNe during the time interval of BATSE operation (1991 - 2000), plus couple of years more. Similar to the case of date-latitude plot: Number of detected SNe grows over passing years; there is an annual periodicity in detection of SNe with respect to galactic latitude. **Upper-left:** BATSE GRBs. Both long and short bursts are approximated as uniformly random on this plane. **Lower-right:** SNe during the Fermi period (2008 - 2017). Similar to the previous cases: SNe detections increase over passing years and there is annual periodicity; very large increase of SNe in the year 2015 (MJD $\approx$ 57.000) and 2016 is present and it is mostly due to SNe Ia while not so much SNe Ib/c. Additionally, there is clustering of Ia SNe in the plot as many have very similar latitude in a relatively short period of time (around years 2015, 2016). **Lower-left:** Fermi-GBM GRBs. Both long are approximated as uniformly random on this plane.

5.3.3 Generating random positions and dates

Random positions of GRBs in the sky are generated by generating random RA and Dec. RA is generated as a uniformly random number (with several digit decimal precision) between $0 \leq RA < 360$.

If Dec (δ) was generated as a uniformly random number, GRBs would be uniformly random on RA-Dec flat plane but on the sky they would concentrate toward the poles. To generate Dec it has to be taken into account that with $|\delta| \to 90°$, the area of the sky shrinks as $\cos\delta$. So, δ should be generated as random numbers with $\cos\delta$ dependency. Since many random number generators generate uniformly random numbers (or non-uniform but corresponding to Poisson, Gauss, and other famous distributions), in order to generate random numbers in a range $x \in [x_{min}, x_{max}]$ with certain $f(x)$ dependency, it has to be obtained from uniform random numbers. To do this, an integral function $F(x) = \int f(x)\,dx$ is needed; then random uniform numbers in the range $x_u \in [F(x_{min}), F(x_{max})]$ should be generated; then each of these numbers should be transformed to $x = F^{-1}(x_u)$ (inverse function); then the random numbers x will be in the range $x \in [x_{min}, x_{max}]$ with $f(x)$ dependency. In the case of $\delta \in [-90, 90]$ with $\cos\delta$ dependency, random numbers in the range [-1, 1] should be generated (with enough decimal precision), then they should be transformed as $\arcsin$. Or, with trigonometry equivalence, they can be transformed as $\arccos$ and then subtracted with 90.

GRB dates (as MJD) are generated as uniformly random numbers in the range from minimal GRB date to maximum (for the GRBs in question: Fermi or BATSE - long or short).

Of course, number of generated RA, Dec, and dates, matches the number of original GRBs in question.

5.3.4 Removing same GRBs

It can happen that some connections share the same GRB but different SNe, especially when time window gets large enough and/or SNe of the type are numerous. This is a physical impossibility. SNe are determined with arc-second precision which means they are definitely coming from different places, and for them to share an event which happens at the same time is not possible. So, the connections which have a GRB that is already in another connection with a different SN, are ignored by the script. This reduces the number of random connections and decreases the *noise* making physical connections stand out more.

It can happen (when finding connections with original GRB set) that a physical GRB-SN connection exists and that GRB is also randomly connected to other SN(e). Since the number of connections for different time windows is a cumulative function, it doesn't matter which connections are excluded. The number of connections vs. time will remain the same whether real connection remains or random one remains. Of course, if a closer examination of all GRB-SN connections is done in order to identify possible physical ones, then all the connections should be shown.

It can also happen that the same SN has more GRBs. Although there is no evidence of this, it is not a physical impossibility like the previous case. GRBs have a large error radius and some may come from the same source. For example, soft gamma repeaters, although not real GRB, are flashes of gamma-rays coming from the same source. So, these connections are not excluded.

Regarding exclusion of *different SNe - same GRB* connections (dSN-sGRB), it should

be noted that this also reflects on the distribution of number of random connections. For simplicity, if both (cataloged) SNe and GRBs were uniformly randomly distributed in the sky and occurred at a constant rate, the distribution of connections would follow Poisson statistics. From just statistical point of view, the dSN-sGRB connections are valid just as any other and they, with other connections, make all the connections which follow Poisson statistics. If dSN-sGRB connections are excluded, then the remaining connections would not follow Poisson statistic even if both GRBs and SNe are uniformly randomly distributed on the sky and time axis. The specific distribution with non uniformly random SNe is also changed by exclusion. This is taken care of by excluding the dSN-sGRB connections for all random sets of GRBs.

5.3.5 Time windows

The general assumption here is that GRBs and SNe go off approximately at the same time which is based on samples of known long GRB-SN Ib/c connections. Detection of SN happens after the explosion (usually one to several weeks). With detailed observation of the photometry and spectrum, explosion dates can be estimated but this is not certain and catalogs mostly contain dates of detection. So, in any case, SN detection should happen after the GRB and time window (TW) corresponds to the time after GRB(s) has happened. As the TW increases, more connections are added to existing ones. In this way a cumulative function of number of connections and CL is obtained.

SN dates are rounded up to the beginning of a certain day (MJD has no decimal points). GRB dates have a decimal point which points to the time of the day they occurred. So, SNe happening on the same day as GRBs will actually have a lower date by a fraction of a day. These SNe are also included in the TW - this is mainly done because most of SN dates of known GRB-SN have been fixed to the day their GRB happened although they might have been discovered after several days.

Based on known long GRB-SN Ib/c, physical connections are contained in the smaller TW and as the TW increases, they become outnumbered by random connections. So, as the TW increases CL should drop but it will not get smooth due to oscillation of random connections. Regarding the number of TWs, the more there are the higher the precision (after 100 days or more). However, the more there are the higher probability that one of them, due to simple chanse, will reach very high CL and this might be mistaken for some new type of physical connection. TWs are chosen in the similar fashion as in the work of 2014: TW = [10days, 20d, 30d, 40d, 50d, 60d, 80d, 100d, 120d, 240d, 360d, 480d].

5.3.6 Example of changes to distributions for long Fermi GRBs and Ia SNe

To demonstrate how non uniform randomness of SNe and exclusion of dSN-sGRB connections affects the distribution of number of connections N (for all TW), 4 cases are considered (Table 5.6). SNe Ia were used in the time interval of Fermi GRBs, since it is clear for them. For each of 4 cases, $n = 1000$ random GRB sets were used. The $\langle N \rangle$ is average number of connections for a given TW; the $\sigma_N^2 = \sum_1^n \left(N - \langle N \rangle\right)^2/(n-1)$ is standard deviation[24] of the $n = 1000$ sample for a given TW.

In first case one uniformly random (u-random) set of SNe was generated and dSN-sGRB connections are included. Since SNe are u-random the N (for a given TW) should follow Poisson distribution. Poisson distribution approximates to Normal distribution for

[24] Sample variance.

TW (days)	10	20	30	40	50	60	80	100	120	240	360	480
u-random SNe including dSN-sGRB connections												
$\langle N \rangle$	39.0	74.5	110.	145.	180.	215.	285.	354.	422.	822.	1206.	1573.
σ_N	6.13	8.47	10.5	12.1	13.2	14.5	16.7	18.4	20.4	28.3	34.6	40.8
$\sqrt{\langle N \rangle}$	6.25	8.63	10.5	12.1	13.4	14.7	16.9	18.8	20.6	28.7	34.7	39.7
u-random SNe excluding dSN-sGRB connections												
$\langle N \rangle$	37.6	69.5	99.4	127.	153.	179.	225.	267.	305.	477.	594.	679.
σ_N	5.79	7.70	9.11	10.2	10.8	11.4	12.5	13.3	13.9	14.8	15.5	15.9
$\sqrt{\langle N \rangle}$	6.13	8.34	9.97	11.3	12.4	13.4	15.0	16.3	17.5	21.8	24.4	26.1
Original SNe including dSN-sGRB connections												
$\langle N \rangle$	39.0	74.3	110.	145.	180.	215.	286.	356.	425.	837.	1234.	1623.
σ_N	7.61	11.6	15.3	18.1	21.4	24.4	30.4	35.7	40.4	65.7	88.1	110.
$\sqrt{\langle N \rangle}$	6.25	8.62	10.5	12.0	13.4	14.7	16.9	18.9	20.6	28.9	35.1	40.3
Original SNe excluding dSN-sGRB connections												
$\langle N \rangle$	32.0	55.9	77.1	96.1	114.	131.	162.	191.	218.	358.	456.	527.
σ_N	5.41	7.07	8.44	9.03	9.82	10.2	10.9	11.6	12.2	14.6	15.7	16.1
$\sqrt{\langle N \rangle}$	5.66	7.47	8.78	9.80	10.7	11.4	12.7	13.8	14.8	18.9	21.4	23.0

Table 5.6: Details are given in the text.

larger values of expected value[25]. So, if the distribution is Poisson, the σ_N should be equal to $\sqrt{\langle N \rangle}$ which is the value of standard deviation for Poisson distribution. As can be seen in the first case, these values are very close.

In the second case, one u-random set of SNe was generated and dSN-sGRB connections are excluded. It can be seen that σ_N and $\sqrt{\langle N \rangle}$ have different values compared to previous case (especially for large TW when dSN-sGRB are more numerous). So, the distribution cannot be considered Poisson when excluding dSN-sGRB connections even though SNe (and GRBs) are u-random.

In the third case, original set of SNe was used and dSN-sGRB connections are included. It can be seen that σ_N is about twice larger than $\sqrt{\langle N \rangle}$.

In the fourth case, original set of SNe was used and dSN-sGRB are excluded. It can be seen that σ_N and $\sqrt{\langle N \rangle}$ have different values, and different proportions than in the previous case.

It can also be seen how for large number of Ia SNe, excluding dSN-sGRB drastically lowers number of connections, especially for larger TWs. The u-randomness of SNe and inclusion/exclusion of dSN-sGRB affects the number of connections, and at a different level for different TWs.

Note: Running simulation for any given case again, changes each of the values on the order of 1%.

For other types of SNe this differences are lesser because of their smaller number which makes their non-u-randomness less clear.

5.4 Analysis of long GRB - SN Ib/c connections, 2017

Here an analysis similar to the one of 2014 will be repeated with extended catalogs of GRBs and SNe (as defined in section 5.1) and new statistical approach (section 5.3). The confidence levels (CL) for long Fermi and BATSE bursts are presented in Table 5.7 and Figure 5.5.

The CLs in Figure 5.5 are also presented as $(1 - CL/100)^{-1}$. For example, increase of CL from 50 to 59 practically doesn't change anything, while the same amount of increase

[25] Usually the limit in practice is set ≥ 20.

TW (days)		10	20	30	40	50	60	80	100	120	240	360	480
Fermi													
Ib/c	N_0	10	12	17	20	22	26	34	43	52	95	138	157
	$\langle N \rangle$	4.77	9.04	13.14	17.13	21.10	25.01	32.62	39.97	47.16	87.98	123.8	154.1
	CL (%)	97	81	83	73	55	56	58	67	76	78	92	59
Ib/c*	N_0	6	7	12	15	17	21	29	38	47	90	133	152
	CL (%)	65	20	34	26	15	18	23	35	46	58	81	41
Ia	N_0	29	49	71	80	104	119	143	179	208	319	436	501
	$\langle N \rangle$	32.04	56.14	77.28	96.55	114.46	131.2	162.3	191.1	218.3	358.5	456.7	527.7
	CL (%)	27	14	21	3.1	14	11	4.2	15	20	0.4	10	5.4
IIn	N_0	2	3	5	7	9	11	11	13	13	34	60	72
	$\langle N \rangle$	2.33	4.41	6.51	8.58	10.60	12.62	16.58	20.43	24.20	46.01	66.36	85.05
	CL (%)	32	18	22	24	27	28	5.5	2.9	0.4	2.2	19	5.4
IIb	N_0	2	4	4	5	7	11	13	17	20	40	60	72
	$\langle N \rangle$	1.72	3.30	4.85	6.41	7.93	9.43	12.41	15.34	18.26	34.76	49.90	63.40
	CL (%)	49	59	28	23	32	66	53	63	63	80	92	86
IIP	N_0	8	12	18	23	33	39	46	58	66	117	157	207
	$\langle N \rangle$	6.10	11.49	16.71	21.87	26.89	31.81	41.43	50.80	59.82	109.90	152.4	187.1
	CL (%)	73	53	59	57	86	89	74	84	78	76	65	95
BATSE													
Ib/c	N_0	1	1	2	2	2	2	2	2	2	6	9	16
	$\langle N \rangle$	0.338	0.635	0.94	1.25	1.56	1.86	2.47	3.08	3.69	7.61	11.97	16.65
	CL (%)	71	53	76	65	54	45	29	18	12	22	15	40
Ib/c*	N_0	0	0	1	1	1	1	1	1	1	5	8	15
	$\langle N \rangle$	0	0	39	29	21	15	7.9	4.2	2.3	12	8.6	30
Ia	N_0	3	9	9	10	15	17	22	27	29	58	76	101
	$\langle N \rangle$	2.80	5.27	7.65	9.89	12.19	14.43	18.78	23.05	27.27	53.22	77.54	98.79
	CL (%)	47	92	64	47	75	71	74	77	60	74	41	58
IIn	N_0	0	0	0	0	1	2	2	2	2	6	8	12
	$\langle N \rangle$	0.289	0.565	0.841	1.11	1.37	1.63	2.17	2.69	3.22	6.46	9.78	13.02
	CL (%)	0	0	0	0	26	52	36	25	17	37	24	35
IIb	N_0	0	0	0	0	0	1	1	1	2	2	3	4
	$\langle N \rangle$	0.039	0.074	0.111	0.145	0.183	0.214	0.283	0.349	0.417	0.830	1.29	1.86
	CL (%)	0	0	0	0	0	81	76	71	93	79	86	88
IIP	N_0	1	1	1	1	1	1	1	1	1	3	5	7
	$\langle N \rangle$	0.142	0.278	0.396	0.528	0.656	0.780	1.04	1.30	1.57	3.10	4.72	6.54
	CL (%)	87	77	67	59	52	46	35	26	20	40	48	52

Table 5.7: Number of original connections N_0, average number of connections $\langle N \rangle$ for $n = 10.000$ random GRB sets, Confidence level CL defined as percentage of times random GRB set gave number of connections N lesser then the original N_0. The decimal places in $\langle N \rangle$ correspond to error estimated as $\sigma_N/\sqrt{n}$. Repeating the process for another $n = 10.000$ gives the $\langle N \rangle$ in the range of an estimated error and CL changes about $\pm 1\%$. The Ib/c* corresponds to original connections minus the known connections. **Fermi:** Number of Fermi long bursts is 1640. Number of SNe in the Fermi period: Ib/c - 273; Ia - 2203; IIn - 133; IIb - 97; IIP - 347. **BATSE:** Number of BATSE long bursts is 1536. Number of SNe in the BATSE period: Ib/c - 45 (62); Ia - 453 (575); IIn - 38 (45); IIb - 5 (7); IIP - 19 (26). Numbers in parentheses correspond to BATSE period of time plus 480 days, so that the last BATSE GRBs don't have a cutoff with for larger TWs.

from 90 to 99 means 10 times higher probability. The $(1-CL/100)^{-1}$ value gives the right proportions between different TWs and types. It is actually the number of random GRB sets needed to expect to obtain value N_0 or higher - once.

Examining Figure 5.5 it can be seen that Fermi GRB and Ib/c SNe have a high significance for TW = 10d. This is due to 5 known connections, 4 of which have SN dates that have been set to the date of the corresponding GRB. The CL for Ib/c without known connections do not show high statistical significance. For BATSE the relatively high CL for TW = 10d is due to single connection which is also the only known BATSE connection. Without it the CL falls even less. For BATSE different types for different TWs have a CL higher than Ib/c for TW = 10d. This is probably just a coincidence since there are many CLs with many TWs. It is interested to note, however, that types IIb and IIP have a relatively high significance for TW $\sim$ 10d - 500d for both Fermi and BATSE. It would be interesting to examine these connections in detail in some future work. Here the focus will be on Ib/c connections. Evan though CLs without known connections do not show high significance doesn't mean there are no physical connections. In the coming text all connections with Ib/c SNe within TW = 20d, 30d will be examined in detail.

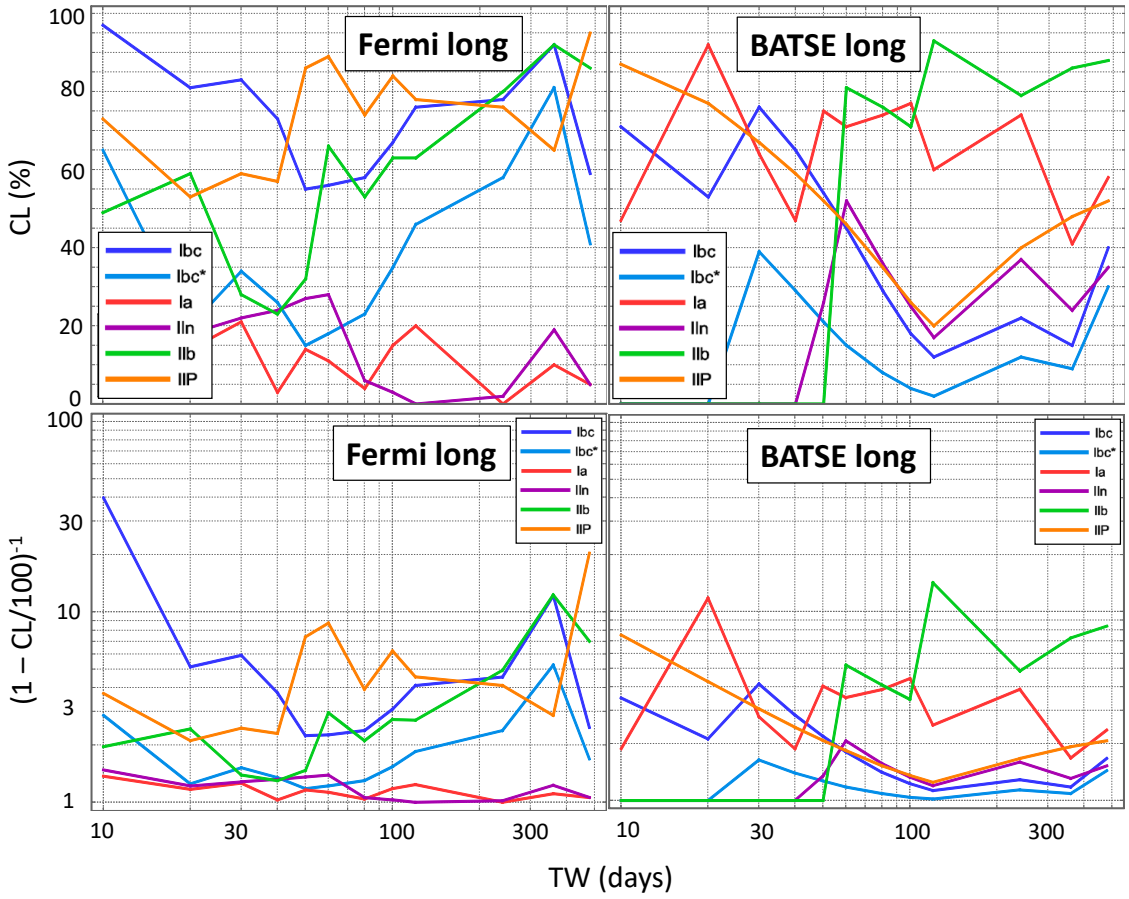

Figure 5.5: Confidence levels from the Table 5.7.

5.4.1 The sample of Ib/c connections

Unlike the case of 2014, the TW = 30d was chosen, not based on CLs, but on the fact that SN may be discovered up to several weeks after maximum and maximum time occurs 10-15 days after the SN-explosion/GRB. To discriminate between coincidences and possible physical connections, SN will be examine further, mainly the time of the explosion and maximum, and absolute magnitude at these phases. The SN explosion should, of course, match the GRB date. Majority of known GRB-SNe have a higher luminosity (absolute magnitude) then ordinary Ib/c SNe, and a broader spectrum lines due to higher expansion velocity of the ejecta. SN 1998bw is taken as a typical representative of this class. Within TW = 30d there are 17 connections, including 5 already known: GRB 091127 – SN 2009nz, GRB 101219B – SN 2010ma, GRB 130215A – SN 2013ez, GRB 130427A – SN 2013cq, GRB 130702A – SN 2013dx. The 12 new ones are presented in Table 5.8.

Note: In the Table 5.1 there are 7 known connections detected by Fermi. The two missing connections: SN iPTF14bfu (- GRB 140606B) is not present in the SNe catalogs used here, and GRB 081007 (- SN 2008hw) is not present in the Fermi GRB catalog although it was reported in GCN 8369 (Bissaldi et al., 2008). The SN iPTF14bfu can be taken into account in the statistics, however, there are also many other non-GRB–SNe which are not in the catalogs. Similar argument goes for the second case. The (random) GRB 110911A – SN 2011gw connection from 2014 work is not present here

GRB	ΔT (days)	SN	z	Phase	M (mag)	References
090320B	0.2	2009di	0.13		-20.1	(Drake et al., 2009b)
090426B	8.9	2009em	0.0058	max + 1m	-15.5	(Monard, 2009b; Folatelli and Morrell, 2009; Navasardyan and Benetti, 2009b)
100210	28.9	2010ak	0.037	max + 2w	-17.9	(Rex et al., 2010; Challis et al., 2010)
110307	27.0	2011bm	0.022	pre-max	-17.9	(Gall et al., 2011; Valenti et al., 2012)
120121B	0.2	2012ba	0.017	pre-max	-18.5*	(Pignata et al., 2012b)
130406	2.6	2013bv	0.06	max + 1w	-18.4	(Benitez et al., 2013; Kamble et al., 2013)
140831	23.6	2014dj	0.017	max + 2d	-17.4	(Tomasella et al., 2014)
150411	14.0	2015K	0.010	max + 1m	-16.9	(Andrews et al., 2015)
151003	21.3	OGLE15rb	0.028	max	-14.6	(Kangas et al., 2015)
160303	9.8	2016bau	0.0039	pre-max	-13	(Granata et al., 2016)
160308	22.3	2016bll	0.019	max	-16.7	(Rui et al., 2016)
160816	4.6	2016fhn	0.025	max + 1m	-15.6	(Terreran et al., 2016)

Table 5.8: Twelve potential Fermi long GRB – SN Ib/c connections within TW = 30d. The ΔT corresponds to time since GRB occurrence (up to 0.1d precision) to SN detection (which is rounded up to the beginning of the day of detection). Both dates are in MJD format. Only for the case of 120121B – 2012ba the exact times of the day were used since both occurred on the same day, otherwise ΔT would have been negative. The $Phase$: whether SN was in the rising, maximum, or post maximum phase at the time of detection. Day is marked by d, week by w and month by m. The M is absolute magnitude at the time of detection of SN, except for SN 2012ba where it corresponds to maximum. References correspond to information regarding SNe. The values $Phase$ and M are approximate.

due to exclusion of GRB 110911A because of its huge error radius.

Based on SN phase, an explosion date can be estimated and compared to GRB date. In this way SN 2016fhn, SN 2015K, SN 2013bv, SN 2011bm, SN 2009em might be excluded since their estimated explosion date greatly differs from GRB date. Specifically: SN 2009em was also excluded in the previous work; SN 2013bv was recognized as a broad lined SN similar to SN 1998bw, however the estimated explosion date doesn't match the GRB one; SN 2011bm was studied in more detail and its explosion date was constrained between 19d and 22d after corresponding GRB; SN 2016fhn and SN 2015K are excluded.

Next, the absolute magnitude (luminosity) might be used. SN 2009di was detected no more than 2d after corresponding GRB. Absolute magnitude of -20 is very high, even higher than the one of SN 1998bw ($M \approx$ -18.5, -19) at maximum (15d - 20d after GRB). If this SN was connected to GRB 090320B, it would imply that it was very young during detection and the magnitude would be to high for this phase. This SN was excluded also in the previous work. Supernova OGLE15rb had an absolute magnitude of -14 during maximum which makes it a weak SN and not a good candidate for GRB-SN. SN 2016bau has a very small magnitude, even for a young rising phase, and is excluded. SN 2016bll has a magnitude at maximum of -16.7, which is not in the range of more luminous GRB-SNe, and makes it an unlikely candidate.

SN 2012ba was analyzed in previous work and was considered as a good candidate for being physically connected to GRB 120121B.

GRB 100210 – SN 2010ak

Finally, only SN 2010ak is left. This SN was discovered on March 11, 2010 with apparent magnitude of 18.2. With the distance of $z = 0.037$, which makes absolute magnitude of -17.9. On March 12 (1 day later), cross-correlation with a library of supernova spectra indicated that 2010ak best matches a type-Ic supernova at a phase of roughly two weeks past maximum light. This would put its explosion date around the time of corresponding GRB 100210 (February 10, 2010). Also, absolute magnitude of -17.9 at two weeks past maximum would imply higher luminosity at maximum, similar to the one of SN 1998bw.

Although SN was classified as type Ic and not as broad lined type Ic, it should be noted that, like it was explained in the previous work, spectrum was obtained 2 weeks past maximum, and even if the pre-maximum spectra showed significantly broader lines, than observed in the post-maximum spectra, this difference might have vanished after maximum. Additionally, spectrum was obtained with low signal to noise ratio.

GRB 100210 was detected by the 2nd and 3rd NaI[26] detectors (n1 and n2)[27] of Fermi-GBM instrument. Emission in the BGO[28] detector is lost in the background noise. Software rmfit was used to view and examine the lightcurves. Due to low signal to noise ratio, it is hard to note whether or not lightcurve is a composed of a single peak or multiple peaks. The T_{90} duration in the catalog was reported to be 29s. The main emission is from $T_0 - 4s$ to $T_0 + 6s$ with T_0 being the burst trigger time. The TTE files of triggered detectors, as well as corresponding detector responses, were obtained. With various *ftool* software[29], TTE files were used to obtain spectrum (with background and responses) with these characteristics: time range in the main burst interval; energy channels were binned to provide enough signal to noise ratio for most of energy bins, lowest and highest energy channels were excluded as well as ones around *K-edge*[30] at 33 keV. The spectrum files were fit with *Xspec* software[31]. The results of the fit with power-law – exponential-cutoff model are: cutoff energy $E_c = 240^{+320}_{-100}$ keV and power-law index $\alpha = 1.25^{+0.18}_{-0.20}$ with 1σ errors. The fluence in the 10 keV – 1000 keV range for the given spectral result is 2.1×10^{-6} erg cm^{-2} which corresponds to the value given in the catalog. Assuming $z = 0.037$ redshift for this burst, the isotropic energy would be $E_{iso} \approx 7 \times 10^{48}$ erg, and peak luminosity (at 1s interval) at $L^p_{iso} \approx 1 \times 10^{48}$ erg/s. This is higher than the one of GRB 980425 (SN 1998bw) $E_{iso} \approx 1 \times 10^{48}$ erg, but still in the low luminosity range.

The position of GRB 100210 (RA = 244.380°, Dec = 16.0800°) is 2.48° away from SN 2010ak (RA = 242.708°, Dec = 17.9767°) with error radius of 6.58°.

The evidence of physical connection GRB 100210 – SN 2010ak is strong as in the case of GRB 120121B – SN 2012ba, and it lies within $z \leq 0.2$ with E_{iso} significantly smaller than the ones for known connections. Like in the previous work, the rate can be estimated. The threshold redshift and volume for detection of GRB 100210 are $z_{max} = 0.052$ and $V_{max} = 0.047$ Gpc^3. With period of observation of T = 8 years, the rate would be $\rho_0 = 3.8^{+14.2}_{-3.6}$ Gpc^{-1} yr^{-1} where the errors are upper and lower limit determined from the 95% statistic for a single count. This is very different than the one obtained in the previous work $\rho_0 = 77^{+289}_{-73}$ Gpc^{-1} yr^{-1} but the huge ranges do overlap. If the difference is real than it could mean that SN-GRB 100210 belongs to a different class of GRBs, i.e. that it is a low energetic end of classical GRBs and not in a special class of low energetic GRBs like SN-GRB 120121B was presumed to be. On the other hand, if SN-GRB 100210 does belong with SN-GRB 120121B, then the rate of occurrence may be estimated from both cases. Since the maximum volumes are different, the higher one will be taken into account, and the number of detections will be $N_{LE} = 1 + 1 \times (V_{max,2}/V_{max,1}) = 6.5$. The

[26] Sodium iodide detectors with energy around 10 keV - 800 keV. There are 12 of them positioned on all sides of the detector. More information: `https://fermi.gsfc.nasa.gov/ssc/data/analysis/documentation/Cicerone/Cicerone_Introduction/GBM_overview.html`

[27] The first detector is named n0.

[28] Bismuth germanate detectors with energy around 500 keV - 40 MeV. There are 2 of them positioned on opposite sides of the detector.

[29] `https://heasarc.gsfc.nasa.gov/ftools/ftools_menu.html`

[30] `https://fermi.gsfc.nasa.gov/ssc/data/analysis/GBM_caveats.html`

[31] `https://heasarc.gsfc.nasa.gov/xanadu/xspec/`

corresponding rate is $\rho_0 = 25^{+54}_{-20}$ Gpc^{-1} yr^{-1} with errors same as before, but for a count of 2. Taking into account presumed beaming of $f_b^{-1} \sim 10$ the rate becomes $\rho_0 = 250^{+540}_{-200}$ Gpc^{-1} yr^{-1} which would put it even closer to the values of $\rho_0 = 380^{+620}_{-225}$ Gpc^{-3} yr^{-1} in (Guetta and Della Valle, 2007), 325^{+352}_{-177} Gpc^{-3} yr^{-1} in (Liang et al., 2007), and 230^{+490}_{-190} Gpc^{-3} yr^{-1} in (Soderberg et al., 2006b).

BATSE GRB – SNe connections

There are just two connection between BATSE GRBs and SNe in TW = 30d (even up to TW = 120d). The one is a known and prototypical connection of GRB 980425 - SN 1998bw. The SN 1998bw (RA = 293.764°, Dec = -52.8458°) was detected, still in rising phase, around 2 days after GRB 980425 (RA = 291.910°, Dec = -53.1100°) which was 1.1° away from the SN and had an error radius of 2.3°.

The other connection is between GRB 961218A (RA = 97.7500°, Dec = -21.7300°) and SN 1997B (RA = 88.2624°, Dec = -17.8732°). GRB was 9.7° away from SN and had an error radius of 12.8°. SN 1997B (Gabrijelcic et al., 1997) was detected on January 13, 25 days after GRB. One day later inspection of a fully-reduced spectrum confirms SN 1997B to be like a type-Ic supernova, about 10 days past maximum. This would put its explosion date around the time of the GRB. The magnitude at this phase was around 16.5, and with redshift of $z = 0.010$ the absolute magnitude would be -16.7, which is a low value for a GRB-SN, 10 days after maximum. This connection is probably random.

5.5 Analysis of short GRB - SN IIn connections

Same analysis with CLs is applied to short GRBs. The CLs for short Fermi and BATSE bursts are presented in Table 5.9 and Figure 5.6.

TW (days)		10	20	30	40	50	60	80	100	120	240	360	480
							Fermi						
Ib/c	N_0	3	6	9	10	13	14	15	20	22	41	51	65
	$\langle N \rangle$	2.32	4.35	6.29	8.15	10.02	11.81	15.22	18.56	21.77	39.65	54.28	65.85
	CL (%)	59	73	82	70	80	70	43	60	49	57	27	42
Ia	N_0	11	25	32	42	50	56	68	77	91	131	152	170
	$\langle N \rangle$	14.48	24.41	32.77	40.01	46.52	52.44	63.16	72.82	81.78	124.16	148.85	164.37
	CL (%)	13	52	41	61	70	70	75	70	89	80	63	75
IIn	N_0	1	3	4	5	7	8	12	14	16	28	34	43
	$\langle N \rangle$	1.14	2.15	3.14	4.13	5.09	6.04	7.91	9.71	11.47	21.43	30.39	38.17
	CL (%)	32	63	61	60	75	74	90	89	88	91	74	79
IIb	N_0	0	0	0	1	3	4	5	8	9	20	32	34
	$\langle N \rangle$	0.848	1.62	2.37	3.11	3.84	4.56	5.99	7.36	8.70	16.30	23.15	29.14
	CL (%)	0	0	0	4.3	26	33	28	54	49	80	96	81
IIP	N_0	2	4	9	10	14	19	25	26	29	50	68	78
	$\langle N \rangle$	2.94	5.51	7.98	10.33	12.64	14.88	19.15	23.22	27.15	48.01	64.48	76.84
	CL (%)	20	19	59	42	62	84	90	71	63	61	68	54
							BATSE						
Ib/c	N_0	1	1	1	1	1	1	2	2	2	6	10	17
	$\langle N \rangle$	0.353	0.684	0.99	1.31	1.64	1.96	2.59	3.23	3.86	7.85	12.19	16.76
	CL (%)	70	51	37	27	19	14	27	16	10	20	23	49
Ia	N_0	0	5	6	6	7	8	11	12	17	42	62	76
	$\langle N \rangle$	2.81	5.22	7.53	9.72	11.83	13.92	17.93	21.82	25.63	48.37	68.09	83.80
	CL (%)	0	40	24	7.9	5.0	3.1	2.8	0.6	2.4	14	19	14
IIn	N_0	2	3	3	5	5	6	7	8	8	9	11	13
	$\langle N \rangle$	0.303	0.582	0.861	1.138	1.416	1.692	2.244	2.801	3.360	6.691	10.13	13.37
	CL (%)	96.3	97.9	94.4	99.4	98.6	99.3	99.3	99.2	97.9	77.2	56.7	41.9
IIb	N_0	0	0	0	0	0	0	0	0	0	1	1	1
	$\langle N \rangle$	0.043	0.080	0.117	0.149	0.187	0.222	0.289	0.362	0.431	0.865	1.35	1.95
	CL (%)	0	0	0	0	0	0	0	0	0	42	26	14
IIP	N_0	0	0	0	0	0	0	0	0	0	2	2	5
	$\langle N \rangle$	0.145	0.273	0.402	0.534	0.661	0.789	1.05	1.32	1.58	3.17	4.84	6.60
	CL (%)	0	0	0	0	0	0	0	0	0	17	4.7	21

Table 5.9: Same properties as in Table 5.7, only for short bursts. For BATSE IIn connections, $n = 100.000$ random GRB sets were used since CLs for some TWs exceed $\mathrm{CL} \geq 99$.

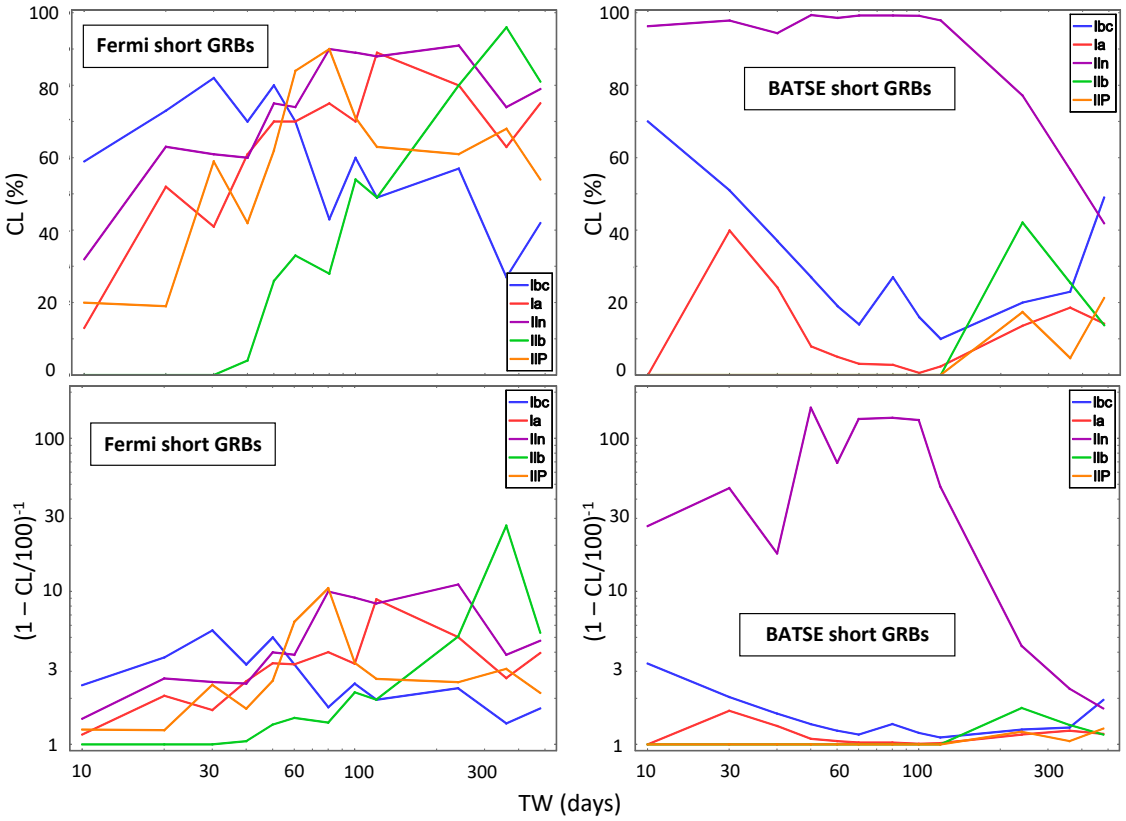

Figure 5.6: Confidence levels from the Table 5.9.

The striking feature of Table 5.9 and Figure 5.6 are very high CLs ($\mathrm{CL} \geq 99$) for type IIn SNe and BATSE short GRBs. For Fermi bursts these SNe have a relatively high CLs in the similar TWs. Another interesting feature is relatively high CLs for IIb and IIP SNe for Fermi bursts. Since similar feature exists for the long bursts, it might imply connections which exist regardless of GRB duration. The relatively high CLs for these two types of SNe exist for BATSE long but not for BATSE short. Reason for this might be due to very low detected number of these types of SNe during BATSE period. Low CLs reflect the probability of physical connection regarding SNe in the catalog, not SNe in total. The possible connection between SNe IIb and IIP with GRBs (long and short) might be interesting to explore in a future work. Here, the possible connection between short GRB and SNe IIn will be further examined.

There are 5 CL cumulative curves for each GRB duration and space mission, which makes total of 20 CLs, each of which has 12 TWs. The BATSE short GRB – IIn is the only one that shows very high CLs but is that expected for 20 cumulative curves? To probe this a 12-point cumulative curve is generated from 48 independent Poisson distributed numbers with the same and large expected value $\lambda = 100$ and then adding them up, so that the ratio between points corresponds to ratios between TWs, i.e. the expected values in a cumulative curve are $[\lambda, 2\lambda, 3\lambda, 4\lambda, 5\lambda, 6\lambda, 8\lambda, 10\lambda, 12\lambda, 24\lambda, 36\lambda, 48\lambda]$. In order to obtain (expect) at least one point with $CL \geq 0.99$ about 20 cumulative curves are needed. In order to obtain a curve with at least 4 points having $CL \geq 0.99$ about 120 are needed. In order to obtain a curve with at least 4 points having $CL \gtrsim 0.993$ (like in the case of IIn CLs) about 200 are needed.

GRB	RA (deg)	Dec (deg)	T_{90} (s)	E_{iso} (erg)	Peak energy (keV)	Error radius (deg)	Distance (deg)	SN	ΔT (days)	RA (deg)	Dec (deg)	z
970308A	166.5	10.6	0.71	6.6×10^{45}	730±310	6.0	4.2	1997bs	37	170.059	12.9721	0.0024
970329B	169.7	8.8	0.46	4.7×10^{45}	400±88	4.9	4.2	1997bs	16	170.059	12.9721	0.0024
970408A	168.0	7.4	0.19	2.0×10^{45}	400±340	9.1	5.9	1997bs	6	170.059	12.9721	0.0024
970430A	259.7	44.9	0.64	3.5×10^{47}	710±260	10.5	10.4	1997cq	32	247.462	39.7556	0.032
970514A	67.6	-60.9	0.64	2.2×10^{48}	350±160	4.1	0.9	1997cy	62	68.228	-61.7160	0.064
971023B	191.4	-36.6	1.02	2.0×10^{46}	420±470	14.9	9.5	1998E	97	202.300	-33.1667	0.008
980501A	223.9	23.4	0.34	1.1×10^{47}	140±57	14.9	12.9	1998ct	59	237.799	21.9433	0.026
991002A	25.2	3.8	1.92	4.6×10^{47}	180±21	2.8	0.9	1999eb	-0.5	25.939	4.2239	0.018

Table 5.10: Sample of 8 BATSE short GRB – SNe IIn within TW = 100d. Column ΔT corresponds to time from GRB to SN detection. In the case of GRB 991002A – SN 1999eb, SN was actually discovered during the same day but before GRB. Peak energy corresponds to peak of the νF_ν spectrum. It was obtained from the BATSE spectral catalog for the power-law-exponential-cutoff model over whole burst duration. Column E_{iso} is calculated from fluence $(20\ \mathrm{keV} - 2\ \mathrm{MeV})$ reported in the spectral catalog for the same model and with assumption of SN redshift.

5.5.1 The sample of BATSE short GRBs – SN IIn connections

The CLs are (very) high from the beginning to the TW = 100d, 120d where $N_0 = 8$ and than it significantly drops in the next TW (TW = 240d) where $N_0 = 9$. The eight potential connections in the interval of TW = 100d are presented in Table 5.10.

SN 1997bs

The first thing to notice are 3 GRBs with similar E_{iso} (assuming the SN redshift) connected to this SN within time period of 40 days. This supernova has been an object of significant study (Van Dyk et al., 2000; Li et al., 2002; Kochanek et al., 2012; Adams and Kochanek, 2015). It is the prototypical supernova impostor - a star that ejects suddenly large amounts of material which interact with previously eject material and this causes optical emission. The optical emission is characterized by narrow Balmer lines superimposed on broader ones in the spectrum which classify them spectroscopically as IIn. The optical emission is generally weaker than standard SN. The nature of these events is such that they evolve on the order of tens of years. The most resent observations and analysis suggests that this SN might have been a real, but sub-luminous, SN (Adams and Kochanek, 2015). It is unclear at this point and more observations and time is needed.

If this SN is indeed a SN impostor, then CLs can be calculated specifically for IIn impostors. There are 38 IIn SNe during BATSE interval of 10 years (48 if additional 480 days are added). There is ambiguity also for other IIn impostor SNe, but if all the potential ones are taken into account (Kochanek et al., 2012; Habergham et al., 2014), then four of them 1997bs, 1999bw, 2000ch, (2001ac) are inside BATSE interval. This reduces number of original connections to just the one of 1997bs $N_0 = [1, 2, 2, 3, ...3]$ and greatly reduces connections from random GRB sets, so the $CL \gtrsim 0.9999$ for $TW = 40d$ when the 3rd burst occurs ($\simeq 100$ more then for all IIn).

In order to probe an event of single IIn SN connected to 3 GRBs, another calculation might involve probability that a single IIn SN has more GRBs connected to it for each TW. The N_0 = [1, 2, 2, 3, ... 3] would be the maximum number of different GRBs a single SN has and so would N for all random GRB sets. In this way CL for TW = 40d is $CL \gtrsim 0.9995$ ($\simeq 50$ more then standard connection with IIn). This means that $CL \geq 0.99$ for IIn doesn't imply that it probably has 3 GRBs connected to one SN, so, these 3-GRB – SN connection is an additional unique feature within very high CLs. In other words, if the $CL \geq 0.99$ was due to pure randomness, than it is more likely that connections would be all single-GRB –

single-SN or maybe have one or more 2-GRB – single-SN connections.

The probability that this specific SN is connected to 3 short GRBs within 40 days can be calculated although question is what does it imply. For example, if there were many, many more SNe so that one would expect a random connection of one SN to 3 GRBs within 40 days, than that SN might be noticed and probability for chance coincidence would be extremely small for that specific SN. If all the SNe within BATSE time (including type I and II) are taken (957 in total), 1997bs still remains only one with triple connection, not just for TW = 40 days but for TW = 480 days as well. The CL for triple connection is $\mathrm{CL} \geq 0.99$ for 40d, 50d, and 60d. This means that CL (regardless of very high CLs for IIn SNe) for having any SN connected to 3 short BATSE GRBs within TW = 40 days is also very high.

Looking at 3 GRBs they have $\mathrm{E_{iso}}$ (fluence) similar to each other. Also their $\mathrm{E_{iso}} \sim 10^{45}$ erg is very low compared to others. This is due to very low redshift of this particular SN. This may be looked from an angle: if the triple connection is random than it is unlikely that it would be with a specific SN with very low redshift. The peak energy is typical of short GRBs. This would put these 3 GRBs in a separate group and away from the long and short GRBs in the $\mathrm{E_p} - \mathrm{E_{iso}}$ plane.

SN 1997cy

Another interesting case is GRB 970514A – SN 1997cy. SN 1997cy was examined in the literature (Germany et al., 2000; Turatto et al., 2000; Silverman et al., 2013; Inserra et al., 2016) while the first two references also covered its possible connection to GRB 970514A which occurred 62 days before. When it was discovered, this SN was the most luminous SN ever and was classified as type IIn. SN was in the post-maximum phase when it was discovered. Later it was understood that this SN is actually a type Ia-CSM SN, i.e. SN Ia which ejecta interacts with circum stellar medium (CSM) previously ejected by the star. The energy from the SN ejecta interacts with slow-moving CSM which causes narrow line from emission from CSM and spectral classification as IIn. The probability of physical connection to the GRB was found to be very likely if the extraordinary nature of the SN is taken into account, i.e. the probability was calculated for just that specific SN (not taking all other SNe into account) (Germany et al., 2000).

Like in the previous case CLs may be calculated only for Ia-CSM SNe. Only two such SNe during BATSE time are 1997cy and 1999E. The $\mathrm{N_0}$ = [0, 0, 0, 0, 0, 0, 1... 1], i.e. only connection with 1997cy exists. The $\mathrm{CL_{80d}} = 0.89$. If SN was discovered around maximum light, i.e. in the lower TW than the CL would be even higher. SN 1999E was found to be possibly connected to GRB 980910 (Rigon et al., 2003). Supernova was detected 125 days after GRB which would put it into TW = 240d. GRB was 4.8° from SN while its error radius was 6.6°. This connection was missed due to lack of $\mathrm{T_{90}}$ parameter for the GRB 980910 and this GRB wasn't included in the analysis. If all the durations are included (2695), than the peaking CLs are $\mathrm{CL_{80d}} = 0.73$ and $\mathrm{CL_{240d}} = 0.76$.

SN 1999eb

The corresponding burst GRB 991002 was observed also by Wind-Konus and BeppoSAX which allowed for a more accurate localization via Interplanetary Network (IPN) localization method. SN 1999eb lies outside 3σ GRB localization region (Pal'shin et al., 2013), therefore this connection is most probably a coincidence and can be excluded from

further examination. Other potential 7 GRBs were not localized by other IPN satellites for which examination has been carried out (Hurley et al., 2005a; Pal'shin et al., 2013; Hurley et al., 2010).

Although GRB 991002A – SN 1999eb is a coincidence connection, doesn't mean it should be excluded from potential connections when calculating CL, i.e. N_0 should not be set to one number lower for affected TWs. The potential connections also include coincidences. The original connection number N_0 was obtained using just BATSE GRB positions and error areas, and average number of random connections $\langle N \rangle$ was obtained from fake GRB sets using just BATSE error areas. During this process CL was obtained. If the given pair is to be excluded from N_0 then also fake GRB sets should be made with IPN-corrected BATSE error areas (for those BATSE GRBs which were detected by other IPN satellites). About quarter to a third of BATSE bursts were localized by IPN and on average reduction in error area was by a factor of 20 for one additional IPN satellite and factor of 87 for 2 satellites (Hurley et al., 2005a). This would produce lower values of $\langle N \rangle$ which would prompt rise in the CL, thereby countering reduction of CL by lower N_0.

Of course that kind of analysis would be more accurate. It is one of the analysis discussed for future work at the end of this chapter.

Still it should be noted that this random connection is present since TW = 10d and affects all the TWs. First random connection is expected to occur at TW = 30d/40d, therefore it can be stated that very high CLs are in part due to higher coincidence connections than would be expected.

Other SNe

For the rest of the SNe - SN 1997cq (Adams et al., 1997; Jha et al., 1997), SN 1997E (Nakano et al., 1997), SN 1998ct (Jha et al., 1998; Schwartz, 1998) - there is nothing in particular about them. They appear to be "ordinary" IIn SNe. Since the possible connection between IIn SNe and GRBs are not confirmed with many direct observations like it was done for Ibc SNe, nothing for certain can be said about explosion dates of possible pairs GRB – IIn SNe, namely do they occur simultaneously, one before the other and how much, and the brightness of SNe. At this point it is hard to further probe these 3 possible connections.

5.5.2 Fermi short GRB – SN IIn connections

From Table 5.9 and Figure 5.6 the IIn CLs are relatively high $\mathrm{CL} \simeq 0.90$ for TW = 80d, 100d, 120d, 240d. Time window TW = 240d has 28 unique pairs and 33 pairs in total. Several GRBs are connected to two or more SNe. There are also several connections with one SN and two GRBs, but this is expected given the sample of SNe and GRBs. Out of numerous connections 3 SNe stand out.

Supernova 2011A was studied in more detail (de Jaeger et al., 2015). It appears to be SN impostor but it cannot be determined for certain. It has special characteristics, such as double plateau in the LC, only observed before in SN 1997bs. Explosion date is estimated, with uncertainty, to be about 50 days before discovery. The corresponding GRB 101031 occurred 62 days before SN discovery. The position of GRB (RA = 184.12°, Dec = -7.47°) is 13.0° away from the SN (RA = 195.255°, Dec = -14.5263°) and GRB error radius is 16.1°. The burst had a duration of $\mathrm{T}_{90} = 0.38$ s. Assuming SN redshift $\mathrm{z} = 0.0089$ the GRB isotropic energy would be $\mathrm{E}_{\mathrm{iso}} \approx 4 \times 10^{46}$ erg and peak energy $\mathrm{E}_{\mathrm{p}} \sim 100$ keV.

Supernova 2011jb (Drake et al., 2011; Silverman et al., 2013) is a Ia-CSM. Discovery occurred about 40, 50 days after maximum. The corresponding GRB 110923 occurred 65 days before SN discovery. The position of GRB (RA = 181.4°, Dec = -1.6°) is 18.5° away from the SN (RA = 174.27°, Dec = 15.471°) and GRB error radius is 22.9°. The burst had a duration of $\mathrm{T}_{90} = 1.66$ s. Assuming SN redshift $\mathrm{z} = 0.084$ the GRB isotropic energy would be $\mathrm{E}_{\mathrm{iso}} \approx 2 \times 10^{48}$ erg and peak energy couldn't be estimated due to low fluence.

The CLs with just IIn impostors or just Ia-CSM subtypes doesn't change much with respect to CLs for all IIn SNe.

Supernova 2010mc was studied in more detail (Ofek et al., 2013; Smith et al., 2014). It is an "ordinary" IIn SN, however, it is a very interesting case because it had a pre-explosion episode which started to occur about 40 days before SN discovery (discovery date is the explosion date). If this episode existed even before, than its luminosity was smaller and couldn't be detected. The episode is defined by a month-long bump which emitted at least $\mathrm{E} \sim 6 \times 10^{47}$ erg. The main explosion emitted $\mathrm{E} \sim 3 \times 10^{49}$ erg. The analysis suggests that the pre-explosion episode, which occurred before SN explosion, was an outburst of material $\sim 10^{-2}\ M_{\odot}$ at a velocity of 2000 $\mathrm{km\ s^{-1}}$. Shortly after the SN explosion, this ejected material was engulfed by the SN ejecta. The GRB 100706 occurred 44 days before SN detection/explosion (7 days before the pre-explosion bump). Another burst connected to this SN, GRB 100417, occurred 124 days before SN explosion, and another short one GRB 090118, 590 days before.

SNe IIn with pre-explosion activities

With improvements of optical instruments in the last decade, it became possible to detect pre-explosion activities from SNe, like SN 2010mc for example. There are still very few of these kinds of discoveries and they all involve SNe IIn. With the possible connection of GRB related to SN 2010mc and its pre-explosion episode, it is interesting to look for other possible bursts connected to such SNe (Table 5.11).

Some SNe don't have an IAU name. These are marked by the discoverer and their observational programs: "PTF" (Palomar Transient Factory), "LSQ" (La Silla Quest), "SNhunt" (Catalina Real-Time Transient Survey). The references for these transients are: 2010mc [a.k.a. PTF 10tel] (Ofek et al., 2013); PTF 10bjb, PTF 10weh, 2011ht, PTF 12cxj (Ofek et al., 2014); 2009ip (Margutti et al., 2014; Smith et al., 2016); LSQ13zm (Tartaglia et al., 2016); SNhunt248 (Mauerhan et al., 2015); 2015bh [a.k.a. SNhunt245] (Elias-Rosa et al., 2016; Thöne et al., 2017). The date column corresponds to start of the LC rise of the strongest peak which in most cases is considered as final SN explosion. For SN 2009ip this actually happened in the year 2012, i.e. SN 2009ip was a SN impostor. The column $\Delta\mathrm{T}$ is the period of time before *date* when the pre-explosion activity started. The $\delta\mathrm{t}$ is the duration of this activity. The distance is the one between SN and GRB. The $\Delta\mathrm{T}$ in the GRB part of the table is the period of time before *date* when the GRB occurred. The $\mathrm{N}_{\mathrm{exp}}$ column is the expected random number of short Fermi GRBs within the $\delta\mathrm{t}$ period which encompass SN position with their error radius.

There are uncertainties in these parameters, especially $\Delta\mathrm{T}$ and $\delta\mathrm{t}$ for SNe. These two depend on observation, binning of LCs, and other analysis procedures. In some cases it is also not clear whether or not the explosion corresponds to final explosion or to another SN impostor event. Some optical transients were always detectable due to their large star luminosity and they showed variations throughout the years, and in these cases it might not be clear whether an event was a pre-explosion outburst or a large variation in star

SN	Date	ΔT (days)	δt (days)	RA (deg)	Dec (deg)	Distance (deg)	GRB	RA (deg)	Dec (deg)	Error radius (deg)	ΔT [GRB] (days)	N_{exp}
PTF 10bjb	2010-05-10	100	100	192.4	-10.8							0.079
2010mc	2010-08-20	40	40	260.4	+48.1	3.7	100706	255.2	+46.9	12.5	45	0.032
PTF 10weh	2010-09-14	100	50	261.7	+58.9	8.5	100417	261.3	+50.4	9.5	150	0.12
2011ht	2011-09-26	200	200	152.0	+51.8							0.16
PTF 12cxj	2012-04-16	12	7	198.2	+46.5							0.0055
PTF 12cxj	2012-04-16	710	15	198.2	+46.5	8.6	100411	210.6	+47.9	31.7	736	0.056
2009ip	2012-09-23	60	60	335.8	-28.9	19.5	121014	320.4	-44.1	22.7	-12	0.095
LSQ13zm	2013-04-08	20	20	156.7	+19.9							0.016
SNhunt248	2014-06-05	60	60	225.0	+1.9							0.047
2015bh	2015-05-14	100	100	137.4	+33.1	5.8	150325	133.1	+37.8	10.5	50	0.079

Table 5.11: SNe with detected pre-explosion activity and corresponding GRBs. Details and explanations are given in the text.

SN	z	E_{pre} (erg)	E_{SN} (erg)	M_R (mag)	GRB	T_{90} (s)	E_{iso} (erg)	E_p (keV)
PTF 10bjb	0.026	2×10^{48}	2×10^{49}	-16.4				
2010mc	0.035	6×10^{47}	2×10^{49}	-18.5	100706	0.13	3×10^{47}	840±330
PTF 10weh	0.138	5×10^{48}	7×10^{50}	-20.7	100417	0.19	2×10^{49}	250±54
2011ht	0.0036	2×10^{47}	3×10^{49}	-16.8				
PTF 12cxj	0.036	9×10^{46}	8×10^{48}	-17.3				
PTF 12cxj	0.036	6×10^{46}	8×10^{48}	-17.3	100411	0.51	6×10^{47}	980±2180
2009ip	0.0059	2×10^{48}	3×10^{49}	-18.5	121014	0.57	9×10^{47}	-
LSQ13zm	0.029	1×10^{48}	1×10^{50}	-18.5				
SNhunt248	0.0045	2×10^{48}	2×10^{49}	-15.0				
2015bh	0.0066	2×10^{48}	2×10^{49}	-17.6	150325	0.88	2×10^{47}	-

Table 5.12: Same rows as in Table 5.11. Column z is redshift of the SN. Column E_{pre} corresponds to radiated energy in the pre-explosion episode while E_{SN} is the energy radiated in the main SN event. Column M_R is absolute peak R magnitude of the main event. Parameter E_{iso} of GRB was calculated based on the fluence ($10\ \mathrm{keV} - 1\ \mathrm{MeV}$) reported in the catalog and assuming SN redshift. Parameter E_p is the peak energy for the power-law-cutoff model reported in the catalog.

luminosity. The detailed examination of the optical transients is not part of this analysis and references should be checked for more details. The N_{exp} is also an estimation and is not intended to precisely quantify the probability. If a GRB was close to the pre-explosion period but not within, then the δt was multiplied by 2, 3, etc. until it encompassed the burst. For 2009ip the focus was on its strongest period in 2012, and GRB occurred during the brightest peak (after start of its rise), but before another weaker peak which occurred about 30 days after, during the decay phase of the stronger one. For PTF 12cxj the conditions on error radius were relaxed which included GRB 100411. Since the specific SNe are in question, it should also be taken into account that if there were GRBs physically connected to them, they might have been missed if they were outside Fermi FoV (2/3 of the sky), and also, the GRB error is 1σ (2/3 of total) error. Even though it is an estimation, it seems unlikely that there would be so many random short Fermi GRBs for the selected optical transients and their periods of activity.

The physical parameters of SNe and GRBs are given in Table 5.12.

5.5.3 Short GRBs – IIn SNe, no direct evidence

Very high confidence levels (CLs) for BATSE short GRBs – IIn SNe coupled with triple GRB connection to supernova impostor SN 1997bs and previously examined connection of a GRB with exceptional Ia-CSM SN 1997cy; relatively high CLs for Fermi short GRB – IIn SNe and GRB occurrence in or close to periods of pre-explosion activity of other IIn SNe - all point to the physical connection between short GRBs and IIn SNe, i.e. SNe that can

Mission	short GRBs	long GRBs	ratio
BATSE	495	1536	$\approx$ 1:3
Fermi	320	1640	$\approx$ 1:5
Swift	102	948	$\approx$ 1:9

Table 5.13: Long and short bursts for BATSE during entire mission period. Long and short bursts for Fermi and Swift up to 2017. For BATSE and Fermi the numbers correspond to the ones with cut on the high error radius but this doesn't change the ratio.

be of different physical origin but all have interaction with circum-stellar medium (CSM) in common. The question is then why these connections don't have any confirmed cases while long GRB – Ib/c SNe have many.

GRBs prompt emission needs to be precisely localized (arc-minute) and then soft X-ray and optical instruments may do follow-ups with arc-second or greater precision and discover GRB afterglow and later physical connection of a GRB and a SN (if there is one). For long GRBs this happened during the late 1990s and since the year 2005 Swift is responsible for majority of long GRB localizations that helped discoveries of a SN connection (Table 5.1). For short GRB the first afterglow discovery (and consequent redshift detection[32]) came in the year 2005 - GRB 050509B (Berger, 2014), again thanks to Swift. Aside from two short GRBs detected by HETE-2 and one detected by INTEGRAL (which have a precise localization), all other short GRBs (about 70) were detected by Swift with at least arc-minute localization up to the beginning of 2013 (Berger, 2014) (about 100 up to the beginning of 2017). So, the question about non-detection of IIn SNe with short GRBs comes down to Swift-BAT. The online Swift catalog of GRBs is hosted here[33] where GRB information can be obtained as a text file and loaded into a program.

First thing to notice are different numbers and ratios of long GRBs to short ones for BATSE, Fermi-GBM and Swift-BAT (Table 5.13). Simply put BATSE is most suitable for detecting short GRBs, then Fermi and then Swift. In (Burns et al., 2016) it is argued that large ratio of long to short bursts for Swift (compared to Fermi) is due to larger Swift sensitivity to long bursts while the sensitivity for detecting short bursts is the same for both detectors, and that larger number of Fermi short burst is due to Fermi larger FoV. In any case, larger number of short bursts for BATSE and Fermi with respect to Swift remains. In (Bromberg et al., 2013) it is argued that division of long and short bursts for Swift should be at $T_{90} \approx 0.8$ s while for Fermi and BATSE the typical value $T_{90} \approx 2$ s is fine. This would further decrease number of Swift short bursts with respect to BATSE and Fermi. However (Burns et al., 2016) argue against such a division for Swift.

From the Tables 5.10 and 5.12, almost all good candidate short GRBs of BATSE and Fermi have isotropic energy in the range $\mathrm{E_{iso}} \sim 10^{45} - 10^{48}$ erg, which is smaller than typical short GRB energies $\mathrm{E_{iso}} \sim 10^{48} - 10^{53}$ erg, especially for SN 1997bs – GRB trio $\mathrm{E_{iso}} \sim 10^{45} - 10^{46}$ erg. This is also the case for majority of Fermi GRBs within the $\mathrm{CL_{240d}}$ which were not selected as good candidates. However, the hardness of all these bursts ($\mathrm{E_p}$) is in the range of typical short ones. Threshold for GRB detection varies on number of criteria, such as sensitivity of the detector, background rate which varies during an orbit, position of GRB with respect to detectors, trigger algorithms which may change during the course of the mission, etc; and on GRB properties itself with most important

[32]Most redshift determinations for short GRBs come from identifying the host galaxy, not from afterglow spectrum.

[33]`https://swift.gsfc.nasa.gov/archive/grb_table/`

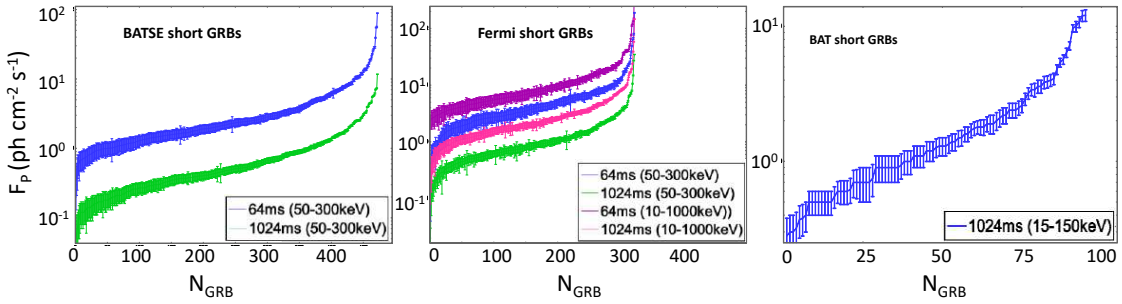

Figure 5.7: Peak fluxes of short GRBs for BATSE, Fermi and Swift with their 1σ errors. **BATSE:** $\mathrm{F_p}$s for 64ms and 1024ms are presented. Due to the spiky nature of the light curve, the $\mathrm{F_p}$s for longer integration time periods are, on average, less intense. Out of 495 short bursts, 472 have determined $\mathrm{F_p}$s and are plotted. The plot for 256ms is not shown for clarity but is in between the two curves. **Fermi:** Same as in previous case with addition of different energy bands. As expected the $\mathrm{F_p}$s for larger energy band are higher. Out of 320 short bursts, all have determined $\mathrm{F_p}$s. **Swift:** Only the 1s $\mathrm{F_p}$s are given. Out of 102 short bursts, 95 have determined $\mathrm{F_p}$s. **Note:** Same place on the horizontal axis ($\mathrm{N_{GRB}}$) for different time (ms) period curves may not correspond to the same GRB.

being the observational property *peak flux*, which depends on the $\mathrm{E_{iso}}$ and distance, but also on the shape of the light curve. Bursts with lower $\mathrm{E_{iso}}$ will *on average* give lower peak flux and these bursts will *on average* be harder to detect.

To compare the 3 instrument capabilities of detecting short GRBs, the peak fluxes ($\mathrm{F_p}$) of the detected short bursts will be compared. For BATSE and Fermi $\mathrm{F_p}$s are in the catalog for 64 millisecond (ms) period, 256 ms, and 1024 ms time range. Depending on the shape of the light curve, any of these (or all) may trigger the instrument. For Swift catalog, only the $\mathrm{F_p}$ for the period of 1s (1024 ms) is present. The energy range for $\mathrm{F_p}$s are $50 - 300$ keV for BATSE, $50 - 300$ keV and $10 - 1000$ keV for Fermi and $15 - 150$ keV for Swift.

First to give an idea on the error of the $\mathrm{F_p}$s, Figure 5.7 is presented. The bursts are sorted by their $\mathrm{F_p}$ and plotted for different instruments, different integration time ranges and energy bands.

The comparison of BATSE and Fermi $\mathrm{F_p}$s is shown in Figure 5.8 with highlighted $\mathrm{F_p}$s of 4 BATSE short GRBs in connection to SN 1997bs and SN1997cy. Comparing $\mathrm{F_p}$s for both detectors in this way takes into account all the peculiarities of two detectors in regards of detecting short GRBs during the course of the mission times. Also, taking into account Fermi bursts till the year 2017 makes its mission time almost the same as the one of BATSE - about 9 years, so the $\mathrm{F_p}$s curves can be read as sensitivity directly without considering difference in time periods. It can be seen that BATSE detected more short GRBs with lower $\mathrm{F_p}$s than Fermi, and more short GRBs in total. It can also be seen that 4 GRBs in question have $\mathrm{F_p}$s than are in lower part of Fermi $\mathrm{F_p}$s distribution for all 3 time integration periods while for BATSE they are average. Especially the case of GRB 970408A (the lowest $\mathrm{E_{iso}}$) which for all 3 time periods has $\mathrm{F_p}$ which is in the range where BATSE has many more detections than Fermi.

From instrument point of view this might explain the very high CLs $\mathrm{CL} \geq 0.99$ for BATSE and not so high $\mathrm{CL} \geq 0.90$ for Fermi. Additionally, Fermi short bursts have on average larger error radius ($8.7°$) then BATSE ones ($7.0°$). This doesn't increase the number of physical connections (if they exist) but does increase number of random connections (as er^2) which reduce CLs.

Finally the comparison of short GRBs from all 3 detectors is shown in Figure 5.9 with

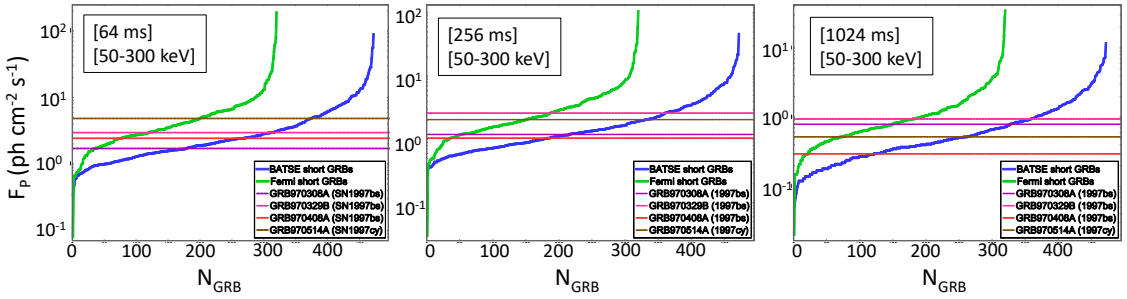

Figure 5.8: Peak fluxes of short GRBs for BATSE and Fermi and specifically the 4 good candidate BATSE GRBs, for 3 different integration time periods. Integration time periods and energy ranges are presented in the left-upper corners. Errors are not shown for clarity.

highlighted $\mathrm{F_p}$s of all the BATSE and Fermi GRBs which are good candidates for physical connection. First thing to notice is significantly smaller number of detected short GRBs by Swift-BAT and higher $\mathrm{F_p}$s for those bursts. The $\mathrm{F_p}$s of good GRB candidates are average ones for BATSE, lower for Fermi and even lower for Swift. Additionally, good candidate GRBs have higher E_p, well above Swift energy range $15 - 150$ keV which would make them even harder for Swift to detect.

If the number of physical connections for BATSE and Fermi is estimated as $\mathrm{N_0} - \langle \mathrm{N} \rangle$ for CLs where it is high, than the number for BATSE would be around 5, and similar for Fermi. Given the ratio of detected short bursts for different missions, Swift should have detected one. If only the bursts with $\mathrm{F_p}$s lower than the maximum $\mathrm{F_p} \approx 1$ of a good GRB candidate are taken into account, then this number for Swift gets closer to zero, especially considering the case of GRB 970408A (lowest $\mathrm{E_{iso}}$) which $\mathrm{F_p}$ is higher than that of just one Swift short GRB.

Detecting optical transient

Even if Swift observed some IIn-SN – GRBs, the optical transient might not have been detected by Swift-UVOT (Ultraviolet and Optical Telescope) and ground-based optical telescopes. Supernovae Ib/c connected to GRBs have by default high luminosity during maximum (which occurs regularly 10 - 15 rest-frame days after GRB) and are relatively easily detected (if they are there). For IIn SNe luminosity varies from high to low depending whether it is actually a SN (final explosion) or supernova impostor. The luminosity of final explosion may also vary and in some cases it is not clear whether an event is final SN explosion or SN impostor. Additional pre-explosion activity, which can occur tens of days or hundreds of days before final explosion, introduces even lower luminosities than those of SN impostors.

The good candidate SNe here are SN 1997bs, SN 1997cy (BATSE era) and SN 2011A, SN 2011jb, SN 2010mc, PTF 10weh, PTF 12cxj, SN 2009ip, SN 2015bh (Fermi era) (Figure 5.10).

SN 1997bs was detected around maximum phase and had an apparent V magnitude (which is close to R magnitude) of $\mathrm{m_V} \sim 17$ and with $\mathrm{z} = 0.0024$ gives absolute V magnitude of $\mathrm{M_V} \sim -14$. It is unclear when was the explosion date. From most recent observations there is possibility that the event was a terminal SN explosion and not an impostor. GRB trio occurred 6, 16 and 37 days before the detection.

SN 1997cy was detected in post-maximum phase. It is unclear when was the maxi-

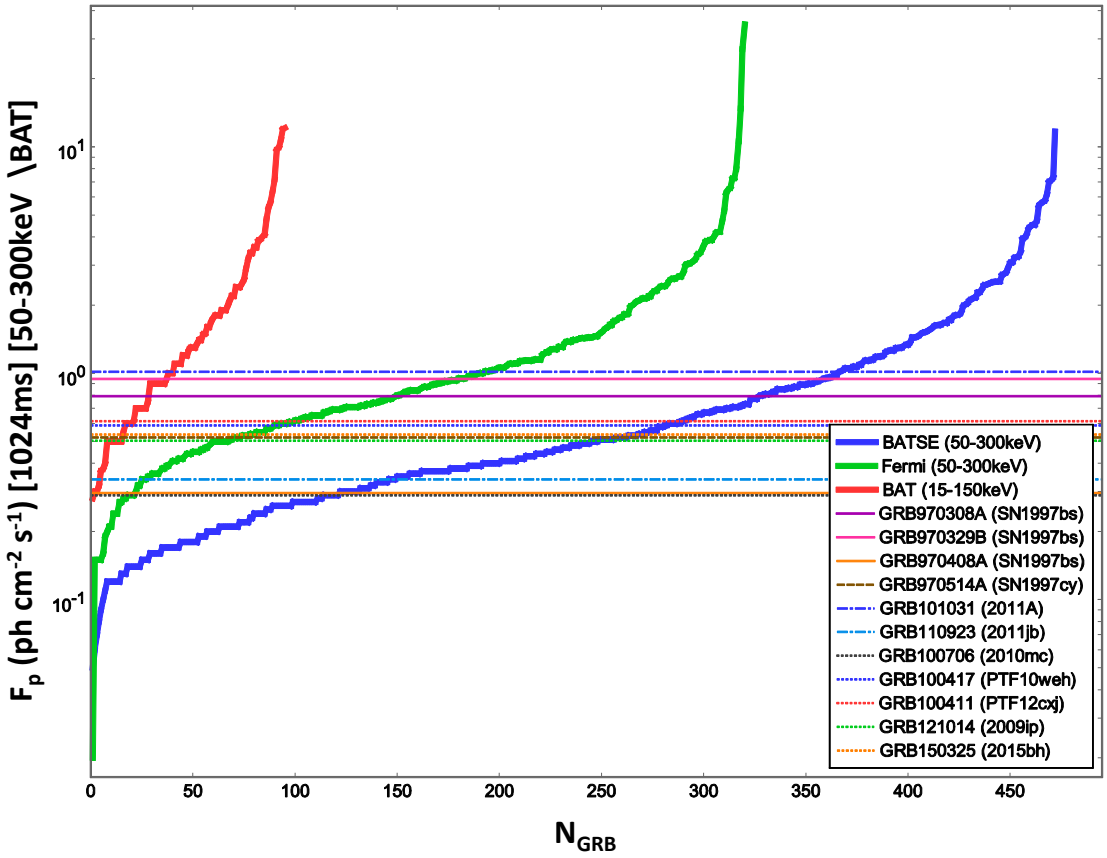

Figure 5.9: Peak fluxes of short GRBs for BATSE, Fermi, Swift and specifically the good candidate GRBs. The integration time for all the instruments is 1024 ms. The energy range for all is $50 - 300$ keV except for Swift which is $15 - 150$ keV.

mum and explosion date. The discovery apparent R magnitude was $m_R \sim 17$ and with $z = 0.064$ gives $M_R \sim -20$ and even more during maximum. This was a Ia-CSM supernova. The GRB was detected 62 days before SN detection.

SN 2011A was detected during maximum – post-maximum phase. It is unclear when was the explosion date. The discovery apparent R magnitude was $m_R \sim 18, 17$ and with $z = 0.0088$ gives $M_R \sim -15, -16$. The luminosity is in between normal IIn (terminal explosions) and impostors. The GRB was detected 62 days before SN discovery.

SN 2011jb was detected in post-maximum phase. It is unclear when was the maximum and explosion date. The discovery apparent R magnitude was $m_R \sim 18$ and with $z = 0.084$ gives $M_R \sim -20$ and even more during maximum. This was a Ia-CSM supernova. The GRB was detected 65 days before SN detection.

SN 2010mc was detected even before explosion. The apparent R magnitude during maximum was $m_R \sim 18, 17$ and with $z = 0.035$ gives $M_R \sim -18, -19$ at maximum. This was typical IIn SN and is considered to be final explosion. The apparent R magnitude of pre-explosion activity was $m_R \sim 22, 21$ which is $M_R \sim -14, -15$. The GRB was detected 45 days before SN explosion - several days before pre-explosion activity.

PTF 10weh was detected even before explosion. The apparent R magnitude during maximum was $m_R \sim 19, 18$ and with $z = 0.138$ gives $M_R \sim -21$ at maximum. This was typical IIn SN and is considered to be final explosion. The apparent R magnitude of pre-

explosion activity was $\mathrm{m_R} \sim 22$ which is $\mathrm{M_R} \sim -17$. The GRB was detected about 150 days before SN explosion - about 50 days before pre-explosion activity which itself lasted for 50 days and stopped 50 days before SN explosion.

PTF 12cxj was detected even before explosion. The apparent R magnitude during maximum was $\mathrm{m_R} \sim 19,18$ and with $\mathrm{z} = 0.036$ gives $\mathrm{M_R} \sim -17$ at maximum. This was typical IIn SN and is considered to be final explosion. The apparent R magnitude of pre-explosion activity which occurred around 700 days before SN explosion was $\mathrm{m_R} \sim 23$ which is $\mathrm{M_R} \sim -13$. The GRB was detected about 735 days before SN explosion - about 25 days before pre-explosion activity which itself lasted for about 15 days.

SN 2009ip was detected several times before final explosion which occurred in September 23, 2012. The apparent V magnitude during maximum was $\mathrm{m_V} \sim 14$ and with $\mathrm{z} = 0.0059$ gives $\mathrm{M_V} \sim -17, -18$ at maximum. Most likely this was typical IIn SN and is considered to be final explosion, however there are some doubts. The second peak occurred 30 days after the main peak and had an $\mathrm{m_V} \sim 15$. The GRB occurred 12 days after the main peak and about 20 days before the second.

SN 2015bh was detected before explosion. The apparent R magnitude during maximum was $\mathrm{m_R} \sim 15$ and with $\mathrm{z} = 0.0066$ gives $\mathrm{M_R} \sim$ -17, -18 at maximum. Most likely this was typical IIn SN and is considered to be final explosion. The apparent R magnitude of pre-explosion activity which started around 100 days before, and lasted till the SN explosion had an apparent R magnitude in the range of $\mathrm{m_R} \sim 20 - 18$. The GRB occurred 50 days before SN explosion and in the middle of pre-explosion activity.

From the above examples it can be seen that GRB may occur several days before the main event or a minor event. In most cases optical follow-ups to Swift short bursts happen within a day or two and if there is no optical emission at that moment, it stops. In this way an optical transient might be missed if GRB occurred before it. Also, optical measurements might not have been sensitive enough to detect week pre-explosion activity if GRB occurred during it. In some cases an uncatalogued optical source was found in the error box of Swift but due to its non-fading characteristics, which is expected for GRB optical afterglows, it was dismissed as being connected to the GRB and optical observations stopped.

5.5.4 Rates

Possible physical connections are found by matching cataloged GRBs with cataloged SNe. While GRB instruments cover almost whole sky, optical ones cover very small part and many detectable SNe are missed. It is assumed that if number of catalog SNe where, for example, doubled, then on average there should be twice as more found physical connections and as many random, and the confidence levels remains similar. So the question is how many short GRBs in the catalog come from IIn SNe. To give a crude estimate the rate of IIn SNe is needed. In (Smartt et al., 2009) the estimated rate of core-collapse SNe is $9.6 \times 10^4\ \mathrm{Gpc^{-3}\ yr^{-1}}$ and percentage of IIn SNe of 3.8% in them, gives $\rho_{\mathrm{IIn}} = 3.6 \times 10^3\ \mathrm{Gpc^{-3}\ yr^{-1}}$. In (Li et al., 2011) only general type II was considered which is $\rho_{\mathrm{II}} = 4.5 \times 10^4\ \mathrm{Gpc^{-3}\ yr^{-1}}$ and is close to the general type II from previous work. In both works, however, it is stated that these are crude estimates.

Now, from Figure 5.10 it can be seen that most cataloged IIn SNe are in the $\mathrm{z} \leq 0.1$ which corresponds to volume of $\mathrm{V} \approx 0.25\ \mathrm{Gpc^3}$. Both Fermi and BATSE operated for about $\mathrm{T} \approx 10\ \mathrm{y}$. So, the total number of SNe for the volume and time period should be $\mathrm{N_{IIn}} \sim 10.000$. The number of cataloged IIn SNe during BATSE period is $\mathrm{N^b_{IIn}} \approx 50$ and in

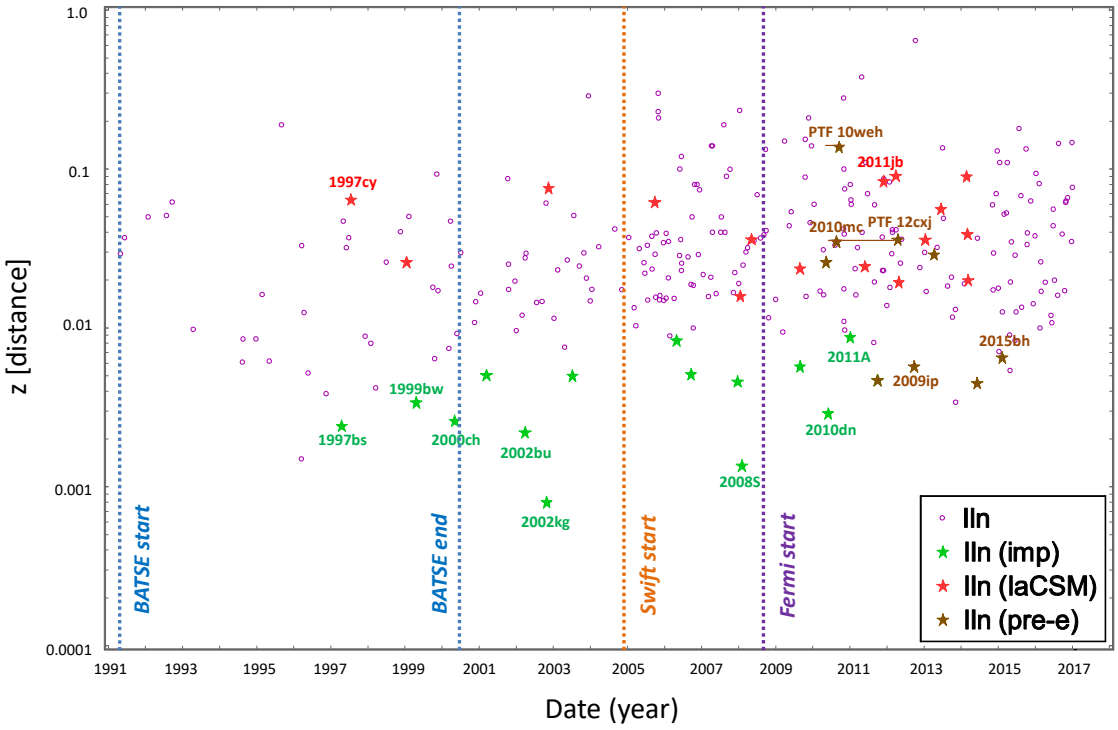

Figure 5.10: Supernovae IIn from the start of BATSE observations up to 2017. For smaller values $z \leq 0.005$ redshift corresponds to distance and not actual redshift which is affected by movement of Earth with respect to SN host galaxy. Marked SNe correspond to good candidates for physical connection to GRB. Also IIn impostors with very small distance, in the range of SN 1997bs, were marked. For SNe with pre-explosion activity (pre-e) the date corresponds to the date of the main peak. If the corresponding GRBs occurred much before than a line is added to the marker (PTF 10weh, PTF 12cxj).

Fermi $N^{f}_{IIn} \approx 150$. So, the catalog SNe in this volume are about ~ 100 times less in number than the entire IIn ones. Taking the number of physical connections for both instruments at ~ 5 (for both instruments they go all the way to $z \leq 0.1$), the total number of short bursts coming from all IIn SNe (not just cataloged ones) is around ~ 500, basically the entire cataloged short GRBs. Again, these are very crude estimates.

If only GRB-trio for the close SN 1997bs ($z = 0.0024$) is considered as good candidate(s), then different results emerge. The maximum distance for detecting GRB in BATSE case is determined from the catalog parameter which corresponds to ratio of counts in second most illuminated detector, to, count threshold for that detector (for BATSE to register a GRB at least two detectors should be triggered). Only 2 out of 3 GRBs have this parameter in the catalog and maximum redshifts for them are $z = 0.0031$ and $z = 0.0047$. For simplicity the value of $z \approx 0.004$ was taken which corresponds to $V \approx 2 \times 10^{-5}$ Gpc^3. In that case the number of IIn SNe in the maximum volume and period of BATSE time would be $N_{IIn} \sim 1$ which is at order of magnitude of cataloged IIn SNe in $z \leq 0.004$. This would mean that not many more short GRBs come from IIn SNe. It is obvious from Figure 5.10 that IIn impostors (which are less luminous) are all very close since they are harder to detect at grater distances, and that they make majority of IIn SNe at lower redshifts, including SN 1997bs. Still, the general result matches order of magnitude regardless of IIn impostor special nature.

On the other hand taking into account Ia-CSM SN1997cy – GRB at $z \lesssim 0.1$ would give

the previous number of IIn SNe which is ~ 100 times larger than cataloged ones and would mean that many short GRBs in the catalog come from IIn SNe (or from Ia-CSM subtype of IIn SNe). For Fermi the good candidates span the range from very low distances to $\mathrm{z} \approx 0.1$ and the same results apply.

If the number of IIn-short GRBs is indeed much larger, than again question might be asked regarding Swift non-detection. Even if all the previous arguments for Swift non-detection are taken into account - why out of 100 short GRBs, 30 of which have measured redshifts, all 30 of them are above $\mathrm{z} \geq 0.1$. In Figure 5.9, the peak fluxes $\mathrm{F_p}$s of good candidate GRBs correspond to 40% of Swift GRBs with lowest $\mathrm{F_p}$ and 8 of them have measured redshift. The uncertainty of these conclusions is large, but Swift short GRBs with measured redshifts suggest that IIn-GRBs are unlikely to make majority of short GRBs.

5.5.5 Properties of IIn-GRBs

The traditional division of GRBs to long and short comes from several observational missions. When GRBs are sorted by their duration, two peaks in the distribution can be seen with the division around $\mathrm{T_{90}} \approx 2$ s. This division in duration is followed by the division in hardness in a way that short GRBs have higher peak energies $\mathrm{E_p}$, and long bursts have smaller. There are additional features such as location in a galaxy, Ib/c SN association, etc. Two distributions are explained in literature as having different physical origin, namely the long ones are coming from death of a massive star while short ones are mergers of two compact objects. The IIn-GRBs should belong to neither of these.

Duration

The question then is why does the limit of $\mathrm{T_{90}} = 2$ s seem also to be a limit on potential IIn-GRBs. The big difference between confidence levels (CLs) for short and long GRBs connected to IIn SNe is very clear for BATSE. For BATSE short bursts and IIn SNe, time windows of 40, 60, 80, 100 days have very high CLs and two final ones contain 8 short GRBs. Their duration of potential candidates takes the range from $\mathrm{T_{90}} \approx 0.2$ s to $\mathrm{T_{90}} \approx 1$ s. If all the long GRBs are taken into account (which number is 3 times higher than short), then only two additional GRBs appear in the 100d time window, one with $\mathrm{T_{90}} \approx 10$ s and another one with $\mathrm{T_{90}} \approx 130$ s. Changing $\mathrm{T_{90}}$ limit to 0.5s, 1.0s and 1.5s doesn't produce big difference, but the highest CLs are for the limit of $\mathrm{T_{90}} \leq 2$ s.

For Fermi bursts the big difference in CLs between long and short is also clear although to a lesser extent because the CLs are not so high for the short as they are for BATSE. For Fermi short bursts, time windows of 80, 100, 120, 240 days have high CLs. The duration for given bursts also takes the range from $T_{90} \approx 0.2$ s to $T_{90} \approx 2$ s and the good candidate GRBs mostly have $T_{90} \leq 1.0$ s. Changing T_{90} limit to 0.5 s, 1.0 s and 1.5 s doesn't produce big difference, and adding long bursts to given time windows introduces several of them already at $T_{90} \leq 3$ s.

The limit of $T_{90} \approx 2$ s might be an argument for chance coincidence.

Peak energy and isotropic energy

Good candidate GRBs have higher peak energies which is typical for short GRBs. The isotropic energy is mostly in the $E_{iso} \sim 10^{45} - 10^{48}$ erg, especially the SN1997bs - GRB trio $E_{iso} \sim 10^{45} - 10^{46}$ erg while "normal" short GRBs have isotropic energies from $E_{iso} \sim 10^{48}, 10^{49}$ erg up to extreme cases of $E_{iso} \sim 10^{53}$ erg. Higher peak energies are expected

since the selected GRBs are actually short GRBs but again - if the IIn-GRBs are different than "standard" short, why do they also have peak energies similar as "normal" short as well as T_{90}. Again, this might be an argument against special class of IIn-GRBs. From the point of view that all connections are coincidences the lower isotropic energy might be explained due to fact that most cataloged SNe lie in the range $z \leq 0.1$; Lower peak flux and fluence are due to fact that coincidence connections prefer GRBs with bigger error radii and they have bigger errors due to lower peak flux and fluence.

On the other hand, IIn-GRBs with lower energies would produce such observational features.

Soft gamma repeaters and Giant flares

Soft gamma repeaters (SGR) are objects that periodically emit bursts of soft (lower energy) gamma radiation. They are much less energetic than GRBs and only several of them are known, all of which reside in Milky Way or its satellite galaxies. The SGR bursts are thought to come from the decay of magnetic field of magnetars. For reviews see (Woods and Thompson, 2006; Turolla et al., 2015).

In addition to "standard" bursts SGR-objects may emit flares and subtype of these flares are called *giant flares*. The flares are thought to originate in strong reconfiguration of magnetars magnetic field. Only three giant flares were observed - in 1979, 1998 and 2004. They have similar characteristics such as high energetics $E_{iso} > 10^{44}\,\mathrm{erg}$ (in gamma-rays), hard-spectrum/peak-energy and they are composed of short initial spike which lasts about $\sim 0.1 - 1\,\mathrm{s}$, and, a lower intensity, decaying tail which lasts for hundreds of seconds and oscillates at the rotational frequency of the star. The strongest giant flare by far is the one from *SGR 1806–20* which occurred on December 2004 (hyper flare). The initial spike had an isotropic energy of $E_{iso} \approx 2 \times 10^{46}\,\mathrm{erg}$, had high peak energy of $\sim 500\,\mathrm{keV}$ (and was detected up to $2\,\mathrm{MeV}$) and lasted $\sim 0.5\,\mathrm{s}$.

It was noticed that if giant flares occurred further away than only the initial spike would be detected and it would seem like a short GRB. This is especially the case for 2004 flare and the topic was studied in (Hurley et al., 2005b; Palmer et al., 2005; Nakar et al., 2006). Such a burst could be detected up to $40, 50\,\mathrm{Mpc}$ ($z \approx 0.01$). Given the fact that the flare/burst occurred in the period of about 30 years (the time period when instruments existed that could detect it) and in one galaxy (Milky Way and satellites), implies that the rate of such events (which would be recognized as short GRBs) matches the rate of short GRBs detected by BATSE, i.e. almost all short GRBs in BATSE catalog should be hyper flares from SGR-objects. Trying to find other evidence to this such as clustering of short GRB positions toward Virgo cluster (since they are relatively close) or searching for close galaxies in data archives for reasonably localized short GRBs, came up with opposite results, i.e. that most short GRBs in BATSE catalog are not from SGR-objects. The discrepancy wasn't resolved and with the Swift precise localization of short GRBs in 2005 and detection of redshifts $z \geq 1$ the issue seems to be abandoned.

The case of hyper flares from SGR-objects relation to "standard" short GRBs is similar to the case of potential IIn-GRBs and "standard" short GRBs. The main difference is that the isotropic energy of IIn-GRBs may reach $E_{iso} \sim 10^{48}\,\mathrm{erg}$ and hence, redshifts of $z \approx 0.1$, unless only GRB-trio of SN 1997bs ($z = 0.0024$) is taken as a good candidate. Now to come back to SGR-objects; the hyper flare of 2004 was about ~ 100 times more energetic than two previous giant flares and, although it would be very hard to explain it theoretically, in the future a new hyper flare might be detected with isotropic energy $E_{iso} \geq 10^{47}\,\mathrm{erg}$.

Finally, with introduction of SGR hyper flares as non-negligible portion of all short GRBs, does it mean that short GRBs may represent 3 different processes - ”standard” short, SGR hyper flares, IIn-GRBs?

In any case SGR-objects show that there are phenomena which are similar to short GRBs, in therms of duration and spectrum (peak energy). On the other hand both of the phenomena, in all different theories, are considered to come from compact objects which doesn't seem to be the case for IIn-GRBs. Compact objects such as NSs produce wide range of electromagnetic (photon) phenomena depending on their age, mass, rotational period, magnetic field strength, on binary companion (if there is one), etc. These include systems, detected in Milky Way galaxy, such as radio pulsars, X-ray pulsars, high and low mass X-ray binaries, optical pulsars, gamma-ray pulsars, SGR-objects - which can have ordinary bursts, flares and giant (hyper) flares. Transient phenomena from SGR-objects most resemble properties of ”normal” short GRBs with hyper flare matching it most and also having largest isotropic energy.

5.5.6 Mechanisms behind IIn-GRBs

Supernovae IIn

These SNe represent spectroscopic classification, and unlike other SNe types, it does not translate into a single pre-explosion stellar group. Narrow hydrogen lines indicate existence of slow moving, hydrogen-rich circum stellar medium (CSM) surrounding the star and this is the astrophysical aspect which binds all IIn SNe in a single group. Based on this definition SNe Ibn should also be in the *narrow* group but in this work they were grouped with Ib/c SNe due to the known connection with long GRBs. The recent works and reviews on SNe IIn: (Habergham et al., 2014; Smith, 2016). The main division of SNe IIn in this work was on ”standard” IIn, impostors and Ia-CSM. However, the variety of stellar activity (which may or may not be the final ”death” of a star) can be much greater. Additionally, the stars may be in a binary system and the companion can be a compact object star. The CSM is not simply a stellar wind but a much more massive shell of stellar material (in some cases even on the order of $\sim 10\ \mathrm{M}_{\odot}$). The interaction of released energy from stellar activity (usually SN ejecta, i.e. its kinetic energy) with the CSM (which can be aspherical) may define the evolution of the light curve and spectrum of the event more than characteristics of the stellar activity itself. If the star isn't in a binary system, the existence of a dense, massive CSM requires large mass ejections by the star. This means that star should be very massive, in some cases with initial masses more than $\sim 50\ \mathrm{M}_{\odot}$. The best candidates are Luminous Blue Variable (LBV) stars which can have relatively short periods of massive stellar eruptions (not the same as continues stellar winds). Massive stellar eruptions are also good explanation for SN impostors. One of the most famous, and best studied, LBVs is Eta Carinae star which resided in Milky Way. It has a mass of $\sim 100\ \mathrm{M}_{\odot}$, is part of a binary system with a similar but less intense star, and had a major eruption of $\sim 10\ \mathrm{M}_{\odot}$ about 150 years ago. While being good candidates LBVs are not the only ones, maybe not even the majority.

In most cases observations on the order of tens of years are needed to probe a IIn phenomenon correctly and determine the underlying stellar activity and whether it was terminal or no. So, many ”normal” IIn SNe may be something else than an ordinary SN II explosion in a CSM, and also SNe IIn classified as impostors or Ia-CSM SNe may turn out to be some other types of IIn. The observations and science of IIn SNe is still in its young

stages.

Recently discovered class of SNe, *superluminous supernovae* (SLSN), are SNe which can have (radiated/photon) energies above $\sim 10^{51}$ erg and peak luminosities in the range $M_V \sim -21, -22.5$, as opposed to ordinary core-collapse SNe which usually have energies up to 2 - 3 orders of magnitude less and peak luminosities in the range $M_V \sim -15, -18$. They are also more energetic and luminous than thermonuclear type Ia or GRB-Ib/c SNe. They are further divided into more common SLSN I which do not show hydrogen in the spectrum and hence correspond to stars without hydrogen envelope; and to SLSN II which show hydrogen in the spectrum and almost all of them also show narrow hydrogen lines which means SLSN II are practically SLSN IIn (Inserra et al., 2018). The high luminosity and energetics of SLSN IIn is explained by interaction of SN ejecta with dense CSM. As in the case of normal-luminous IIn, SLSN IIn probably have a wide variety of underling stellar activity/explosions.

It is interesting to note that IIb SNe may also have significant interaction with CSM, particularly at later times as exemplified by SN 1993J. The type IIb in this work have relatively high CLs ($\simeq 0.9$) for long BATSE and Fermi bursts at $TW \sim 100$ d. One of the BATSE candidates is SN 1993J (GRB 930203A), which probably has a binary B-type companion and resides in a nearby galaxy (≈ 3 Mpc).

Short GRBs

The purpose of this part is not to produce a model for IIn-GRBs but to explore some possibilities.

It is not uncommon to have gamma-rays (which can go all the way to GeV-TeV energies) from stellar activities such as novae, supernovae, eruptions and winds of massive stars, but these are continuous emissions with much lower luminosity than expected from IIn-GRBs $L_{IInGRB} \sim 10^{45} - 10^{48}$ erg/s. For example, Eta Carinae binary stars produce stellar winds which collide. It is considered that in the collision particles such as electrons are accelerated to high energies and then inverse Compton (IC) scattered of low-energy photons which gain energy and become gamma-rays. This was measured by INTEGRAL to have a luminosity of $L = 7 \times 10^{33}$ erg/s in the $20 - 100$ keV band (Leyder et al., 2008).

Supernovae IIn are defined by existence of CSM and interaction of SN ejecta (or impostor ejecta) with it. The collision of the SN shell with slow moving CSM reminds of collisions of fireball shells in GRB scenario but these happen at ultra relativistic speed while SN ejecta moves at $v \sim 0.03 - 0.1$ c. However, in (Katz et al., 2012) the case of expansion of the SN ejecta into dense, optically thick CSM (dense wind) was studied. It was found that at one point a collisionless shock will form and energy will be radiated in hard X-rays/gamma-rays ($E \gtrsim 50$ keV) which can reach $E_{iso} \sim 10^{51}$ erg but the duration of the emission is on the order of 1 day which would make luminosity $L \sim 10^{46}$ erg/s. This is in the range of luminosity expected but would last longer than ~ 1 s and the peak energy should be an order of magnitude higher. The CSM in the model was wind-like, decaying with $1/r^2$ and starting from the stars surface. If the energy requirements are lower $E_{iso} \sim 10^{45} - 10^{48}$ erg and CSM is apsherical with different density distribution, the resulting gamma emission might produce GRB within required parameters. Also, the emission might be longer but have a peak (detectable by GRB instruments) which last on the order of a 1 s.

The GRBs may be related to CSM but not come from the interaction with it. In (Chevalier, 2012) massive CSM in IIn systems is explained as originating from a common enve-

lope phase of a massive star and its binary compact object companion - neutron star (NS) or a black hole (BH). The compact object ejects the outer stellar envelope as it orbits the core of the star inside the star. The compact binary star may also explain large radiated SN energies in some IIn SNe when the CSM isn't too massive (which also implies the star isn't too massive). In the cited work it was found that rates of such binary systems and IIn SNe are different by order of magnitude but overlap within the large errors. Having a NS (which might be a magnetar) or a BH as a binary companion makes the possibility of a GRB occurring more probable and various mechanisms may be introduced. In fact the cited work suggested occurrence of GRBs related to IIn SNe but proposed it was suppressed by the CSM because of no known or possible observed connections except the possible one of IIn SN 1997cy – short GRB 970514 (Germany et al., 2000).

There are speculation on the existence of a *quark nova* which occurs when the neutron degeneracy in the NS cannot oppose the gravitational pressure and neutrons are dissolved into constituent quarks and a *quark star* is created. Released gravitational and nuclear energy create a quark nova (QN). In (Ouyed et al., 2013) it is argued that SN 2010mc and SN 2009ip, which have pre-explosion activity shortly before the main explosion, are a case of SN and a QN. The SN is responsible for the first peak and a QN for a second and more stronger peak (the main peak). Also in (Ouyed et al., 2011) it is argued that QNe may produce short GRBs, although this is speculated for low mass X-ray binaries when the massive NS goes QN and the QN ejecta interacts with dense circumbinary disk. With the right tuning of parameters in the model, as well as asymmetric CBM in IIn SNe, it might be possible to produce short GRBs with enrgetics lower than standard ones $E_{iso} < 10^{48}$ erg.

Finally, since SNe IIn represent significant number of different stellar activities the GRBs may be produced from different mechanisms in IIn SNe.

5.5.7 Future work

Statistical analysis

The basis of searching for connection in this work was whether a GRB encompasses SN with its $1\ \sigma$ statistical (plus systematic) error radius or not. This is an approximation. For example, if a GRB error radius is 10° and a SN is 1° from a GRB position (center of the error circle), second SN is 9° and a third one is 11° from it; then the first two SNe would be counted as *inside* with same probability and a third one would be *outside* and ignored. In reality the first one has the highest probability, the second and third have similar spacial probabilities of connection to GRB. Second, the connections with GRBs with smaller error radii should have more statistical weight. Third, GRB error surfaces were approximated as circles but are actually ellipses. Fourth, the GRB sky positions are not uniformly random.

In order to do everything properly map exposure of Fermi and BATSE should be taken into account when generating positions of random GRB sets. The exact error spread distribution for all GRBs should be known and more SNe (within 99% probability contour for example) should be taken into account for every single GRB. Also for each GRB detected by other satellites the combined error spread probability should be taken into account. This information is not available in the catalogs and has to be obtained, or approximated, in another way. The confidence levels for time windows should be obtained, again by randomizing GRB positions and dates, but taking above considerations into account.

Detailed analysis of GRBs

The good candidate GRBs should be checked in detailed, namely the morphology of the light curve and spectral analysis.

Search for nearby host galaxies of short GRBs localized by Swift

Since IIn-GRBs have lower energetics they should reside in nearby ($z \leq 0.1$) galaxies. The search for the galaxies in archival optical data may be performed at the position of error surface of short GRBs localized by Swift.

SNe type IIb and IIP

Since connections with these SNe show relatively high CLs it would be interesting to explore it furhter.

Final remarks

The purpose of this work isn't to claim existence of short GRB – IIn SN connections but to explore the possibility and its implications. The original idea was to look for well established connections between long GRBs and Ib/c SNe which might have been mist if only Fermi observed the GRB, and a SN was discovered serendipitously. Then the statistical approach was adopted in order to see if there is excess of these connections to random ones and in which time windows they reside in order to see from statistical point of view how many might have been mist and in which time windows to look for them. Other types of SNe were used as a comparison. Then the very high CLs were noted for short IIn SNe and BATSE short GRBs and the exploration into this possible connection started.

The majority of short GRB sample comes from BATSE (around 500) which has on average lower peak fluxes and fluences than the Swift sample, and to a lesser extent from Fermi (around 300 up to 2017). Detectors BATSE and Fermi are not suited for localizing bursts and hence, determination of the redshift. Up to year 2017 about 30 short GRBs have measured redshift and about 10 of those were also detected by Fermi. It seems there is room left for short GRBs with lower isotropic energies at distances $z \leq 0.1$. If this is the case then these could be giant flares from SGRs, IIn-GRBs, something else or combination of them.

In August, 2017 a gravitational wave GW 170817 was detected coinciding in sky-position and time with short GRB 170817A detected by Fermi-GBM (Abbott et al., 2017; Troja et al., 2017). The distance to the object is $\sim 40\ \mathrm{Mpc}$ which implies isotropic energy of $E_{iso} \approx 5 \times 10^{46}\ \mathrm{erg}$. This is by far the closest short GRB and with lowest isotropic energy. General conclusion seems to be that this was regular short GRB detected off-axis. This event gives an example of, from observational point of view, short GRB occurring well below $z \approx 0.1$ and $E_{iso} < 10^{48}\ \mathrm{erg}$. Question now is how many of short GRBs detected by Fermi are "local" and how many are at cosmological distances; this question can also be extended to BATSE and other detector samples of short GRBs. Further events detected by both gravitational wave, gamma and optical detectors are needed to probe into the specific event of GW-GRB 170817 and population statistics of short GRBs.

Bibliography

Abbott, B. et al. (2017). Gravitational Waves and Gamma-Rays from a Binary Neutron Star Merger: GW170817 and GRB 170817A. ApJ, 848:L13.

Ackermann et al. (2014). Fermi-LAT Observations of the Gamma-Ray Burst GRB 130427A. *Science*, 343:42–47.

Adams, M. T. et al. (1997). Supernova 1997cq in Anonymous Galaxy. IAU Circ., 6674.

Adams, S. M. and Kochanek, C. S. (2015). LOSS's first supernova? New limits on the 'impostor' SN 1997bs. MNRAS, 452:2195–2207.

Aksenov, A. G., Ruffini, R., and Vereshchagin, G. V. (2007). Thermalization of Nonequilibrium Electron-Positron-Photon Plasmas. *Physical Review Letters*, 99(12):125003.

Aksenov, A. G., Ruffini, R., and Vereshchagin, G. V. (2010). Pair plasma relaxation time scales. Phys. Rev. E, 81(4):046401.

Andrews, J. et al. (2015). ATel 7456: Spectroscopic classification of PSN J23355226+2336521 as a Type Ic. *The Astronomer's Telegram*, 7456.

Ashall, C. et al. (2017). GRB 161219B-SN 2016jca: a powerful stellar collapse. *ArXiv e-prints*.

Band, D. L. (2003). Comparison of the Gamma-Ray Burst Sensitivity of Different Detectors. ApJ, 588:945–951.

Barbon, R., Buondi, V., Cappellaro, E., and Turatto, M. (2010). VizieR Online Data Catalog: Asiago Supernova Catalogue (Barbon et al., 1999-). *VizieR Online Data Catalog*, 1.

Basak, R. and Rao, A. R. (2015a). Discovery of Smoothly Evolving Blackbodies in the Early Afterglow of GRB 090618: Evidence for a Spine-Sheath Jet? ApJ, 812:156.

Basak, R. and Rao, A. R. (2015b). Thermal Emissions Spanning the Prompt and the Afterglow Phases of the Ultra-long GRB 130925A. ApJ, 807:34.

Becerra, L., Cipolletta, F., Fryer, C. L., Rueda, J. A., and Ruffini, R. (2015). Angular Momentum Role in the Hypercritical Accretion of Binary-driven Hypernovae. ApJ, 812:100.

Bellm, E. C. et al. (2014). X-Ray Spectral Components Observed in the Afterglow of GRB 130925A. ApJ, 784:L19.

Belvedere, R., Pugliese, D., Rueda, J. A., Ruffini, R., and Xue, S.-S. (2012). Neutron star equilibrium configurations within a fully relativistic theory with strong, weak, electromagnetic, and gravitational interactions. *Nuclear Physics A*, 883:1–24.

Benedetti, A., Han, W.-B., Ruffini, R., and Vereshchagin, G. V. (2011). On the frequency of oscillations in the pair plasma generated by a strong electric field. *Physics Letters B*, 698:75–79.

Benitez, S. et al. (2013). Nearby Supernova Factory II classification of Five Supernovae. *The Astronomer's Telegram*, 4994.

Berger, E. (2014). Short-Duration Gamma-Ray Bursts. ARA&A, 52:43–105.

Bernardini, M. G., Bianco, C. L., Caito, L., Dainotti, M. G., Guida, R., and Ruffini, R. (2007). GRB 970228 and a class of GRBs with an initial spikelike emission. A&A, 474:L13–L16.

Bernardini, M. G., Bianco, C. L., Chardonnet, P., Fraschetti, F., Ruffini, R., and Xue, S.-S. (2005). Theoretical Interpretation of the Luminosity and Spectral Properties of GRB 031203. ApJ, 634:L29–L32.

Bersier, D. et al. (2006). Evidence for a Supernova Associated with the X-Ray Flash 020903. ApJ, 643:284–291.

Bhat, P. N. et al. (2016). VizieR Online Data Catalog: The third Fermi/GBM GRB catalog (6yr) (Bhat+, 2016). *VizieR Online Data Catalog*, 222.

Bianco, C. L., Massucci, F. A., and Ruffini, R. (2011). The Luminosity Evolution Over the Equitemporal Surfaces in the Prompt Emission of Gamma-Ray Bursts. *International Journal of Modern Physics D*, 20:1919–1929.

Bianco, C. L. and Ruffini, R. (2004). Exact versus Approximate Equitemporal Surfaces in Gamma-Ray Burst Afterglows. ApJ, 605:L1–L4.

Bianco, C. L. and Ruffini, R. (2005a). Exact versus Approximate Solutions in Gamma-Ray Burst Afterglows. ApJ, 633:L13–L16.

Bianco, C. L. and Ruffini, R. (2005b). Exact versus Approximate Solutions in Gamma-Ray Burst Afterglows. ApJ, 633:L13–L16.

Bianco, C. L. and Ruffini, R. (2005c). On the Exact Analytic Expressions for the Equitemporal Surfaces in Gamma-Ray Burst Afterglows. ApJ, 620:L23–L26.

Bianco, C. L. and Ruffini, R. (2005d). On the Exact Analytic Expressions for the Equitemporal Surfaces in Gamma-Ray Burst Afterglows. ApJ, 620:L23–L26.

Bianco, C. L. and Ruffini, R. (2006). Exact versus Approximate Beaming Formulae in Gamma-Ray Burst Afterglows. ApJ, 644:L105–L108.

Bianco, C. L., Ruffini, R., and Xue, S.-S. (2001). The elementary spike produced by a pure e^+e^- pair-electromagnetic pulse from a Black Hole: The PEM Pulse. A&A, 368:377–390.

Bissaldi, E. et al. (2008). GRB 081007 and GRB 081007B: Fermi GBM detection. *GRB Coordinates Network*, 8369.

Bloom, J. S. et al. (1999). The unusual afterglow of the γ-ray burst of 26 March 1998 as evidence for a supernova connection. Nature, 401:453–456.

Bloom, J. S. et al. (2001). The Redshift and the Ordinary Host Galaxy of GRB 970228. ApJ, 554:678–683.

Bloom, J. S. et al. (2002). Detection of a Supernova Signature Associated with GRB 011121. ApJ, 572:L45–L49.

Briggs, M. S. et al. (1999). Observations of GRB 990123 by the Compton Gamma Ray Observatory. ApJ, 524:82–91.

Bromberg, O. et al. (2013). Short versus Long and Collapsars versus Non-collapsars: A Quantitative Classification of Gamma-Ray Bursts. ApJ, 764:179.

Bufano, F., Pian, E., Sollerman, J., Benetti, S., Pignata, G., Valenti, S., Covino, S., D'Avanzo, P., Malesani, D., Cappellaro, E., Della Valle, M., Fynbo, J., Hjorth, J., Mazzali, P. A., Reichart, D. E., Starling, R. L. C., Turatto, M., Vergani, S. D., Wiersema, K., Amati, L., Bersier, D., Campana, S., Cano, Z., Castro-Tirado, A. J., Chincarini, G., D'Elia, V., de Ugarte Postigo, A., Deng, J., Ferrero, P., Filippenko, A. V., Goldoni, P., Gorosabel, J., Greiner, J., Hammer, F., Jakobsson, P., Kaper, L., Kawabata, K. S., Klose, S., Levan, A. J., Maeda, K., Masetti, N., Milvang-Jensen, B., Mirabel, F. I., Møller, P., Nomoto, K., Palazzi, E., Piranomonte, S., Salvaterra, R., Stratta, G., Tagliaferri, G., Tanaka, M., Tanvir, N. R., and Wijers, R. A. M. J. (2012). The Highly Energetic Expansion of SN 2010bh Associated with GRB 100316D. ApJ, 753:67.

Burns, E. et al. (2016). Do the Fermi Gamma-Ray Burst Monitor and Swift Burst Alert Telescope see the Same Short Gamma-Ray Bursts? ApJ, 818:110.

Caito, L., Amati, L., Bernardini, M. G., Bianco, C. L., de Barros, G., Izzo, L., Patricelli, B., and Ruffini, R. (2010). GRB 071227: an additional case of a disguised short burst. A&A, 521:A80.

Caito, L., Bernardini, M. G., Bianco, C. L., Dainotti, M. G., Guida, R., and Ruffini, R. (2009). GRB060614: a "fake" short GRB from a merging binary system. A&A, 498:501–507.

Campana, S., Mangano, V., Blustin, A. J., Brown, P., Burrows, D. N., Chincarini, G., Cummings, J. R., Cusumano, G., Della Valle, M., Malesani, D., Mészáros, P., Nousek, J. A., Page, M., Sakamoto, T., Waxman, E., Zhang, B., Dai, Z. G., Gehrels, N., Immler, S., Marshall, F. E., Mason, K. O., Moretti, A., O'Brien, P. T., Osborne, J. P., Page, K. L., Romano, P., Roming, P. W. A., Tagliaferri, G., Cominsky, L. R., Giommi, P., Godet, O., Kennea, J. A., Krimm, H., Angelini,

L., Barthelmy, S. D., Boyd, P. T., Palmer, D. M., Wells, A. A., and White, N. E. (2006). The association of GRB 060218 with a supernova and the evolution of the shock wave. Nature, 442:1008–1010.

Cano, Z. (2013). A new method for estimating the bolometric properties of Ibc supernovae. MNRAS, 434:1098–1116.

Cano, Z. et al. (2011). A tale of two GRB-SNe at a common redshift of z=0.54. MNRAS, 413:669–685.

Cano, Z. et al. (2014). A trio of gamma-ray burst supernovae:. GRB 120729A, GRB 130215A/SN 2013ez, and GRB 130831A/SN 2013fu. A&A, 568:A19.

Cano, Z. et al. (2015). GRB 140606B/iPTF14bfu: detection of shock-breakout emission from a cosmological γ-ray burst? MNRAS, 452:1535–1552.

Cano, Z. et al. (2016). The Observer's Guide to the Gamma-Ray Burst-Supernova Connection. *LPI Contributions*, 1962:4116.

Challis, P. et al. (2010). Supernova 2010ak in MCG +03-41-142. *Central Bureau Electronic Telegrams*, 2206.

Cherubini, C., Geralico, A., Rueda, H. J. A., and Ruffini, R. (2009). e^--e^+ pair creation by vacuum polarization around electromagnetic black holes. Phys. Rev. D, 79(12):124002.

Cherubini, C., Ruffini, R., and Vitagliano, L. (2002). On the electromagnetic field of a charged collapsing spherical shell in general relativity. *Physics Letters B*, 545:226–232.

Chevalier, R. A. (2012). Common Envelope Evolution Leading to Supernovae with Dense Interaction. ApJ, 752:L2.

Chornock, R. et al. (2010). Spectroscopic Discovery of the Broad-Lined Type Ic Supernova 2010bh Associated with the Low-Redshift GRB 100316D. *ArXiv e-prints*.

Christodoulou, D. and Ruffini, R. (1971). Reversible Transformations of a Charged Black Hole. Phys. Rev. D, 4:3552–3555.

Cobb, B. E. et al. (2010). Discovery of SN 2009nz Associated with GRB 091127. ApJ, 718:L150–L155.

Daigne, F. and Mochkovitch, R. (2002). The expected thermal precursors of gamma-ray bursts in the internal shock model. MNRAS, 336:1271–1280.

Damour, T. and Ruffini, R. (1975). Quantum Electrodynamical Effects in Kerr-Newmann Geometries. *Physical Review Letters*, 35:463–466.

D'Avanzo, P., Melandri, A., Palazzi, E., Campana, S., Della Valle, M., Pian, E., Salvaterra, R., and Tagliaferri, G. (2012). GRB 111228A: possible detection of the SN with the TNG. *GRB Coordinates Network*, 13069.

de Barros, G., Amati, L., Bernardini, M. G., Bianco, C. L., Caito, L., Izzo, L., Patricelli, B., and Ruffini, R. (2011). On the nature of GRB 050509b: a disguised short GRB. A&A, 529:A130.

de Jaeger, T. et al. (2015). SN 2011A: A Low-luminosity Interacting Transient with a Double Plateau and Strong Sodium Absorption. ApJ, 807:63.

de Ugarte Postigo, A. et al. (2012). GRB 111211A: detection of the SN with the 10.4m GTC. *GRB Coordinates Network*, 12802.

de Ugarte Postigo, A. et al. (2015). GRB 150818A: Spectroscopic confirmation of the SN from GTC. *GRB Coordinates Network*, 18213.

Della Valle, M. et al. (2003). Evidence for supernova signatures in the spectrum of the late-time bump of the optical afterglow of GRB 021211. A&A, 406:L33–L37.

Della Valle, M. et al. (2006). Hypernova signatures in the late rebrightening of grb 050525a. ApJ, 642(2):L103.

Dong, S. et al. (2016). ASASSN-15lh: A highly super-luminous supernova. *Science*, 351:257–260.

Drake, A. J. et al. (2009a). Supernovae 2008iw, 2008ix, 2009bx, and 2009de-2009dk. *Central Bureau Electronic Telegrams*, 1766.

Drake, A. J. et al. (2009b). Supernovae 2008iw, 2008ix, 2009bx, and 2009de-2009dk. *Central Bureau Electronic Telegrams*, 1766.

Drake, A. J. et al. (2011). Supernova 2011jb. *Central Bureau Electronic Telegrams*, 2947.

Elias-Rosa, N. et al. (2016). Dead or Alive? Long-term evolution of SN 2015bh (SNhunt275). MNRAS, 463:3894–3920.

Folatelli, G. and Morrell, N. (2009). Supernovae 2009el and 2009em. *Central Bureau Electronic Telegrams*, 1807.

Friis, M. and Watson, D. (2013). Thermal Emission in the Early X-Ray Afterglows of Gamma-Ray Bursts: Following the Prompt Phase to Late Times. ApJ, 771:15.

Frontera, F. et al. (1998). High resolution imaging of the X-ray afterglow of GRB970228 with ROSAT. A&A, 334:L69–L72.

Fryer, C. L., Oliveira, F. G., Rueda, J. A., and Ruffini, R. (2015). Neutron-Star-Black-Hole Binaries Produced by Binary-Driven Hypernovae. *Physical Review Letters*, 115(23):231102.

Fryer, C. L., Rueda, J. A., and Ruffini, R. (2014). Hypercritical Accretion, Induced Gravitational Collapse, and Binary-Driven Hypernovae. ApJ, 793:L36.

Fynbo, J. P. U. et al. (2004). On the Afterglow of the X-Ray Flash of 2003 July 23: Photometric Evidence for an Off-Axis Gamma-Ray Burst with an Associated Supernova? ApJ, 609:962–971.

Gabrijelcic, A., Valles, P., Benetti, S., and Lidman, C. (1997). Supernova 1997B in IC 438. IAU Circ., 6535.

Galama, T. J. et al. (1998). An unusual supernova in the error box of the γ-ray burst of 25 April 1998. Nature, 395:670–672.

Galama, T. J. et al. (2000). Evidence for a Supernova in Reanalyzed Optical and Near-Infrared Images of GRB 970228. ApJ, 536:185–194.

Gall, E. et al. (2011). Supernova 2011bm in IC 3917 = PSN J12565389+2222282. *Central Bureau Electronic Telegrams*, 2695:2.

Gehrels, N. (1986). Confidence limits for small numbers of events in astrophysical data. ApJ, 303:336–346.

Germany, L. M. et al. (2000). SN 1997CY/GRB 970514: A New Piece in the Gamma-Ray Burst Puzzle? ApJ, 533:320–328.

Gorosabel, J. et al. (2005). A possible bright blue supernova in the afterglow of GRB 020305. A&A, 437:411–418.

Granata, V. et al. (2016). Asiago spectroscopic and photometric observations of AT2016bau. *The Astronomer's Telegram*, 8818.

Gruber, D. et al. (2014). The Fermi GBM Gamma-Ray Burst Spectral Catalog: Four Years of Data. ApJS, 211:12.

Guetta, D. and Della Valle, M. (2007). On the Rates of Gamma-Ray Bursts and Type Ib/c Supernovae. ApJ, 657:L73–L76.

Habergham, S. M. et al. (2014). Environments of interacting transients: impostors and Type IIn supernovae. MNRAS, 441:2230–2252.

Hakkila, J. et al. (1998). BATSE sky exposure. In Meegan, C. A., Preece, R. D., and Koshut, T. M., editors, *Gamma-Ray Bursts, 4th Hunstville Symposium*, volume 428 of *American Institute of Physics Conference Series*, pages 144–148.

Hakkila, J. et al. (2003). BATSE 5B Sky Exposure and Trigger Efficiency. In Ricker, G. R. and Vanderspek, R. K., editors, *Gamma-Ray Burst and Afterglow Astronomy 2001: A Workshop Celebrating the First Year of the HETE Mission*, volume 662 of *American Institute of Physics Conference Series*, pages 176–178.

Han, W.-B., Ruffini, R., and Xue, S.-S. (2010). Electron-positron pair oscillation in spatially inhomogeneous electric fields and radiation. *Physics Letters B*, 691:99–104.

Han, W.-B., Ruffini, R., and Xue, S.-S. (2012). Electron and positron pair production of compact stars. Phys. Rev. D, 86(8):084004.

Hill, J. et al. (2007). GRB 070419A, deep LBT photometry and possible supernova detection. *GRB Coordinates Network*, 6486.

Hjorth, J. and Bloom, J. S. (2012). *The Gamma-Ray Burst - Supernova Connection*, pages 169–190.

Holland, S. T. et al. (2010). GRB 100418A: possible evidence for a supernova. *GRB Coordinates Network*, 10661.

Hurley, K., Briggs, M., Kippen, R. M., Kouveliotou, C., Fishman, C. M. G., Cline, T., Trombka, J., McClanahan, T., Stern, M. B. B., Kommers, J., Mazets, E., Golenetskii, S., Feroci, J. G. M., Frontera, F., Guidorzi, C., Montanari, E., Sinha, W. L. S., and Seetha, S. (2005a). The interplanetary network supplements to the BATSE 5B and untriggered burst catalogs. *Nuovo Cimento C Geophysics Space Physics C*, 28:299.

Hurley, K. et al. (2005b). An exceptionally bright flare from SGR 1806-20 and the origins of short-duration γ-ray bursts. Nature, 434:1098–1103.

Hurley, K., Guidorzi, C., Frontera, F., Montanari, E., Rossi, F., Feroci, M., Mazets, E., Golenetskii, S., Frederiks, D. D., Pal'shin, V. D., Aptekar, R. L., Cline, T., Trombka, J., McClanahan, T., Starr, R., Atteia, J.-L., Barraud, C., Pélangeon, A., Boër, M., Vanderspek, R., Ricker, G., Mitrofanov, I. G., Golovin, D. V., Kozyrev, A. S., Litvak, M. L., Sanin, A. B., Boynton, W., Fellows, C., Harshman, K., Goldsten, J., Gold, R., Smith, D. M., Wigger, C., and Hajdas, W. (2010). The Interplanetary Network Supplement to the BeppoSAX Gamma-ray Burst Catalogs. ApJS, 191:179–184.

Inserra, C. et al. (2016). On Type IIn/Ia-CSM supernovae as exemplified by SN 2012ca*. MNRAS, 459:2721–2740.

Inserra, C. et al. (2018). On the nature of hydrogen-rich superluminous supernovae. MNRAS, 475:1046–1072.

Iwamoto, K. et al. (1998). A hypernova model for the supernova associated with the γ-ray burst of 25 April 1998. Nature, 395:672–674.

Izzo, L., Ruffini, R., Penacchioni, A. V., Bianco, C. L., Caito, L., Chakrabarti, S. K., Rueda, J. A., Nandi, A., and Patricelli, B. (2012a). A double component in GRB 090618: a proto-black hole and a genuinely long gamma-ray burst. A&A, 543:A10.

Izzo, L., Ruffini, R., Penacchioni, A. V., Bianco, C. L., Caito, L., Chakrabarti, S. K., Rueda, J. A., Nandi, A., and Patricelli, B. (2012b). A double component in GRB 090618: a proto-black hole and a genuinely long gamma-ray burst. A&A, 543:A10.

Jha, S. et al. (1997). Supernova 1997cq in Anonymous Galaxy. IAU Circ., 6675.

Jha, S. et al. (1998). Supernova 1998ct in UGC 10062. IAU Circ., 6964.

Jin, Z.-P., Covino, S., Della Valle, M., Ferrero, P., Fugazza, D., Malesani, D., Melandri, A., Pian, E., Salvaterra, R., Bersier, D., Campana, S., Cano, Z., Castro-Tirado, A. J., D'Avanzo, P., Fynbo, J. P. U., Gomboc, A., Gorosabel, J., Guidorzi, C., Haislip, J. B., Hjorth, J., Kobayashi, S., LaCluyze, A. P., Marconi, G., Mazzali, P. A., Mundell, C. G., Piranomonte, S., Reichart, D. E., Sánchez-Ramírez, R., Smith, R. J., Steele, I. A., Tagliaferri, G., Tanvir, N. R., Valenti, S., Vergani, S. D., Vestrand, T., Walker, E. S., and Woźniak, P. (2013). Grb 081007 and grb 090424: The surrounding medium, outflows, and supernovae. ApJ, 774(2):114.

Kamble, A. et al. (2013). JVLA observations of SN2013bv. *The Astronomer's Telegram*, 5034.

Kangas, T. et al. (2015). PESSTO spectroscopic classification of optical transients. *The Astronomer's Telegram*, 8296.

Kann, D. A. et al. (2016). Highly Luminous Supernovae associated with Gamma-Ray Bursts I.: GRB 111209A/SN 2011kl in the Context of Stripped-Envelope and Superluminous Supernovae. *ArXiv e-prints*.

Katz, B. et al. (2012). X-rays, γ-rays and neutrinos from collisionless shocks in supernova wind breakouts. In Roming, P., Kawai, N., and Pian, E., editors, *Death of Massive Stars: Supernovae and Gamma-Ray Bursts*, volume 279 of *IAU Symposium*, pages 274–281.

Kleinert, H., Ruffini, R., and Xue, S.-S. (2008). Electron-positron pair production in space- or time-dependent electric fields. Phys. Rev. D, 78(2):025011.

Klose, S. et al. (2012). Supernova 2012eb = GRB 120714B. *Central Bureau Electronic Telegrams*,

3200.

Kochanek, C. S. et al. (2012). Unmasking the Supernova Impostors. ApJ, 758:142.

Kovacevic, M., Izzo, L., Wang, Y., Muccino, M., Della Valle, M., Amati, L., Barbarino, C., Enderli, M., Pisani, G. B., and Li, L. (2014). A search for Fermi bursts associated with supernovae and their frequency of occurrence. A&A, 569:A108.

Kumar, P. and Zhang, B. (2015). The physics of gamma-ray bursts and relativistic jets. Phys. Rep., 561:1–109.

Larsson, J. et al. (2015). Evidence for Jet Launching Close to the Black Hole in GRB 101219b - A Fermi GRB Dominated by Thermal Emission. ApJ, 800:L34.

Lazzati, D., Covino, S., Ghisellini, G., Fugazza, D., Campana, S., Saracco, P., Price, P. A., Berger, E., Kulkarni, S., Ramirez-Ruiz, E., Cimatti, A., Della Valle, M., di Serego Alighieri, S., Celotti, A., Haardt, F., Israel, G. L., and Stella, L. (2001). The optical afterglow of GRB 000911: Evidence for an associated supernova? A&A, 378:996–1002.

Levan, A. et al. (2005). GRB 020410: A Gamma-Ray Burst Afterglow Discovered by Its Supernova Light. ApJ, 624:880–888.

Leyder, J.-C. et al. (2008). Hard X-ray emission from η Carinae. A&A, 477:L29–L32.

Li, W. et al. (2002). A Hubble Space Telescope Snapshot Survey of Nearby Supernovae. PASP, 114:403–415.

Li, W. et al. (2011). Nearby supernova rates from the Lick Observatory Supernova Search - II. The observed luminosity functions and fractions of supernovae in a complete sample. MNRAS, 412:1441–1472.

Liang, E. et al. (2006). Thermal Emission from a Hot Cocoon Surrounding the Jet of XRF 060218. *ArXiv Astrophysics e-prints*.

Liang, E. et al. (2007). Low-Luminosity Gamma-Ray Bursts as a Unique Population: Luminosity Function, Local Rate, and Beaming Factor. ApJ, 662:1111–1118.

Malesani, D., Tagliaferri, G., Chincarini, G., Covino, S., Della Valle, M., Fugazza, D., Mazzali, P. A., Zerbi, F. M., D'Avanzo, P., Kalogerakos, S., Simoncelli, A., Antonelli, L. A., Burderi, L., Campana, S., Cucchiara, A., Fiore, F., Ghirlanda, G., Goldoni, P., Götz, D., Mereghetti, S., Mirabel, I. F., Romano, P., Stella, L., Minezaki, T., Yoshii, Y., and Nomoto, K. (2004). SN 2003lw and GRB 031203: A Bright Supernova for a Faint Gamma-Ray Burst. ApJ, 609:L5–L8.

Margutti, R. et al. (2014). A Panchromatic View of the Restless SN 2009ip Reveals the Explosive Ejection of a Massive Star Envelope. ApJ, 780:21.

Masetti, N., Palazzi, E., Pian, E., Simoncelli, A., Hunt, L. K., Maiorano, E., Levan, A., Christensen, L., Rol, E., Savaglio, S., Falomo, R., Castro-Tirado, A. J., Hjorth, J., Delsanti, A., Pannella, M., Mohan, V., Pandey, S. B., Sagar, R., Amati, L., Burud, I., Castro Cerón, J. M., Frontera, F., Fruchter, A. S., Fynbo, J. P. U., Gorosabel, J., Kaper, L., Klose, S., Kouveliotou, C., Nicastro, L., Pedersen, H., Rhoads, J., Salamanca, I., Tanvir, N., Vreeswijk, P. M., Wijers, R. A. M. J., and van den Heuvel, E. P. J. (2003). Optical and near-infrared observations of the GRB020405 afterglow. A&A, 404:465–481.

Mauerhan, J. C. et al. (2015). SN Hunt 248: a super-Eddington outburst from a massive cool hypergiant. MNRAS, 447:1922–1934.

Meegan, C. A. (1997). The BATSE Catalog of Gamma-Ray Bursts. *NASA STI/Recon Technical Report N*, 1.

Melandri, A., Pian, E., D'Elia, V., D'Avanzo, P., Della Valle, M., Mazzali, P. A., Tagliaferri, G., Cano, Z., Levan, A. J., Møoller, P., Amati, L., Bernardini, M. G., Bersier, D., Bufano, F., Campana, S., Castro-Tirado, A. J., Covino, S., Ghirlanda, G., Hurley, K., Malesani, D., Masetti, N., Palazzi, E., Piranomonte, S., Rossi, A., Salvaterra, R., Starling, R. L. C., Tanaka, M., Tanvir, N. R., and Vergani, S. D. (2014). Diversity of gamma-ray burst energetics vs. supernova homogeneity: SN 2013cq associated with GRB 130427A. A&A, 567:A29.

Melandri, A., Pian, E., Ferrero, P., D'Elia, V., Walker, E. S., Ghirlanda, G., Covino, S., Amati, L., D'Avanzo, P., Mazzali, P. A., Della Valle, M., Guidorzi, C., Antonelli, L. A., Bernardini, M. G.,

Bersier, D., Bufano, F., Campana, S., Castro-Tirado, A. J., Chincarini, G., Deng, J., Filippenko, A. V., Fugazza, D., Ghisellini, G., Kouveliotou, C., Maeda, K., Marconi, G., Masetti, N., Nomoto, K., Palazzi, E., Patat, F., Piranomonte, S., Salvaterra, R., Saviane, I., Starling, R. L. C., Tagliaferri, G., Tanaka, M., and Vergani, S. D. (2012). The optical SN 2012bz associated with the long GRB 120422A. A&A, 547:A82.

Mészáros, P. (2006). Gamma-ray bursts. *Reports on Progress in Physics*, 69:2259–2321.

Mészáros, P. and Rees, M. J. (2000). Steep Slopes and Preferred Breaks in Gamma-Ray Burst Spectra: The Role of Photospheres and Comptonization. ApJ, 530:292–298.

Monard, L. A. G. (2009a). Supernova 2009em in NGC 157. *Central Bureau Electronic Telegrams*, 1798.

Monard, L. A. G. (2009b). Supernova 2009em in NGC 157. *Central Bureau Electronic Telegrams*, 1798.

Muccino, M., Ruffini, R., Bianco, C. L., Izzo, L., and Penacchioni, A. V. (2013a). GRB 090227B: The Missing Link between the Genuine Short and Long Gamma-Ray Bursts. ApJ, 763:125.

Muccino, M., Ruffini, R., Bianco, C. L., Izzo, L., Penacchioni, A. V., and Pisani, G. B. (2013b). GRB 090510: A Disguised Short Gamma-Ray Burst with the Highest Lorentz Factor and Circumburst Medium. ApJ, 772:62.

Nakano, S. et al. (1997). Supernova 1997E in NGC 2258. IAU Circ., 6538.

Nakar, E., Gal-Yam, A., Piran, T., and Fox, D. B. (2006). The Distances of Short-Hard Gamma-Ray Bursts and the Soft Gamma-Ray Repeater Connection. ApJ, 640:849–853.

Nappo, F. et al. (2017). The 999th Swift gamma-ray burst: Some like it thermal. A multiwavelength study of GRB 151027A. A&A, 598:A23.

Navasardyan, H. and Benetti, S. (2009a). Supernova 2009em in NGC 157. *Central Bureau Electronic Telegrams*, 1806.

Navasardyan, H. and Benetti, S. (2009b). Supernova 2009em in NGC 157. *Central Bureau Electronic Telegrams*, 1806.

Ofek, E. O. et al. (2013). An outburst from a massive star 40 days before a supernova explosion. Nature, 494:65–67.

Ofek, E. O. et al. (2014). Precursors Prior to Type IIn Supernova Explosions are Common: Precursor Rates, Properties, and Correlations. ApJ, 789:104.

Ouyed, R. et al. (2011). Quark-novae in Low-mass X-ray Binaries with Massive Neutron Stars: A Universal Model for Short-hard Gamma-ray Bursts. ApJ, 729:60.

Ouyed, R. et al. (2013). SN 2009ip and SN 2010mc as dual-shock Quark-Novae. *Research in Astronomy and Astrophysics*, 13:1463–1470.

Page, K. L. et al. (2011). GRB 090618: detection of thermal X-ray emission from a bright gamma-ray burst. MNRAS, 416:2078–2089.

Palmer, D. M. et al. (2005). A giant γ-ray flare from the magnetar SGR 1806 - 20. Nature, 434:1107–1109.

Pal'shin, V. D., Hurley, K., Svinkin, D. S., Aptekar, R. L., Golenetskii, S. V., Frederiks, D. D., Mazets, E. P., Oleynik, P. P., Ulanov, M. V., Cline, T., Mitrofanov, I. G., Golovin, D. V., Kozyrev, A. S., Litvak, M. L., Sanin, A. B., Boynton, W., Fellows, C., Harshman, K., Trombka, J., McClanahan, T., Starr, R., Goldsten, J., Gold, R., Rau, A., von Kienlin, A., Savchenko, V., Smith, D. M., Hajdas, W., Barthelmy, S. D., Cummings, J., Gehrels, N., Krimm, H., Palmer, D., Yamaoka, K., Ohno, M., Fukazawa, Y., Hanabata, Y., Takahashi, T., Tashiro, M., Terada, Y., Murakami, T., Makishima, K., Briggs, M. S., Kippen, R. M., Kouveliotou, C., Meegan, C., Fishman, G., Connaughton, V., Boër, M., Guidorzi, C., Frontera, F., Montanari, E., Rossi, F., Feroci, M., Amati, L., Nicastro, L., Orlandini, M., Del Monte, E., Costa, E., Donnarumma, I., Evangelista, Y., Lapshov, I., Lazzarotto, F., Pacciani, L., Rapisarda, M., Soffitta, P., Di Cocco, G., Fuschino, F., Galli, M., Labanti, C., Marisaldi, M., Atteia, J.-L., Vanderspek, R., and Ricker, G. (2013). Interplanetary Network Localizations of Konus Short Gamma-Ray Bursts. ApJS, 207:38.

Pastorello, A. (2012). Supernova Taxonomy - New Types. *Memorie della Societa Astronomica*

Italiana Supplementi, 19:24.

Patricelli, B., Bernardini, M. G., Bianco, C. L., Caito, L., de Barros, G., Izzo, L., Ruffini, R., and Vereshchagin, G. V. (2012). Analysis of GRB 080319B and GRB 050904 within the Fireshell Model: Evidence for a Broader Spectral Energy Distribution. ApJ, 756:16.

Pe'er, A., Ryde, F., Wijers, R. A. M. J., Mészáros, P., and Rees, M. J. (2007). A New Method of Determining the Initial Size and Lorentz Factor of Gamma-Ray Burst Fireballs Using a Thermal Emission Component. ApJ, 664:L1–L4.

Penacchioni, A. V., Ruffini, R., Bianco, C. L., Izzo, L., Muccino, M., Pisani, G. B., and Rueda, J. A. (2013). GRB 110709B in the induced gravitational collapse paradigm. A&A, 551:A133.

Penacchioni, A. V., Ruffini, R., Izzo, L., Muccino, M., Bianco, C. L., Caito, L., Patricelli, B., and Amati, L. (2012). Evidence for a proto-black hole and a double astrophysical component in GRB 101023. A&A, 538:A58.

Peng, F.-K. et al. (2014). Photosphere Emission in the X-Ray Flares of Swift Gamma-Ray Bursts and Implications for the Fireball Properties. ApJ, 795:155.

Pignata, G. et al. (2011). Supernova 2011gw in IC 2200 = Psn J07281702-6221189. *Central Bureau Electronic Telegrams*, 2869.

Pignata, G. et al. (2012a). Supernova 2012ba in ESO 328-46 = Psn J15222512-3812042. *Central Bureau Electronic Telegrams*, 3058.

Pignata, G. et al. (2012b). Supernova 2012ba in ESO 328-46 = Psn J15222512-3812042. *Central Bureau Electronic Telegrams*, 3058.

Piran, T. (1999). Gamma-ray bursts and the fireball model. Phys. Rep., 314:575–667.

Piro, L. et al. (2014). A Hot Cocoon in the Ultralong GRB 130925A: Hints of a POPIII-like Progenitor in a Low-Density Wind Environment. ApJ, 790:L15.

Pisani, G. B., Izzo, L., Ruffini, R., Bianco, C. L., Muccino, M., Penacchioni, A. V., Rueda, J. A., and Wang, Y. (2013). Novel distance indicator for gamma-ray bursts associated with supernovae. A&A, 552:L5.

Pozanenko, A. et al. (2015). GRB 150518A: possible SN observations. *GRB Coordinates Network*, 17903.

Preparata, G., Ruffini, R., and Xue, S.-S. (1998). The dyadosphere of black holes and gamma-ray bursts. A&A, 338:L87–L90.

Rees, M. J. (1966). Appearance of Relativistically Expanding Radio Sources. Nature, 211:468–470.

Reichart, D. E. (1997). Observations and Theoretical Implications of GRB 970228. ApJ, 485:L57–L60.

Rex, J. et al. (2010). Supernova 2010ak in MCG +03-41-142. *Central Bureau Electronic Telegrams*, 2203.

Rigon, L. et al. (2003). SN 1999E: another piece in the supernova-gamma-ray burst connection puzzle. MNRAS, 340:191–196.

Rueda, J. A. and Ruffini, R. (2012). On the Induced Gravitational Collapse of a Neutron Star to a Black Hole by a Type Ib/c Supernova. ApJ, 758:L7.

Ruffini, R., Aimuratov, Y., Becerra, L., Bianco, C. L., Chen, Y. C., Karlica, M., Kovacevic, M., Melon Fuksman, J. D., Moradi, R., Muccino, M., Pisani, G. B., Primorac, D., Rueda, J. A., and Wang, Y. (2017a). On the nature of prompt emission, X and gamma ray flares and extended thermal emission in GRB 151027A. *ArXiv e-prints*.

Ruffini, R., Bernardini, M. G., Bianco, C. L., Caito, L., Chardonnet, P., Dainotti, M. G., Fraschetti, F., Guida, R., Rotondo, M., Vereshchagin, G., Vitagliano, L., and Xue, S.-S. (2007a). The Blackholic energy and the canonical Gamma-Ray Burst. In Novello, M. and Perez Bergliaffa, S. E., editors, *XIIth Brazilian School of Cosmololy and Gravitation*, volume 910 of *American Institute of Physics Conference Series*, pages 55–217.

Ruffini, R., Bernardini, M. G., Bianco, C. L., Chardonnet, P., Fraschetti, F., Guida, R., and Xue, S.-S. (2006). GRB 050315: A Step toward Understanding the Uniqueness of the Overall Gamma-Ray

Burst Structure. ApJ, 645:L109–L112.

Ruffini, R., Bernardini, M. G., Bianco, C. L., Chardonnet, P., Fraschetti, F., Gurzadyan, V., Lattanzi, M., Vitagliano, L., and Xue, S.-S. (2005a). Extracting energy from black holes: 'Long' and 'short' GRBs and their astrophysical settings. *Nuovo Cimento C Geophysics Space Physics C*, 28:589.

Ruffini, R., Bernardini, M. G., Bianco, C. L., Chardonnet, P., Fraschetti, F., and Xue, S.-S. (2004a). GRB 980425, SN1998BW and the EMBH model. *Advances in Space Research*, 34:2715–2722.

Ruffini, R., Bianco, C. L., Chardonnet, P., Fraschetti, F., Vitagliano, L., and Xue, S.-S. (2003a). New perspectives in physics and astrophysics from the theoretical understanding of Gamma-Ray Bursts. In Novello, M. and Perez Bergliaffa, S. E., editors, *Cosmology and Gravitation*, volume 668 of *American Institute of Physics Conference Series*, pages 16–107.

Ruffini, R., Bianco, C. L., Chardonnet, P., Fraschetti, F., and Xue, S.-S. (2002). On the Structures in the Afterglow Peak Emission of Gamma-Ray Bursts. ApJ, 581:L19–L22.

Ruffini, R., Bianco, C. L., Fraschetti, F., Xue, S.-S., and Chardonnet, P. (2001a). On the Interpretation of the Burst Structure of Gamma-Ray Bursts. ApJ, 555:L113–L116.

Ruffini, R., Bianco, C. L., Fraschetti, F., Xue, S.-S., and Chardonnet, P. (2001b). Relative Spacetime Transformations in Gamma-Ray Bursts. ApJ, 555:L107–L111.

Ruffini, R., Bianco, C. L., Xue, S.-S., Chardonnet, P., Fraschetti, F., and Gurzadyan, V. (2004b). On the Instantaneous Spectrum of Gamma-Ray Bursts. *International Journal of Modern Physics D*, 13:843–851.

Ruffini, R., Bianco, C. L., Xue, S.-S., Chardonnet, P., Fraschetti, F., and Gurzadyan, V. (2005b). Emergence of a Filamentary Structure in the Fireball from GRB Spectra. *International Journal of Modern Physics D*, 14:97–105.

Ruffini, R., Izzo, L., Bianco, C. L., Rueda, J. A., Barbarino, C., Dereli, H., Enderli, M., Muccino, M., Penacchioni, A. V., Pisani, G. B., and Wang, Y. (2015a). Induced gravitational collapse in the BATSE era: The case of GRB 970828. *Astronomy Reports*, 59:626–638.

Ruffini, R., Izzo, L., Muccino, M., Pisani, G. B., Rueda, J. A., Wang, Y., Barbarino, C., Bianco, C. L., Enderli, M., and Kovacevic, M. (2014a). Induced gravitational collapse at extreme cosmological distances: the case of GRB 090423. A&A, 569:A39.

Ruffini, R., Muccino, M., Aimuratov, Y., Bianco, C. L., Cherubini, C., Enderli, M., Kovacevic, M., Moradi, R., Penacchioni, A. V., Pisani, G. B., Rueda, J. A., and Wang, Y. (2016a). GRB 090510: a genuine short-GRB from a binary neutron star coalescing into a Kerr-Newman black hole. *ArXiv e-prints*.

Ruffini, R., Muccino, M., Bianco, C. L., Enderli, M., Izzo, L., Kovacevic, M., Penacchioni, A. V., Pisani, G. B., Rueda, J. A., and Wang, Y. (2014b). On binary-driven hypernovae and their nested late X-ray emission. A&A, 565:L10.

Ruffini, R., Muccino, M., Bianco, C. L., Enderli, M., Izzo, L., Kovacevic, M., Penacchioni, A. V., Pisani, G. B., Rueda, J. A., and Wang, Y. (2014c). On binary-driven hypernovae and their nested late X-ray emission. A&A, 565:L10.

Ruffini, R., Muccino, M., Kovacevic, M., Oliveira, F. G., Rueda, J. A., Bianco, C. L., Enderli, M., Penacchioni, A. V., Pisani, G. B., Wang, Y., and Zaninoni, E. (2015b). GRB 140619B: a short GRB from a binary neutron star merger leading to black hole formation. ApJ, 808:190.

Ruffini, R., Rodriguez, J., Muccino, M., Rueda, J. A., Aimuratov, Y., Barres de Almeida, U., Becerra, L., Bianco, C. L., Cherubini, C., Filippi, S., Gizzi, D., Kovacevic, M., Moradi, R., Oliveira, F. G., Pisani, G. B., and Wang, Y. (2016b). On the rate and on the gravitational wave emission of short and long GRBs. *ArXiv e-prints*.

Ruffini, R., Rueda, J. A., Muccino, M., Aimuratov, Y., Becerra, L. M., Bianco, C. L., Kovacevic, M., Moradi, R., Oliveira, F. G., Pisani, G. B., and Wang, Y. (2016c). On the classification of GRBs and their occurrence rates. *ArXiv e-prints*.

Ruffini, R., Salmonson, J. D., Wilson, J. R., and Xue, S.-S. (1999). On the pair electromagnetic pulse of a black hole with electromagnetic structure. A&A, 350:334–343.

Ruffini, R., Salmonson, J. D., Wilson, J. R., and Xue, S.-S. (2000). On the pair-electromagnetic

pulse from an electromagnetic black hole surrounded by a baryonic remnant. A&A, 359:855–864.

Ruffini, R., Siutsou, I. A., and Vereshchagin, G. V. (2013). A Theory of Photospheric Emission from Relativistic Outflows. ApJ, 772:11.

Ruffini, R., Siutsou, I. A., and Vereshchagin, G. V. (2014d). Spreading of ultrarelativistically expanding shell: An application to GRBs. New A, 27:30–33.

Ruffini, R., Vereshchagin, G. V., and Wang, Y. (2017b). Thermal emission in the early afterglow of gamma-ray bursts from their interaction with supernova ejecta. A&A, 600:A131.

Ruffini, R., Vereshchagin, G. V., and Xue, S.-S. (2007b). Vacuum polarization and plasma oscillations. *Physics Letters A*, 371:399–405.

Ruffini, R. and Vitagliano, L. (2002). Irreducible mass and energetics of an electromagnetic black hole. *Physics Letters B*, 545:233–237.

Ruffini, R. and Vitagliano, L. (2003). Energy Extraction from Gravitational Collapse to Static Black Holes. *International Journal of Modern Physics D*, 12:121–127.

Ruffini, R., Vitagliano, L., and Xue, S.-S. (2003b). On a separatrix in the gravitational collapse to an overcritical electromagnetic black hole. *Physics Letters B*, 573:33–38.

Ruffini, R., Vitagliano, L., and Xue, S.-S. (2003c). On plasma oscillations in strong electric fields. *Physics Letters B*, 559:12–19.

Ruffini, R., Wang, Y., Aimuratov, Y., Barres de Almeida, U., Becerra, L., Bianco, C. L., Chen, Y. C., Karlica, M., Kovacevic, M., Li, L., Melon Fuksman, J. D., Moradi, R., Muccino, M., Penacchioni, A. V., Pisani, G. B., Primorac, D., Rueda, J. A., Shakeri, S., Vereshchagin, G. V., and Xue, S.-S. (2018). Early X-Ray Flares in GRBs. ApJ, 852:53.

Ruffini, R., Wang, Y., Enderli, M., Muccino, M., Kovacevic, M., Bianco, C. L., Penacchioni, A. V., Pisani, G. B., and Rueda, J. A. (2015c). GRB 130427A and SN 2013cq: A Multi-wavelength Analysis of An Induced Gravitational Collapse Event. ApJ, 798:10.

Ruffini, R., Wang, Y., Enderli, M., Muccino, M., Kovacevic, M., Bianco, C. L., Penacchioni, A. V., Pisani, G. B., and Rueda, J. A. (2015d). GRB 130427A and SN 2013cq: A Multi-wavelength Analysis of An Induced Gravitational Collapse Event. ApJ, 798:10.

Ruffini, R. and Wheeler, J. A. (1971). Introducing the black hole. *Physics Today*, 24:30.

Ruffini, R. and Xue, S.-S. (2011). Electron-positron pairs production in a macroscopic charged core. *Physics Letters B*, 696:416–421.

Rui, L. et al. (2016). Spectroscopic Classification of SN 2016bll (=PTSS-16ckr) as a Type Ib Supernova. *The Astronomer's Telegram*, 8908.

Schwartz, M. (1998). Supernova 1998ct in UGC 10062. IAU Circ., 6957.

Silverman, J. M. et al. (2013). Type Ia Supernovae Strongly Interacting with Their Circumstellar Medium. ApJS, 207:3.

Singer, L. P. et al. (2013). Discovery and Redshift of an Optical Afterglow in 71 deg^2: iPTF13bxl and GRB 130702A. ApJ, 776:L34.

Smartt, S. J. et al. (2009). The death of massive stars - I. Observational constraints on the progenitors of Type II-P supernovae. MNRAS, 395:1409–1437.

Smith, N. (2016). Interacting Supernovae: Types IIn and Ibn. *ArXiv e-prints*.

Smith, N. et al. (2014). SN 2009ip and SN 2010mc: core-collapse Type IIn supernovae arising from blue supergiants. MNRAS, 438:1191–1207.

Smith, N. et al. (2016). Massive stars dying alone: the extremely remote environment of SN 2009ip. MNRAS, 463:2904–2911.

Soderberg, A. M. et al. (2006a). An HST Study of the Supernovae Accompanying GRB 040924 and GRB 041006. ApJ, 636:391–399.

Soderberg, A. M. et al. (2007). A Spectacular Radio Flare from XRF 050416a at 40 Days and Implications for the Nature of X-Ray Flashes. ApJ, 661:982–994.

Soderberg, A. M., Kulkarni, S. R., Nakar, E., Berger, E., Cameron, P. B., Fox, D. B., Frail, D., Gal-Yam, A., Sari, R., Cenko, S. B., Kasliwal, M., Chevalier, R. A., Piran, T., Price, P. A., Schmidt, B. P., Pooley, G., Moon, D.-S., Penprase, B. E., Ofek, E., Rau, A., Gehrels, N., Nousek, J. A., Burrows, D. N., Persson, S. E., and McCarthy, P. J. (2006b). Relativistic ejecta from X-ray flash XRF 060218 and the rate of cosmic explosions. Nature, 442:1014–1017.

Sparre, M. et al. (2011). Spectroscopic Evidence for SN 2010ma Associated with GRB 101219B. ApJ, 735:L24.

Sparre, M. and Starling, R. L. C. (2012). A search for thermal X-ray signatures in gamma-ray bursts - II. The Swift sample. MNRAS, 427:2965–2974.

Stanek, K. Z. et al. (2003). Spectroscopic Discovery of the Supernova 2003dh Associated with GRB 030329. ApJ, 591:L17–L20.

Starling, R. L. C. et al. (2011). Discovery of the nearby long, soft GRB 100316D with an associated supernova. MNRAS, 411:2792–2803.

Starling, R. L. C. et al. (2012). A search for thermal X-ray signatures in gamma-ray bursts - I. Swift bursts with optical supernovae. MNRAS, 427:2950–2964.

Tanvir, N. R. et al. (2010). Late-time Observations of GRB 080319B: Jet Break, Host Galaxy, and Accompanying Supernova. ApJ, 725:625–632.

Tartaglia, L. et al. (2016). Interacting supernovae and supernova impostors. LSQ13zm: an outburst heralds the death of a massive star. MNRAS, 459:1039–1059.

Taylor, G. B. et al. (2004). The Angular Size and Proper Motion of the Afterglow of GRB 030329. ApJ, 609:L1–L4.

Terreran, G. et al. (2016). Asiago spectroscopic classification of 5 supernovae. *The Astronomer's Telegram*, 9419.

Thöne, C. C. et al. (2017). SN 2015bh: NGC 2770's 4th supernova or a luminous blue variable on its way to a Wolf-Rayet star? A&A, 599:A129.

Tomasella, L. et al. (2014). Asiago spectroscopic classification of PSN J00574018+4347342 as a type-Ic SN. *The Astronomer's Telegram*, 6506.

Toy, V. L. et al. (2016). Optical and Near-infrared Observations of SN 2013dx Associated with GRB 130702A. ApJ, 818:79.

Troja, E. et al. (2017). The X-ray counterpart to the gravitational-wave event GW170817. Nature, 551:71–74.

Turatto, M. (2003). Classification of Supernovae. In Weiler, K., editor, *Supernovae and Gamma-Ray Bursters*, volume 598 of *Lecture Notes in Physics, Berlin Springer Verlag*, pages 21–36.

Turatto, M., Suzuki, T., Mazzali, P. A., Benetti, S., Cappellaro, E., Danziger, I. J., Nomoto, K., Nakamura, T., Young, T. R., and Patat, F. (2000). The Properties of Supernova 1997CY Associated with GRB 970514. ApJ, 534:L57–L61.

Turolla, R. et al. (2015). Magnetars: the physics behind observations. A review. *Reports on Progress in Physics*, 78(11):116901.

Valenti, S. et al. (2012). A Spectroscopically Normal Type Ic Supernova from a Very Massive Progenitor. ApJ, 749:L28.

Van Dyk, S. D. et al. (2000). SN 1997bs in M66: Another Extragalactic η Carinae Analog? PASP, 112:1532–1541.

Vereshchagin, G. V. (2014). Physics of Nondissipative Ultrarelativistic Photospheres. *International Journal of Modern Physics D*, 23:1430003–125.

von Kienlin, A. et al. (2014). VizieR Online Data Catalog: The second Fermi/GBM GRB catalog (4yr) (von Kienlin+, 2014). *VizieR Online Data Catalog*, 221.

Wanderman, D. and Piran, T. (2010). The luminosity function and the rate of Swift's gamma-ray bursts. MNRAS, 406:1944–1958.

Woods, P. M. and Thompson, C. (2006). *Soft gamma repeaters and anomalous X-ray pulsars: magnetar candidates*, pages 547–586.

Woosley, S. E. and Bloom, J. S. (2006). The Supernova Gamma-Ray Burst Connection. ARA&A, 44:507–556.

Zeh, A. et al. (2004). A Systematic Analysis of Supernova Light in Gamma-Ray Burst Afterglows. ApJ, 609:952–961.